

Aus dem Bereich medizinische Biochemie
Theoretische Medizin und Biowissenschaften
Der Medizinischen Fakultät
Der Universität des Saarlandes, Homburg/Saar

**The baker's yeast *Saccharomyces cerevisiae*
as a model for studying chronic diseases
related to lipid-based ER-stress**

Dissertation zur Erlangung des Grades eines
Doktors der Naturwissenschaften
Der Medizinischen Fakultät
Der Universität des Saarlandes
2023

vorgelegt von: Carsten Mattes
geb. am: 28.12.1990 in Trier

Tag der Promotion: 13.09.2023

Dekan: Univ.-Prof. Dr. med. Michael D. Menger

Berichterstatter: Prof. Robert Ernst

Prof. Tobias Hartmann

I Index

I	Index.....	1
II	List of abbreviations	5
III	List of figures	7
IV	List of tables	10
V	Zusammenfassung	11
VI	Abstract	17
VII	Declaration	22
1	Introduction.....	23
1.1	The importance of models in biology.....	23
1.2	The endoplasmic reticulum – hallmark of the eukaryotic cell and the maestro of interorganellar communication.....	26
1.3	The unfolded protein response – a holistic view on maintaining cellular integrity through organellar homeostasis.....	29
1.4	The dominance of <i>S. cerevisiae</i> in lipid metabolic research	36
1.4.1	The three categories of eukaryotic membrane lipids	36
1.4.2	The OLE pathway – maintaining membrane fluidity	42
2	Materials	48
2.1	Consumables.....	48
2.2	Chemicals.....	49
2.3	Enzymes.....	50
2.4	Kits	51
2.5	Media and buffers	52
2.6	Oligonucleotids	54
2.7	Plasmids	59
2.8	Strains	60
3	Methods.....	65
3.1	Microbiological methods.....	65
3.1.1	Generation and transformation of chemically competent <i>E. coli</i>	65

3.1.2	Generation, transformation and storage of <i>S. cerevisiae</i> strains	66
3.1.3	Cultivation of <i>S. cerevisiae</i> strains	66
3.2	Molecular biological methods	67
3.2.1	Polymerase chain reaction (PCR)	67
3.2.2	Agarose gel electrophoresis.....	68
3.2.3	Gibson assembly technique	68
3.2.4	Minimal inhibitory concentration assay.....	70
3.2.5	Temperature gradient growth Assay	70
3.2.6	Quantitative real time PCR (qRT-PCR).....	71
3.3	Biochemical methods.....	71
3.3.1	Cell lysate preparation and lipid extraction.....	71
3.4	Cell imaging	72
3.4.1	Phenotypic high-throughput microscopy screening	72
3.4.2	Live cell imaging (epifluorescence microscopy)	72
3.4.3	Confocal laser scanning microscopy and FRAP.....	73
4	Results.....	74
4.1	The impact of established UPR inducing drugs on the lipidome of <i>Saccharomyces cerevisiae</i>	74
4.1.1	A systematic screen to find complete minimal inhibitory concentrations that allow for a comparison between DTT and TM as UPR inducing drugs	74
4.1.2	Acute ER-stress and its consequences on cellular growth	76
4.1.3	The impact of DTT and TM on the lipid class composition of acutely stressed <i>S. cerevisiae</i>	78
4.2	A closer look at Ire1p dimeric TMD signaling-active conformation under LBS and proteotoxic ER-stress	84
4.2.1	Generation of a cysteine-less Ire1p and validation of its function	84
4.2.2	Validating the functionality of cysteine-less Ire1p constructs with single cysteine substitutions in the TMD.....	87
4.2.3	Proteotoxic and lipid bilayer stress converge in a common signaling-active architecture of Ire1p's TMH region	89

4.2.4	Does the unusual X-shaped conformation of Ire1p account for its lipid bilayer stress sensing potential?.....	90
4.3	<i>S. cerevisiae</i> as a model for studying chronic diseases related to ER-stress	94
4.3.1	The phenotypes of the <i>mga2Δ</i> strain of <i>S. cerevisiae</i>	94
4.3.2	A systematic genome wide high throughput screen with <i>mga2Δ</i> to identify phenotype alleviating and aggravating genetic interactions.....	99
4.3.3	The degree of lipidome saturation correlates with the emergence of aberrant ER morphologies	109
4.3.4	Finding the missing link between the UPR and aberrant ER morphology in <i>mga2Δ</i>	115
4.3.5	The aberrant ER phenotype in <i>mga2Δ</i> shows a cell cycle dependent dynamic	120
4.3.6	Probing the origin of the aberrant ER with a set of distinct localizing subdomain ER-marker proteins.....	125
4.3.7	A putative role for ROS in promoting the formation of aberrant ER structures	130
5	Discussion	135
5.1	The UPR has little to no effect on remodeling of the lipidome within one hour of acute ER-stress	135
5.1.1	The impact of DTT and TM on the cellular growth of <i>S. cerevisiae</i>	135
5.1.2	Impact of the medium on the lipid composition under ER-stress	136
5.2	Consequences of a maintained TMD architecture of Ire1p dimer under proteotoxic and lipid bilayer stress	138
5.2.1	Single-cysteine crosslinking and its potential on completing insights into the structural organization of single-spanning transmembrane proteins.....	138
5.2.2	Attempting to understand the membrane-based source of ER-stress under prolonged ER-stress inducing conditions	140
5.2.3	Utilizing interface mutants to investigate the contribution of Ire1p's X-shaped signaling-active configuration under acute and prolonged scenarios of ER-stress	144
5.3	Establishing an experimental framework to study lipid-induced ER-stress in eukaryotic cells by genetically manipulating the OLE pathway of <i>S. cerevisiae</i>	148
5.3.1	Phenotypes associated with a reduced membrane fluidity in <i>mga2Δ</i>	148

5.3.2	FRAP experiments show that membrane fluidity is maintained in the aberrant ER	151
5.3.3	Homeoviscous adaptation in context of <i>mga2</i> Δ	152
5.3.4	High throughput genomic screen uncovers cell cycle and mitochondrial processes to be involved in alleviating or aggravating the aberrant ER phenotype	153
5.3.5	<i>De novo</i> lipid synthesis – either regulated during the cell cycle or UPR dependent – could be detrimental in context of an impaired OLE pathway	160
5.3.6	The Aberrant ER is related to the lipid composition.....	163
5.3.7	A preliminary model for the aberrant ER phenotype.....	165
5.3.8	Outlook	166
6	References	168
7	Supplementary Information	218
8	Acknowledgements.....	221
9	Lebenslauf	225

II List of abbreviations

Acyl-CoA	Acyl coenzyme A
AH	Amphipathic helix
<i>B. subtilis</i>	<i>Bacillus subtilis</i>
bp	Base pair
CaCl ₂	Calcium chloride
CDP-DAG	Cytidine diphosphate diacylglycerol
<i>C. elegans</i>	<i>Caenorhabditis elegans</i>
cLD	Core luminal domain
CSM	Complete synthetic mixture
DAG	Diacylglycerol
DMSO	Dimethylsulfoxid
dNTP	Deoxynucleotide triphosphate
DTT	Dithiothreitol
ER	Endoplasmic reticulum
ERAD	ER-associated degradation
<i>E. coli</i>	<i>Escherichia coli</i>
FW	forward
GOI	Gene of interest
GPL	Glycerophospholipid
HCl	Hydrochloric acid
Ire1p	Inositol-requiring enzyme 1
MD	Molecular dynamics
MgCl ₂	Magnesium chloride
MHC 1	Major-histocompartibility complex 1
NaCl	Sodium chloride
NAD ⁺	Nicotinamide adenine dinucleotide (oxidized)
NADH	Nicotinamide adenine dinucleotide (reduced)
NADP	Nicotinamide adenine dinucleotide phosphate (oxidized)
NADPH	Nicotinamide adenine dinucleotide phosphate (reduced)
NE	Nuclear envelope
OD	Optical density
PA	Phosphatidic acid
PBS	Phosphate buffered saline
PC	Phosphatidylcholine

Table continues on the following page

PCR	Polymerase chain reaction
PE	Phosphatidylethanolamine
PEG	Polyethylene glycol
PI	Phosphatidylinositol
PS	Phosphatidylserine
RER	Rough ER
RV	reverse
RNase	Ribonuclease
RT	Room temperature or reverse transcription
<i>S. cerevisiae</i>	<i>Saccharomyces cerevisiae</i>
SCD	Synthetic complete medium
SDS	Sodium dodecyl sulfate
SER	Smooth ER
TAG	Triacylglycerol
TM	Transmembrane domain
Tm	Tunicamycin
TMD	Transmembrane domain
TMH	Transmembrane helix
UPR	Unfolded protein response
YNB	Yeast nitrogen base

III List of figures

Figure 1 Evolutionary steps towards a modern eukaryotic cell	28
Figure 2 The role of Ire1p as the most conserved UPR sensor in adaptive and pro-apoptotic cell signaling	31
Figure 3 Structural organization of Ire1p's ER-luminal, transmembrane and cytosolic domain and a peptide binding groove	34
Figure 4 The three major membrane lipid categories	37
Figure 5 Simplified metabolic map of <i>S. cerevisiae</i> 's lipid <i>de novo</i> synthesis pathways	41
Figure 6 A schematic representation of the OLE pathway responsible for regulating the lipid saturation in the ER membrane.....	46
Figure 7 Impact of DTT and TM on cellular growth in chemically defined minimal medium (SCD) and complex medium (YPD).....	75
Figure 8: Consequences of acute ER-stress on cellular growth in complex medium (YPD)	77
Figure 9: Consequences of acute ER-stress on cellular growth in chemically defined minimal medium (SCD)	77
Figure 10 The lipid class composition of WT and <i>ire1Δ</i> cells grown in YPD medium after one hour of proteotoxic stress exposure	79
Figure 11 The lipid class composition of WT and <i>ire1Δ</i> cells grown in SCD medium after one hour of proteotoxic stress exposure	80
Figure 12 The impact of cultivation medium on the lipid class composition of WT and <i>ire1Δ</i> cells	82
Figure 13 Schematic representation of the <i>IRE1</i> knock-in construct used in this study with highlighted functional domains and elements.....	85
Figure 14 Cysteine-less Ire1p is functionally indistinguishable from the native form.....	86
Figure 15 <i>HAC1</i> mRNA splicing under proteotoxic stress for single-cysteine variants along the TMD of Ire1p.....	88
Figure 16: <i>HAC1</i> mRNA splicing during lipid bilayer stress (inositol depletion) of single cysteine variants of the TMD of Ire1p.....	88
Figure 17 A model for Ire1's dimeric TMD architecture.....	90
Figure 18 The conceived structural model of Ire1's dimer interface and the consequences for prolonged ER-stress in the absence of higher oligomeric state	93
Figure 19 Phenotype of the <i>mga2Δ</i> strain of <i>S. cerevisiae</i>	95
Figure 20 The <i>mga2Δ</i> phenotypic consequences for growth can be rescued or worsened by supplying exogenous fatty acids	97
Figure 21 The <i>mga2Δ</i> causes aberrant ER formations.....	98

Figure 22: FRAP experiments indicate impaired ER protein mobility in the aberrant ER structure opposed to the WT nuclear ER.....	99
Figure 23 Schematic representation of a genome-wide high throughput screening approach and its evaluation	100
Figure 24 Genome-wide high throughput screening results.....	103
Figure 25 A screening workflow illustration with quantitative and qualitative data for the worse and rescue categories.....	104
Figure 26 Aberrant ER structure emergence correlates with saturation of lipidome.....	110
Figure 27 The lipid class composition of wildtype cells and <i>mga2Δ</i> cells grown in YPD medium	111
Figure 28 lipid class composition of all candidates from the genome-wide high throughput screen in comparison to that of the query strains	112
Figure 29 lipid class composition of all candidates from the genome-wide high throughput screen in comparison to that of the query strains	114
Figure 30 Schematic overview of an inducible ER membrane biogenesis system.....	116
Figure 31 Membrane synthesis as a cause for aberrant ER morphology in <i>mga2Δ</i>	117
Figure 32 UPR independent ER membrane synthesis is sufficient to promote aberrant ER formation in <i>mga2Δ</i>	119
Figure 33 Manipulation of cell cycle progression affects aberrant ER formation	121
Figure 34 The emergence of the aberrant ER phenotype is dynamic and potentially linked to cell cycle progression during batch cultivation.....	124
Figure 35 Z-stacks reveal complex 3D orientation of aberrant ER and hint at its nuclear envelope origin.....	126
Figure 36 A visual and quantitative colocalization study with a set of distinct localizing ER membrane proteins in <i>mga2Δ</i> cells	128
Figure 37 3D rendering of z-stack images of aberrant ER structures reveals the step of inheritance of these structures and gives clues to changes in ER subdomain distribution.	129
Figure 38 A 96-well plate screening identifies compounds and conditions that promote and inhibit the growth of <i>mga2Δ</i> hinting at ROS production as one of the driving forces	130
Figure 39 Supplementation of antioxidants to the growth medium prevent the emergence of aberrant ER structures	131
Figure 40 CL species distribution of all worse candidates from the genome wide screen in comparison to those of the WT and <i>mga2Δ</i> query strains	133
Figure 41 CL species distribution of all rescue candidates from the genome wide screen in comparison the <i>mga2Δ</i> query strain	134
Figure 42 Physical interaction partners of Ubc4p and Ubc5p	158

Figure 43 Membrane synthesis – by growth or ER membrane expansion - promotes aberrant ER formation in <i>mga2Δ</i>	218
Figure 44 The <i>mga2Δ</i> strain accumulates in all glycerophospholipids saturated acyl chains – albeit to various degrees compared to the WT.	219
Figure 45 Visual co-localization of aberrant ER and microtubules (Tub1-mWasabi).....	219
Figure 46 The aberrant ER might be involved in perpetuating the UPR by entrapping Ire1p in subdomains thereby promoting the clustering of Ire1p	220

IV List of tables

Table 1 Gene expression error rates in <i>S. cerevisiae</i> :	29
Table 2 Consumables:	48
Table 3 Chemicals:	49
Table 4 Enzymes:	50
Table 5 Commercial Kits:	51
Table 6 Buffers and media:	53
Table 7 Oligonucleotides:.....	54
Table 8 Plasmids:	59
Table 9 Strains:.....	60
Table 10 Standard reaction conditions for PCR.....	67
Table 11 Standard PCR reaction mixture	67
Table 12 Gibson assembly mastermix components	69
Table 13 General qPCR program.....	71
Table 14 Complete list of all overlapping candidates from the <i>mga2</i> Δ phenotype screen..	105

V Zusammenfassung

Die Komposition biologischer Membranen ist ein komplexes Zusammenspiel aus Lipiden und Proteinen. Der Lipidanteil organisiert sich in Form einer Lipiddoppelschicht die eine integrale Aufnahme von Membranproteinen erlaubt als auch deren periphere Assoziation ermöglicht. Membranen erlauben die Bildung von Kompartimenten die ein optimiertes Ablaufen von biochemischen Prozessen gewährleisten. Erreicht wird diese Optimierung von Stoffwechselprozessen, indem jede Membran eine spezifische Protein- und Lipidzusammensetzung aufweist. Die Komposition und Funktion biologischer Membranen gehen Hand in Hand und bedingen einander. So beruht die Barrierefunktion der Plasmamembran in eukaryotischen Zellen auf einer erhöhten Packungsdichte der Lipide, die durch Aufrechterhaltung eines Sterol-Gradienten entlang des sekretorischen Weges gewährleistet wird. Da der molare Anteil der Lipide den Anteil der Membranproteine innerhalb einer Membran übersteigt, kommt Ihnen eine besondere Rolle bei der Bestimmung physiochemischer Eigenschaften zu. Ferner unterliegt die zelluläre Lipidzusammensetzung stärker externen Reizen wie sie beispielsweise bei Änderungen der Diät auftreten und wird dynamischer reguliert. Demnach ist es erstrebenswert ein genaueres Verständnis über die Wirkung der Lipidumgebung auf die Funktionalität von Membranproteinen zu erhalten. Obwohl das Wissen bezüglich der Unterschiedlichkeit von Membranzusammensetzungen stetig wächst bleiben Mechanismen, die für die Adaption und Aufrechterhaltung dieser Membranzusammensetzungen verantwortlich sind weitestgehend unverstanden.

Das endoplasmatische Retikulum (ER) ist das zentrale Organell für die Lipidbiosynthese in den meisten eukaryotischen Zellen und markiert den Eintrittspunkt zum sekretorischen Weg. Es ist daher das ideale Organell, um Fragen der zellulären Regulation von Membranzusammensetzungen zu adressieren. Das ER bildet ein kontinuierliches und verzweigtes Membranzusammensetzungsnetzwerk aus, welches sich sowohl strukturell als auch funktionell in spezialisierte Subdomänen unterteilen lässt. Die beiden prominentesten funktionellen Subdomänen sind das raue ER (englisch *rough* ER (RER)) und das glatte ER (englisch *smooth* ER (SER)). Die Namensgebung der Domänen leitet sich aus dem Erscheinungsbild der Membranoberfläche ab. Im Fall des RER ist die Membranoberfläche mit translatierenden Ribosomen bestückt. Das RER ist somit ein Hotspot der Proteinbiosynthese. Das SER hingegen ist frei von Ribosomen, beherbergt jedoch unter anderem Enzyme die für die *de novo* Lipidsynthese verantwortlich sind. Beide Subdomänen des ER ergänzen sich demnach funktional und ermöglichen eine koordinierte Membranbiogenese. Ferner ist das ER maßgeblich für die Reifung sekretorischer Proteine, die knapp ein Drittel der zellulären Proteinsynthese stellen, verantwortlich. Feine Störungen im Gleichgewicht von Proteinproduktion und Proteinfaltung können die

Faltungskapazitäten des ER überfordern und in Folge zu einer Akkumulation ungefalteter oder fehlgefalteter Proteine führen. Ein solcher Zustand wird allgemein als ER-Stress bezeichnet. Eine Blockierung oder langfristige Beeinträchtigung der Funktionalität des ER hat weitreichende Folgen und steht im Verdacht an der Entstehung von komplexen metabolischen Erkrankungen wie Diabetes mellitus und der nicht-alkoholischen Fettleber beteiligt zu sein. Eine besondere Bedeutung in der Bekämpfung und Vorbeugung von ER-Stress kommt der *unfolded protein response* (UPR) zu. Die UPR ist ein hoch-konservierter Signalweg in eukaryotischen Zellen, der kurze sekretorische Belastungsspitzen abfangen soll indem er dynamisch die sekretorische Kapazität des ER reguliert. Seit der Entdeckung der UPR hat sich der Kanon der aktivierenden Signale stets erweitert und beinhaltet inzwischen auch eine gestörte Lipidzusammensetzung der ER-Membran. Aberrante Lipidzusammensetzung, die eine Aktivierung der UPR zur Folge haben, werden als *lipid bilayer stress* (LBS) bezeichnet.

Die vorliegende Arbeit ist in drei Abschnitte unterteilt und jeder Abschnitt ist einem übergreifenden Thema einer LBS getriebenen UPR gewidmet.

Im ersten Abschnitt wurde untersucht, inwiefern eine funktionale UPR an der Modellierung der zellulären Lipidkomposition im steady state einer Kultivierung beteiligt ist. Ferner wurde die Frage bearbeitet inwieweit die UPR aktiv an einer Adaption der Lipidzusammensetzung bei ER-Stress beteiligt ist. Um diesen Fragen gerecht zu werden, wurde sich die Tatsache zu Nutze gemacht, dass die UPR in *S. cerevisiae* von einem einzigen Sensorprotein, dem *inositol requiring enzyme 1* protein (Ire1p) vermittelt wird. Demnach konnte durch Verwendung eines Wildtyp-Stammes (WT) und dem isogenen *ire1Δ* Stamm zwischen UPR-abhängigen und UPR-unabhängigen Vorgängen bei der Remodellierung der zellulären Lipidkomposition unterschieden werden. Als Auslöser eines proteotoxischen ER-Stress wurde das Reduktionsmittel Dithiothreitol (DTT), welches unter anderem mit der Ausbildung von Disulfidbrücken im Lumen des ER interferiert, sowie der Wirkstoff Tunicamycin (TM), der die N-Glykosylierung von neu synthetisierten Proteinen unterbindet, verwendet. Die Potenz beider Wirkstoffe wurde systematisch in einem wachstumsbasierten *minimal inhibitory concentration* (MIC) Assay für beide Stämme für komplexes reichhaltiges Nährmedium als auch für synthetisch definiertes Nährmedium bestimmt. Konzentrationen die zuverlässig die UPR auslösten wurden in Folgeexperimenten eingesetzt und deren Wirkung auf Zellwachstum und Lipidkomposition analysiert. Dabei zeigte sich im Hinblick auf das Zellwachstum, dass es keine signifikanten Unterschiede zwischen den Stämmen gab. Der größte Unterschied in der Wachstumsrate zeigte sich im Vergleich zwischen beiden Medien im Fall der ungestressten Bedingung. Wurden die Stämme in reichem, komplexem Medium kultiviert zeigten sie eine Verdopplungsrate von 86 min, im Fall des synthetisch-definiertem Medium eine Verdopplungsrate von 107 min. Die gewählten Konzentrationen von DTT und

TM zeigten für beide Stämme einen wachstumshemmenden Effekt der eine Stunde nach Applikation unabhängig vom Medium eintrat. Quantitative Lipidomanalysen der gestressten und ungestressten Zellen zeigten, dass bei kurzzeitiger Behandlung (1 Stunde) sowohl DTT als auch TM in Fall des synthetisch-definiertem Medium nur einen vernachlässigbaren Effekt auf die Lipidkomposition von WT und *ire1Δ* Zellen hatten. Im Fall des reichen und komplexen Mediums hingegen, kam es in mit DTT gestressten Zellen zu einer signifikanten Akkumulation von Phosphatidat (PA) gegenüber der ungestressten Kontrolle.

Der Vergleich der Lipidkomposition zeigte wie schon im Fall der Wachstumsrate, dass die größten Unterschiede zwischen den Medien auftraten. Hier wurden signifikante Änderungen in der Lipidklasse von Ergosterol, den komplexen Sphingolipiden, den Phosphoglyceriden Phosphatidylethanolamin und Phosphatidylinositol sowie den Speicherlipiden Triacylglyceriden und dem Ergosterolester festgestellt. Die Studie hat systematisch die Frage adressiert inwiefern DTT und TM als Wirkstoffe zur Induktion einer UPR einen Einfluss auf die Lipidkomposition nehmen. Zusammenfassend lässt sich sagen, dass die UPR keinen Einfluss auf die Lipidkomposition in Abwesenheit von ER Stress induzierenden Wirkstoffen nimmt. Ferner zeigte sich, dass die UPR ausgelöst durch DTT oder TM in der akuten Phase eine Stunde nach Initiation der Signalkaskade keinen signifikanten Einfluss auf die Membranzusammensetzung in synthetisch-definiertem Medium unter den hier etablierten Bedingungen nimmt.

Im zweiten Abschnitt lag der Fokus auf dem Dimerisierungsverhalten von Ire1p. Voraussetzung für die Ire1p abhängige Aktivierung der UPR ist die Oligomerisierung einzelner Ire1p Protomere. Kristallstrukturanalysen der löslichen Sensordomäne von Ire1p haben Interaktionsflächen für die Di- und Oligomerisierung offenbart und zu unserem Verständnis einer Aktivierung von Ire1p durch proteotoxischen Stress beigetragen. Zudem konnte in der Vergangenheit ein Mechanismus für eine Membran vermittelte Oligomerisierung durch aberrante Lipidzusammensetzung beschrieben. Dieser Mechanismus beruht auf dem ungewöhnlichen Aufbau der Transmembrandomäne von Ire1p. Sie besteht aus einer kurzen hydrophoben Transmembranhelix (TMH) welche an Ihrem N-Terminus in eine amphipathische Helix (AH) übergeht. Diese ungewöhnliche Architektur bewirkt, dass die AH mit der hydrophoben Seite in die ER-Membran inseriert und dadurch eine Neigung der kurzen TMH veranlasst. Zusätzlich führt die Transmembrandomäne (TMD) von Ire1p zu einer lokalen Kompression der Membran. Die energetischen Kosten für die Deformierung der Membran ist abhängig von der Lipidzusammensetzung, die größtenteils mit der vorherrschenden Lipidpackungsdichte korreliert. Ire1p kann die erhöhten energetischen Kosten einer Membranversteifung durch eine Oligomerisierung minimieren, indem es die zu komprimierende Membranfläche minimiert.

Ob allerdings unterschiedliche Formen von ER-Stress, also proteotoxischer ER-Stress oder LBS, die Architektur von Ire1p in der TMD unterschiedlich beeinflussen war ungeklärt. Um strukturelle Änderungen im Bereich der TMD aufzulösen, wurde ein systematisches Cystein-vermitteltes Crosslinking durchgeführt. Dazu wurde zunächst eine Cystein-freie Variante von Ire1p generiert und mittels homologer Rekombination genomisch integriert. Die genomische Integration und Expression durch den nativen Ire1p Promotor diente dazu der Oligomerisierung-bedingten Aktivierung von Ire1p durch ein endogenes Expressionslevel Rechnung zu tragen. Die Funktionalität dieser Cystein-freien Variante wurde auf zellulärer Ebene in Form von Wachstumsassays und molekularer Ebene via RT-qPCR von UPR spezifischen mRNAs validiert. Anschließend wurden einzelne Cysteine durch Mutagenese der TMD in das Cystein-freie Konstrukt eingebracht. Die so generierten Einzelcysteinvarianten wurden erneut auf Ihre Fähigkeit hin untersucht eine UPR auszulösen. Um Reste zu identifizieren, die in Signal-aktiven Clustern von Ire1p potentiell eine Interaktionsfläche herstellen, wurden ER-Membranen aus Zellen gewonnen die entweder ungestresst waren oder zuvor mittels DTT, TM oder durch Inositol-Depletion, als Form eines reinen LBS, behandelt wurden. Dabei zeigte sich, dass die Einzelcysteinmutante F544C die höchste Quervernetzungseffizienz für alle getesteten Stressbedingungen aufwies. Ferner zeichnete sich ein vergleichbares Quervernetzungsmuster für alle Stressbedingungen ab, sodass die TMD von Ire1p scheinbar unabhängig von der Art des angewandten ER-Stresses bei Aktivierung eine einzige eine einzige Konformation einnimmt.

Im dritten Abschnitt der vorliegenden Arbeit habe ich mich dem Wissen um eine Mutante des OLE-Signalwegs bedient. Diese Mutante zeichnet sich durch einen erhöhten Sättigungsgrad von Membranlipiden im Vergleich zu wildtypischen Zellen aus. In *S. cerevisiae* existiert lediglich ein einziges Gen, *OLE1*, welches für eine Δ -9-Desaturase kodiert, die Doppelbindungen in Azy-CoA Vorläufer von Membranlipiden einfügt. Der OLE-Signalweg beschreibt die Regulation der Expression von *OLE1* und wird durch die beiden Transkriptionsfaktoren Mga2p und Spt23p vermittelt. Durch Deletion des *MGA2* Gens kann eine Fehlregulation herbeigeführt werden, die neben dem Anstieg des Sättigungsgrades auch eine Aktivierung der UPR verantwortet. Ziel war es, mit *S. cerevisiae* ein Modellsystem zu schaffen mit dem die Rolle gesättigter Lipide bei der chronischen Aktivierung der UPR untersucht werden kann. Diese Fragestellung ist relevant, weil eine Vielzahl komplexer, metabolischer Krankheitsbilder wie z.B. ein Diabetes mellitus oder die nicht-alkoholische Fettleber in Verbindung mit erhöhten Mengen an saturierten Lipiden gebracht wurden. Die vorliegenden Ergebnisse geben Hinweise auf die molekularen Mechanismen die bei der Entstehung solcher Erkrankungen involviert sein könnten. Zunächst wurden die Wachstumsbedingungen dahingehend optimiert, dass sich der Membran-basierte Stress

maximal ausprägt. Dieser Zeitpunkt war gekennzeichnet durch eine stark verminderte Zellvitalität und Zellviabilität. Ferner stieg der Anteil der gesättigten Membranlipide auf 50-mol % an. Die signifikante Veränderung der Lipidzusammensetzung ging mit dramatischen, morphologischen Veränderungen des ER einher, die in bis zu 70 % der mikroskopisch analysierten Zellen auftraten. Mit *fluorescence recovery after photobleaching* (FRAP) Experimenten konnte gezeigt werden, dass die Diffusionsgeschwindigkeit von ER-ständigen Membranproteinen innerhalb des aberranten ER gegenüber einem gesunden ER signifikant verringert war. Um Modulatoren dieses morphologisch, aberranten ER zu identifizieren, wurde ein Genom-weiter *high-content* Screen durchgeführt. Es wurde eine Vielzahl von Gendeletionen identifiziert, die das Auftreten der aberranten Strukturen entweder verringern („rescue“) oder verstärken („worse“). Während Gendeletionen aus der „rescue“ Klasse vermehrt Mutanten aufwiesen, die den Zellzyklus und speziell die Mitose regulieren, so waren die Vertreter der „worse“ Klasse überwiegend mitochondrialen Ursprungs. Die Validierung ausgewählter Vertreter beider Klassen auf Ebene der Lipidzusammensetzung und der prozentualen Verteilung des aberranten ER zeigte, dass die Ausbildung des aberranten ER erwartungsgemäß mit der Menge der gesättigten Glycerophospholipide korreliert. Außerdem zeigten diese Mutanten ein signifikant erhöhtes Level an Ceramiden, Phosphatidsäuren und Diacylglyceriden.

Die Formation des aberranten ER konnte mittels Zeitraffer-Mikroskopie auf den Vorgang der Mitose eingegrenzt werden. Diesem Prozess ist eine signifikante Zunahme der Membranmasse in der Interphase vorgeschaltet. Weitere unterstützende Daten, die für eine Beteiligung des Zellzyklus an der Entstehung der Strukturen sprechen, konnten in einem sekundären, gezielten Screen erhoben werden. In diesem sekundären Screen wurden einzelne Gene überexprimiert, die einen Einfluss auf die Verweildauer in einzelnen Zellzyklusphasen haben. Die prozentualen Anteile des aberranten ER-Phänotyps übertrafen die Werte aus dem ursprünglichen Screen der „rescue“ als auch der „worse“ Klasse. Es wurde weiter untersucht, ob eine UPR-bedingte Membranexpansion einen Beitrag zu der Entstehung der Strukturen leisten könnte. Die Expression von induzierbaren Membranexpansionselementen, als auch die Überexpression des *ICE2* Gens, welches zu einer ER-Membranexpansion in wildtypischen Zellen führt, sorgte im *mga2Δ* Stammhintergrund zu einer signifikanten Zunahme der aberranten ER-Strukturen.

In einem dritten Wachstums-basierten Nachscreening wurden Mutanten und Additive untersucht, die das Wachstum der *mga2Δ* Mutante beeinflussen. Dies ist interessant, weil zuvor gezeigt wurde, dass *mga2Δ* Zellen gegenüber wildtypischen beim Wechsel vom fermentativen Wachstum zur Respiration einen deutlichen Wachstumsdefekt aufweisen. Eine Beteiligung der Mitochondrien konnte somit durch Korrelation des Wachstumsdefekts mit der

Entstehung reaktiver Sauerstoffspezies (englisch *reactive oxygen species* (ROS)) identifiziert werden. Die Überexpression von *HAP4*, einem Transkriptionsfaktor, der mitochondriale Aktivitäten hochreguliert und zur übermäßigen Bildung von ROS führt, sorgte lediglich im *mga2Δ* Stammhintergrund für eine Verschlechterung des Zellwachstums. Durch Supplementation des Mediums mit dem Radikalfänger Vitamin C konnte der Wachstumsdefekt von *mga2Δ* deutlich verringert werden. Folgerichtig konnte auch mikroskopisch gezeigt werden, dass die Entstehung eines aberranten ER in *mga2Δ* Zellen sowohl durch Vitamin C als auch reduziertes Glutathion verhindert wird.

Insgesamt wurde ein Modellsystem etabliert, das eine Untersuchung des Zusammenspiels der *unfolded protein response* mit der Zellzyklusregulierung, dem Lipidstoffwechsel und der mitochondrialen Funktion ermöglicht.

VI Abstract

The composition of biological membranes is a complex interplay of lipids and proteins. The lipid part is organized in the form of a lipid bilayer that allows integral uptake of membrane proteins as well as their peripheral association. Membranes allow the formation of compartments that ensure an optimized execution of biochemical processes. This optimization of metabolic processes is achieved through maintaining a membrane specific protein and lipid composition. The composition and function of biological membranes go hand in hand and are interdependent. For example, the barrier function of the plasma membrane in eukaryotic cells is based on an increased packing density of lipids, which is ensured by maintaining a sterol gradient along the secretory pathway. Since the molar fraction of lipids exceeds the fraction of membrane proteins within a membrane, they exert a significant impact on the determination of physicochemical properties. Furthermore, cellular lipid composition is more subject to external stimuli such as dietary changes and is more dynamically regulated. Thus, it is desirable to obtain a more detailed understanding of the impact lipid environments exert on the functionality of membrane proteins. Although knowledge about the diversity of membrane compositions is growing, mechanisms responsible for the adaptation and maintenance of these membrane compositions remain poorly understood.

The endoplasmic reticulum (ER) is the central organelle for lipid biosynthesis in most eukaryotic cells and marks the entry point to the secretory pathway. It is therefore the ideal organelle to address questions of cellular regulation of membrane composition. The ER forms a continuous and branched membrane network that can be subdivided both structurally and functionally into specialized subdomains. The two most prominent functional subdomains are the rough ER (RER) and the smooth ER (SER). The naming of the domains is derived from the appearance of the membrane surface. In the case of the RER, the membrane surface is populated with translating ribosomes. The RER is thus a hotspot of protein biosynthesis. The SER, on the other hand, is devoid of ribosomes but harbors, among other things, enzymes responsible for *de novo* lipid synthesis. Thus, both subdomains of the ER functionally complement one another and enable a coordinated membrane biogenesis. Furthermore, the ER is largely responsible for the maturation of secretory proteins, which account for nearly one third of cellular protein synthesis. Subtle perturbations in the balance of protein production and protein folding can overwhelm the folding capacities of the ER and subsequently lead to an accumulation of unfolded or misfolded proteins. Such a condition is commonly referred to as ER-stress. Blockage or long-term impairment of ER functionality has far-reaching consequences and is suspected to be involved in the development of complex metabolic diseases such as diabetes mellitus and non-alcoholic fatty liver disease. The unfolded protein

response (UPR) is of particular importance in combating and preventing ER-stress. The UPR is a highly conserved signaling pathway in eukaryotic cells that is thought to buffer short secretory stress peaks by dynamically regulating the secretory capacity of the ER. Since the discovery of the UPR, the canon of activating signals has continued to expand and now includes perturbed lipid composition of the ER membrane. Aberrant lipid compositions that result in the activation of the UPR are termed lipid bilayer stress (LBS).

The present work is divided into three sections and each section is devoted to an overarching theme of an LBS-driven UPR.

In the first section, the extent to which a functional UPR is involved in modeling cellular lipid composition in the steady state of a cultivation was investigated. Furthermore, the question was addressed to what extent the UPR is actively involved in an adaptation of lipid composition under ER stress. To address these questions, we took advantage of the fact that the UPR in *S. cerevisiae* is mediated by a single sensor protein, the inositol requiring enzyme 1 protein (Ire1p). Hence, by using a wild-type (WT) strain and the isogenic *ire1Δ* strain, it was possible to distinguish between UPR-dependent and UPR-independent processes in the remodeling of cellular lipid composition. The reducing agent dithiothreitol (DTT), which interferes with the formation of disulfide bridges in the lumen of the ER, and the pharmacologically active compound tunicamycin (TM), which inhibits N-glycosylation of newly synthesized proteins, were used as inducers of proteotoxic ER stress. The potency of both agents was systematically determined in a growth-based minimal inhibitory concentration (MIC) assay for both strains for complex rich culture medium as well as for synthetic defined minimal medium. Concentrations that reliably triggered the UPR were used in follow-up experiments and their effects on cell growth and lipid composition were analyzed.

It was found that there were no significant differences between the strains in terms of cell growth. The greatest difference in growth rate was seen in the comparison between the two media in the case of the unstressed condition. When the strains were cultured in rich complex medium they showed a doubling rate of 86 min, opposed to a doubling rate of 107 min in the case of the synthetic-defined minimal medium. The selected concentrations of DTT and TM showed a growth inhibitory effect for both strains that occurred one hour after application regardless of the medium. Quantitative lipidomic analyses of the stressed and unstressed cells showed that for short-term treatment (1 h), both DTT and TM had negligible effects on the lipid composition of WT and *ire1Δ* cells in case of the synthetic-defined minimal medium. On the other hand, in the case of the rich and complex medium, there was a significant accumulation of phosphatidate (PA) in cells stressed with DTT compared to the unstressed control.

Comparison of lipid composition showed, as in the case of growth rate, that the greatest differences occurred between the media. Here, significant changes were found in the lipid class of ergosterol, the complex sphingolipids, the phosphoglycerides phosphatidylethanolamine and phosphatidylinositol, and the storage lipids triacylglycerides and ergosterol ester. The study systematically addressed the question of the extent to which DTT and TM, as agents for inducing a UPR, have an effect on the cellular lipid composition. In conclusion, the UPR does not affect lipid composition in the absence of ER stress-inducing agents. Furthermore, the data imply that the UPR induced by DTT or TM in the acute phase one hour after drug application has no significant effect on the membrane composition in synthetic-defined minimal medium under the here established conditions.

In the second section, the dimerization behavior of Ire1p under proteotoxic and LBS conditions was investigated. A prerequisite for Ire1p-dependent activation of the UPR is oligomerization of individual Ire1p protomers. Crystal structure analyses of the soluble sensor domain of Ire1p have revealed interaction sites for di- and oligomerization and contributed to our understanding of an activation of Ire1p by proteotoxic stress. In addition, a mechanism for membrane-mediated oligomerization by aberrant lipid composition has been described in the past. This mechanism is based on the unusual structure of the transmembrane domain of Ire1p. It consists of a short hydrophobic transmembrane helix (TMH) which transitions into an amphipathic helix (AH) at its N-terminus. This unusual architecture causes the AH to insert into the ER membrane with the hydrophobic side, thereby inducing a tilt of the short TMH. In addition, the transmembrane domain (TMD) of Ire1p causes local compression of the membrane. The energetic cost of membrane deformation is dependent on the lipid composition, which largely correlates with the prevailing lipid packing density. Ire1p can minimize the increased energetic cost of membrane stiffening via oligomerization by minimizing the membrane area to be compressed. However, whether different forms of ER stress, i.e. proteotoxic ER stress or LBS, differentially affect the architecture of Ire1p in the TMD was unresolved. To resolve structural changes in the TMD, systematic cysteine-mediated crosslinking was performed. For this purpose, a cysteine-free variant of Ire1p was first generated and genomically integrated by homologous recombination. Genomic integration and expression by the native Ire1p promoter were used to account for the oligomerization-induced activation of Ire1p by an endogenous expression level. The functionality of this cysteine-free variant was validated at the cellular level in the form of growth assays and on the molecular level via RT-qPCR of UPR specific mRNAs. Subsequently, single cysteines were introduced into the cysteine-free construct by mutagenesis of the TMD. The single cysteine variants generated in this way were reassessed for their ability to trigger a UPR. To identify residues that potentially establish an interaction surface in signal-acting

clusters of Ire1p, ER membranes were obtained from cells that were either unstressed or previously treated by DTT, TM, or by inositol depletion, as a form of pure LBS. This showed that the single cysteine mutant F544C exhibited the highest cross-linking efficiency for all stress conditions tested. Furthermore, a comparable cross-linking pattern emerged for all stress conditions, such that the TMD of Ire1p appears to adopt a single conformation upon activation regardless of the type of ER-stress applied.

In the third section of the presented thesis, I utilized a mutant of the OLE signaling pathway to study the role of the UPR in context of LBS. This mutant is characterized by an increased degree of saturation of membrane lipids compared to wild-type cells. In *S. cerevisiae*, there is only a single gene, *OLE1*, which encodes a Δ -9 desaturase that inserts double bonds into acyl-CoA precursors of membrane lipids. The OLE pathway describes the regulation of *OLE1* expression and is mediated by the two transcription factors Mga2p and Spt23p. Deletion of the *MGA2* gene can induce a dysregulation that is responsible for an increase in the degree of saturation concomitant with an activation of the UPR. The aim was to use *S. cerevisiae* to create a eukaryotic model system with which the role of saturated lipids in perpetuating an ER-stress condition could be investigated. This question is relevant because a variety of complex metabolic diseases, such as diabetes mellitus or non-alcoholic fatty liver disease, have been associated with elevated levels of saturated lipids. The presented results provide clues to the molecular mechanisms that may be involved in the development of such diseases.

Initially, growth conditions were optimized to maximize membrane-based stress. As a result, cell viability and cell viability were strongly reduced in the *mga2* Δ mutant opposed to the WT. Furthermore, the proportion of saturated membrane lipids increased to 50-mol %. The significant change in lipid composition was accompanied by dramatic, morphological changes in the ER, which occurred in up to 70% of the microscopically analyzed *mga2* Δ cells. Fluorescence recovery after photobleaching (FRAP) experiments demonstrated that the diffusion rate of ER-derived membrane proteins within the aberrant ER was significantly reduced compared with a healthy ER. To identify modulators of this morphologically aberrant ER, a genome-wide high-content screen was performed. A variety of gene deletions were identified that either decreased ("rescue") or increased ("worse") the appearance of the aberrant structures. While gene deletions from the "rescue" class showed an increased number of mutants regulating the cell cycle and specifically mitosis, the representatives of the "worse" class were predominantly of mitochondrial origin. Validation of selected representatives of both classes at the level of lipid composition and percent distribution of aberrant ER showed that, as expected, aberrant ER formation correlated with the amount of saturated glycerophospholipids. In addition, these mutants showed significantly increased levels of ceramides, phosphatidic acids, and diacylglycerides.

The formation of the aberrant ER could be narrowed down to the act of mitosis by time-lapse microscopy. This process is preceded by a significant increase in membrane mass in interphase. Further supporting data indicative of cell cycle involvement in the formation of the aberrant ER structures could be collected in a secondary targeted screen. In this secondary screen, individual genes were overexpressed that had an effect on the residence time in individual cell cycle phases. The percentages of aberrant ER harboring cells exceeded the values from the original screen of the "rescue" as well as the "worse" category. It was further investigated whether UPR-induced membrane expansion could contribute to the formation of the structures. Expression of inducible membrane expansion systems, as well as overexpression of the *ICE2* gene, which leads to ER membrane expansion in wild-type cells, caused a significant increase in aberrant ER structures in the *mga2Δ* strain background.

In a third growth-based post-screening, mutants and additives affecting the growth of the *mga2Δ* mutant were investigated. This is interesting because it has previously been shown that *mga2Δ* cells exhibit a distinct growth defect compared to wild-type ones when switching from fermentative growth to respiration. Mitochondrial involvement could thus be identified by correlating the growth defect with the generation of reactive oxygen species (ROS). Overexpression of *HAP4*, a transcription factor that upregulates mitochondrial activities and leads to the excessive generation of ROS, caused a deterioration of cell growth only in the *mga2Δ* strain background. Supplementation of the medium with the free radical scavenger vitamin C significantly reduced the growth defect of *mga2Δ*. Consequently, it was also shown microscopically that the development of an aberrant ER in *mga2Δ* cells was prevented by both vitamin C and reduced glutathione.

Overall, a model system was established that allows an investigation of the interplay of the unfolded protein response with cell cycle regulation, lipid metabolism and mitochondrial function.

VII Declaration

I hereby certify that the work presented in this thesis is the result of original research of my own unless it is stated explicitly in the form of references or acknowledgements. The following data was obtained in context of collaborative research:

Figure 3 – Molecular dynamic simulations were carried out and analyzed by Dr. Roberto Covino. Graphical representations were provided by Toni Radanović.

Figure 10, Figure 11, Figure 12 – Lipidomics experiments were performed by Lipotype GmbH. Data were curated and represented in plots by John Reinhard. Raw data are published¹ and reevaluated using an unpaired, two-tailed t-test, assuming Gaussian distribution.

Figure 15 and Figure 16 – Heike Stumpf assisted with RNA-isolation and subsequent qPCR

Figure 17 – Molecular dynamics simulations and the graphical representation was kindly provided by Dr. Roberto Covino. All cloning, assay development for cysteine crosslinking and the cysteine crosslinking data were performed and analyzed by Dr. Kristina Văth. The data is published².

Figure 22 – Images were acquired with John Reinhard.

Figure 24 – The high-content genetic screen was performed by Dr. Michael Gecht in the laboratory of Prof. Maya Schuldiner. Visual inspection of the data was carried out independently by John Reinhard, Dr. Michael Gecht and myself.

Figure 28 and Figure 29 - – Lipidomics experiments were performed by Lipotype GmbH.

Figure 35, Figure 36, Figure 37, Figure 45, Figure 46 – Images were acquired with John Reinhard

Further this thesis contains data of the following publications:

Reinhard J*, **Mattes C***, Văth K*, *et al.* A Quantitative Analysis of Cellular Lipid Compositions During Acute Proteotoxic ER Stress Reveals Specificity in the Production of Asymmetric Lipids. *Front Cell Dev Biol.* 2020;8.

Văth K*, **Mattes C***, Reinhard J*, *et al.* Cysteine cross-linking in native membranes establishes the transmembrane architecture of Ire1. *Journal of Cell Biology.* 2021;220(8)

Mattes C*, Reinhard J*, Harald Hofbauer, Michael Gecht, Schuldiner M. and Ernst R. Investigating aberrant ER morphology in the absence of the lipid packing sensor Mga2p in yeast *Saccharomyces cerevisiae*. (*in preparation*)

*denotes equal contribution

1 Introduction

1.1 The importance of models in biology

The 19th century marks the transition from natural philosophy to the era of modern science. The main difference between both forms of study is that in natural philosophy the investigator deduces principles of nature solely by observation without the rigorous experimental examination that is part of the modern scientific approach. Hence, the validation of the observation-based inferences was neglected in natural philosophy. In this period, multiple important theories and concepts were published that have shaped the way we perceive the world to this very day. In 1808, John Dalton published his book “A New System of Chemical Philosophy”³ in which he enunciates his atomic theory. In 1869, Dmitri Mendeleev published his first version of the periodic table⁴ and in 1859 Charles Darwin published his revolutionary ideas for the diversity of life in “On the origin of species by means of natural selection, or the preservation of favored races in the struggle for life”⁵. One explanation for the success of these theories beyond the scope of the scientific community is that all of these scientists managed to systematically organize knowledge of that time and transformed it into a simple pictorial representation⁶. Whether the concept of indivisible and indestructible atoms that make up all matter, the creation of a table that accommodated all known elements of that time with empty spaces left for those to be discovered, or the representation of the diversity of life in the form of a tree. All of these theories aimed at building a rational framework to unify observable natural phenomena. These frameworks not only housed answers to current questions of that time, they also had room for predictions and invited to expand the knowledge. With the growing knowledge since these frameworks had been postulated these concepts had to accommodate to the new information to survive. For instance, we now know of the existence of subatomic particles, and that the similar chemical properties of elements within a periodic group is linked to their number of valence electrons and not determined by their mass, and the age of earth is estimated to be 4.5 billion years old instead of 300 million years as assumed by Charles Darwin^{5,7}. These insights are the result of a series of theoretical advances supported by the development of more sophisticated instruments and techniques for experimental measurements. How our understanding of biology and technical advances are interlinked is best exemplified through the advances made in microscopy. In 1665, the natural philosopher Robert Hooke published “Micrographia”, a record of observations made by him with a simple compound microscope⁸. In his studies he described structures found in thin slices of cork that appeared to him as perforated and porous, resembling a honeycomb⁸. In hindsight, he looked at the cell walls of plant cells. Thereby, he unknowingly visualized, aided by his microscope,

for the first time the smallest unit of life, the cell. It was in fact Robert Hook that coined the term cell, as the cork tissue reminded him of cells that house hermit monks in a monastery. A contemporary of Robert Hook was Antoni van Leeuwenhoek who used his single lens microscopes to study numerous biological samples and can be seen as one of the founding fathers of protozoology and bacteriology as he was the first person to discover protists and bacteria⁹. It took until the 19th century to develop the theoretical underpinnings of modern light microscopy by works of Ernst Abbe's diffraction-limit theory¹⁰ and the formulation of the Rayleigh criterion that determines the minimum distance between two objects to be resolvable to ~200 nm¹¹. Attempts to circumvent this limit of spatial resolution led to the development of electron microscopy (EM) to visualize nanoscale structures at the expense of sample integrity¹². The improved resolution led to the discovery of the highly organized subcellular structures of eukaryotic cells pioneered by the work of Albert Claude, George Palade and Christian de Duve who received in 1974 the Nobel Prize in Physiology and Medicine for their contributions¹³⁻¹⁵. The application of the electron microscope to study biological samples was therefore pivotal for the creation of modern cell biology. The quality of biological microscopy images is not only determined by the resolution but further determined by the contrast. The single most impactful improvement in enhancing the contrast was seen with the advent of fluorescent staining. The fluorescence of a molecule is an electrical phenomenon comprising two events. Firstly, the molecule will absorb energy in the form of light of a specific wavelength referred to as excitation. This causes electrons of the molecule to be raised from the ground state to the excited state. As the excited state has a limited lifetime of 10^{-8} s, the electrons return to the ground state¹⁶. The return to the ground state represents the second event as some of that absorbed energy is emitted in the form of light therefore referred to as emission. Both events, excitation and emission, depend on the particular fluorophore i.e. a molecule with fluorescent properties. The first fluorescent stain, termed fluorescein, was developed in 1871 by Adolf von Bayer¹⁷. An isothiocyanate derivative of fluorescein was used in the first immunofluorescence study by Albert Coons who could show that labeling of an antibody with this fluorescent molecule does not interfere with its immunological properties¹⁸. These findings enabled researches to study the cell at a new level of detail yet the greatest discovery for fluorescent microscopy was the identification of a naturally self-sufficient fluorescent protein, called green fluorescent protein (GFP)^{19,20}. This protein was isolated from the marine organism *Aequorea Victoria*. As the information for the chromophore that is responsible for the fluorescence of GFP is contained within the coding sequence, scientists would soon generate fusion proteins by adding the GFP coding sequence to any gene of interest^{21,22}. This led to the "green revolution" of cell biology and allowed scientist to study the inter- and intramolecular processes in living cells via fluorescence microscopy²³. All of the aforementioned advances deepened our understanding of cell physiology but the newly found fluorophores still had to

abide the physical law described by Ernst Abbe. It wasn't until 1994 that this barrier that had seemed insurmountable for over a century was ultimately brought down by Stephan Hell's proposed stimulated emission depletion (STED) microscopy²⁴, which he was able to implement in 1999²⁵. His invention belongs to the growing class of super-resolution techniques that enable imaging of dynamic structures in living cells below the diffraction limit, allowing scientist to observe single molecules. This shortened recap of over 300 years of advances in microscopy has demonstrated the benefit of cross-fertilization among different disciplines such as physics, chemistry, mathematics, and biology and how science contributed to our understanding of the microscopic world. It also revealed an inclination of scientists to become fascinated with the dissection of a scientific question and to tend towards a reductionist approach in studying phenomena. The predictive power of reductionism for model building was elegantly showcased with the fluid mosaic model of biological membranes unifying and integrating a variety of findings from many scientists²⁶. While there is no denying that the application of reductionism has enabled us to explore the physiology from "man to molecule" one might lose sight of another equally important school of thought in this data-driven era, namely that of holism. To progress and advance further, we need to apply what we have learned in studying pathways down to the molecular level to close the gap again "from molecule to man"²⁷.

I, therefore, think that when practicing science, one should consistently question one's own findings and see them in the light of results of partners and predecessors. When one is in the beginning of a project, it is helpful to be guided by theories and models that have withstood the test of time such as the theory of evolution or the concept of homeostasis in physiology. But to progress in one's own field, it is important to develop your own model or working hypothesis that in accordance to the scientific method has to be falsifiable. Only then one can design and carry out experiments such that new insights can be gained and the model can be refined or corrected appropriately.

1.2 The endoplasmic reticulum – hallmark of the eukaryotic cell and the maestro of interorganellar communication

The characteristic cellular architecture of modern eukaryotes is the evolutionary consequence of metabolic compartmentalization that led to highly specialized organelles. The compartments of contemporary eukaryotes are bound by membranes of either autogenous origin, derived from an early endomembrane system, or acquired through endosymbiotic events as proposed by the endosymbiotic hypothesis^{28,29}. Recently it was postulated that the host cell of the endosymbiotic event was related to Lokiarchaeota, a phylum of the archaea that encodes many eukaryotic signature proteins that could have instituted such a crude endomembrane system³⁰. Sequence-based functional predictions of these eukaryotic signature proteins indicate that they provide the host with membrane remodeling capabilities and primordial forms of cytoskeletal proteins in the form of actin³¹ and tubulin³² homologues³³. It is believed that the emergence of such an organism marked the first step in eukaryogenesis i.e. the collection of evolutionary events that have enabled the transition from prokaryotic to eukaryotic life forms. These proteins would prepare the last eukaryotic common ancestor, from which all living eukaryotes descend, for the phagocytosis of the α -proteobacterium that was the predecessor of modern mitochondria. It is believed that this is the key event in the origin of eukaryotes and that the engulfment of the α -proteobacterium liberated the plasma membrane from its former role in energy production in the form of chemiosmotic ATP synthesis³⁰. This relocation of energy production to the mitochondrial inner membrane is often seen as the driving force behind the rise in complexity of the eukaryotic cell plan as the plasma membrane could in turn acquire novel functions with respect to signaling and communication. Contrary to the prevailing paradigm that mitochondria are essential constituents of the eukaryotic cell, it was shown that eukaryotic life without them is indeed possible as demonstrated in case of *Monocercomonoides sp*, an organism devoid of mitochondria or mitochondria related organelles³⁴. It is believed that the absence is due to a secondary loss as a consequence of redundancy of mitochondrial functions. Although most known for their role in oxidative phosphorylation, mitochondria or mitochondria related organelles are retained in anaerobic eukaryotes for their most conserved function, namely the provision of the iron sulfur cluster pathway³⁵. This pathway is important for the maturation of cytosolic and nuclear Fe-S proteins by the downstream situated cytosolic iron-sulfur assembly pathway. In case of *Monocercomonoides sp* the mitochondrial iron-sulfur assembly pathway for Fe-s cluster synthesis was replaced by the prokaryotic sulfur utilization factor pathway, presumably through horizontal gene transfer³⁵, thus paving the way for the loss of the semi-autonomous organelle.

This example demonstrates that the “plan” of a eukaryotic cell is not carved in stone and that entire organelles can disappear once their functions become obsolete or are replaced by more efficient pathways. With the disappearance of the cellular “powerplant” in the form of the mitochondria, only a few essential organelles remain that might have become irreplaceable. For one the nucleus as the “safe” that contains most of the genetic information that encodes the architectural plans for the eukaryotic cell by separating the nucleoplasm from the cytoplasm. Second to the nucleus is the ER, which is contiguous with the outer nuclear membrane and is the architect that puts this plan into action³⁶. Early studies of the architecture of the ER via EM revealed that this organelle can be divided into two distinct domains: the rough ER (RER) and the smooth ER (SER) that fulfill distinct functions. The term RER is the result of the appearance of this subdomains surface which is studded with translating ribosomes and marks the hotspot for protein synthesis and their co-translational translocation. The SER is considered a hot-spot for lipid biosynthesis. It houses many enzymes involved in the *de novo* lipid synthesis of important membrane lipids such as sterols, glycerophospholipids and sphingolipids. The ER therefore is a key organelle of membrane biogenesis. It is the entry point to the secretory pathway for all secretory and membrane proteins, which are distributed throughout the endomembrane system by vesicular carriers and which represent roughly one third of the entire proteome^{37,38}. The ER further embodies the wording “form follows function” as its reticular network of branching membrane tubules and sheets extends throughout the cytoplasm of the cell and allows for the formation of membrane contact sites (MCS) with every other organelle allowing for inter-organellar communication (Figure 1). These contact sites provide an additional option for the distribution of *de novo* synthesized lipids next to the vesicular transport mechanism via lipid transfer proteins that are hosted at these MCS³⁹. Through EM studies it was revealed that within MCS two opposing organellar membranes approach on another and establish a physical contact keeping the membranes at a distance of ~10-30 nm⁴⁰. MCS are based on membrane microdomains that help exchanging lipids, ions and signaling molecules thereby contributing to cellular homeostasis and signaling. Rapid exchange of lipids can occur rapidly and without the need for membrane fusion, thereby allowing both organelles to maintain their specialized compositions and functions that are rooted in their defined sets of proteins and lipids. The ER is the largest organelle in most eukaryotic cells and - in contrast - to mitochondria, peroxisomes or lipid droplets comes as a single copy. As previously described the ER has taken on a role as a communicator between highly specialized organelles and the plasma membrane and is involved in the coordination of the metabolic interplay dispersed across them. Thus, it is imaginable that a singular organelle, that can not be *de novo* synthesized and from which other organelles such as lipid droplets originate needs to remain functional during and after mitosis by equipping it with a vast spectrum of organellar surveillance systems that assure the preservation of homeostasis⁴¹.

The ER has a central role in the evolution of the eukaryotic cellular architecture

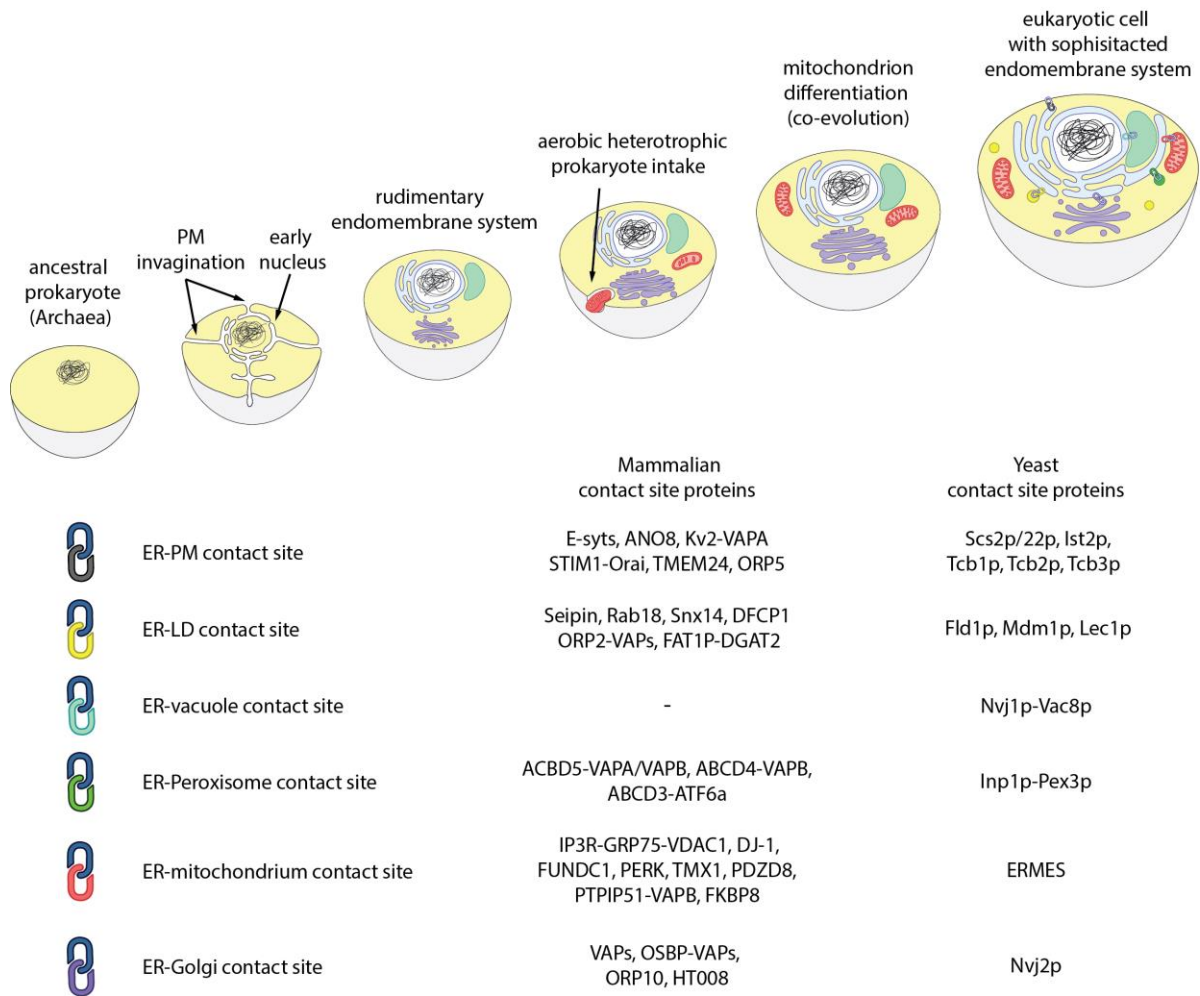


Figure 1 Evolutionary steps towards a modern eukaryotic cell

Depicted is a possible scenario for the evolution of the modern eukaryotic cell plan with particular emphasis on the role of the endomembrane system in establishing numerous contact sites between the ER and other organelles. Contact site proteins and complex annotations are based on Lin *et al.*⁴² and Casto *et al.*⁴³

1.3 The unfolded protein response – a holistic view on maintaining cellular integrity through organellar homeostasis

Cellular life relies on a constant flow of genetic information described by the central dogma of molecular biology. Information contained in DNA is transcribed to mRNA, which then is translated by ribosomes to a chain of covalently linked amino acids. The amino acid sequence of the polypeptide chain, referred to as the primary structure of a protein, must undergo folding and maturation to be shaped into its three-dimensional tertiary and quaternary structure to become a fully functional protein. While a high fidelity of gene expression enabled through the previously mentioned processes is essential for all life forms, each step is error-prone in an increasing manner (Table 1).

Table 1 Gene expression error rates in *S. cerevisiae*:

Determined error rates associated with processes involved in gene expression

Process	Error rates in <i>S. cerevisiae</i>
Replication	2.6×10^{-10} per base pair ⁴⁴
Transcription	1.0×10^{-5} per base pair ⁴⁵
Translation	4.0×10^{-5} to 6.9×10^{-4} per codon ⁴⁶
Folding & maturation	Protein dependent

Fortunately, all gene products have short half-lives compared to an organism's life span and can be readily replaced by correct gene products lowering their individual impact on cellular integrity. Furthermore, all cellular life is equipped with quality control mechanisms to deal with faulty gene products. Many proteins undergo complex posttranslational modifications that can be challenging to the folding capacity of the ER and in times of high demand can bring the capacity to its limit. A sudden increase in the secretory load or an interference with steady state ER protein folding efficiency can lead to an accumulation of misfolded or unfolded proteins in the lumen of the ER – a state referred to as ER-stress⁴⁷. The dominant pathway responsible for resolving ER-stress is the unfolded protein response (UPR)⁴⁸. Since its discovery, the canonical scope of activating signals expanded from the accumulation of misfolded proteins through stress caused by calcium depletion in mammalian cells⁴⁹, excessive levels of reactive oxygen species⁵⁰, hypoxia⁵¹ or viral infections⁵² to purely ER membrane perturbations in the form of aberrant lipid compositions summarized under the term lipid bilayer stress (LBS)⁴⁷. UPR-activation through changes of the glycerophospholipid composition⁵³ including increased sterol levels⁵⁴, increased levels of lipid saturation⁵⁵ or caused by inositol-depletion in *S. cerevisiae*⁵⁶ are in agreement with the regulative response of the UPR that comprises adaptive changes aiming at restoring homeostasis to the entire

secretory pathway by upregulating lipid synthesis, ER-associated protein degradation (ERAD), COPI and COPII vesicular transport and ER-resident foldases and chaperones⁵⁷. This dual sensitivity for aberrancies in protein folding and ER membrane properties can translate to opposing binary cell fate outputs, which can lead to adaptation or cell death (Figure 2). In response to ER-stress, independent of the triggering event, the UPR initiates a wide transcriptional response that aims at reestablishing ER homeostasis⁵⁷. If the adaptive measurements are insufficient and fail to restore ER homeostasis, the UPR will switch from its adaptive mode into its pro-apoptotic mode-of-action to drive the affected cell into apoptosis⁵⁸. A growing number of studies indicate that a chronic activation or ill-adaptive UPR is involved in the transition of physiological to pathological cell states. It is therefore not surprising that the UPR, which governs the functionality of the ER as the central organelle for lipid biosynthesis, protein folding and intracellular organellar communication, is implicated to be involved in the context of a myriad of metabolic diseases such as diabetes⁵⁹⁻⁶¹ and non-alcoholic fatty liver disease⁶²⁻⁶⁵.

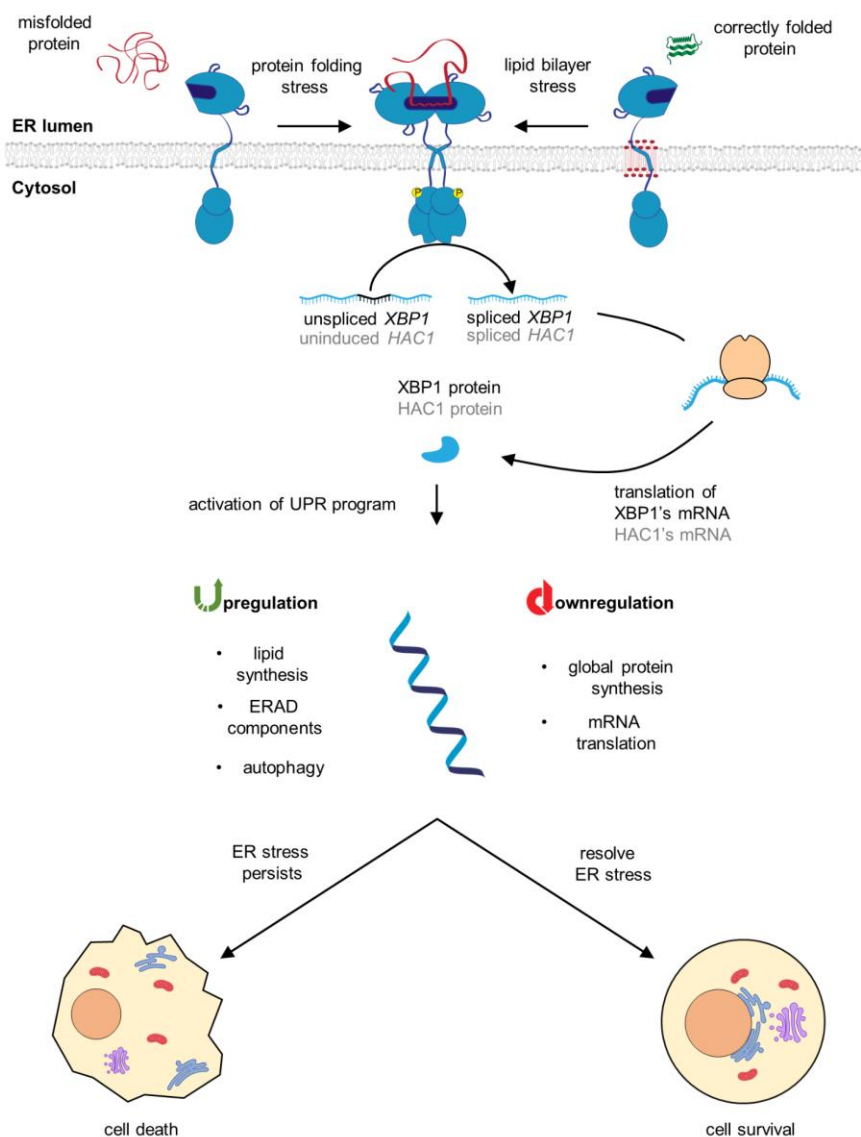


Figure 2 The role of Ire1p as the most conserved UPR sensor in adaptive and pro-apoptotic cell signaling

Ire1p initiates a signaling cascade upon exposure to proteotoxic and lipid bilayer stress. The inactive Ire1p monomers dimerize upon accumulation of misfolded proteins or upon lipid bilayer stress. Dimer formation and presumably the formation of higher oligomers leads to *trans*-autophosphorylation of Ire1p's cytosolic effector domains. Subsequently, the activated RNase domain will cleave the unspliced *XBP1* mRNA to thereby initiate an unconventional splicing. Translation of the spliced *XBP1* mRNA gives rise to the XBP1 transcription factor that will migrate into the nucleus to initiate the expression of UPR specific target genes. Once initiated, the UPR will cause an increase in lipid synthesis, ERAD component expression and autophagy while attenuating the general protein synthesis and mRNA translation for non-specific UPR target genes. Depending on the effectiveness of these measures there are two possible outcomes. ER-stress either persists thereby leading to pro-apoptotic signals, or the ER-stress is resolved and therefore the cell will be able to survive and recover. The *S. cerevisiae* homologs are indicated in light grey compared to the mammalian counterparts depicted in black for each step of the signaling cascade. Parts of this figure are adapted from Radanović *et al.*⁴⁷.

One of the deciding advances in deciphering the molecular basis for UPR signaling was made 1988 by Kozutsumi *et al.*⁶⁶ who showed that the accumulation of misfolded proteins in the early secretory pathway is the cause for the upregulation of a pair of ER-resident chaperones. The authors speculated how the status of the ER lumen may be monitored by a sensor and how these signals are transduced to the nucleus. The identification and characterization of the ER-stress transducer was simultaneously made by Mori *et al.*⁶⁷ and Cox *et al.*⁶⁸ both of which carried out their screening approaches in *S. cerevisiae*. They discovered that the Inositol-requiring protein-1 (Ire1p), is responsible for the surveillance of the ER folding status. Ire1p is a type 1 transmembrane protein which harbors an ER-stress sensing domain on the luminal side of the ER and a kinase and RNase domain on the cytosolic side required for ER-stress signal propagation. Under ER-stress, a fraction of Ire1p molecules form higher oligomers that drive the juxtaposition of Ire1p's cytosolic effector domains, triggering a trans-autophosphorylation of the kinase domain, resulting in its activation⁶⁹. The activated RNase domain initiates the unconventional splicing of its substrate *HAC1* mRNA by excising a small intron sequence⁷⁰. The unconventional splicing reaction is completed by ligating the two exons, mediated by the tRNA ligase Trl1p, to form the spliced *HAC1* mRNA that serves as a template for the transcription factor Hac1p⁷¹. Hac1p belongs to the basic leucine zipper family of transcription factors and after migrating into the nucleus will bind to DNA sequences called UPR elements located in the promotor of UPR-regulated genes such as the protein chaperone Kar2p⁷². The mechanism by which Ire1p and *HAC1* mRNA interact with one another and the molecular nature of how the pathway initiates and relays the ER stress signals is still subject of current research. Structures for the ER-luminal⁷³ and cytosolic domains⁷⁴ have provided insights into the molecular organization of Ire1p protomers during oligomerization, a process widely accepted to be a prerequisite for UPR activation⁷⁵⁻⁷⁹ (Figure 3 A). Compelling evidence for an oligomerization-driven activation model came from studies that showed that UPR activation can be achieved in absence of UPR inducing drugs when homo-dimerization is enforced by replacing the ER-luminal domain with a leucine zipper dimerization motif⁸⁰. Analysis of the ER-luminal domain crystal structure further revealed two interfaces for dimerization and oligomerization, respectively. The first interface (IF_{L1}) is established between two Ire1p protomers (Figure 3 B). The second interface (IF_{L2}) is on the opposite side of the ER-luminal domain mediating a back-to-back packing of Ire1p dimers. Mutating the residues involved diminishes Ire1p's activity, and given the fact that mutating both interfaces abolishes Ire1p's activity completely implies that Ire1p activation relies on oligomerization and not just dimerization alone. Close inspection of the crystal structure further revealed a putative peptide-binding groove spanning both protomers in the dimeric Ire1p conformation. (Figure 3 C). This peptide binding groove resembles the peptide binding groove found in major histocompatibility complex I (MHC I) molecules with antiparallel β -sheets forming the bottom

and two α -helices shaping the walls of the peptide-binding groove. A direct binding model for the Ire1p activation was proposed that suggests a binding of hydrophobic polypeptides, stemming of unfolded proteins, to the peptide binding groove formed across the Ire1p dimer interface. This model thus helps to explain how unfolded proteins are sensed by the ER-luminal domain and how they contribute to the activation and maintenance of UPR signaling by stabilizing the dimeric state of Ire1p. Mutating the highly conserved residues located at the bottom of the polypeptide binding groove involved in the binding of hydrophobic polypeptides where shown to be important for Ire1p ability to react to unfolded proteins *in vivo* and nullify the ER-luminal domains chaperone activity *in vitro*⁸¹.

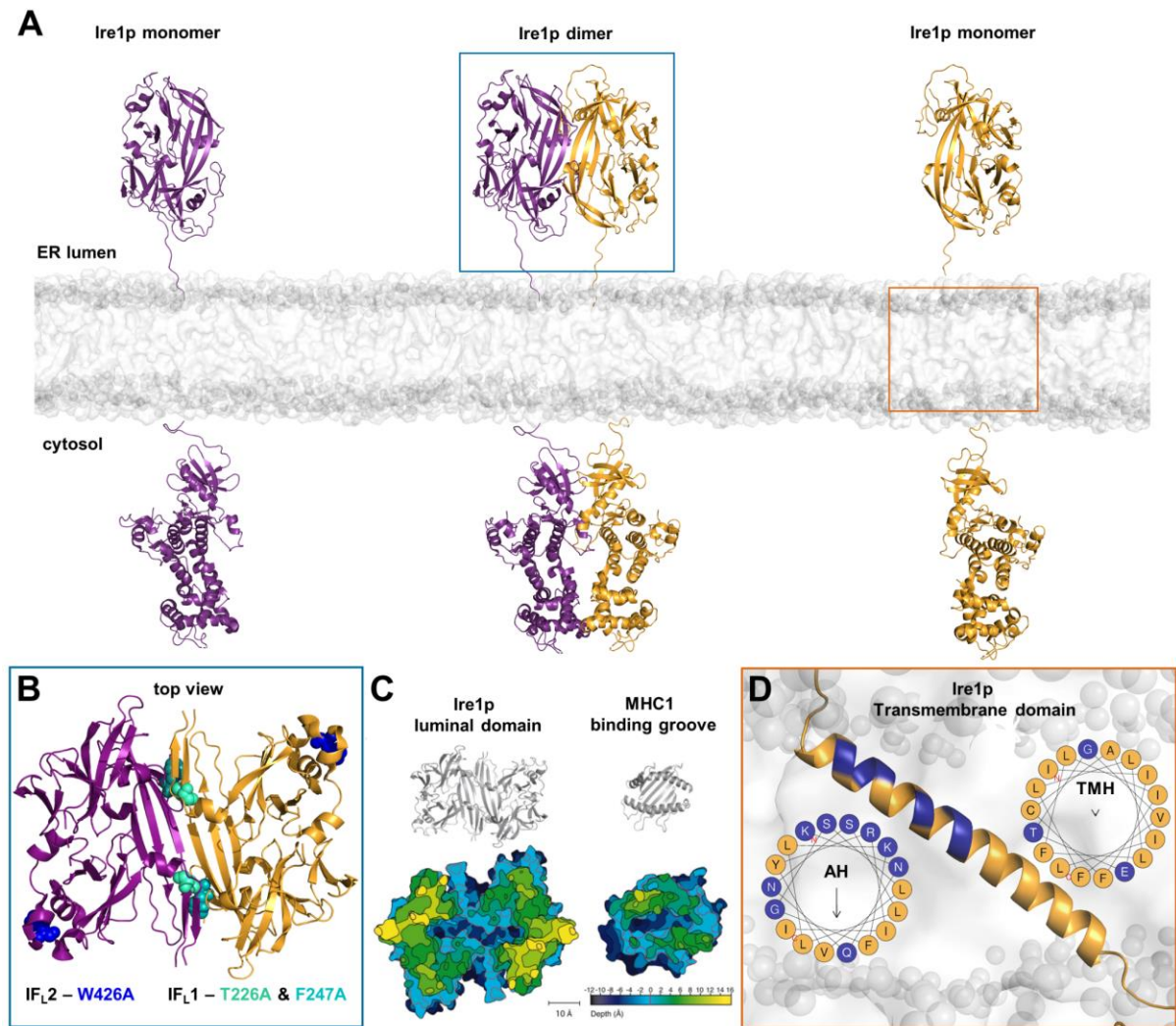


Figure 3 Structural organization of Ire1p's ER-luminal, transmembrane and cytosolic domain and a peptide binding groove

A) Schematic representation of full-length Ire1p as a monomer and dimer based on the published structure of the ER-luminal domain by Credle *et al.*⁷³ (pdb: 2BE1) and the cytosolic effector domains by Korennykh *et al.*⁷⁴ (pdb:3SDJ). The structural models were generated by my colleague Toni Radanović. **B)** Top view of the dimeric ER-luminal domain⁷³. Ire1p monomers are shown in purple and gold. The interface for dimer formation (IF_{L1}) including the residues T226 and F247 and the interface for the back-to-back oligomer assembly of dimers (IF_{L2}) involving W426 are shown as cyan and blue spheres, respectively. **C)** Illustration was adapted from the original Credle *et al.*⁷³ publication, showing a scale comparison of the x-ray structures of the peptide binding grooves of the Ire1p dimer and MHC1 along with a topographic map to highlight the depth of the groove. **D)** Structural model of the TMD of Ire1p taken from molecular dynamics simulations provided by Dr. Roberto Covino. The TMD comprises a short TMH adjacent to an amphiphatic helix. Hydrophilic and hydrophobic residues are indicated by a blue and a yellow shade, respectively. A helical wheel projection illustrates how the amphiphatic and TMH differ in their hydrophobic moment (indicated by the length of the arrow in the center)⁸².

The stability of dimeric and oligomeric assemblies of Ire1p are not only determined by ER-luminal interfaces, but also by cytosolic interfaces. These have been identified by structural studies and they are crucial for signal transduction. Functional cytosolic interfaces between the kinase and RNase domain are crucial for the trans-autophosphorylation of the kinase domain and stabilization of the RNase domain to form the binding cavity for the unspliced *HAC1* mRNA substrate^{74,83}. Three cytosolic interfaces are described, and upon mutation of residues involved in the formation of these interfaces Korennykh *et al.* reported an impairment of the RNase activity⁷⁴. As a functional RNase activity of Ire1p is essential to process unspliced *HAC1* mRNA and given the fact that the RNase activity of Ire1p is highly cooperative, in that cleavage of the *HAC1^u* mRNA contained intron is more efficient in an oligomeric state^{74,84}, it was surprisingly shown that the kinase activity of Ire1p is not required for its activation⁸⁵. Evidence rather supports a regulatory purpose for the phosphorylation to be involved in the disassembly of higher oligomeric states of Ire1p^{85,86}.

Despite important contribution by the discussed structural biological work on both soluble domains their predictive power in terms of stress sensing is limited to the ER lumen as described for the direct binding model, not covering a mechanism by which Ire1p can directly sense aberrant ER-lipid compositions. Biophysical and bioinformatical work by Halbleib *et al.* provided a structural basis for an intrinsic sensitivity of Ire1p to directly sense and respond to changes of the physicochemical properties of the ER lipid bilayer⁸⁷. The authors could show that the transmembrane domain (TMD) of Ire1p consists of an ER-luminal amphipathic helix, that inserts into the ER-luminal leaflet of the bilayer with an adjacent short transmembrane helix (Figure 3 D). These structural features force the TMH in a tilted and bend configuration. The unusual architecture comes at energetic costs from a hydrophobic mismatch between the TMD and the surrounding lipid bilayer. The membrane is locally “squeezed” around the TMH and the amphipathic helix. Moreover, this architecture renders Ire1p also sensitive to aberrant stiffening of the ER membrane. To minimize the energetic costs of membrane deformation and acyl chain disordering e.g. from increased lipid saturation or sterol levels in the ER membrane, Ire1p would dimerize. Mutational analysis provided evidence that, disruption of the amphipathic helix interferes with Ire1p’s ability to respond to lipid bilayer stress. How signals from unfolded proteins and LBS are processed by Ire1p, and whether Ire1p is capable of tailoring its response to the type of activating signals remains unknown. It was observed, however that targets of Ire1p-mediated upregulation are differently regulated under conditions of LBS and proteotoxic stress⁸⁸.

1.4 The dominance of *S. cerevisiae* in lipid metabolic research

S. cerevisiae is a model system for eukaryotic biology and has due to its genetic tractability to this day a leading role in unraveling cellular and molecular workings through functional genomic studies⁸⁹. The sequenced genome of *S. cerevisiae* in 1996⁹⁰, together with *S. cerevisiae*'s natural tendency to carry out homologous recombination, was pivotal in cloning and subsequent functional analysis of genes involved in the lipid metabolism⁹¹. After all, to distinguish physiological from pathological conditions, one must have a clear understanding of the role of the involved enzymes and how they are embedded in the interwoven cellular metabolic pathways of lipid synthesis.

1.4.1 The three categories of eukaryotic membrane lipids

Lipids are, together with proteins, constituents of biological membranes. In the past important cellular functions were ascribed to the embedded proteins alone, neglecting the influence of lipids on protein activity^{92,93}. Next to their contribution as membrane building blocks, lipids are further used as a way of energy storage in *S. cerevisiae* in the form of the neutral lipids triacylglycerol (TAG) and ergosterol ester (EE). Both neutral lipids are stored in lipid droplets⁹⁴. Eukaryotic membranes are composed of three major categories of lipids: phospholipids, sphingolipids and sterols (Figure 4 and Figure 5)⁹⁵. Phospholipids and sphingolipids are amphiphilic molecules that share a general structure. Both have a hydrophilic "head" and two hydrophobic "tails" formed by acyl chains of variant length and saturation^{26,96}. The type of lipid headgroup attached to the respective backbone can differ in charge, shape and chemistry and determines the lipid class. The degree of saturation found in the acyl chains, as well as the steric and electrostatic properties granted by the polar headgroups contribute to physicochemical properties of the membrane. Long and fully saturated acyl chains will contribute to a thicker more rigid membrane by increasing the acyl chain packing between cellular lipids^{97,98}. Shorter more unsaturated acyl chains will "fluidize" said membrane as their kinked acyl chains will disrupt the dense packing and subsequently increase membrane fluidity^{99,100}. *S. cerevisiae* has a fairly concise lipid fatty acid pool consisting predominantly of C-16:0 (palmitic acid), C-18:0 (stearic acid) and their monounsaturated counterparts C-16:1 (palmitoleic acid) and C-18:1 (oleic acid)⁹¹. This reduced complexity is owned to the fact that in *S. cerevisiae* only a single fatty acid desaturase exists encoded by the *OLE1* gene¹⁰¹. Ole1p is a $\Delta 9$ -desaturase and responsible for the conversion of palmitic acid (16:0) and stearic acid (18:0) into their respective monounsaturated counterparts. In higher eukaryotes, such as mammals, a greater diversity of fatty acid desaturases exists. The Stearoyl-CoA desaturase

1 (SCD-1) is like Ole1p a $\Delta 9$ desaturase and works in concert with $\Delta 5$ and $\Delta 6$ -desaturases to generate a broader repertoire of mono-, di- and poly-unsaturated fatty acids^{102,103}. As a consequence, the repertoire of possible lipid species to be found in both model systems differs greatly. In *S. cerevisiae*, the pool of possible lipids is limited to a few hundred species¹⁰⁴, whereas in mammalian cells the number of possible combinations is in the thousands due to the diversity found in their acyl chains¹⁰⁵.

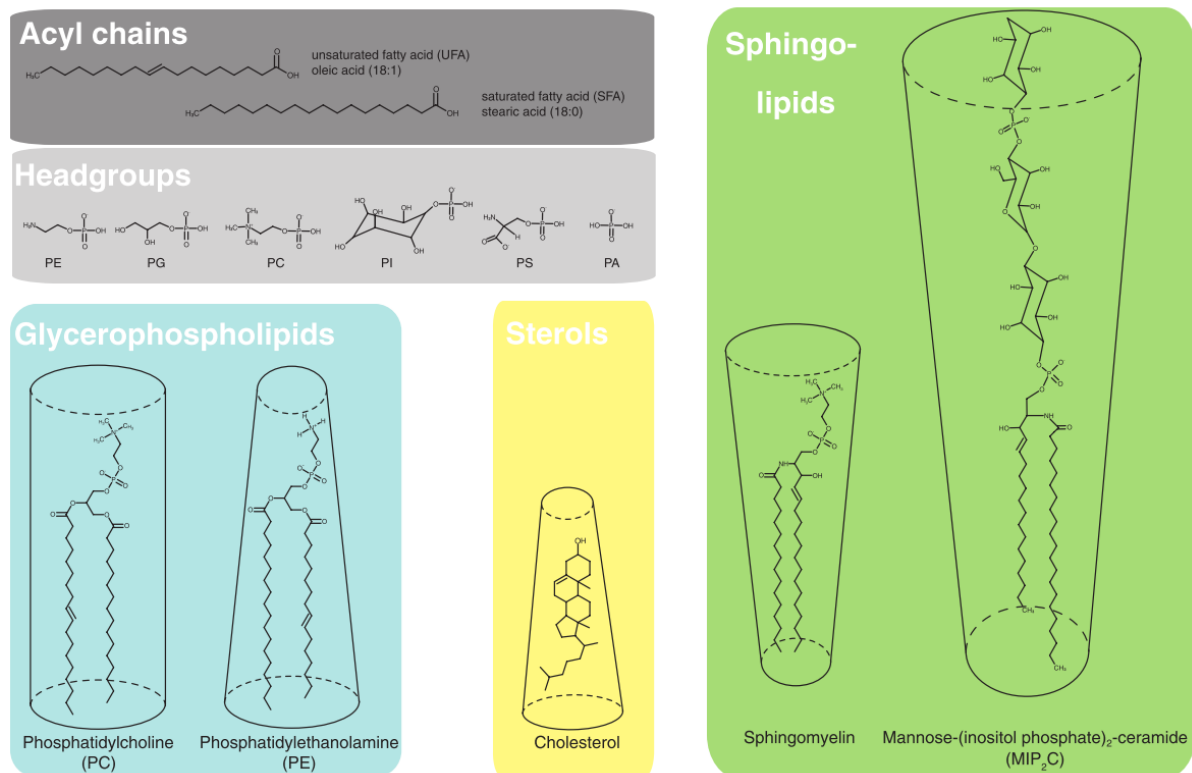


Figure 4 The three major membrane lipid categories

Eukaryotic membranes consist of the following three major lipid categories: Glycerophospholipids (blue shade), sterols (yellow shade) and sphingolipids (green shade). Glycerophospholipids consist of a central glycerol moiety which is esterified with two fatty acids (dark grey shade) and a phosphoric acid group that can further be esterified with various alcohols (light grey shade). *S. cerevisiae* glycerophospholipids often contain acyl chains with a length of 16- and 18- carbon atoms that are either fully saturated (C16:0 and C18:0) or monounsaturated (C16:1 or C18:1). Common headgroups include ethanolamine (phosphatidyl ethanolamine, PE), glycerol (phosphatidyl glycerol, PG), choline (phosphatidyl choline, PC), inositol (phosphatidyl inositol, PI), serine (phosphatidyl serine, PS) and sole phosphate (phosphatidic acid, PA). Sphingolipids consist of a central sphingosine molecule which usually is linked to a very long chain saturated fatty acid (C26:0) by an amid bond. The headgroup and acyl chain diversity contributes to the combinatoric lipid complexity found in glycerophospholipids and sphingolipids. Sterols feature a central four carbon ring structure that is flanked by a polar hydroxyl group and a short non-polar hydrocarbon tail on the opposing site. To illustrate the relative size and shape diversity among the categories PC (with C18:1 and C16:0), PE (with C18:0 and C16:1), cholesterol and sphingomyelin and MIP₂C are depicted. Illustration adapted from Stordeur *et al*¹⁰⁶.

The Phospholipids represent the most abundant category of eukaryotic membrane lipids and constitute up to 84.9 mol% of all membrane lipids^{107,108}. The classes phosphatidylcholine (PC), phosphatidic acid (PA), phosphatidylethanolamine (PE), phosphatidylserine (PS) and phosphatidylinositol (PI) are the major representatives of the phospholipid category. In *S. cerevisiae* PI, PC and PE are the most abundant classes of phospholipids¹⁰⁹. The third and last category, the sterols, are unique in structure and function. They consist of four linked hydrocarbon rings, referred to as the steroid structure. In case of ergosterol the rigid steroid structure is flanked by a single polar hydroxyl group on one side and a short non-polar hydrocarbon tail on the opposing site granting the lipid its amphiphilic property⁹¹. Sterols can not form a bilayer structure by themselves but are incorporated into existing phospholipid bilayers. Sterols do so by positioning their hydroxyl moiety in proximity to the polar headgroups of phospholipids and consequently align their rigid ring structure and aliphatic chain parallel to the acyl chains of phospholipids and sphingolipids in the center of the bilayer¹¹⁰. The incorporation of sterols was shown to increase along membranes of the secretory pathway and culminates up to 40 mol% in the plasma membrane⁹⁶.

All three categories have in common that they use fatty acids (FA) as building blocks – either as an integral component in case of phospholipids or sphingolipids – or as a way to regulate sterol levels by esterification of free sterol and subsequent storage in lipid droplets^{111,112}. FA can be acquired in three different ways: either through exogenous FA uptake, endogenous lipid turnover or via *de novo* synthesis and elongation¹¹³. To incorporate exogenous FA into complex lipids they need to be activated via a thioesterification with coenzyme A by an Acyl-CoA synthetase¹¹⁴. It is worth to mention that complex sphingolipids contain so called very long chain fatty acids (VLCFA) which are derivatives of the previously mentioned four fatty acid representatives, obtained via the metabolic pathway of fatty acid elongation carried out by Elo3p and related enzymes⁹¹.

A common trait in the *de novo* synthesis of major membrane embedded glycerophospholipids such as PI, PS, PE and PC is that they can all be derived from PA. PA itself is a derivative of two successive acyl CoA-dependent acylation reactions. In the first step the stereospecific sn-1 acyltransferases Sct1p and Gpt2p form lysoPA (LPA) by acylation of glycerol-3-P (G3P)¹¹⁵. LPA can then undergo a second acylation at the sn-2 position and react to PA, which is catalyzed by the ER resident enzymes Slc1p and Slc4p^{116,117}. The *de novo* synthesis of PA reflects the first of many branching points in lipid synthesis, leaving the cell with the option to channel the PA towards cytidine diphosphate-diacyl-glycerol (CDP-DAG) pathway for phospholipid synthesis or the option to channel PA towards DAG thereby initiate the lipid storage pathway culminating in the formation of triacylglycerol (TAG). In *S. cerevisiae* Dga1p and Lro1p are the dominant terminal acyltransferases for TAG synthesis¹¹⁸. While both

enzymes use DAG as a substrate, they differ in their fatty acid substrate spectrum. Dga1p uses activated fatty acids to acylate DAG to form TAG while Lro1p couples TAG formation to phospholipid diacylation by transferring a fatty acid from a phospholipid thereby generating lysophospholipids in the process^{119–121}. Hence TAGs represent neutral lipids that have each of their glycerol hydroxy groups esterified with a fatty acid. Due to their nonpolar nature, TAGs are minor components of biological membranes such as the ER membrane, where they constitute ~ 3 mol% of total lipids¹⁰⁸. Since *S. cerevisiae* does not have a mitochondrial β -oxidation, TAGs are not primarily used as a source of energy but rather serve as a storage form of fatty acids for the incorporation into phospholipids in times of membrane biosynthesis⁹¹.

The CDP-DAG pathway resembles a second important branching point in phospholipid synthesis. Three different synthases compete for CDP-DAG to generate different products. PI via Pis1p, phosphatidylglycerolphosphate (PGP) via Pgs1p or PS via Cho1p¹²². For the synthesis of PI, inositol is required, which is either derived from glucose-6-phosphate by Ino1p¹²³ or taken up from the medium via one of the two inositol permeases Itr1p and Itr2p¹²⁴. PI is synthesized via Pis1p in the cytosolic leaflet of the ER from CDP-DAG and inositol¹²⁵. PGP is a precursor for the biosynthesis of cardiolipin (CL) in mitochondria and is generated from CDP-DAG and G3P by Pgs1p¹²⁶. CL is the signature lipid of mitochondria¹²⁷. To generate CL PGP will first be dephosphorylated by Gep4p to yield PG¹²⁷, which can then react with CDP-DAG to form CL, catalyzed by Crd1p (cardiolipin synthase)¹²⁸. Two additional enzymes are further involved in the remodeling of the four acyl chains of CL, namely Cld1p¹²⁹ (cardiolipin phospholipase) and Taz1p¹³⁰ (cardiolipin acyltransferase).

*CHO1*¹³¹ encodes for the ER resident PS synthase catalyzing the formation of PS through a displacement of cytidine monophosphate (CMP) from CDP-DAG with serine¹³². PS represents the first member of the amino glycerophospholipids and serves as a precursor for the biosynthesis of PE and PC. PE is obtained by a decarboxylation of PS carried out by Pds1p, which localizes dominantly to the inner mitochondrial membrane or less frequently to the ER membrane, or alternatively, by the Golgi associated enzyme Pds2p¹³³. PE can be converted into PC by the step-wise addition of three methyl groups catalyzed by the ER resident enzymes Cho2p and Opi3p highlighting again the importance of inter-organellar lipid exchange^{134,135}.

Alternatively, PE or PC can be synthesized through the Kennedy pathway if ethanolamine (Etn) or choline (Cho) are taken up by cells from the environment. Both substrates are transported into the cytosol by the plasma-membrane resident protein Hnm1p¹³⁶. Each of the two compounds are further processed by a specific kinase i.e. the ethanolamine kinase Eki1p

and the choline kinase Cki1p, respectively^{137,138}. The phosphorylated intermediates will then be activated with CTP by Ect1p for Eth-phosphate and Pct1p for Cho-phosphate to form CDP-Etn and CDP-Cho^{139,140}. The terminal reaction is a condensation of either CDP-Etn or CDP-Cho with DAG by the phosphotransferases Ept1p or Cpt1p to generate PE and PC respectively^{141,142}.

The second major category of lipids, sphingolipids, are characterized by their sphingoid base backbone opposed to the glycerol backbone found in phospholipids⁹¹. The *de novo* synthesis of sphingolipids is distributed between two organelles namely the ER and the Golgi complex¹⁴³. The initial steps occur in the ER, where a condensation of L-serine and palmitoyl-CoA catalyzed by the serine palmitoyltransferase (SPT) complex gives rise to 3-ketodihydrosphingosine¹⁴⁴. 3-ketodihydrosphingosine represents the first building block of the sphingolipids namely the long-chain base (LCB). The 3-ketodihydrosphingosine is further converted by Tsc10p to dihydrosphingosine (DHS)¹⁴⁵. DHS can in a hydroxylation be transformed into phytosphingosine (PHS) and together both LCBs can further be processed into ceramides¹⁴⁶. For that an N-acylation at the free amino group with a VLCFA will be catalyzed by the ceramide synthase complex formed by Lag1p, Lac1p and Lip1p¹⁴⁷⁻¹⁴⁹. The product of this reaction is dihydroceramide (DHCer) or phytoceramide (PHCer). Once synthesized DHCer and PHCer have to be transported from the ER to the Golgi complex, where a polar head group is added to the ceramide backbone to form the first complex sphingolipid inositol phosphoryl-ceramide (IPC)¹⁴⁶. Inositol phosphate stems from PI and is added to the 1-OH head group of the sphingoid base by Aur1p¹⁵⁰. IPC can undergo an additional modification in the Golgi complex to form mannose-inositol-phosphoceramide (MIPC). This reaction is catalyzed by the MIPC synthase complex comprised of the catalytic subunit Csg1p and the regulatory subunit Csg2p^{151,152}. A second transfer of inositol phosphate will yield the most complex sphingolipid found in the baker's yeast, M(IP₂)C. All complex sphingolipids in *S. cerevisiae* have in common that their distribution along the secretory pathway increases, a trend that they have in common with sterols the third major category of membrane lipids^{153,154}.

The biosynthesis of the third category of membrane lipids, sterols, represents a major energetic commitment for the cell. It requires the consumption of 24 molecules of ATP, 16 molecules of NADPH and 9 molecules of oxygen^{155,156}. The *de novo* synthesis can be divided into three major steps each mediated in several enzymatic steps (Figure 5). The first step is completely conserved among all three eukaryotic kingdoms and leads to the production of mevalonic acid, initiated by the condensation of two acetyl-coenzyme A molecules. Farnesyl pyrophosphate (farnesyl-PP) is formed in the second step. Notably, farnesyl-PP is also used for the post-translational modification of proteins and it represents a key intermediate for the

biosynthesis of competing pathways involved in the synthesis of ubiquinone and heme groups^{155,157}. The enzyme squalene synthetase encoded by the ERG9 gene catalyzes the condensation of two farnesyl-PP molecules to produce squalene¹⁵⁸. Squalene synthesis via Erg9p therefore regulates the flux of farnesyl-PP molecules into the, from then on, linear sterol biosynthetic pathway. The remaining steps of this pathway (discussed in great detail by Hu *et al.*¹⁵⁵) facilitate the formation of ergosterol which can be incorporated into membranes. Alternatively, the sterol can be esterified via Are1p or Are2p and subsequently stored in lipid droplets^{159,160}.

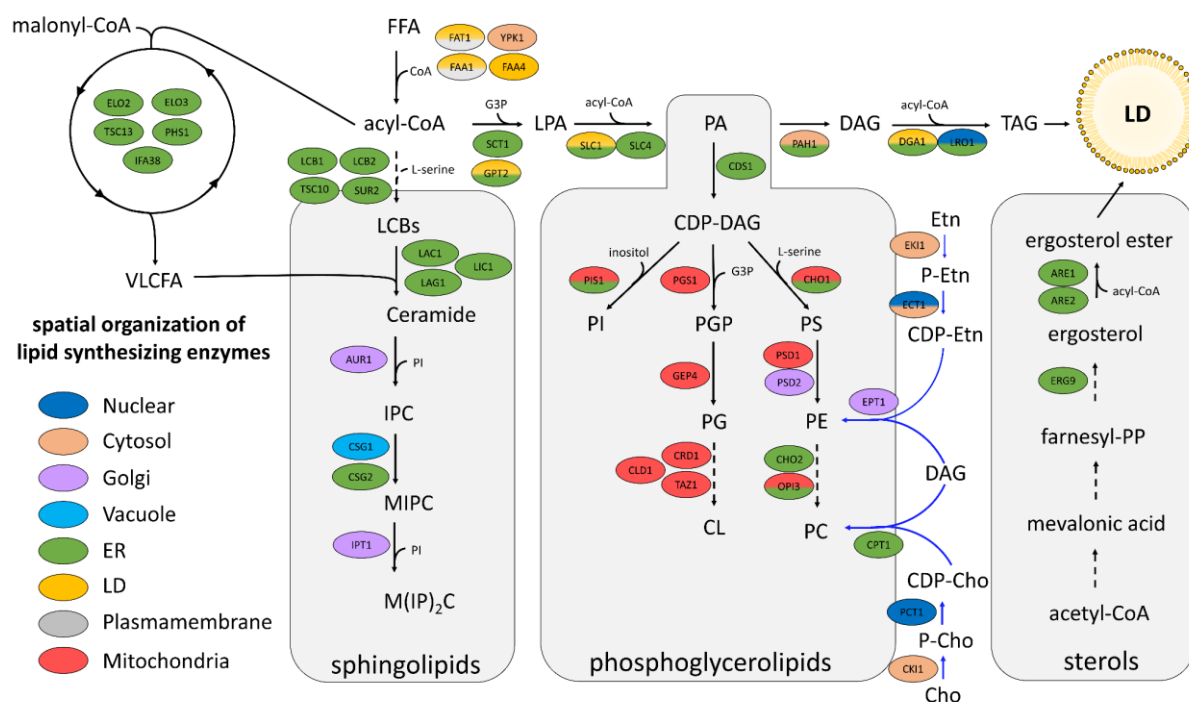


Figure 5 Simplified metabolic map of *S. cerevisiae*'s lipid *de novo* synthesis pathways

Depicted are the pathways for the *de novo* synthesis of the three major classes of membrane lipids in the form of sphingolipids, phosphoglycerolipids and sterols. Lipids and intermediates are given as sole text, while enzyme names are encapsulated in a compartment specific colored bubble. Solid arrows indicate that it's a single enzymatic reaction, dashed arrows indicate reactions in which intermediate metabolites have been omitted for the purpose of clarity. Blue colored arrows represent the Kennedy pathway. Annotation of protein localization is based on a study by Natter *et al.* and uniprot entries^{135,161}. Abbreviations translate to: Free fatty acid = FFA; Coenzyme A = CoA; glyceraldehyde 3-phosphate = G3P; triacylglyceride = TAG; lipid droplet (organelle) = LD; Long-chain (sphingoid) Bases = LCB; cytidine diphosphate diacylglycerol = CDP-DAG; ethanolamine = Etn; phosphoethanolamine = P-Etn; cytidyldiphosphate-ethanolamine = CDP-Etn; diacylglycerol = DAG; choline = CHO; phosphocholine = P-Cho; cytidine diphosphocholine = CDP-Cho; lysophosphatidic acid = LPA; phosphatidic acid = PA; phosphatidylinositol = PI; phosphatidylglycerolphosphate = PGP; phosphatidylglycerol = PG; cardiolipin = CL; phosphatidylethanolamine = PE; phosphatidylcholine = PC; phosphatidylserine = PS; inositol phosphorylceramide = IPC; Mannoinositol phosphorylceramide = MIPC; mannosyl-di-(inositolphosphoryl) ceramide = M(IP)₂C; very long chain fatty acid = VLCFA; farnesyl pyrophosphate = farnesyl-PP; endoplasmatic reticulum = ER.

1.4.2 The OLE pathway – maintaining membrane fluidity

In the second section of this lipid metabolism overview a focus is laid how unsaturated and saturated lipids contribute to the maintenance of membrane fluidity. Membrane fluidity is defined in this thesis as a parameter describing the rotational and translational mobility of membrane constituents e.g. proteins or lipids. A contributing factor to membrane fluidity is the underlying phase behavior of the biological membrane, which is predominantly determined by the temperature and chemical structures of the respective lipid constituents¹⁶². There are two extremes of lipid phase states in membranes, namely the solid/gel phase and the liquid phase¹⁶³. Both phase states are interconvertible e.g. when the transition temperature is surpassed. Fully saturated acyl chains of phospholipids are prone to thermally induced conformational adaptations referred to as the *trans-gauche* isomerization^{164,165}. At low temperatures, the hydrocarbon chain adopts an all-*trans* arrangement, resulting in a fully straightened fatty acyl chain that produces a fully maximized van-der-Waals intermolecular interaction network¹⁶². As a consequence, the membrane structure becomes highly ordered and more densely packed as the proportion of all-*trans* configured acyl chains increases. Lipids of membranes in the solid-ordered state are characterized by a reduced lateral diffusion coefficient ($D_T = \sim 10^{-3} \mu\text{m}^2 \text{s}^{-1}$)¹⁶³, which impedes not only the lateral movement of lipids but also that of embedded proteins. When the temperature exceeds the transition temperature, the solid-ordered state membrane phase is converted into a liquid state phase¹⁶². On the molecular level this conversion is facilitated by converting a greater proportion of fully saturated hydrocarbon chains from the all-*trans* into the *gauche* conformation. The *gauche* conformation induces a kinked structure of the saturated fatty acid that resembles the *cis*-configuration found in unsaturated acyl chains and thereby strongly interferes with the lipid packing density and degree of order. Thus, the liquid disordered membrane is characterized by a high lateral diffusion coefficient ($D_T = \sim 1 \mu\text{m}^2 \text{s}^{-1}$)¹⁶³ and will consequently enable faster rotational and translational diffusion of all membrane components. Since the kinked structure of unsaturated fatty acids is a consequence of the *cis*-configured C-C double bond and therefore stable independent of thermal energization, their incorporation into membrane lipids serves as a way to maintain a liquid-disordered phase state even at low temperatures.

In complex biological membranes the majority of unsaturated fatty acids are found in glycerophospholipids and in *S. cerevisiae* approximately 65-80 % of the total glycerophospholipid acyl chains are monounsaturated¹⁶⁶. Glycerophospholipids therefore tend to adopt a liquid-disordered phase in which they are further enriched¹⁶⁷. In contrast, sphingolipids contain saturated VLCFA and are involved in adopting a solid-ordered phase. The tendency of sphingolipids to segregate together is rooted in the thermodynamically gained

stability conferred through van-der-Waals interactions of their straight hydrocarbon chains^{168,169}. According to the lipid raft hypothesis¹⁷⁰, which postulates that membranes are not homogenous mixtures of lipids but rather characterized by the abundance of short-lived nanoscale assemblies composed of sphingolipids and sterols that are embedded in the sea of glycerophospholipids, a third phase state exists termed the liquid-ordered phase. This phase combines properties of the solid-ordered¹⁷¹ and liquid-disordered phase^{172,173} and is characterized by a high conformational order while still maintaining a high lateral mobility ($D_T = \sim 1 \mu\text{m}^2 \text{s}^{-1}$)¹⁶³.

Since signaling across and within biological membranes often relies on an unrestricted diffusion, it is apparent why a high lateral mobility is crucially important to support membrane associated processes. Budin *et al.* could in fact show that the efficacy of the electron transport chain correlates in a positive manner with the degree of lipid unsaturation in *S. cerevisiae*¹⁷⁴. Further it was shown that the activity of the Ca^{2+} -ATPase is reduced in solid-ordered phase lipid bilayers and increases during liquid-ordered phase transition¹⁷⁵. Although the previously mentioned example resembles *in vitro* work, there is a recent study by Gohrbrandt *et al.* demonstrating that gel/fluid phase separation can co-exist in living cells¹⁷⁶. They have established an experimental framework to study membrane phase separation in bacterial cells by using genetically modified model organisms of *E. coli* and *B. subtilis*. Key findings of their study are that the phase transition is reversible and therefore does not *per se* lead to immediate cell death via membrane rupture. Their data further indicates a drastic demixing of the lipids and consequently membrane proteins are excluded from the gel phase areas and are “enriched” in the remaining liquid regions. In consequence various biological functions are impeded e.g. cell wall synthesis, chromosome segregation, energy production and cell division. Especially for the process of cell division supporting evidence exists from independent laboratories. MreB is an actin homologue of bacterial cells which has an active role in cell elongation by promoting the formation of membrane regions with increased fluidity and thereby influences the distribution of membrane proteins in fluid lipid domains¹⁷⁷. With MinD another cell cycle related protein was identified that shows a membrane phospholipid composition dependent localization behavior. MinD is a member of the Min system which is essential to establish the correct division site in *E. coli*^{178,179}. Both cell cycle candidates mentioned have in common, that they use an amphipathic helix motif to interact with the membrane^{177,179,180} and it is well documented that amphipathic helices have a preference to insert into liquid disordered regions¹⁸¹. Thus, it is interesting to consider the extent to which non-physiological manipulations of membrane phase behavior affect the functionality of proteins containing amphipathic interaction domains and how such manipulation might enable the broad range of observable phenotypes.

These examples demonstrate how membrane fluidity and the closely linked phase behavior of differently composed and energized bilayers contribute to cellular functions. Therefore, it is no surprise that organisms have evolved means to monitor and maintain a physiologically optimal degree of membrane fluidity to support membrane associated biological functions. This process of adaptation is referred to as homeoviscous adaptation¹⁸². The regulation of this membrane property is crucial for all living cells but especially for poikilothermic organisms that have to adapt their membrane composition in regard to environmental temperatures¹⁰⁰. The adaptive response often involves a remodeling of the acyl chain composition e.g. through an increase in poorly packing unsaturated acyl chains in the cold as extensively shown for the DesK/DesR system in *Bacillus subtilis*^{182,183}. For eukaryotic cells the most extensively studied system for homeoviscous adaptation is the OLE pathway present in *S. cerevisiae*¹⁸⁴. In *S. cerevisiae* *OLE1* encodes for the essential Δ^9 -fatty acid desaturase, the only enzyme capable of introducing a double bond in coenzyme-A activated fatty acids, leading to the formation of monounsaturated Coenzyme-A-activated fatty acids prior to their incorporation into lipids¹⁸⁵. The OLE pathway includes all components that are required for the sensing of membrane fluidity to adjusting the level of unsaturated fatty acids if required via Ole1p activity^{186,187}. As *S. cerevisiae* relies on a single fatty acid desaturase to regulate the degree of lipid saturation, its activity has to be tightly regulated. The regulation of Ole1p activity is predominantly facilitated on the transcriptional level¹⁸⁷. An increase in the levels of *OLE1* mRNA are reported for obligate respiratory conditions concomitant with an increase in mitochondrial activities. Smith *et al.* reports 6-fold elevated levels of *OLE1* mRNA when cells are grown on glycerol compared to glucose¹⁸⁸. *OLE1* is associated with the class of hypoxic genes whose expression is regulated in a positive manner as cells switch from aerobic growth to hypoxic or anoxic growth conditions¹⁸⁷. One oxygen related regulatory aspect appears to involve a functional mitochondrial respiratory chain in a redox-sensitive manner. The increase in ROS, generated through the mitochondrial respiratory chain, as cells switch to hypoxic conditions¹⁸⁹, is concomitant with the increase in *OLE1* levels which made investigators propose a signaling function of ROS in hypoxic gene induction¹⁹⁰. Of interest is the finding that the anaerobic induction of *OLE1* was blocked by inhibition of the cytochrome c oxidase, the terminal step in the respiratory chain¹⁹¹. It was further shown that the expression of *COX5b* a hypoxic isoform of cytochrome c oxidase subunit COXV, could serve as an early determinant in the signaling pathway as its expression led to a higher induction of *OLE1* when compared to the aerobic isoform *COX5a*^{190,191}. The presence of unsaturated fatty acids in the culture medium were shown to be another metabolic determinant to regulate the level of *OLE1* transcript and stability^{192,193}. The *OLE1* mRNA half-life under basal growth conditions i.e. fatty acid free medium is 10-12 min¹⁹³. Data by Vemula *et al.* suggests that *OLE1* mRNA half-life is controlled by the general eukaryotic mRNA decay pathway¹⁹⁴ mediated by Xrn1p exonuclease

degradation as in *xrn1*Δ cells the half-life increased to >50 min¹⁹⁵. It was however shown that the supplementation of unsaturated fatty acids reduced the half-life in *xrn1*Δ cells to 23 min suggesting the existence of an additional regulative exonuclease activity outside of the general decay pathway for *OLE1*^{193,195}. One candidate involved in the fatty acid regulated decay is the cytoplasmic exosome complex. Studies that involve mutants related to the cytoplasmic exosome complex show no regulated *OLE1* mRNA decay when exposed to unsaturated fatty acids thereby suggest that *OLE1* mRNA destabilization is conferred via exosomal 3'-5' degradation activity by the cytoplasmic exosome complex¹⁹⁶⁻¹⁹⁸. The dominant positive genetic regulators for *OLE1* expression are Spt23p and Mga2p¹⁸⁷. It was shown that the two ER membrane resident proteins, Spt23p and Mga2p, are responsible for the regulation of *OLE1* gene expression (Figure 6)¹⁹⁹. Both proteins are synthesized as dormant ER membrane anchored transcription factors with a molecular weight of 120 kDa. Upon an increase in the degree of lipid saturation in the ER membrane both proteins become ubiquitylated by the E3 ligase Rsp5p²⁰⁰. Subsequently the ER bound transcription factors will undergo proteasome-dependent processing to liberate soluble transcriptionally competent 90 kDa fragments²⁰¹. These fragments can then migrate into the nucleus and stimulate the expression of *OLE1*.

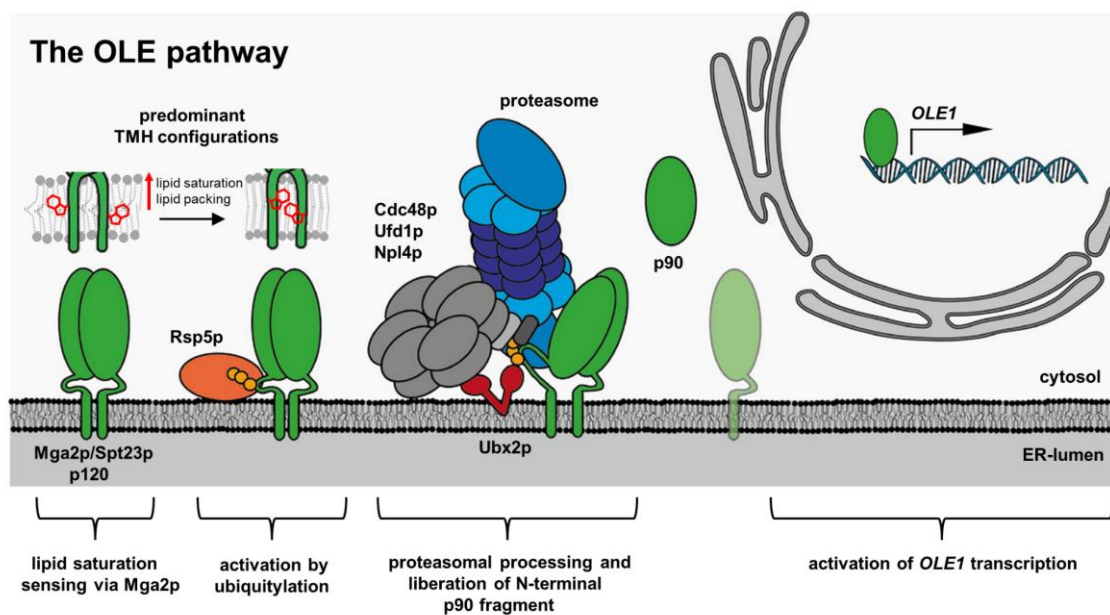


Figure 6 A A schematic representation of the OLE pathway responsible for regulating the lipid saturation in the ER membrane

In *S. cerevisiae* Mga2p or Spt23p homodimers sense via their transmembrane helix (TMH) the lipid packing density of the ER membrane. In a loosely packed ER membrane a relative rotational state is stabilized in which the bulky tryptophan residue (W1042) extends into the surrounding lipid environment. This relative rotational state is defined as the off-condition. An increase in lipid saturation results in a more densely packed ER membrane which will favor a relative rotational state in which the tryptophan residues are pointed towards the dimer interface. This TMH configuration resembles the on-condition and promotes the Rsp5p-mediated ubiquitination of both protomers. The ubiquitin marked proteins will subsequently undergo partial processing by the proteasome and ERAD components which culminates in the liberation of the transcriptionally competent p90 polypeptide. The p90 fragment will then migrate into the nucleus and stimulate the expression of *OLE1* and thereby complete the OLE signaling pathway. The figure was adapted from Ballweg *et al.*¹⁸⁶

Based on this brief depiction of the OLE pathway, the question arises how *S. cerevisiae* detects the changes in the degree of acyl chain saturation when the feature of interests i.e. the presence or absence of a double bond, is located in the hydrophobic core of the membrane? A molecular mechanism was proposed by Covino *et al.* by which the TMH of Mga2p harbors an intra-membrane situated sensory mechanism²⁰². The authors propose a rotation-based mechanism for sensing lipid saturation with a tryptophan residue at its heart. In light of the lipid saturation-dependent processing of Mga2p, Covino *et al.* studied the conformational dynamics in Mga2p's transmembrane region by molecular dynamics (MD) simulations in two lipid environments²⁰². One resembling with its acyl chain composition the loosely packed ER membrane, the second a more saturated ER environment membrane mimicking conditions that enable Mga2p processing *in vivo*. Both conditions showed that Mga2p dimerizes with an apparent preference in the formed dimer interface between the lipid environments. In the loosely packed simulation that is mimicking a fluid membrane the bulky

tryptophan side chains could be easily accommodated for in the loosely packed lipid environment and the TMHs of Mga2p feature a characteristic rotational orientation with both tryptophan residues pointing away from one another. This rotational state of both TMHs is referred to as the off-condition as it resembles a physiological membrane fluidity. In contrast, an increase in packing density and a concomitant decrease in membrane fluidity caused the bulky tryptophan residues to exhibit an inward rotation, stabilizing an alternative TMH orientation in which both tryptophan residues are hidden in the dimer interface. As this membrane composition correlates with the activation of the OLE pathway *in vivo*, this rotational state was referred to as the on-condition. In a follow up study, Ballweg *et al.* propose that the dynamic rotational states in the TMH regions of the Mga2p dimer are rooted the different packing densities for saturated and unsaturated membranes found at the level of the sensory tryptophan residue²⁰³. The authors stress that the TMHs of Mga2p are constantly rotating against each other and thereby explore a variety of rotational states but it is the underlying lipid composition that determines the population of the respective on and off rotational states. Since upregulation of *OLE1* leads to the formation of more unsaturated fatty acids and ultimately to liquefaction of the ER membrane after incorporation into glycerophospholipids, the regulatory loop closes, as physiological membrane fluidity is reached. Since the two rotational states of the on and off conformation are not separated by high energy barriers, future work is needed to address how the inherently weak activating signal of the membrane can be amplified to mount a robust cellular response on the timescale of hours.

2 Materials

2.1 Consumables

All materials used in this study are listed in Table 2

Table 2 Consumables: List of consumables used in this study

Material	Company
96-well plates, sterile	Sarstedt
Reagent reservoirs (50 mL)	Heathrow Scientific®
Bottle top filter, PES-membrane (0,2 µm)	Sarstedt
Conic reagent tube (15 mL and 50 mL)	Sarstedt
Cover glasses, precision No. 1.5H, round 24 mm	Marienfeld-superior
Cryogenic Tube (2 mL)	Genfollower
Glass beads, acid-washed, 425-600 µm	Sigma Aldrich
Microcentrifuge tubes (1,5 and 2,0 mL)	Sarstedt
Microscope slides 26x76 mm	Carl Roth
Nitrile gloves	Starlab
PCR tubes	Sarstedt
Petri dish 92x16 mm	Sarstedt
Polystyrol cuvettes	Sarstedt
Serological pipettes (2, 5, 10, 25 and 50 mL)	Sarstedt
Screw Cap tubes 2 mL	Sarstedt
Scotch tape	Tesa®
Tips (10, 200 and 1000 µL)	Star Lab
Tips, filtered (10, 200 and 1000 µL)	Star Lab

2.2 Chemicals

All chemicals used in this study were of analytical quality and are listed in Table 3

Table 3 Chemicals: List of chemicals used in this study.

Chemical	Company
Agar-Agar	ForMedium
Agarose	Sigma-Aldrich
Ammonium sulfate	Carl Roth
Ampicillin sodium salt	Carl Roth
L-Ascorbic acid sodium salt	ACROS Organics
Calcium chloride (CaCl ₂)	Carl Roth
Complete supplement mixture (CSM)	ForMedium
w/o histidine	
w/o leucine	
w/o uracile	
D(+)-Glucose	Carl Roth
Dimethyl sulfoxide (DMSO)	Fisher Scientific
Dithiothreitol (DTT)	Carl Roth
Deoxynucleotide (dNTP) mix	NEB
Ethanol 96% + 1% MEK	Carl Roth
Ethanol 96 %	NeoLab
Ethidium bromide	Invitrogen™
G418 disulfate salt	Sigma-Aldrich
L-Glutathione reduced	Sigma-Aldrich
Glycerol	Grüssing
Isopropanol	Fisher Scientific
Kanamycin	Carl Roth
Lithium acetate (LiAc)	Carl Roth
Nourseothricin (clonNAT)	Jena Bioscience
Phosphate buffered saline (PBS)	Sigma-Aldrich
Sodium dodecyl sulfate (SDS)	Carl Roth
TERGITOL™ -solution (Type NP-40, 70% aq)	Sigma-Aldrich
Yeast extract	Carl Roth
Yeast nitrogen base (YNB)	ForMedium
w/o amino acids and ammonium sulfate	
Yeast nitrogen base (YNB)	ForMedium
w/o amino acids, ammonium sulfate and inositol	
Tryptone/Peptone	Carl Roth
Tunicamycin	Carl Roth
Salmon sperm DNA solution	Invitrogen™

2.3 Enzymes

A list of all enzymes used in this study (Table 4)

Table 4 Enzymes: List of enzymes used in this study.

Enzyme	Company
Antarctic Phosphatase	NEB
<i>DpnI</i>	NEB
<i>HindIII</i>	NEB
<i>PmeI</i>	NEB
<i>XhoI</i>	NEB
<i>SpeI</i>	NEB
Phusion DNA polymerase	NEB
T5 exonuclease	NEB
Taq DNA ligase	NEB

2.4 Kits

All commercially available kits used in this study are listed in Table 5 according to the manufacturer's protocol unless stated otherwise.

Table 5 Commercial Kits: List of kits that were used in this study.

Name of the Kit	Company
CloneAmp™ HiFi PCR Premix	TaKaRa
Oligo(dT)12-18 Primer	Invitrogen™
ORA™ qPCR Green ROX L Mix	highQu
RNeasy Plus Mini Kit	Qiagen
QIAprep Spin Miniprep Kit	Qiagen
QIAquick PCR Purification Kit	Qiagen
SuperScript™ II Reverse Transcriptase	Invitrogen™

2.5 Media and buffers

Composition of all buffers and media are listed in Table 6. For solid media the respective composition was modified to yield a final agar concentration of 1.5 % (w/v).

Table 6 Buffers and media: List of buffers and media used in this study.

Buffer/medium name	Composition
Colony PCR suspension buffer	200 mM lithium acetat
LB medium	1% (w/v) SDS 1% (w/v) NaCl 1% (w/v) peptone/tryptone
YPD medium	0..5% (w/v) yeast extract 2% (w/v) glucose 2% (w/v) peptone/tryptone 1% (w/v) yeast extract
SCD complete medium	0.5% (w/v) ammonium sulfate 0.079% (w/v) CSM complete 2% (w/v) glucose 0.19% (w/v) YNB
SCD complete medium w/o inositol	0.5% (w/v) ammonium sulfate 0.079% (w/v) CSM complete 2% (w/v) glucose 0.19% (w/v) YNB w/o inositol
SOB-Medium	0.5% (w/v) yeast extract 2% (w/v) peptone/tryptone 10 mM NaCl 2.5 mM KCl (adjust pH with NaOH to 7.0; autoclave) 10 mM MgCl ₂ (adjust prior to use only)
Lipidomics storage buffer	155 mM ammonium bicarbonate 10 mM sodium azide
5x Isothermal reaction buffer	500 mM Tris-HCl pH 7,5 50 mM MgCl ₂ 50 mM DTT 5 mM NAD ⁺ 1 mM dATP 1 mM dTTP 1 mM dGTP 1 mM dCTP 25% (w/v) PEG-4000
1,3x Gibson assembly master mix	25 U/μL Phusion DNA polymerase 4 U/μL Taq Ligase 4 U/μL T5 Exonuclease 20% (v/v) 5x Isothermal reaction buffer
Inoue Transformation-Buffer (ITB)	55 mM MnCl ₂ 15 mM CaCl ₂ 250 mM KCl 10 mM PIPES (pH 6.7)

2.6 Oligonucleotids

All oligonucleotides used in this study are listed in Table 7. Oligonucleotides were purchased from Sigma-Aldrich and purified via High-Performance Liquid Chromatography (HPLC).

Table 7 Oligonucleotides: List of oligonucleotides used in this study.

Name	Sequence 5' → 3'	Description
qRT-PCR oligonucleotides		
TP127	CTTTGTCGCCCAAGAGTATGCG	Spliced <i>HAC1</i> (FW) ²⁰⁴
TP287	ACTGCGCTTCTGGATTACGC	Spliced <i>HAC1</i> (RV) ²⁰⁴
JC099	TCTACCGTCACTCAAATGCC	<i>OLE1</i> (FW)
JC100	ACCAGTTTCGTAGATTTACCTC	<i>OLE1</i> (RV)
TP169	TGTCACCAACTGGGACGATA	<i>ACT1</i> (FW) ²⁰⁴
TP170	AACCAGCGTAAATTGGAACG	<i>ACT1</i> (RV) ²⁰⁴
CM120	TACCTGCCGTAGACAACAAC	Spliced <i>HAC1</i> (FW)
CM121	ACTGCGCTTCTGGATTAC	Spliced <i>HAC1</i> (RV)
CM110	ATATTCCAGGATCAGGTCTTCCGTAGC	<i>TAF10</i> (FW) ²⁰⁵
CM111	GTAGTCTTCTCATTCTGTTGATGTTGTTGTTG	<i>TAF10</i> (RV) ²⁰⁵
Ire1-mNeongreen construction		
CM61	GAAAATCTTCGAATTTTGATATCATCAGACTTTG GTCTTTGCAAAA	<i>IRE1</i> N terminal FW
CM62	CCTTAGAAACAGCGTAATCTGGAACGTCATATG GA	<i>IRE1</i> N terminal RV
CM63	AGATTACGCTGTTTCTAAGGGTGAAGAAGACAA C	mNeongreen FW
CM64	GCGTAGAAGACTTGTACAATTCGTCCATACCC	mNeongreen RV
CM65	ATTGTACAAGTCTTCTACGCGTCATACAGTAG	<i>IRE1</i> C terminal FW
CM66	AACGGGCCCTCTAGACTCGAGGGCAATAATCAA CCAAGAAGAAGC	<i>IRE1</i> C terminal RV
pDDI2-based INO2* overexpression plasmid		
CM174	CACCGAAGTCGGTGATGCTGT	FW primer pCM62 backbone generation
CM175	GTTTCGTTTCCCGATACATGCGA	RV primer pCM62 Backbone generation

Table continues next page

CM182	AGAATCAATCCCCGGATTCTAGAACTAGTGGATCC	FW INO2* amplification for pCM62 insertion
CM179	CAGCATCACCGACTTCGGTGGGCCGCAAATTAA AGCCTTCG	RV INO2* amplification for pCM62 insertion
CM180	GCATGTATCGGGAAACGAACGGAAAATCCAAGC TTTCAAGATGCG	FW primer pDDI2 amplification
CM181	AGAATCCGGGGATTGATTCTTTTGAAGAGGAGC AA	RV primer pDDI2 amplification

Integrative HO locus pTDH3-based overexpression plasmids

CM212	TCAGAAACGGCCTTAAC	FW primer pCM63 backbone generation
CM213	GGTATGTAGATATACTAGAAGTTCTC	RV primer pCM63 backbone generation
CM214	AAGCTGggccggccatttaaagttaaacAATTATCCTGG GCACGAGTG	FW primer HO locus left
CM215	GGCGTTTGTCTCGAACATGAC	RV primer HO locus right
CM216	AGTATTGTGTCATGTTTCGAGACAAACGCCTCATT ATCAATACTCGCCATTTTC	FW primer pTDH3 amplification
CM217	GGAGGGCGTGAATGTAAGCGTGACATAACTAAT TACATGATCGAACTAAGTTCTGGTG	RV primer pTDH3 amplification
CM218	TCATGTAATTAGTTATGTCACG	FW primer tCYC1 amplification
CM219	GCAAATTAAAGCCTTCGAG	RV primer tCYC1 amplification
CM220	GGGACGCTCGAAGGCTTTAATTTGCGACATGGA GGCCCAGAATAC	FW primer kanMX cassette amplification
CM221	ACATTCTGTGAAGTTGTTCCCCAGCAGTATAGC GACCAGCATTC	RV primer kanMX cassette amplification
CM222	CTGGGGGAACAACCTTCACAG	FW primer HO locus right
CM223	GGCGAATTGggccagcgtggccgttaaactGTAAGAT TCCGCCACATTTTATAC	RV primer HO locus right

Table continues next page

CM244	TCGAAACTAAGTTCTGGTG	RV primer, use in conjunction with CM218 on pCM63 to generate overexpression plasmid
CM224	GTTTTAAAACACCAGAACTTAGTTTCGAATGGAT ACATCAAACCTTTGGTTTG	FW SWI5 amplification
CM225	GTAAGCGTGACATAACTAATTACATGATTACCTT TGATTAGTTTTTATTGG	RV SWI5 amplification
CM226	GTTTTAAAACACCAGAACTTAGTTTCGAATGGAT TCCACAGGCGCTTC	FW MSN5 amplification
CM227	GTAAGCGTGACATAACTAATTACATGATCAGTTG TCATCAAAGAGATTACC	RV MSN5 amplification
CM228	GTTTTAAAACACCAGAACTTAGTTTCGAATGGAC CCGATTGGAATAAAC	FW DOC1 amplification
CM229	GTAAGCGTGACATAACTAATTACATGATTAACGT AATATAGCATCCTG	RV DOC1 amplification
CM230	GTTTTAAAACACCAGAACTTAGTTTCGAATGATG GATATCAGCCCTAC	FW ROF1 amplification
CM231	GTAAGCGTGACATAACTAATTACATGACTACTTT GAGTATTGGTGG	RV ROF1 amplification
CM232	GTTTTAAAACACCAGAACTTAGTTTCGAATGACC GCAAAGACTTTTCTAC	FW HAP4 amplification
CM233	GTAAGCGTGACATAACTAATTACATGATCAAAT ACTTGTACCTTTAAAAAATCG	RV HAP4 amplification
CM234	GTTTTAAAACACCAGAACTTAGTTTCGAATGAAG TTCGAAGACCTCTTG	FW IES3 amplification
CM235	GTAAGCGTGACATAACTAATTACATGATTAAGA ATGTTTTCCAAAAGG	RV IES3 amplification
CM238	GTTTTAAAACACCAGAACTTAGTTTCGAATGCGC AATGCAGGTG	FW NIP100 amplification
CM239	GTAAGCGTGACATAACTAATTACATGATCATTG TAATATGTAACAACATTTTGAG	RV NIP100 amplification
CM247	GTTTTAAAACACCAGAACTTAGTTTCGAATGGTT TTAAAACACCAGAACTT	FW NEM1 amplification

Table continues next page

CM248	GTAAGCGTGACATAACTAATTACATGATCAGTAA GCGTGACATAACTAAT	RV NEM1 amplification
CM249	GTTTTAAACACCAGAACTTAGTTTCGAATGATG ACCAGTTTGTCCAAAAG	FW ICE2 amplification
CM250	GTAAGCGTGACATAACTAATTACATGATCATCAA CTACCAGAACCTATTA	RV ICE2 amplification
oligonucleotides for homologous recombination		
JR65	GCATTTAAAGGCACTTATTGAAGGTCATTTTGGC GAACAGAACATTTTCGTTcatagctcaaaatgttctactc	FW knockout <i>MGA2</i> with KAR2SS-dsRED-HDEL + NatMX
JR66	GTCTTTTCATTATACACACATATATATATATATA CGTAAAAAAGCAGAgacatggaggcccagaatac	RV knockout <i>MGA2</i> with KAR2SS-dsRED-HDEL + NatMX
CM144	ATACTGATATCGATACGGATACAGAAGCTGAAGA TGATGAATCACCAGAACGGATCCCCGGGTTAAT TAAC	FW <i>SEC63</i> c-terminal mNeongreen tagging
CM145	ATATACGTCTAAGAGCTAAAATGAAAACTATAC TAATCACTTATATCTACATCGATGAATTCGAGCT CG	RV <i>SEC63</i> c-terminal mNeongreen tagging
CM146	CTTCTACTGGTGTCAAGACCTCTAACACCAAGGT CTCTTCCAGGAAAGCTCGGATCCCCGGGTTAAT TAAC	FW <i>ELO3</i> c-terminal mNeongreen tagging
CM147	TTAATTTTTTTCTTTTTTCATTCGCTGTCAAAAATTC TCGCTTCCTATTTACATCGATGAATTCGAGCTCG	RV <i>ELO3</i> c-terminal mNeongreen tagging
CM148	GAAAAGTACAAAAA ACTTGCAAATGAATTGGAA AAAAACAACGCTCGGATCCCCGGGTTAATTAAC	FW <i>RTN1</i> c-terminal mNeongreen tagging
CM149	CAAAAGTTAGCTATTCTTGTTTGAATGAAAAAAA AAAAGCACTCACATCGATGAATTCGAGCTCG	RV <i>RTN1</i> c-terminal mNeongreen tagging
CM184	CCAAACCAACCAAACTTACACACAATAATATACA ATTACAATTATTTACAGACATGGAGGCCAGAAT ACCCTCC	FW <i>ATG41</i> knockout with kanMX
CM185	ATATGCGATGCAAGGGGTCGTGAGAACAAGTAG AGATGTGGTAAAATGCGCAGTATAGCGACCAGC ATTCACATAC	RV <i>ATG41</i> knockout with kanMX

Table continues next page

CM186	TTAAGTGATTAAGGGTGTTGGAGTATACTGAAAC ACGCTTTTTGGCCATTGACATGGAGGCCAGAA TACCCTCC	FW PET309 knockout with kanMX
CM187	TGATTTTTTGATATATATGCAGTTGATTATACAAT ATGATATATGCATTTTCAGTATAGCGACCAGCATT CACATAC	RV PET309 knockout with kanMX
CM188	CAATACTACGTGAGCAGCAACGAAAGCACATAT ATAGACGACAAAGTAGTGACATGGAGGCCAGAA ATACCCTCC	FW COA3 knockout with kanMX
CM189	CAAAGCCTATTGATGGAAGACCACAGCGTACCT CCACATTAACGGTCTTTTCAGTATAGCGACCAGCA TTCACATAC	RV COA3 knockout with kanMX
CM190	TAAATTTCACTGACTATAGAGTACATACATAAACA AGCATCCAAAAAACGACATGGAGGCCAGAAAT ACCCTCC	FW UBC4 knockout with kanMX
CM191	AATCCCATATAAATCTTGCTTCTCTTTTTTCAGCTG AGTAAGGACTTCTGTCAGTATAGCGACCAGCATT CACATAC	RV UBC4 knockout with kanMX
CM192	TGCTATTGTCCATCCCTATCCTAGTTTTAAAAATA TAATTCTATCAAGTTGACATGGAGGCCAGAAATA CCCTCC	FW NCS2 knockout with kanMX
CM193	TAAATAAATAAATACATAACCATTGGAATAGCGA AGCCTTTGACATTTTCACAGTATAGCGACCAGCAT TCACATAC	RV NCS2 knockout with kanMX
CM194	CAGCGAAGATAACGGTTACACAATTATCACGTTG ATTCGTCAACTTAAAGGACATGGAGGCCAGAA TACCCTCC	FW YCL001W-A knockout with kanMX
CM195	TTTCAGCAGTGTCTTCGCATAAAATCCAGGGGA GCATAATATTATTATTCCAGTATAGCGACCAGCA TTCACATAC	RV YCL001W-A knockout with kanMX
CM196	GAATATCAAACATCGAACGAGAGCATCTTGAAGA TATTTATGTTCTAAATGACATGGAGGCCAGAAAT ACCCTCC	FW MAL33 knockout with kanMX

Table continues next page

CM197	CACTCTATCAGTATATCTATCTCGTATAAGTGAA CGGCGTGAACAATAAACAGTATAGCGACCAGCA TTCACATAC	RV MAL33 knockout with kanMX
%HAC1 splicing primers		
CM95	TACAGGGATTTCCAGAGCACG	%HAC1 splicing FW ²⁰⁵
CM96	TGAAGTGATGAAGAAATCATTCAATTC	%HAC1 splicing RV ²⁰⁵

2.7 Plasmids

All plasmids used are listed in Table 8.

Table 8 Plasmids: List of plasmids used in this study

Name	Description	Source
pRE451	pcDNA3.1(+)-IRE1-3xHA-GFP WT	(Halbbleib <i>et al.</i> , 2017) ²⁰⁶
pSS474	pNH605-PADH-GEM-PGAL1	(Papagiannidis <i>et al.</i> , 2021) ²⁰⁷
pSS475	pNH605-PADH-GEM-PGAL1-INO2(L119A)	(Papagiannidis <i>et al.</i> , 2021) ²⁰⁷
pSS455	pRS303N-PTEF-KAR2SS-dsRED-HDEL	Provided by Sebastian Schuck ²⁰⁴
pSS445	pFA6a-mNeongreen-kanMX6	(Schäfer <i>et al.</i> , 2020) ²⁰⁸
pCM08	pcDNA3.1(+)-IRE1-3xHA-mNeongreen WT	This study
pCM59	pHIS3p:yomWasabi-Tub1+3'UTR::URA3	(Markus <i>et al.</i> , 2015) ²⁰⁹
pCM62	pCM62-PDDI2-INO2*(L119A)-TCYC1-LEU2	This study
pCM63	pCM63-PTDH3-TCYC1-kanMX	This study
pCM65	pCM63-PTDH3-SWI5-TCYC1-kanMX	This study
pCM66	pCM63-PTDH3-MSN5-TCYC1-kanMX	This study
pCM67	pCM63-PTDH3-DOC1-TCYC1-kanMX	This study
pCM68	pCM63-PTDH3-ROF1-TCYC1-kanMX	This study
pCM69	pCM63-PTDH3-HAP4-TCYC1-kanMX	This study
pCM70	pCM63-PTDH3-IES3-TCYC1-kanMX	This study
pCM72	pCM63-PTDH3-NIP100-TCYC1-kanMX	This study
pCM75	pCM63-PTDH3-NEM1-TCYC1-kanMX	This study
pCM76	pCM63-PTDH3-ICE2-TCYC1-kanMX	This study
pCM76	pCM63-PTDH3-SWI5-TCYC1-kanMX	This study

2.8 Strains

All strains used in this study are listed in Table 9.

Table 9 Strains: List of strains used in this study

Name	Genotype	Source
<i>E. coli</i> strains used in this study		
TOP10	F- <i>mcrA</i> Δ (<i>mrr-hsdRMS-mcrBC</i>) ϕ 80 <i>lacZ</i> Δ M15 Δ <i>lacX74</i> <i>recA1 araD139</i> Δ (<i>araleu</i>)7697 <i>galU galK rpsL</i> (Str ^R) <i>endA1 nupG</i>	Invitrogen
<i>S. cerevisiae</i> strains used in this study		
yRE001	<i>MATa; hisΔ1; leu2Δ0; met15Δ0; ura3Δ0</i>	EUROSCARF
yRE046	<i>MATa; hisΔ1; leu2Δ0; met15Δ0; ura3Δ0; ire1ΔkanMX3</i>	EUROSCARF
yRE127	<i>MATa; hisΔ1; leu2Δ0; met15Δ0; ura3Δ0;</i> <i>pIRE1+ire1ΔURA</i>	(Halbleib <i>et al</i> , 2017)
yRE342	<i>MATa; hisΔ1; leu2Δ0; met15Δ0; ura3Δ0; ire1Δ::URA cys-</i> <i>less IRE1-3xHA-GFP C552::HIS</i>	(Väth <i>et al</i> , 2021)
yRE343	<i>MATa; hisΔ1; leu2Δ0; met15Δ0; ura3Δ0; ire1Δ::URA cys-</i> <i>less IRE1-3xHA-GFP::HIS</i>	(Väth <i>et al</i> , 2021)
yRE425	<i>MATa; hisΔ1; leu2Δ0; met15Δ0; ura3Δ0; ire1Δ::URA</i> <i>IRE1-3xHA-GFP::HIS</i>	(Halbleib <i>et al</i> , 2017) ⁸⁷
yRE428	<i>MATa; hisΔ1; leu2Δ0; met15Δ0; ura3Δ0; ire1Δ::URA</i> <i>IRE1-3xHA-GFP W426A (IF2)::HIS</i>	(Halbleib <i>et al</i> , 2017)
yRE522	<i>MATa; hisΔ1; leu2Δ0; met15Δ0; ura3Δ0; ire1Δ::URA cys-</i> <i>less IRE1-3xHA-GFP L545C::HIS</i>	(Väth <i>et al</i> , 2021)
yRE530	<i>MATa; hisΔ1; leu2Δ0; met15Δ0; ura3Δ0; ire1Δ::URA cys-</i> <i>less IRE1-3xHA-GFP E540C::HIS</i>	(Väth <i>et al</i> , 2021)
yRE531	<i>MATa; hisΔ1; leu2Δ0; met15Δ0; ura3Δ0; ire1Δ::URA cys-</i> <i>less IRE1-3xHA-GFP T541C::HIS</i>	(Väth <i>et al</i> , 2021)
yRE532	<i>MATa; hisΔ1; leu2Δ0; met15Δ0; ura3Δ0; ire1Δ::URA cys-</i> <i>less IRE1-3xHA-GFP G542C::HIS</i>	(Väth <i>et al</i> , 2021)
yRE533	<i>MATa; hisΔ1; leu2Δ0; met15Δ0; ura3Δ0; ire1Δ::URA cys-</i> <i>less IRE1-3xHA-GFP V543C::HIS</i>	(Väth <i>et al</i> , 2021)
yRE534	<i>MATa; hisΔ1; leu2Δ0; met15Δ0; ura3Δ0; ire1Δ::URA cys-</i> <i>less IRE1-3xHA-GFP F544C::HIS</i>	(Väth <i>et al</i> , 2021)
yRE535	<i>MATa; hisΔ1; leu2Δ0; met15Δ0; ura3Δ0; ire1Δ::URA cys-</i> <i>less IRE1-3xHA-GFP L546C::HIS</i>	(Väth <i>et al</i> , 2021)
yRE640	<i>MATa; his31 leu20 met150ura30 can1::STE2pr-spHIS5</i> <i>lyp1::STE3pr-LEU2; Elo3mCherry • KAR2ss-sfGFP-</i> <i>HDEL</i>	This study
yRE641	<i>MATa; his31 leu20 met150ura30 can1::STE2pr-spHIS5</i> <i>lyp1::STE3pr-LEU2; Elo3mCherry • KAR2ss-sfGFP-</i> <i>HDEL; mga2ΔNAT</i>	This study

Table continues next page

yRE717	<i>MATa; hisΔ1; leu2Δ0; met15Δ0; ura3Δ0; ire1Δ::URA cys-less IRE1-3xHA-GFP L547C::HIS</i>	(Väth <i>et al</i> , 2021)
yRE718	<i>MATa; hisΔ1; leu2Δ0; met15Δ0; ura3Δ0; ire1Δ::URA cys-less IRE1-3xHA-GFP F548C::HIS</i>	(Väth <i>et al</i> , 2021)
yRE719	<i>MATa; hisΔ1; leu2Δ0; met15Δ0; ura3Δ0; ire1Δ::URA cys-less IRE1-3xHA-GFP L549C::HIS</i>	(Väth <i>et al</i> , 2021)
yRE720	<i>MATa; hisΔ1; leu2Δ0; met15Δ0; ura3Δ0; ire1Δ::URA cys-less IRE1-3xHA-GFP I550C::HIS</i>	(Väth <i>et al</i> , 2021)
yRE721	<i>MATa; hisΔ1; leu2Δ0; met15Δ0; ura3Δ0; ire1Δ::URA cys-less IRE1-3xHA-GFP F551C::HIS</i>	(Väth <i>et al</i> , 2021)
yRE773	<i>MATa; hisΔ1; leu2Δ0; met15Δ0; ura3Δ0; ire1Δ::URA cys-less IRE1-3xHA-GFP E540C W426A (IF2)::HIS</i>	(Väth <i>et al</i> , 2021)
yRE774	<i>MATa; hisΔ1; leu2Δ0; met15Δ0; ura3Δ0; ire1Δ::URA cys-less IRE1-3xHA-GFP T541C W426A (IF2)::HIS</i>	(Väth <i>et al</i> , 2021)
yRE776	<i>MATa; hisΔ1; leu2Δ0; met15Δ0; ura3Δ0; ire1Δ::URA cys-less IRE1-3xHA-GFP F544C W426A (IF2)::HIS</i>	(Väth <i>et al</i> , 2021)
yRE792	<i>MATa; hisΔ1; leu2Δ0; met15Δ0; ura3Δ0; ire1Δ::URA IRE1-3xHA-GFP::HIS; pSS455</i>	This study
yRE793	<i>MATa; hisΔ1; leu2Δ0; met15Δ0; ura3Δ0; ire1Δ::URA cys-less IRE1-3xHA-GFP::HIS; pSS455</i>	This study
yCM171	<i>MATa; hisΔ1; leu2Δ0; met15Δ0; ura3Δ0; ire1Δ::URA IRE1-3xHA-GFP R537Q::HIS</i>	This study
yCM175	<i>MATa; his31 leu20 met150ura30 can1::STE2pr-spHIS5 lyp1::STE3pr-LEU2; Elo3mCherry • KAR2ss-sfGFP-HDEL::URA; atg41ΔkanMX3</i>	This study
yCM176	<i>MATa; his31 leu20 met150ura30 can1::STE2pr-spHIS5 lyp1::STE3pr-LEU2; Elo3mCherry • KAR2ss-sfGFP-HDEL::URA; pet309ΔkanMX3</i>	This study
yCM177	<i>MATa; his31 leu20 met150ura30 can1::STE2pr-spHIS5 lyp1::STE3pr-LEU2; Elo3mCherry • KAR2ss-sfGFP-HDEL::URA; coa3ΔkanMX3</i>	This study
yCM178	<i>MATa; his31 leu20 met150ura30 can1::STE2pr-spHIS5 lyp1::STE3pr-LEU2; Elo3mCherry • KAR2ss-sfGFP-HDEL::URA; mal33ΔkanMX3</i>	This study
yCM179	<i>MATa; his31 leu20 met150ura30 can1::STE2pr-spHIS5 lyp1::STE3pr-LEU2; Elo3mCherry • KAR2ss-sfGFP-HDEL::URA; ncs2ΔkanMX3</i>	This study
yCM180	<i>MATa; his31 leu20 met150ura30 can1::STE2pr-spHIS5 lyp1::STE3pr-LEU2; Elo3mCherry • KAR2ss-sfGFP-HDEL::URA; ubc4ΔkanMX3</i>	This study

Table continues next page

yCM181	<i>MATa; his31 leu20 met150ura30 can1::STE2pr-spHIS5 lyp1::STE3pr-LEU2; Elo3mCherry • KAR2ss-sfGFP-HDEL::URA; YCL001W-AΔkanMX3</i>	This study
yRE846	<i>MATa; his31 leu20 met150ura30 can1::STE2pr-spHIS5 lyp1::STE3pr-LEU2; Elo3mCherry • KAR2ss-sfGFP-HDEL::URA; mga2ΔNAT; pet309ΔkanMX3</i>	This study
yRE847	<i>MATa; his31 leu20 met150ura30 can1::STE2pr-spHIS5 lyp1::STE3pr-LEU2; Elo3mCherry • KAR2ss-sfGFP-HDEL::URA; mga2ΔNAT; coa3ΔkanMX3</i>	This study
yRE848	<i>MATa; his31 leu20 met150ura30 can1::STE2pr-spHIS5 lyp1::STE3pr-LEU2; Elo3mCherry • KAR2ss-sfGFP-HDEL::URA; mga2ΔNAT; atg41ΔkanMX3</i>	This study
yRE849	<i>MATa; his31 leu20 met150ura30 can1::STE2pr-spHIS5 lyp1::STE3pr-LEU2; Elo3mCherry • KAR2ss-sfGFP-HDEL::URA; mga2ΔNAT; mal33ΔkanMX3</i>	This study
yRE850	<i>MATa; his31 leu20 met150ura30 can1::STE2pr-spHIS5 lyp1::STE3pr-LEU2; Elo3mCherry • KAR2ss-sfGFP-HDEL::URA; mga2ΔNAT; ncs2ΔkanMX3</i>	This study
yRE851	<i>MATa; his31 leu20 met150ura30 can1::STE2pr-spHIS5 lyp1::STE3pr-LEU2; Elo3mCherry • KAR2ss-sfGFP-HDEL::URA; mga2ΔNAT; ubc4ΔkanMX3</i>	This study
yRE852	<i>MATa; his31 leu20 met150ura30 can1::STE2pr-spHIS5 lyp1::STE3pr-LEU2; Elo3mCherry • KAR2ss-sfGFP-HDEL::URA; mga2ΔNAT; YCL001W-AΔkanMX3</i>	This study
yCM126	<i>MATa; hisΔ1; leu2Δ0; met15Δ0; ura3Δ0; ire1Δ::URA IRE1-3xHA-mNeongreen::HIS</i>	This study
yCM139	<i>MATa; hisΔ1; leu2Δ0; met15Δ0; ura3Δ0; ire1Δ::URA IRE1-3xHA-mNeongreen::HIS; mga2Δ KAR2ss-dsRED-HDEL::NAT</i>	This study
yCM144	<i>MATa; hisΔ1; leu2Δ0; met15Δ0; ura3Δ0; mga2Δ KAR2ss-dsRED-HDEL::NAT</i>	This study
yCM152	<i>MATa; hisΔ1; leu2Δ0; met15Δ0; ura3Δ0; mga2Δ KAR2ss-dsRED-HDEL::NAT; SEC63mNeongreen::kanMX3</i>	This study

Table continues next page

yCM153	<i>MATa; hisΔ1; leu2Δ0; met15Δ0; ura3Δ0; mga2Δ</i> <i>KAR2ss-dsRED-HDEL::NAT;</i> <i>ELO3mNeongreen::kanMX3</i>	This study
yCM154	<i>MATa; hisΔ1; leu2Δ0; met15Δ0; ura3Δ0; mga2Δ</i> <i>KAR2ss-dsRED-HDEL::NAT;</i> <i>RTN1mNeongreen::kanMX3</i>	This study
yCM210	<i>MATa; hisΔ1; leu2Δ0; met15Δ0; ura3Δ0;</i> <i>SEC63mNeongreen::kanMX3</i>	This study
yCM211	<i>MATa; hisΔ1; leu2Δ0; met15Δ0; ura3Δ0;</i> <i>ELO3mNeongreen::kanMX3</i>	This study
yCM212	<i>MATa; hisΔ1; leu2Δ0; met15Δ0; ura3Δ0;</i> <i>RTN1mNeongreen::kanMX3</i>	This study
yRE858	<i>MATa; hisΔ1; leu2Δ0; met15Δ0; ura3Δ0; ire1Δ::URA</i> <i>IRE1-3xHA-mNeongreen::HIS; mga2Δ KAR2ss-dsRED-</i> <i>HDEL::NAT; YDL227CΔpTDH3-SWI5-tCYC1::kanMX3</i>	This study
yRE859	<i>MATa; hisΔ1; leu2Δ0; met15Δ0; ura3Δ0; ire1Δ::URA</i> <i>IRE1-3xHA-mNeongreen::HIS; mga2Δ KAR2ss-dsRED-</i> <i>HDEL::NAT; YDL227CΔpTDH3-MSN5-tCYC1::kanMX3</i>	This study
yRE860	<i>MATa; hisΔ1; leu2Δ0; met15Δ0; ura3Δ0; ire1Δ::URA</i> <i>IRE1-3xHA-mNeongreen::HIS; mga2Δ KAR2ss-dsRED-</i> <i>HDEL::NAT; YDL227CΔpTDH3-DOC1-tCYC1::kanMX3</i>	This study
yRE861	<i>MATa; hisΔ1; leu2Δ0; met15Δ0; ura3Δ0; ire1Δ::URA</i> <i>IRE1-3xHA-mNeongreen::HIS; mga2Δ KAR2ss-dsRED-</i> <i>HDEL::NAT; YDL227CΔpTDH3-ROF1-tCYC1::kanMX3</i>	This study
yRE862	<i>MATa; his31 leu20 met150ura30 can1::STE2pr-spHIS5</i> <i>lyp1::STE3pr-LEU2; Elo3mCherry • KAR2ss-sfGFP-</i> <i>HDEL; mga2ΔNAT; YDL227CΔpTDH3-HAP4-</i> <i>tCYC1::kanMX3</i>	This study
yRE863	<i>MATa; hisΔ1; leu2Δ0; met15Δ0; ura3Δ0; ire1Δ::URA</i> <i>IRE1-3xHA-mNeongreen::HIS; mga2Δ KAR2ss-dsRED-</i> <i>HDEL::NAT; YDL227CΔpTDH3-IES3-tCYC1::kanMX3</i>	This study
yRE864	<i>MATa; hisΔ1; leu2Δ0; met15Δ0; ura3Δ0; ire1Δ::URA</i> <i>IRE1-3xHA-mNeongreen::HIS; mga2Δ KAR2ss-dsRED-</i> <i>HDEL::NAT; YDL227CΔpTDH3-NIP100-tCYC1::kanMX3</i>	This study

Table continues next page

Materials

yRE865	<i>MATa; hisΔ1; leu2Δ0; met15Δ0; ura3Δ0; ire1Δ::URA</i> <i>IRE1-3xHA-mNeongreen::HIS; mga2Δ KAR2ss-dsRED-</i> <i>HDEL::NAT; YDL227CΔpTDH3-NEM1-tCYC1::kanMX3</i>	This study
yRE866	<i>MATa; hisΔ1; leu2Δ0; met15Δ0; ura3Δ0; ire1Δ::URA</i> <i>IRE1-3xHA-mNeongreen::HIS; mga2Δ KAR2ss-dsRED-</i> <i>HDEL::NAT; YDL227CΔpTDH3-ICE2-tCYC1::kanMX3</i>	This study
yRE867	<i>MATa; his31 leu20 met150ura30 can1::STE2pr-spHIS5</i> <i>lyp1::STE3pr-LEU2; Elo3mCherry • KAR2ss-sfGFP-</i> <i>HDEL; YDL227CΔpTDH3-HAP4-tCYC1::kanMX3</i>	This study
yCM200	<i>MATa; hisΔ1; leu2Δ0; met15Δ0; ura3Δ0; ire1Δ::URA</i> <i>IRE1-3xHA-mNeongreen::HIS; mga2Δ KAR2ss-dsRED-</i> <i>HDEL::NAT; YCL018WΔpDDI2-INO2(L119A)-</i> <i>tCYC1::kanMX3</i>	This study
yCM201	<i>MATa; hisΔ1; leu2Δ0; met15Δ0; ura3Δ0; ire1Δ::URA</i> <i>IRE1-3xHA-mNeongreen::HIS; pSS455;</i> <i>YCL018WΔpDDI2-INO2(L119A)-tCYC1::kanMX3</i>	This study
yCM172	<i>MATa; hisΔ1; leu2Δ0; met15Δ0; ura3Δ0; ire1Δ::URA</i> <i>IRE1-3xHA-mNeongreen::HIS; mga2Δ KAR2ss-dsRED-</i> <i>HDEL::NAT; leu2::GEM-PGAL1-LEU2</i>	This study
yCM173	<i>MATa; hisΔ1; leu2Δ0; met15Δ0; ura3Δ0; ire1Δ::URA</i> <i>IRE1-3xHA-mNeongreen::HIS; mga2Δ KAR2ss-dsRED-</i> <i>HDEL::NAT; leu2::GEM-PGAL1-INO2(L119A)-LEU2</i>	This study

3 Methods

3.1 Microbiological methods

3.1.1 Generation and transformation of chemically competent *E. coli*

To generate chemically competent cells a derivative of the Inoue method was used in this study²¹⁰. To that extent ITB was prepared by dissolving 15.1 g piperazine-N,N'-bis(2-ethanesulfonic acid) (PIPES) in 80 mL MQ. The pH was adjusted to 6.7 by titration with 5 M KOH and subsequently solution was brought to a final volume of 100 mL. After filter sterilization the solution was aliquoted and stored at -20 °C. Finally, the solutes listed in Table 6 were mixed, filter sterilized and stored at -20°C. Preparation of cells started out by inoculating 25 mL of SOB medium in a 250-mL flask with a single bacterial colony. After 6 h of incubation at 37°C and 220 rpm 100 µL of said culture was used to inoculate a main culture of 250 mL SOB medium. The main culture was grown over night at 18°C with constant agitation at 220 rpm. When cells reached an OD₆₀₀ of 0.5 the cells were harvested by centrifugation at 2500 g for 10 min at 4°C. After the supernatant was discarded, cells were resuspended in 80 mL ice-cold ITB. Cells were again pelleted by centrifugation at 2500 g for 10 min at 4°C. Supernatant was discarded and cells were resuspended in 20 mL of ice-cold ITB. To that cell suspension 1.5 mL DMSO was added and the suspension was mixed by gently swirling the suspension in ice-water followed by an incubation in ice for 10 min. Consequently, the cells were dispensed into chilled sterile microcentrifuge tubes and immediately snap frozen by immersing the aliquots in liquid nitrogen. Until further use the cells were stored at -80°C.

Transformation of generated chemically competent cells started by thawing an aliquot on ice for 5 min. Transforming DNA was added and suspension was mixed with a pipette. After incubating the cells for 30 min on ice a heat shock was applied at 42 °C for 45 seconds. Cells were allowed to cool for 2 min on ice and then received a recovery treatment by adding 500 µL LB-media. After 45 min of incubation at 37°C under agitation 30 µL of the cell suspension were plated out on the respective selective LB-agar plates, the remaining culture was centrifuged at 3000 g for 5 min at RT and the cell pellet was resuspended in 30 µL LB-media and plated out to guarantee formation of single colonies after incubating both plates at 37 °C over night.

3.1.2 Generation, transformation and storage of *S. cerevisiae* strains

Competent yeast cells were generated by using the lithium acetate-based method as described by Ito *et al.*²¹¹. To this end, a single colony of the desired yeast strain was used to inoculate a 3 mL pre-culture in YPD and grown at 30°C overnight at 220 rpm. The following day, 50 mL of YPD was inoculated to an OD₆₀₀ of 0.2. The main culture was grown at 30°C until an OD₆₀₀ of 0.8 was reached. The cells were harvested by centrifugation at 3000 g for 5 min at RT. The supernatant was discarded and the cells were washed with 1 mL LATE buffer and after a second centrifugation step with the exact settings as the previous resuspended in 250 µL LATE buffer and stored at 4°C until further usage.

For the transformation, 5 µL of ssDNA salmon sperm, which was previously denatured at 95 °C for 10 min and cooled on ice prior to use, was added to 50 µL of chemically competent cells. Transforming effective DNA in the range of 0,5-2 µg were added and the mixture was incubated for 20 min at RT. The reaction was supplemented with 10 µL DMSO followed by 150 µL PLATE buffer. After 30 min of incubation at 30 °C the cells were exposed to a heat shock at 42 °C for 15 min. Subsequently the cells were centrifuged at 6000 g for 5 min at RT. The supernatant was carefully removed as the pelleting behavior is affected by the DMSO/PLATE buffer and the cells were washed with 1 mL sterile MQ. After one washing step the cells were resuspended in 80 µL sterile MQ water and plated on selective agar plates. The plates were incubated at 30 °C for 2 days before single colonies were transferred to new selective plates. In total each clone was subjected to two selective agar plate selection steps, followed by a cultivation on YPD plates without any selective pressure prior to their transfer on a third selective agar plate which was followed by an overnight culture in selective media for long term storage preparation. Long term storage was achieved by mixing 500 µL of the stationary over night culture with 400 µL of sterile 50% (w/v) glycerol solution. The glycerol stock was move immediately to the -80° C freezer and allowed to freeze. The newly generated strains were tested via colony-PCR.

3.1.3 Cultivation of *S. cerevisiae* strains

Unless stated otherwise the cultivation of *S. cerevisiae* strains was carried out in flasks at 30 °C and 220 rpm. In general, an experiment started by streaking out desired strain on appropriate agar plates followed by an incubation step of 2-3 days at 30 °C. These plates were stored at RT and were used a maximum of one week to start experiments. For that matter, a

pre-culture was started at a defined OD₆₀₀ of 0.4 in 3 mL of adequate liquid medium. After 19 h of incubation at 30 °C and 220 rpm, the culture was stationary and a main culture was inoculated to an OD₆₀₀ of 0.1.

3.2 Molecular biological methods

3.2.1 Polymerase chain reaction (PCR)

The PCR method was used for *in vitro* amplification of specific DNA sequences or site directed mutagenesis. The standard PCR protocol is shown in Table 10.

Table 10 Standard reaction conditions for PCR

Phase	Temperature [°C]	Time	Number of cycles
Initial denaturation	95	1 min	1
Denaturation	95	30 sec	
Annealing	50-60	30 sec	30
Elongation	72	30 sec kb ⁻¹	
Finale Extension	72	10 min	1

Table 11 contains the standard pipetting scheme for a 50 µL PCR reaction. The Corresponding oligonucleotides used in this study are listed in Table 7.

Table 11 Standard PCR reaction mixture

Reagents	Amount [µL]
ddH ₂ O	31,5
5x HF-Buffer	10
FW-Primer (10 pM)	2.5
RV-Primer (10 pM)	2.5
dNTPs (10 mM)	2
Template (5-50 ng)	1
PHUSION DNA polymerase	0.5

3.2.2 Agarose gel electrophoresis

The agarose gel electrophoresis technique was used to separate individual DNA fragments based on their size in the electric field. A 2% (w/v) agarose gel was used for fragments with an expected size of 1000 bp or less, and a 1% (w/v) agarose gel was used for fragments with a size of 1000 bp and greater. The DNA was mixed with 6x DNA-loading dye (NEB) and loaded into the pockets of an agarose gel. In addition, a size standard (New England Biolabs) was applied to each gel for later analysis. Separation was performed at 130 V for 35 min in 1x TAE buffer. Subsequently agarose gels were incubated for 20 min in an ethidium bromide bath followed by a visualization by UV light illumination.

3.2.3 Gibson assembly technique

For the assembly of multiple DNA fragments the gibson assembly cloning technique was used²¹². Table 12 contains all components for the homemade 1.33x gibson assembly mastermix. After preparation 15 μ L aliquots were stored at -20°C until needed. To increase the efficiency of DNA fragment assembly the molar ratio of insert to backbone was adjusted to a 3:1 ratio and subsequently the gibson assembly was carried out at 50°C for 60 min in a PCR cycler.

Table 12 Gibson assembly mastermix components

Reagents	
5x isothermal buffer	final concentration
Tris-HCl pH 7.5	500 mM
MgCl ₂	50 mM
dATP	1 mM
dCTP	1 mM
dGTP	1 mM
dTTP	1 mM
DTT	50 mM
PEG-8000	25 % (w/v)
NAD ⁺	5 mM
1.33x gibson assembly master mix	amount [μL]
5x isothermal buffer	100
Taq DNA ligase	50
T5 exonuclease	0.5
Q5 Hi-Fi DNA polymerase	6.25
ddH ₂ O	218.25

3.2.4 Minimal inhibitory concentration assay

Yeast strains were struck out on YPD plates three days prior to starting the assay. A 3 mL YPD over night culture was inoculated to an OD₆₀₀ of 0.4 and grown for 19 h at 30 °C at 220 rpm. The stationary overnight culture was then used to inoculate 3 mL of a preculture in either SCD or YPD to an OD₆₀₀ of 0.2. After 6 hours of incubation at 30 °C and 220 rpm the OD₆₀₀ was measured and a 250 µL main culture of SCD or YPD was inoculated to an OD₆₀₀ of 0.01 with the respective proteotoxic drug concentrations in a 96-well plate. The plate was incubated at 30 °C for 18-19 h without agitation. Cells were subsequently resuspended in 200 µL and transferred into a fresh 96-well plate for the final OD₆₀₀ measurement in the microplate reader Tecan Spark.

3.2.5 Temperature gradient growth Assay

Cells were treated as described in 3.2.4 with appropriate adjustments to the cultivation conditions for the main culture in the form of medium additives and the change from the 96-well format to single PCR tube format. Subsequently, the PCR reaction tubes were transferred to a gradient PCR cycler and grown for 19 h at a 20 °C spanning temperature gradient, starting at 20 °C and ending at 40 °C. Finally, the main culture was resuspended and 50-100 µL of the suspension was transferred to a 96-well plate, in which 100 µL of the respective main culture medium was pre-cast with 1 % (w/v) SDS to remove the turbidity of the unused free fatty acids prior to the final OD₆₀₀ measurement in the Tecan Spark.

3.2.6 Quantitative real time PCR (qRT-PCR)

To assess relative changes in mRNA levels RNA was isolated from 5 OD₆₀₀ units of cells by following the instructions of the RNeasy Plus RNA isolation Kit (Qiagen). Subsequently, 500 ng of total RNA served as a template for Oligo(dT) based cDNA synthesis by following the instructions of the Superscript II RT protocol. The cDNA was diluted 1:10 prior to using it as a template in a ORA qPCR Green ROX L Mix based reaction run in a Mic qPCR cycler system. Primers enlisted in Table 7 were used at a final concentration of 400 nM. In Table 13 the qPCR program is shown. Data analysis was carried out by using the comparative $\Delta\Delta C_t$ method²¹³.

Table 13 General qPCR program

Phase	Temperature [°C]	Time	Number of cycles
Initial denaturation	95	15 min	1
Denaturation	95	20 sec	
Annealing	62	20 sec	40
Elongation	72	30 sec	
Finale Extension	72	5 min	1

3.3 Biochemical methods

3.3.1 Cell lysate preparation and lipid extraction

Cells destined for whole cell lipidomic analysis were pelleted when the respective conditions of interest were matched and snap-frozen with liquid nitrogen prior to storage at -80°C until further use. To obtain cell lysates, frozen pellets were allowed to thaw on ice prior to resuspending them in 1 mL of 155 mM ammonium bicarbonate. The cell suspension was transferred to a reaction tube containing 200 μ L of baked zirconia beads (0.5 mm diameter) and cell disruption was carried out using the Disruptor Genie® for 10 min at 4°C. Afterwards, 350 μ L of the resulting lysate was transferred into a new reaction tube and snap-frozen prior to lipid extraction and analysis via shotgun mass spectrometry. The lipid extraction and subsequent spiking of internal lipid standard mixture for consequent mass spectrometry was performed by Lipotype GmbH (Dresden, Germany) as described in Reinhard *et al.*¹.

3.4 Cell imaging

3.4.1 Phenotypic high-throughput microscopy screening

The genome wide microscopic screen was carried out at the Weizmann Institute of Science (Rehovot, Israel) in the lab of Maya Schuldiner by a former colleague Michael Gecht²¹⁴. In short, first two query strains were created that harbor two genetically encoded fluorescent marker to visualize the ER morphology by my former colleague Harald Hofbauer. Subsequently the SGA methodology and a RoTor replicator was used to create a custom library based on the Yeast Knockout²¹⁵ and Yeast DAMP library²¹⁶ in the lab of Maya Schuldiner. The newly generated strains were then inoculated from agar plates to liquid plates and grown in a shaking incubator. Cells were then transferred by a liquid handling device into microscope plates and subsequently fed to the microscope stage for image acquisition. For each well/strain three images were acquired by the fully automated fluorescence microscope and the images were then manually analyzed by three different scientists based on their deviation of percentage of aberrant ER formation compared to the query strain.

3.4.2 Live cell imaging (epifluorescence microscopy)

Before imaging cell suspension was prepared as following. After harvesting 1 OD₆₀₀ unit of cells they were washed once with 1 mL of SCD medium and subsequently resuspended in a total of 15 μ L SCD. Next, a circular 25 mm glass coverslip was mounted into an Attotfluor cell chamber. 10 μ L of the cell suspension were placed in the center of the coverslip and the cell suspension was covered with a circular 2% SCD-agarosepad.

Image acquisition was carried out with an inverted AXIO Observer Z1 microscope (Zeiss) controlled by the Zen 2.6 blue software. Images were taken with a Rolera-EM-C2 camera (Qimaging). All images were acquired after applying immersion oil to the Plan-Apochromat 63x/1.40 NA oil DIC M27 objective (Zeiss). For eGFP an excitation wavelength of 488 nm was used in conjunction with the 38 HE Green fluorescent filter for detection in the range of 500 – 550 nm emission wavelength. For dsRED an excitation wavelength of 567 nm was used in conjunction with the 43 HE DsRed filter for detecting in the range of 570 – 640 nm. If not stated differently, a light intensity of 3 % was used with a 300 ms exposure time.

3.4.3 Confocal laser scanning microscopy and FRAP

Cells were prepared as described in 3.4.2. Microscopy was performed at an LSM 880 confocal laser scanning microscope (Zeiss) driven by the Zen 2.6 black software with a Plan-Apochromat 63x1.40 NA oil DIC M27 oil immersion objective. The eGFP/mNeongreen fluorophores were excited at a wavelength of 488 nm with 2 % laser power and for subsequent detection an emission wavelength of 523 nm was used. For dsRED the excitation wavelength was 561 nm at 2 % laser power and detection occurred at an emission wavelength of 579 nm. For Z-Stack acquisition a step size of 190 nm was chosen with an image size of 240x240 pixel using the Airyscan SuperResolution® mode.

Fluorescence recovery after photobleaching (FRAP), was performed on the previously described LSM 880 Airyscan microscope. Cells were imaged in the Airyscan Fast mode®. A square with a pixel size of 8x8 defined in all experiments the region of interest (ROI) and was placed on top of a healthy or aberrant ER. Then 5 frames were measured to determine the initial fluorescence in the ROI and subsequently using the 405,458 and 488 nm lasers at 100 % laser power the fluorescence of the ROI was brought down to 20 % of its initial value. Intensity was monitored over time in the ROI every 150 ms for a total of 40 seconds. To determine the recovery every dataset was analyzed using FIJI®. In total for each FRAP experiment the intensity of three ROI's were measured, the bleached region, a control region of an unaffected cell in the same image and a background region outside of the cell. For all regions the intensity over time was determined. The recovery in the bleached region was derived by normalizing to the loss of intensity in the control region after subtraction of background intensity values. The corrected intensity values were then plotted against the time between image acquisition in GraphPad Prism. After normalization the data was fitted with the one phase association equation giving the recovery time defined as the timepoint at which 50 % of the initially measured intensity is reached again after application of the bleach pulse.

4 Results

4.1 The impact of established UPR inducing drugs on the lipidome of *Saccharomyces cerevisiae*

The accumulation of unfolded proteins in the ER lumen poses a great danger to the viability of a cell. Therefore, multiple ways evolved to cope with this situation. Historically, Ire1p's role as a communicator of ER-stress between the ER and the nucleus was often studied by inducing ER-stress via proteotoxic drugs such as dithiothreitol (DTT) and tunicamycin (TM). DTT is a potent reducing agent that induces ER-stress by disrupting disulfide bond formation in the ER. TM blocks the N-glycosylation of newly synthesized proteins in the ER²¹⁷. One goal of this thesis is to determine how DTT and TM affect the cellular lipid composition.

4.1.1 A systematic screen to find complete minimal inhibitory concentrations that allow for a comparison between DTT and TM as UPR inducing drugs

As the goal of this study was to reveal the impact DTT and TM might have on the lipidome of acutely stressed cells the first challenge was to settle for a concentration for both drugs with different pharmacological properties. To this end, I established the most conservative concentration i.e. the lowest possible concentration to inhibit growth of cells with a fully functional UPR in minimal (SCD) and complex medium (YPD). To determine the respective growth inhibiting drug concentration I exposed the wildtype strain BY4741 of the BY series and its isogenic *ire1Δ* counterpart to various concentrations of DTT and TM for 19 hours via a minimal inhibitory concentration (MIC) assay. Cellular growth was assayed subsequently by measuring the OD₆₀₀ (Figure 7). As seen in Figure 7 (A-D), the wildtype strain is much more resilient to proteotoxic drugs when compared to the *ire1Δ* strain, presumably due to a functional UPR. Notably, the medium has a substantial impact on the drug resistance phenotype. In YPD medium, higher concentrations of DTT are required to fully inhibit the growth of wildtype and *ire1Δ* cells (Figure 7 A and C). Intriguingly, the medium has an opposite effect on the TM resistance (Figure 7 B and D) meaning that higher concentrations of TM are required to fully impair growth in SCD medium. The MIC assays helped to choose appropriate concentrations of TM and DTT to effectively inhibit growth for each medium. For all future experiments the following conditions were used: 8 mM DTT or 1,0 µg/mL TM for YPD and 2 mM DTT or 1,5 µg/mL TM for the cultivation in SCD medium.

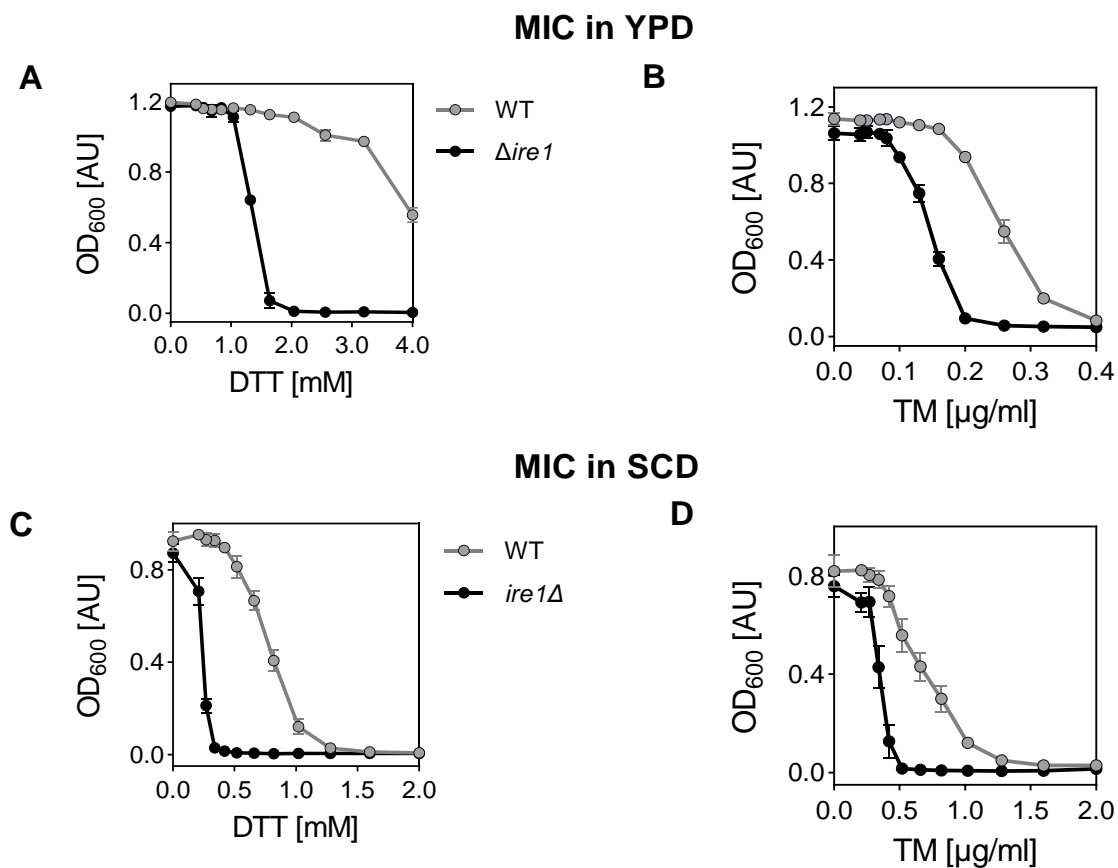


Figure 7 Impact of DTT and TM on cellular growth in chemically defined minimal medium (SCD) and complex medium (YPD)

The impact of varying concentrations of DTT and TM on cellular growth under prolonged exposure was determined. To this end, stationary cells of an overnight culture in YPD were used to inoculate a main culture in either YPD (A, B) or SCD (C, D) to an OD₆₀₀ of 0.2. After 6 h of cultivation, exponentially growing cells were used to inoculate a 96-well plate to an OD₆₀₀ of 0.01 with the respective plotted concentrations of either DTT or TM. After 16 h of cultivation without agitation, the cells were resuspended, transferred into a new 96-well plate and a final OD₆₀₀ measurement was carried out. Plotted are biological triplicates with technical duplicates with each datapoint representing the average \pm SD.

4.1.2 Acute ER-stress and its consequences on cellular growth

Having seen that DTT and TM affect cellular growth under prolonged conditions I was interested to learn more about their immediate effects on cellular growth. Hence, the cells were cultivated in liquid media by inoculating YPD or SCD to an OD₆₀₀ of 0.1 using stationary cells cultivated in the same medium. As the cultures reached an OD₆₀₀ of 0.8 (indicated by dotted lines in Figure 8 and Figure 9), they were either left untreated resulting in the unstressed control condition, termed “no stress”, or exposed DTT or TM for YPD (Figure 8) and SCD (Figure 9). Both figures show a representative growth curve at 30°C under constant agitation at 220 rpm. When the growth curves are fitted to the Malthusian exponential growth model, they reveal that the doubling time (86 min for YPD opposed to 107 min for SCD) differs between media but not between the two different strains in the no stress condition. Furthermore, one can see for both drugs and slightly more pronounced for the DTT treatment a decrease in the growth rate for both the wildtype and the *ire1Δ* strain after one hour of drug application in both media. This is surprising, as these strains exhibited remarkably different resilience to proteotoxic stresses in overnight experiments lasting 19 hours in total.

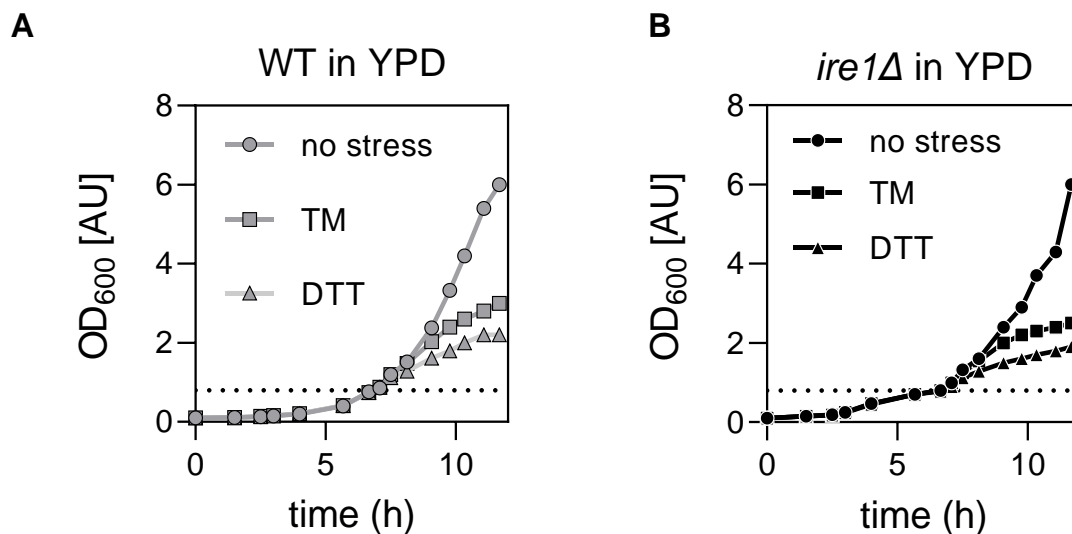


Figure 8: Consequences of acute ER-stress on cellular growth in complex medium (YPD)

Plotted are representative growth curves of the WT and *ire1Δ* strain in YPD medium. Cells were grown at 30 °C and under constant agitation (220 rpm). A stationary overnight culture in YPD was used to inoculate the main culture to an OD₆₀₀ of 0.1. When the cells reached an OD₆₀₀ of 0.8, they were either left untreated or stressed with TM (1.0 μg/mL) or DTT (8 mM). Data shown are from a single representative experiment.

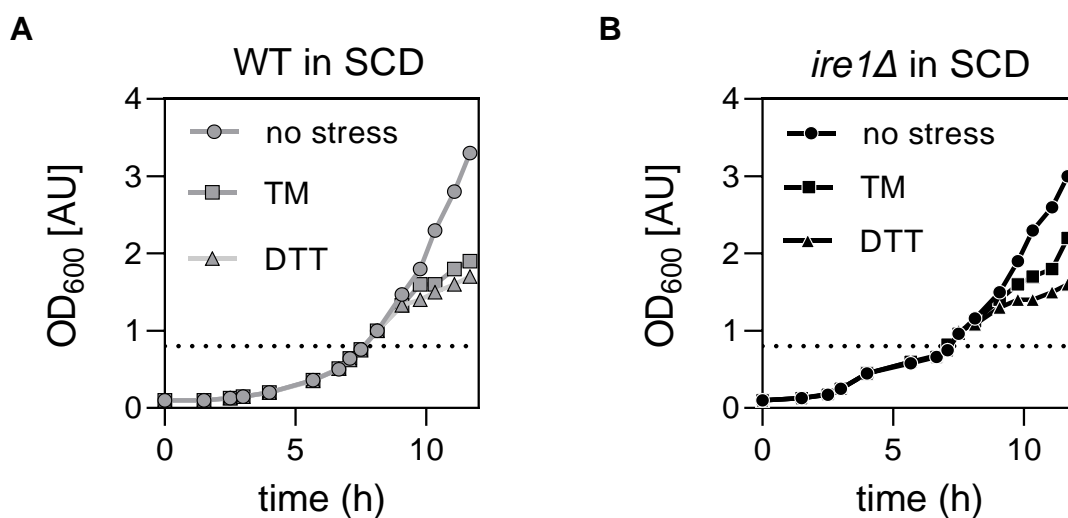


Figure 9: Consequences of acute ER-stress on cellular growth in chemically defined minimal medium (SCD)

Plotted are representative growth curves of the WT and *ire1Δ* strain in SCD medium. Cells were grown at 30 °C and under constant agitation (220 rpm). A stationary overnight culture in SCD was used to inoculate the main culture to an OD₆₀₀ of 0.1. When the cells reached an OD₆₀₀ of 0.8, they were either left untreated or stressed with TM (1.5 μg/mL) or DTT (2 mM). Data shown are from a single representative experiment.

4.1.3 The impact of DTT and TM on the lipid class composition of acutely stressed *S. cerevisiae*

Prolonged UPR activation triggers apoptosis²¹⁸. However, the molecular basis for chronic ER-stress remains poorly defined. While the accumulation of misfolded proteins after application of proteotoxic drugs is well documented, their effect on the cellular lipid composition is insufficiently studied. Changes in membrane lipid class composition thereby represent an unexplored mechanism that may contribute to perpetuating the UPR synergistically with unfolded proteins. Therefore, the whole cell lipid composition of cells cultivated in different media in presence or absence of proteotoxic drugs was determined by quantitative shotgun lipidomic analysis²¹⁹. The sample acquisition followed the cultivation protocol described in 4.1.2. Since UPR signaling peaks within 1 hour of drug application^{56,220}, which coincides with the timing of growth inhibition (Figure 8 and Figure 9), samples were taken one hour after drug application. Next to the WT, the *ire1* Δ strain served as a control as its lipidome should reveal UPR dependent contributions in the tested conditions. Strikingly, the TM treatment seemed to have little to no impact on the lipidome of both WT and *ire1* Δ cells (Figure 10). DTT, however, caused a significant increase in the levels of PA in wildtype and *ire1* Δ cells cultivated in YPD.

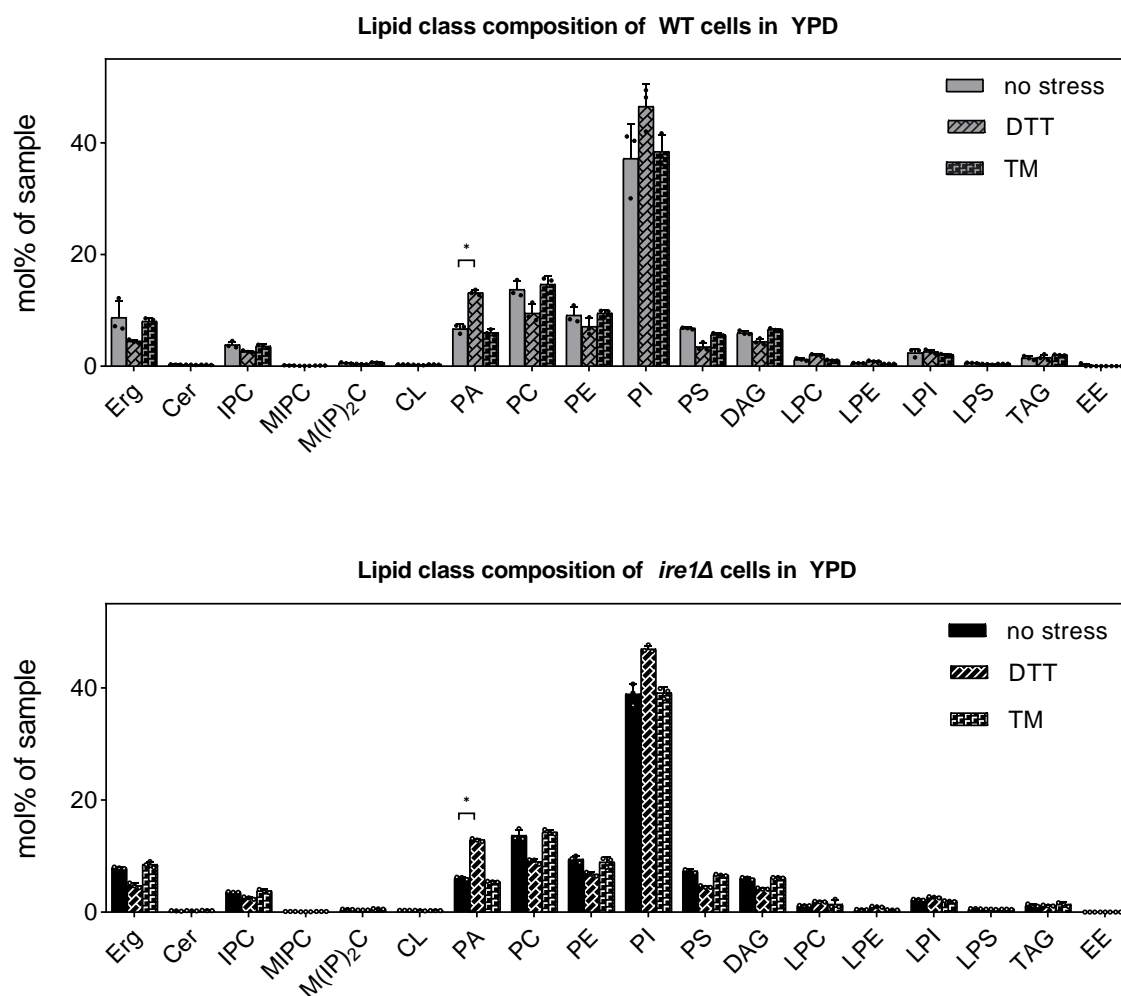


Figure 10 The lipid class composition of WT and *ire1Δ* cells grown in YPD medium after one hour of proteotoxic stress exposure

Lipid class composition in mol% of the sample. Sample generation was carried out as followed: Stationary cells cultivated in YPD medium were used to inoculate fresh YPD to an OD₆₀₀ of 0.1. Cells were subsequently grown until they reached an OD₆₀₀ of 0.8. Consequently, cells were left untreated for 1 hour, leading to the no stress sample, or stressed with 8 mM DTT or 1 μg/mL TM prior to harvesting. Abbreviations translate to Erg = ergosterol; Cer = ceramide; IPC = inositolphosphorylceramide; MIPC = mannosyl-IPC; M(IP)2C = mannosyl-di-IPC; CL = cardiolipin; PA = phosphatidic acid; PC = phosphatidylcholine; PE = phosphatidylethanolamine; PI = phosphatidylinositol; PS = phosphatidylserine; DAG = diacylglycerol; LPC = lyso-PC; LPE = lyso-PE; LPI = lyso-PI; LPS = lyso-PS; TAG = triacylglycerol; EE = ergosteryl ester. Plotted are biological triplicates, their average and ± SD. Raw data taken from Reinhard *et al.*¹ but reevaluated with an unpaired two-tailed t-test, assuming Gaussian distribution. Benjamini, Krieger and Yekutieli method was used to correct for false discovery rate (Q=5%).

The robustness of the cellular lipidome against a short time perturbation with proteotoxic drugs becomes even more apparent when considering the lipid class composition shown for the two strains cultivated in SCD medium (Figure 11). Here, practically no difference is seen between the DTT or TM treatment for the cells apart from an increase in ergosterol esters for the WT

when exposed to DTT. Furthermore, DTT leads to a significant reduction of the very low abundant MIPC lipids in case of the *ire1Δ* strain cultivated in SCD.

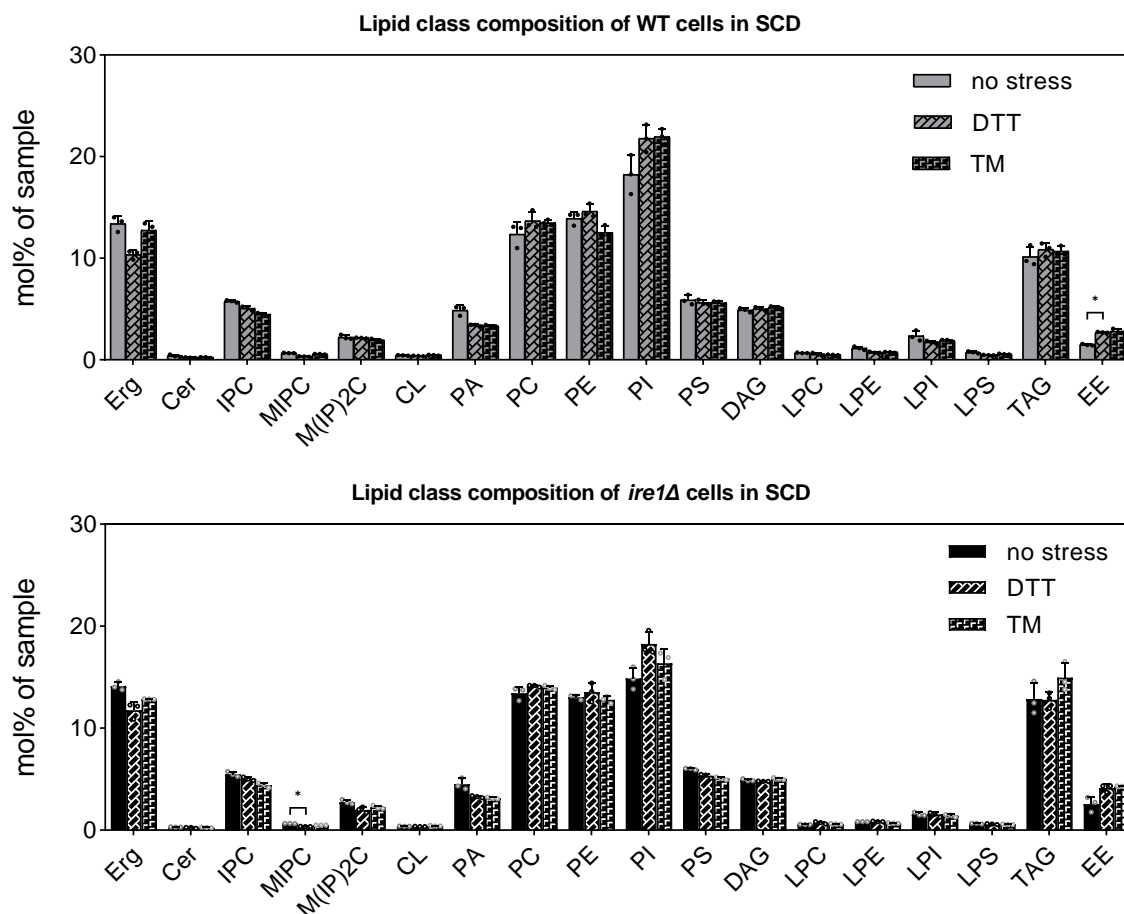


Figure 11 The lipid class composition of WT and *ire1Δ* cells grown in SCD medium after one hour of proteotoxic stress exposure

Lipid class composition in mol% of the sample. Sample generation was carried out as followed. Stationary cells cultivated in SCD medium were used to inoculate fresh SCD to an OD₆₀₀ of 0.1. Cells were subsequently grown until they reached an OD₆₀₀ of 0.8. Consequently, cells were left untreated for 1 hour, leading to the no stress sample, or stressed with 2 mM DTT or 1.5 μg/mL TM prior to harvesting. Abbreviations translate to Erg = ergosterol; Cer = ceramide; IPC = inositolphosphorylceramide; MIPC = mannosyl-IPC; M(IP)2C = mannosyl-di-IPC; CL = cardiolipin; PA = phosphatidic acid; PC = phosphatidylcholine; PE = phosphatidylethanolamine; PI = phosphatidylinositol; PS = phosphatidylserine; DAG = diacylglycerol; LPC = lyso-PC; LPE = lyso-PE; LPI = lyso-PI; LPS = lyso-PS; TAG = triacylglycerol; EE = ergosteryl ester. Plotted are biological triplicates, their average and ± SD. Raw data taken from Reinhard *et al.*¹ but reevaluated with an unpaired two-tailed t-test, assuming Gaussian distribution. Benjamini, Krieger and Yekutieli method was used to correct for false discovery rate (Q=5%).

In summary, the lipidomes of cells grown in either YPD (Figure 10) or SCD (Figure 11) show that acute proteotoxic stress does not cause major, immediate changes. Furthermore, the observable changes were mirrored for the wildtype strain with the functional UPR and the

*ire1*Δ strain incapable of mounting a UPR. The results imply that UPR activity has little to no impact by itself on the lipidomes within one hour of proteotoxic drug exposure.

A much greater impact on the cellular lipid composition has the medium (Figure 12), which is consistent with previous observations by Klose *et al.*²¹⁹. For instance, cells grown in SCD show increased levels of storage lipids i.e. TAGs and EEs as opposed to cells grown in YPD medium. Ergosterol as the precursor for EE is also elevated in SCD cultivated cells when compared to cells grown in YPD. For the category of membrane glycerophospholipids a noteworthy deviation is the level of PI between both media, in which the YPD lipidomes show twice as high levels compared to their SCD counterparts, highlighting a potential inositol deficiency in SCD medium formulation for the BY series as reported by Hanscho *et al.*²²¹. This is especially of concern for the investigation of the UPR: Ire1p has been identified as the inositol-requiring enzyme²²² and it is activated through inositol depletion⁵⁶, implying an important role for PI lipids. Next to PI, the abundance of PE differs significantly for the two different media tested in that it is reduced for both strains when cultivated in YPD opposed to SCD. The sensitivity and activity of the UPR could also be affected by this, as aberrant PE-to-PC ratios are associated during chronic activation of the UPR in yeast, worms and mammals^{223–225}. In case of *ire1*Δ cell lipidomes, there are significant changes found in two of the more complex sphingolipids, IPC and MIPC. Both species are less abundant when cells are grown in YPD medium opposed to SCD medium. While statistically significant only for *ire1*Δ cells, the trend towards lower levels of complex sphingolipids seems to become apparent also in the WT lipidome. Validating this potential change would require a higher sample number for a greater statistical power.

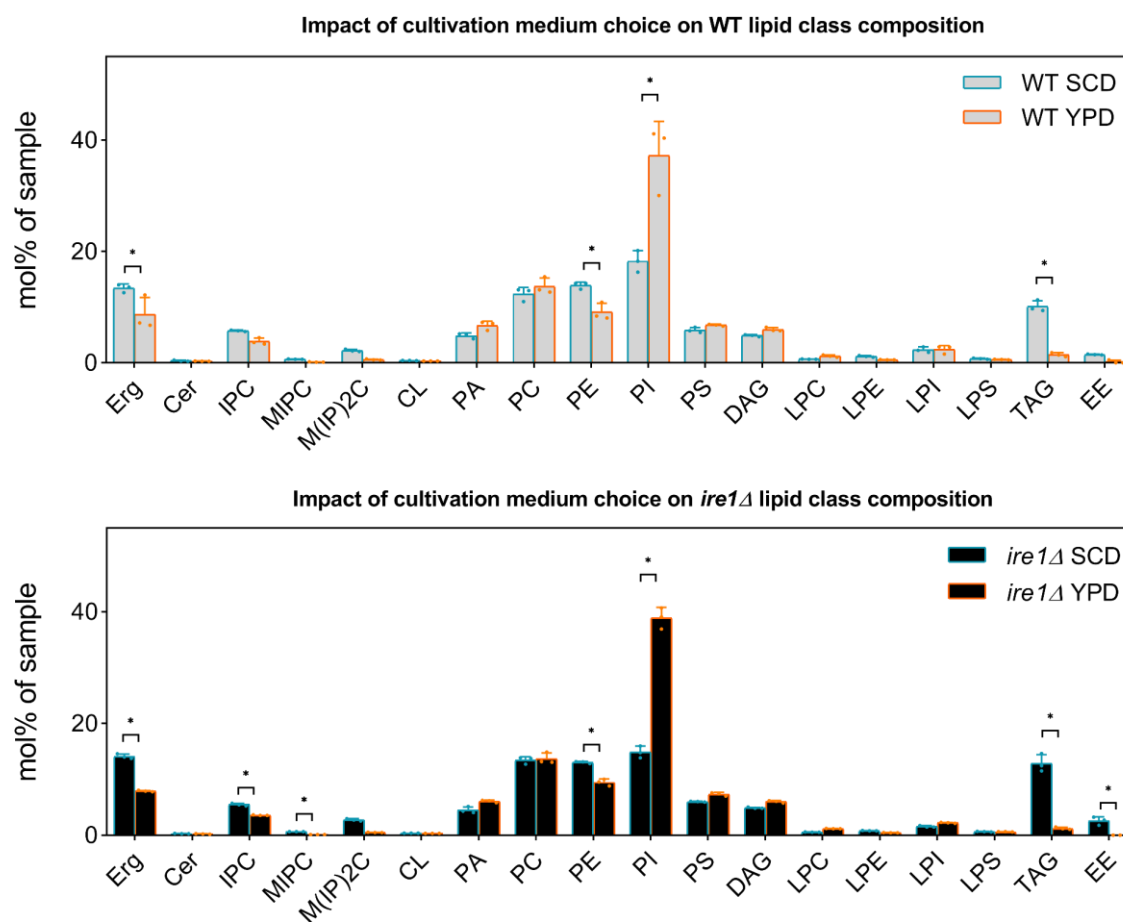


Figure 12 The impact of cultivation medium on the lipid class composition of WT and *ire1Δ* cells

Lipid class composition in mol% of the sample. Sample generation was carried out as followed. Stationary cells cultivated in the respective medium were used to inoculate fresh corresponding medium to an OD₆₀₀ of 0.1. Cells were subsequently grown until they reached an OD₆₀₀ of 0.8. Consequently, cells were left untreated for 1 hour prior to harvesting. Abbreviations translate to Erg = ergosterol; Cer = ceramide; IPC = inositolphosphorylceramide; MIPC = mannosyl-IPC; M(IP)2C = mannosyl-di-IPC; CL = cardiolipin; PA = phosphatidic acid; PC = phosphatidylcholine; PE = phosphatidylethanolamine; PI = phosphatidylinositol; PS = phosphatidylserine; DAG = diacylglycerol; LPC = lyso-PC; LPE = lyso-PE; LPI = lyso-PI; LPS = lyso-PS; TAG = triacylglycerol; EE = ergosteryl ester. Plotted are biological triplicates, their average and \pm SD. Raw data taken from Reinhard *et al.*¹ but reevaluated with an unpaired two-tailed t-test, assuming Gaussian distribution. Benjamini, Krieger and Yekutieli method was used to correct for false discovery rate (Q=5%).

In summary, this section raised awareness and provides guidelines when studying the UPR. To understand signals that can perpetuate the UPR only a quantitative approach on the level of unfolded proteins in the ER lumen and on the lipid composition of the ER membrane during acute and prolonged stress will unambiguously allow to dissect the relative ER-stress signal contributions. The here presented data suggest the use of defined SCD medium over ill-defined YPD medium. However, the established SCD medium formulation should be supplemented with additional inositol, as suggested by Hanscho *et al.*²²¹ to account for possible deficiency as cultivation progresses beyond the here chosen duration. The use of TM over DTT at the here indicated concentrations is recommended as its mode of action is more specifically aimed towards affecting the protein folding in the ER and showed no significant impact on the lipidome when applied for the timespan of one hour. Finally, unstressed WT and *ire1Δ* cells show almost identical whole cell lipid compositions, which implies that basal UPR signaling – or the lack thereof – does not have a significant impact on the cellular lipid composition.

4.2 A closer look at Ire1p dimeric TMD signaling-active conformation under LBS and proteotoxic ER-stress

In order to learn more about the signaling active conformation of Ire1p upon activation by different types of ER-stress, a systematical exchange of all native cysteine residues to serine residues was carried out by Dr. Kristina V  th to generate subsequently single cysteine mutants that were applicable for single-cysteine crosslinking experiments. The strategy aimed at further completing our understanding of Ire1p's signaling-active architecture of the TMD under proteotoxic stress and lipid bilayer stress, which has not been resolved by the crystal structures of Ire1p's isolated soluble domains^{73,74,226,227}. As the previous studies focused solely on understanding the structure in presence of unfolded proteins, this study was destined to complete our understanding of Ire1p's dimer architecture under aberrant lipid compositions compared to purely proteotoxic conditions induced via TM and DTT in the environment of the ER.

4.2.1 Generation of a cysteine-less Ire1p and validation of its function

Resolving the orientation of Ire1p's protomers during proteotoxic ER stress and lipid bilayer stress via cysteine crosslinking experiments required the generation of a cysteine-less version of Ire1p. A "cysteine-less" variant of *IRE1* was cloned by Dr. Kristina V  th by substituting 12 cysteine residues to serine. The modified "cysteine-less" *IRE1* was targeted to the endogenous locus based on a previously established approach by Halbleib *et al.* that assures near-native expression levels and near-native UPR signaling⁸⁷. Based on the Halbleib *et al.* construct the resulting Ire1 protein contained an internal 3xHA-tag and a codon optimized fluorescent GFP tag (yeGFP) inserted at the position of histidine 875 for detection by immunoblotting and fluorescence microscopy^{84,87,228,229}. Notably the "cysteine-less" construct did actually encode for three cysteine residues: Two in the signal sequence, which is co-translationally removed and one in the yeGFP tag (C70), which is, however, not accessible for mediating cysteine crosslinks (Figure 13)²³⁰.

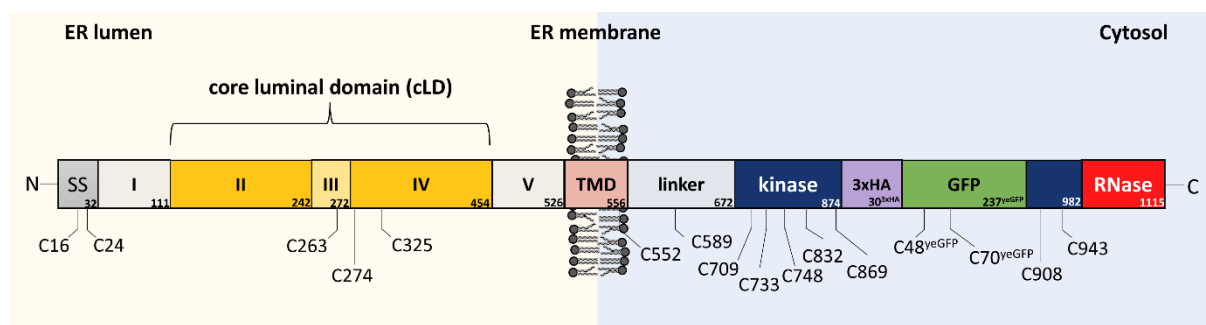


Figure 13 Schematic representation of the *IRE1* knock-in construct used in this study with highlighted functional domains and elements

Depicted is the IRE1 knock-in construct used in this study. The length of each functional domain is annotated in the bottom right of each segment⁷⁴. SS represents the signal sequence. The roman numerals represent the ER-luminal section of the Ire1 protein with its known five subregions. Subregions II-IV form the core luminal domain (cLD) important for ER stress sensing. The TMD, transmembrane domain, is composed of an AH and a TMH which is followed by a flexible linker region. The cytosolic side of Ire1 encompasses further a kinase domain and a RNase domain. A flexible loop within the kinase domain allowed the introduction of an affinity 3xHA tag together with a fluorescent GFP tag at position H875. Additionally, all native cysteine residues are indicated.

The functionality of cysteine-less Ire1p was tested by carrying out a MIC assay in YPD medium (Figure 14 A). Across all tested concentrations of DTT, the cysteine-less version of Ire1p did not differ in its resistance to DTT compared to the wildtype version. The *ire1* Δ strain served again as a positive control resembling the growth under prolonged ER-stress in an absence of a functional UPR characterized by its premature absolute growth inhibition marked at 2 mM DTT. A more direct readout of the functionality of cysteine-less Ire1p can be seen in Figure 14 B, where the splicing of *HAC1* mRNA was analyzed on an agarose gel. Cysteine-less Ire1p as well as its wildtype counterpart did not show any signs of spliced *HAC1* in the absence of DTT compared to the significant increase of spliced *HAC1* seen under ER stress. Both assays confirm the functionality of a cysteine-less Ire1p both on the cellular and on the molecular level.

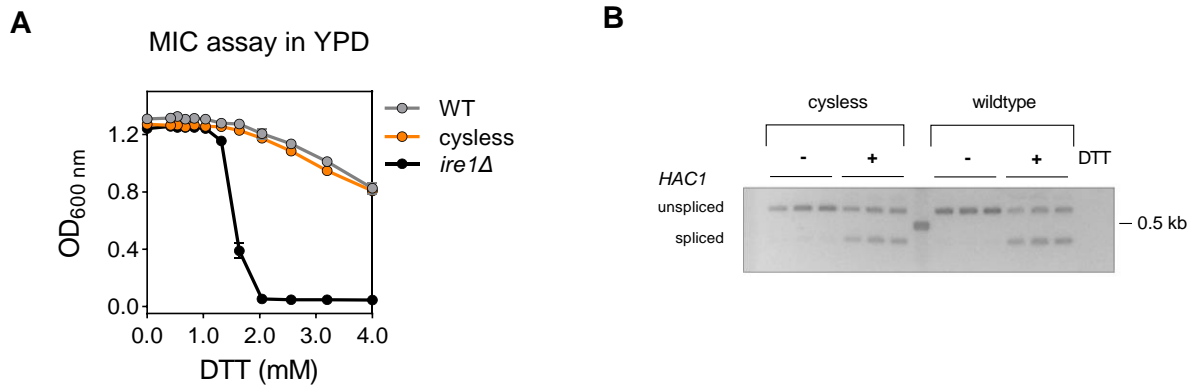


Figure 14 Cysteine-less Ire1p is functionally indistinguishable from the native form

In **(A)** the performance of the cysteine-less version of Ire1p is shown in comparison to an *ire1Δ* strain and the native form, here termed WT, in an ER-stress resistance assay. Stress resistance is measured in biomass formation after exposure to DTT at indicated concentrations for 19 h at 30 °C. Plotted are biological triplicates with technical duplicates with each datapoint representing the average \pm SD. In **(B)** the splicing efficiencies of cysteine-less Ire1p and wildtype Ire1p are visualized on an agarose gel. For that the respective strains were grown to stationary phase overnight, and subsequently a main culture of SCD was inoculated to an OD₆₀₀ of 0.2 and cells were grown to an OD₆₀₀ of 0.7. The - conditions resembles cells that were left untreated, while the + indicates stressing with 2 mM DTT for 1 h respectively. The cDNA generated from the RNA of those samples was subjected to a PCR with primers that do not discriminate in their primer efficiency for the unspliced *HAC1* or spliced *HAC1* cDNA. Shown are the results of three independent experiments. Data is already published in ².

4.2.2 Validating the functionality of cysteine-less Ire1p constructs with single cysteine substitutions in the TMD

As the main goal of this study was to discover interface-forming residues within the TMD of Ire1p, all single cysteine mutants had to be tested for their functionality under the studied ER-stress forms. The systematic screen of Ire's TMD began with E540C and ended on the native C552, covering three helical turns. The functionality of these constructs was assessed on the molecular level by RT-qPCR. Notably, the RT-qPCR conditions for quantifying the degree of *HAC1* mRNA splicing as the most immediate reporter for UPR activity were optimized yielding the protocol described in the material and method section. All single cysteine variants were evaluated under proteotoxic stress conditions after UPR induction using the proteotoxic stressor DTT by quantifying the level of spliced *HAC1* mRNA (Figure 15). Furthermore, a subset of variants was tested under lipid bilayer stress conditions, induced by inositol depletion (Figure 16). In both figures the dotted line marks the level of spliced *HAC1* mRNA from DTT stressed wildtype cells validating that the chosen stressing conditions provoke a similar strong UPR response and allows for a comparison of these two different stress forms. Both assays indicate that single cysteine variants of Ire1p are, when compared to the wildtype version of Ire1p, functional and responsive to ER-stress, which allowed us to proceed with the planned crosslinking experiments to study TMD dimer interface.

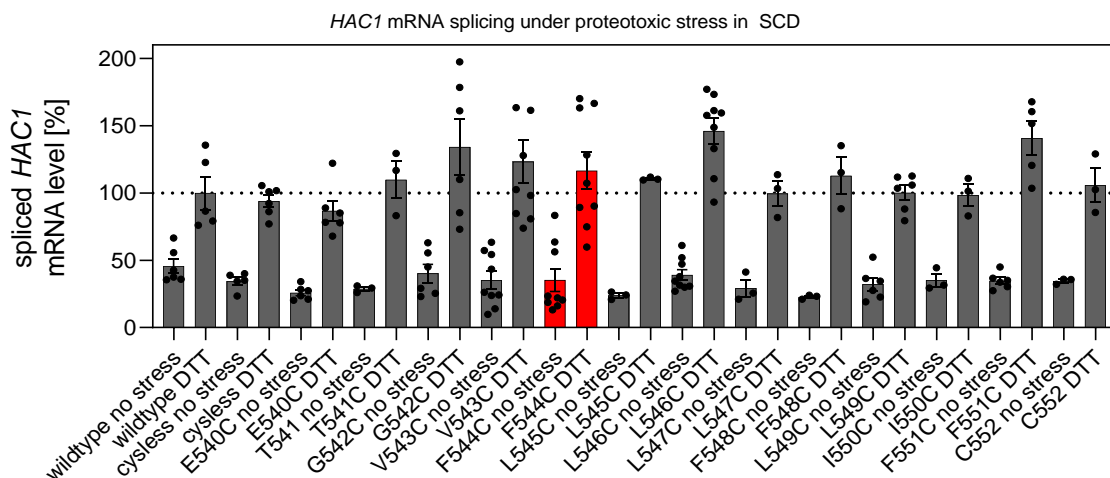


Figure 15 *HAC1* mRNA splicing under proteotoxic stress for single-cysteine variants along the TMD of Ire1p

Shown are relative quantifications of spliced *HAC1* mRNA determined by RT-qPCR for the respective strains. Data was obtained by inoculating a main culture of SCD to an OD_{600} of 0.2 with a stationary preculture. Once the cells reached an OD_{600} of 0.7, the cells were either left untreated (no stress) or stressed with 2 mM DTT (DTT) for 1 hour prior to cell harvesting. Data is normalized, as indicated by the dotted line, to the wildtype level of spliced *HAC1* mRNA. Number of independent experiments with technical duplicates for +DTT condition: WT: n = 5; cysteine-less: n = 6; E540C: n = 6; T541C: n = 3; G542C: n = 6; V543C: n = 9; F544C: n = 9; L545C: n = 3; L546C: n = 9; L547C: n = 3; F548C: n = 3; L549C: n = 6; I550C: n = 3; F551C: n = 5; C552: n = 3. Number of experiments with technical duplicates for the unstressed, -DTT condition: WT: n = 6; cysteine-less: n = 5; E540C: n = 6; T541C: n = 3; G542C: n = 6; V543C: n = 9; F544C: n = 9; L545C: n = 3; L546C: n = 9; L547C: n = 3; F548C: n = 3; L549C: n = 6; I550C: n = 3; F551C: n = 6; C552: n = 3. Data is published in ².

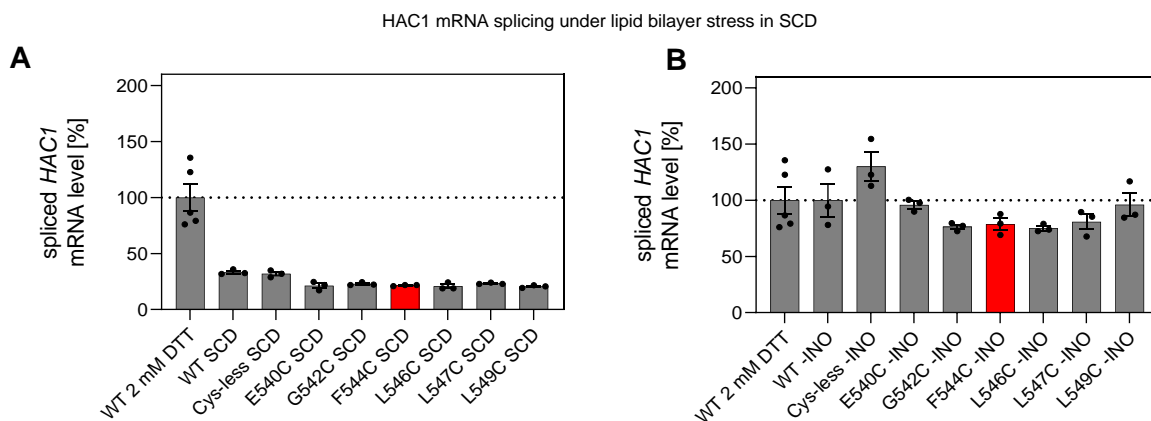


Figure 16: *HAC1* mRNA splicing during lipid bilayer stress (inositol depletion) of single cysteine variants of the TMD of Ire1p

Shown are the relative levels of spliced *HAC1* mRNA determined by RT-qPCR for the respective strains. Data was obtained by taking a sample of exponentially growing cells in SCD as the unstressed condition (A), followed by two washing steps with inositol-free SCD and consequent grow of the cells in preheated 30°C inositol-free SCD medium (-INO) for 3 hours to induce lipid bilayer stress (B). Data is normalized, indicated by the dotted line, to the level of spliced *HAC1* mRNA of the wildtype strain under proteotoxic stress by 2 mM DTT exposure. Bar graphs for inositol depletion (-INO) represent the average \pm SD of three independent biological replicates, with technical duplicates. The WT 2 mM DTT was replotted from Figure 15. Data is published in ².

4.2.3 Proteotoxic and lipid bilayer stress converge in a common signaling-active architecture of Ire1p's TMH region

The data shown in this section were generated by my co-authors and are displayed for the purpose of giving the reader more context to follow the line of arguments presented in this thesis. To study the proximity of residues within the TMD in all single-cysteine variants, microsomes were prepared from ER-stressed cells that reconcile the protein and lipid composition of the native ER. Stressing of the cells lead to the formation of Ire1p-containing clusters allowing for the proximity based cross linking to occur. The crosslinking event was catalyzed by application of CuSO₄ supporting the oxidation sulfhydryl groups from two adjacent cysteines leading to the formation of a covalent disulfide bond. The 3xHA tag present in each Ire1p variant enabled a densitometric determination of the fraction of cross linked Ire1p species after SDS-PAGE and subsequent immunoblotting. In Figure 17 A the quantification for all single cysteine mutants for each type of stress is depicted. Opposed to the RT-qPCR results that showed no significant differences between the single cysteine variants, the crosslinking revealed different efficiencies among all tested variants. For certain residues (G542C, L546C, L547C, F548C and F551C) no crosslinking could be observed while other residues had a moderate cross-linking efficiency (E540C, T541C, V543C, L549C and C552). Remarkable was the F544C variant, which displayed the greatest cross-linking efficiency irrespective of the form of ER-stress that was used to induce the oligomerization/clustering of Ire1p. Furthermore, an overarching pattern for all cross-linking efficiencies across all tested ER-stress forms could be observed, which implied that the structural organization of Ire1p, independent of the stress form at hand, resembles an X-shaped configuration as modeled and observed in molecular dynamics simulations performed by Dr. Roberto Covino (Figure 17 B). The details of the molecular dynamic simulation are explained to a greater extend in our publication (Väth *et al.*, 2021)².

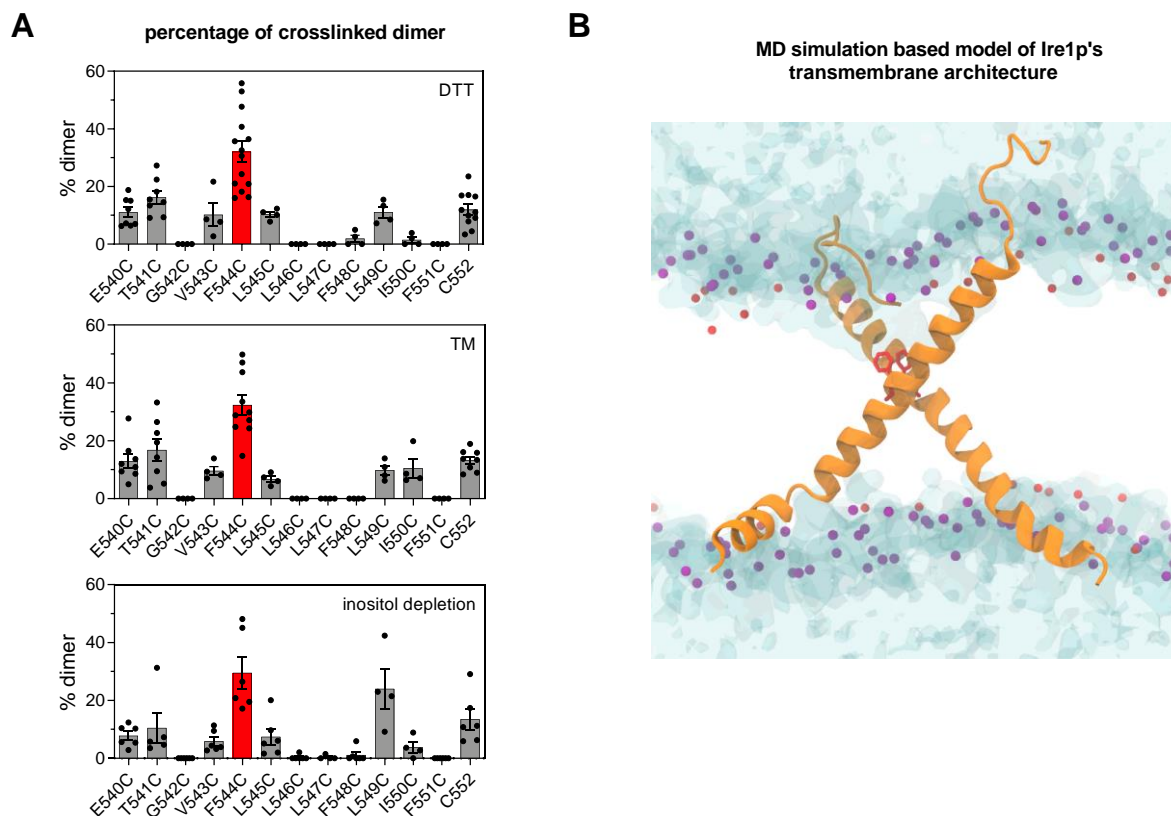


Figure 17 A model for Ire1's dimeric TMD architecture

(A) shows the quantification of cysteine crosslinking in microsomes under the indicated ER-stress forms indicated in the top right of each panel. Crosslinking tendency is given in % of dimer for each single cysteine variant tested. Plotted is the mean \pm SEM with an $n > 4$. This data is published in V  th *et al.*, 2021². **(B)** Shown is a snapshot of an atomistic molecular dynamics simulation of Ire1p's TMD. Ire1p's are shown as orange ribbons. F544 is shown as a stick model and coloured red, highlighting its position at the interface of both protomers. Water is indicated with a transparent surface representation. Purple spheres represent the phosphate atoms from glycerophospholipids. MD simulation and snapshot was kindly provided by Dr. Robert Covino. The crosslinking data were provided by Dr. Kristina V  th. The graphical representations are adapted from V  th *et al.*, 2021².

4.2.4 Does the unusual X-shaped conformation of Ire1p account for its lipid bilayer stress sensing potential?

The previous section focused on evidence from biochemical experiments and molecular dynamic simulations that support the idea that Ire1p forms an X-shaped dimer independent of the type of ER-stress. This model is in harmony with the previously postulated idea that the TMD of Ire1p can be divided into an AH-helix (Ire1p⁵²⁶⁻⁵⁴³) and an adjacent partially overlapping TMH (Ire1p⁵³⁸⁻⁵⁵⁵) that stabilizes the entire TMD in a tilted and bend orientation in the lipid bilayer⁸⁷. Via a hydrophobic mismatch-based mechanism, the TMD of Ire1p causes a local membrane deformation, which can be envisioned as a squeezing of the lipid bilayer. This "squeezing" comes with an energetic cost based on the present degree of lipid acyl chain

disordering and membrane thickness^{231,232}. By this postulated mechanism, Ire1p would be more sensitive than other single pass membrane proteins to the general physicochemical properties of the surrounding bilayer opposed to proteins that lack this amphipathic helix, in that aberrant lipid compositions would penalize Ire1p to remain as a monomer in the lipid bilayer and would act as a driving force for the oligomerization of Ire1p. How the X-shaped model extends this concept is illustrated in Figure 18 A. In short, the unusual combination of the AH and the short TMH of Ire1p generates an ellipsoid “footprint”, causing a local compression of the membrane over a greater area. Other single pass membrane proteins that do not have an AH will leave a circular footprint on the ER membrane. If true, then there would be a greater benefit for Ire1p to dimerize as the ellipsoid shape allows to coalesce a greater area thereby minimizing energetic costs opposed to membrane proteins with circular footprints.

As the previously described model for dimerization was derived from data obtained of acutely proteotoxically stressed cells by TM or DTT exposure, which was shown to not significantly disturb the cellular lipid composition¹, the question arose what the exact contribution of the X-shaped conformation to the activation of Ire1p would be. Considering that the dimeric assembly propensity was identical irrespective of the nature of ER stress one might ask whether a membrane-based mechanism of activation, as envisioned here for the dimer of Ire1p, might become dominant under prolonged ER stress conditions. There is indeed pioneering work by Promlek *et al.* showing that the UPR can be equally strong evoked solely via a membrane-based mechanism⁵⁶. A truncation mutant of Ire1p’s ER luminal domain, Δ III-Ire1p, is de-sensitized to the accumulation of unfolded proteins in the ER lumen and will therefore not react as strongly to the acute ER-stress signal after exposure to DTT or TM⁵⁶. However, the Δ III mutant is capable of mounting a fully blown UPR, just like wildtype Ire1p, after prolonged treatment with DTT⁵⁶. The Δ III mutant further shows an identical activation profile as the wildtype Ire1p under inositol depletion⁵⁶, a stress form that was shown to not cause a significant accumulation of misfolded proteins in the ER lumen²³³. To estimate the sole contribution of LBS impaired Ire1p mutants a set of interface mutants that specifically interfere with the formation of higher oligomeric states can be used. There are two prominent mutants that are used in the field, namely the interface-1 (IF1 – T226A & F247A) and the interface-2 (IF2 – W426A) mutant, both discovered through structural analysis of the ER-luminal X-ray crystallography⁷³. Both interfaces serve different purposes with the IF1 required for dimerization and the latter IF2 involved in the back-to-back association of already formed dimers to allow higher oligomeric assemblies²³⁴. To test whether a dimeric assembly of Ire1p through the TMD based sensing mechanism is sufficient under LBS, I decided to pair a subset of single cysteine variants with the IF2 mutant that was shown to still form dimers but is unable

to form higher oligomeric assemblies of Ire1p^{B1}. In Figure 18 B cells carrying the disruptive IF2 mutant are more sensitive to prolonged DTT exposure than wildtype cells. The panel contains further three single cysteine variants in the IF2 background, two of which (E540C & IF2 and T541C & IF2) showed increased sensitivity under prolonged exposure to DTT compared to their standalone mutants published by Vãth *et al.*², presumably because the amphipathic character of the AH is compromised. The F544C & IF2 mutant, which harbors its cysteine at the crossing point of the X-shaped dimer, is less compromised in its sensitivity towards DTT presumably because the AH character of Ire1p's AH helix is unchanged in this mutant. The prolonged stress assays in Figure 18 B demonstrate that a lack of oligomeric capacity of Ire1p mediated by mutating the IF2 unmasks the importance of a functional TMD of Ire1p, as both AH-mutants show a performance indistinguishable from *ire1Δ* cells while the F544C & IF2 mutant, which leaves the AH helix intact, is less compromised. More interestingly the F544C & IF2 mutant improves the resistance to DTT compared to the stand alone IF2 mutant. The three single cysteine and IF2 mutants were further subjected to time course experiments after stressing the cells with either DTT (Figure 18 C) or by inositol depletion (Figure 18 D). To study the UPR dependent signaling output of the single-cysteine variants the level of spliced *HAC1* mRNA was determined. The DTT time course experiment showed that the cysteine-less Ire1p as well as the F544C & IF2 double mutant show an increase in their spliced *HAC1* mRNA levels over the 6-hour time course with spliced *HAC1* mRNA levels peaking 4 hours after the treatment. The AH comprised IF2 mutants (E540C & IF2 and T541C & IF2), however, show no signs of UPR activation as measured by the level of the spliced *HAC1* mRNA. The delayed increase in spliced *HAC1* in case of the F544C & IF2 mutant opposed to the fully functional cysteine-less Ire1p under DTT exposure suggested that the slow increase is predominantly caused by lipid bilayer stress that slowly builds up. This activation profile is reminiscent of the previously discussed Δ III-Ire1p mutant DTT time course profile published by Promlek *et al.*⁵⁶ as it is lacking the acute ER-stress response shortly after DTT drug administration. To test the hypothesis that lipid aberrancies are the underlying cause for the slow and steady increase of spliced *HAC1*, I repeated the time course experiment using inositol depletion as an ER-stress form. Under these conditions the F544C & IF2 double mutant was indistinguishable from cysteine-less Ire1p, and the two AH-compromised single cysteine double mutants (E540C & IF2 and T541C & IF2) are characterized by an almost fully compromised UPR response. These findings highlight the importance of a functional AH for Ire1p's ability to sense lipid bilayer stress.

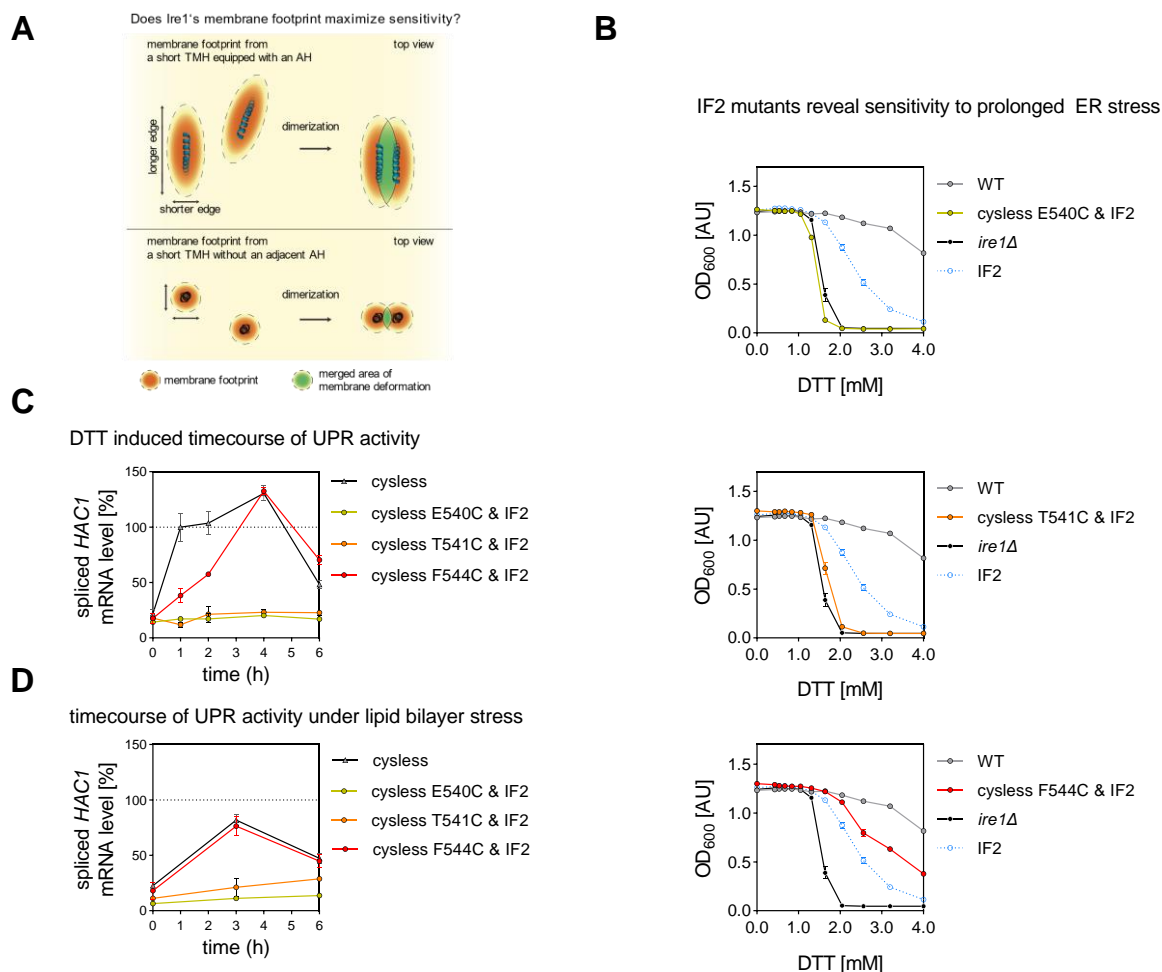


Figure 18 The conceived structural model of Ire1's dimer interface and the consequences for prolonged ER-stress in the absence of higher oligomeric state

(A) depicts the working model for Ire1p's membrane sensitivity. The unusual TMD of Ire1p, with its AH next to its short TMH increases the "footprint" on the ER membrane, i.e. the area deformed by the presence of the protein itself. The upper section of the schematic shows that Ire1 would leave an ellipsoid footprint on the bilayer while other single-pass transmembrane proteins lacking an AH have a smaller circular footprint. Following that simple geometric assumption, Ire1p would benefit under aberrant membrane composition greater from a dimerization than membrane proteins lacking the AH as Ire1p can merge a greater area as it aligns itself in an X-shaped manner. The benefit of single-pass transmembrane proteins with circular footprints is neglectable therefore the contribution to form dimers under conditions of a stiffer membrane is not compelling. Figure taken from 65. In (B) a set of prolonged ER stress assays are shown in complex YPD medium. Exponentially growing cells were exposed to the indicated DTT concentrations for 18 hours at 30 °C without agitation prior to measuring the OD₆₀₀ as a readout for formed biomass. In (C) the level of spliced *HAC1* mRNA was determined via RT-qPCR after exposing the cells to 2 mM DTT. The dotted line indicates that the data was normalized to the measured mRNA levels for the cysless Ire1p strain after 1 hour of DTT exposure. In (D) the level of spliced *HAC1* mRNA was determined via RT-qPCR under lipid bilayer stress caused by inositol depletion of the medium. The dotted line represents the normalized level of the spliced *HAC1* mRNA measured in the cysless strain shown in (C). All data plotted in this figure stem from three biological replicates, with technical duplicates. Shown is the average \pm SD. Data is published in 65.

4.3 *S. cerevisiae* as a model for studying chronic diseases related to ER-stress

S. cerevisiae is an excellent model organism for studying the physiology and pathophysiology of lipid metabolism. Most enzymes involved in lipid synthesis are conserved from yeast to man, and they have been cloned and characterized extensively^{235,236}. Lipid metabolism in baker's yeast is to a great extent regulated on the transcriptional level. The transcriptional regulator Mga2p for example regulates the abundance of the sole fatty acid desaturase in yeast, Ole1p¹⁸⁶. This simplicity results in a rather restricted diversity in the acyl chain composition of glycerophospholipids and prompted me to establish growth conditions and experimental outlines that would allow me to study the effect of lipid bilayer stress through changes in the degree of saturation (Figure 19 A, B and C). After all, there is an increasing number of studies that have linked metabolic diseases to saturated fatty acids and in particular to ER-stress²³⁷⁻²⁴⁰.

4.3.1 The phenotypes of the *mga2*Δ strain of *S. cerevisiae*

Surma *et al.* previously reported that *mga2*Δ strains are characterized by increased levels of saturated lipids due to a reduced level of Ole1p compared to WT cells²⁴¹. These findings could be replicated under my own experimental conditions as seen by an exert of the lipidomic data depicted in Figure 19 D. The *mga2*Δ strain shows elevated levels of fully saturated glycerophospholipids (49 mol% for *mga2*Δ compared to 15 mol% for WT) primarily at the expense of glycerophospholipids with a total of two double bonds, one in each of their acyl chains. The increased lipid saturation probably contributes to the lower growth rate (Figure 19 B) and a reduced cell viability of *mga2*Δ cells by a yet unknown mechanism (Figure 19 C).

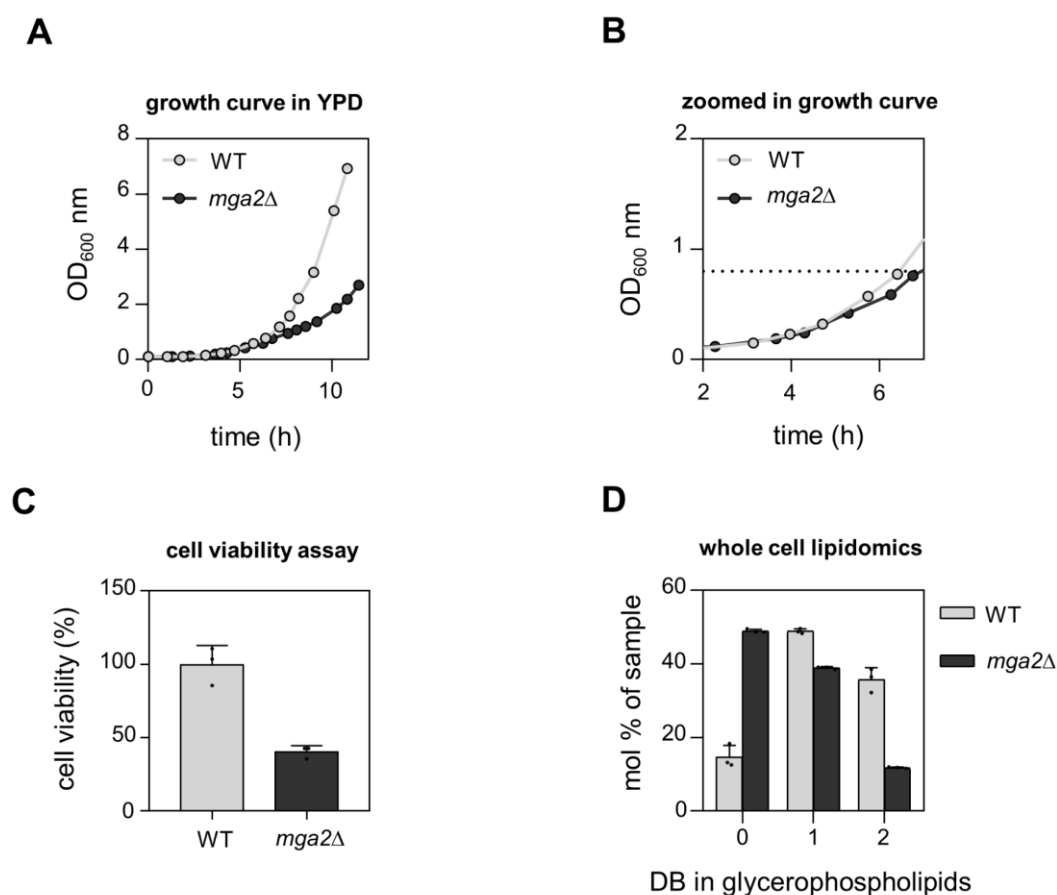


Figure 19 Phenotype of the *mga2* Δ strain of *S. cerevisiae*

In **(A)** a growth curve in YPD is shown of a wildtype strain and the *mga2* Δ strain. Both strains were grown to the stationary phase at 30 °C before the main culture was inoculated to an OD₆₀₀ of 0.1. The cells were then grown for the indicated time and their OD₆₀₀ was measured to analyze the biomass formation. Plotted is the average \pm SD of three biological replicates. In **(B)** a zoomed in version of the growth curve depicted in **(A)** is shown by plotting only a subset of the data to highlight the point of growth deviation indicated by the dotted line at an OD₆₀₀ of 0.8. Panel **(C)** shows the cell viability determined by counting the number of colonies formed after 72 h. WT and *mga2* Δ cells were cultivated as described in **(A)** and as an OD₆₀₀ of 0.8 was reached cells were adjusted to 10³ mL⁻¹ of which 30 μ L were plated out on YPD plates. The result is presented as a relative value compared to the WT given in %. Each bar represents the average \pm SD of three biological replicates. In **(D)** an excerpt of the lipidome of the wildtype strains (WT) and the *mga2* Δ strain is depicted. Shown is total amount of double bonds (DB) in glycerophospholipids given as the sum of DB in both acyl chains. The abundance of either completely saturated lipids (0), monounsaturated (1) or polyunsaturated (2) is given in mol%. Bar charts represent the average \pm SD of three biological replicates.

Lipid saturation is a critical regulator of membrane fluidity and increased lipid saturation can cause the formation of non-fluid gel phases even in living cells¹⁷⁶. Because lipid acyl chains are dramatically remodeled in response to changes in the cultivation temperature²⁴², which may represent a homeoviscous adaptation^{100,182}, I tested if and how the dramatically increased lipid saturation in *mga2* Δ cells affects the growth rate at different temperatures. WT and *mga2* Δ cells were cultivated at different temperatures between 20 °C and 40 °C (Figure 20 A). Surprisingly, neither the optimal growth temperature nor the higher or lower end of the temperature spectrum was shifted for the *mga2* Δ strain compared to the WT. The growth

defect of *mga2* Δ cells, which was observed over a broad range of temperatures, was corrected by supplementing the medium with the unsaturated fatty acids oleate or linoleate (Figure 20 B and C) but further aggravated by palmitate (Figure 20 D). The observable growth defect is consistent with alternative model systems that interfere with membrane fluidity by increasing globally the acyl chain saturation. De Smet *et al.* could show that the acyltransferase Sct1p competes with Ole1p for the activated C16:0-CoA substrate to be either directly used for lipid synthesis or desaturated by Ole1p²⁴³. By overexpressing Sct1p the degree of fatty acid desaturation could be manipulated towards more saturated fatty acyl chains resulting in a similar growth defect. Pineau *et al.* and others used the *hem1* Δ strain, a mutant deficient in the first step of heme biosynthesis, to interfere with fatty acid desaturation, which again resulted in a significant growth retardation^{244,245}. Notably, studies by Pineau *et al* did further show that heme synthesis impairment is an inducer of ER-stress²⁴⁶. These data point towards a lipid-based origin of the observed growth defect.

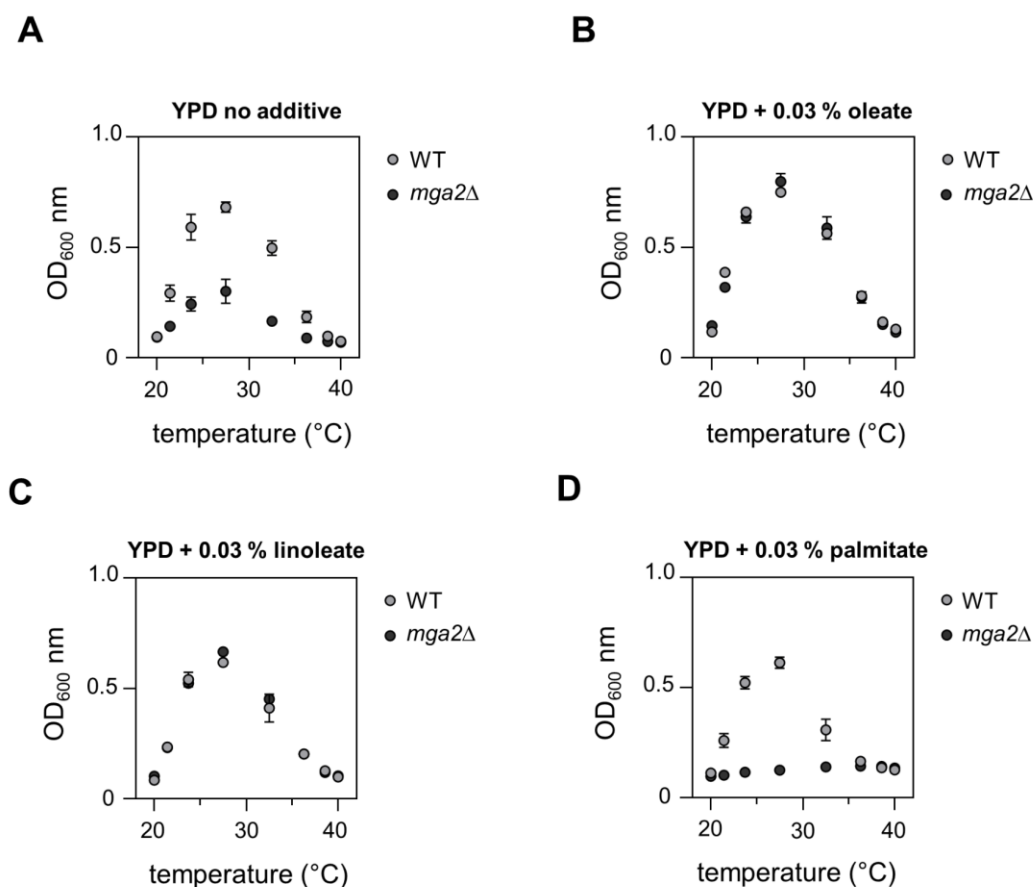


Figure 20 The *mga2Δ* phenotypic consequences for growth can be rescued or worsened by supplying exogenous fatty acids

In (A) the wildtype strain (WT) as well as the *mga2Δ* strain were grown at indicated temperatures without agitation for 19 hour prior to taking final OD₆₀₀ measurements to validate the biomass formed. In (B-D) the assay was modified to the extent that a fatty acid was provided at the indicated concentration. As the supplementation of fatty acids into medium causes a clouding, which would interfere with OD₆₀₀ measurements, the final cell suspension was spiked with 0,5 % SDS detergent. All graphs resemble the average \pm SD of three biological replicates.

As the ER is defined by its loosely packed membrane^{247,248}, this organelle is likely to suffer the most from a global increase in saturated membrane lipids in the absence of the membrane property sensor Mga2p. Under my experimental conditions an aberrant morphological ER phenotype can be visualized via confocal microscopy by expressing an ER targeted sfGFP with a carboxy terminal HDEL retrieval sequence (Figure 21 A and B).

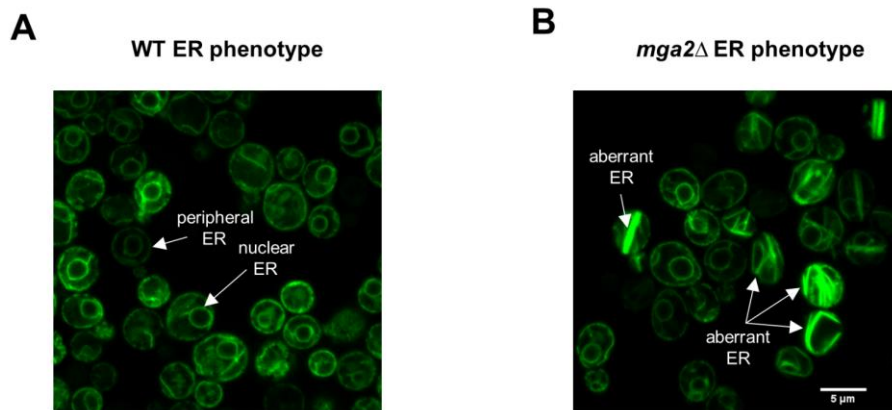


Figure 21 The *mga2*Δ causes aberrant ER formations

The morphological phenotype of wildtype cells **(A)** and *mga2*Δ cells **(B)** is visualized by expressing in both shown strains sfGFP with a KAR2 signal sequence and a c-terminal ER retention signal in the form of an HDEL sequence. Indicated is the healthy ER morphology in the WT panel with the peripheral ER at the outer rim of a yeast cell and a second circuit structure close to the nucleus called the nuclear ER. In the *mga2*Δ panel one can see a change of that morphology in a *mga2*Δ background where the ER takes a straight angular shape. Scalebar represents 5 μm.

A healthy ER morphology appears in the here presented confocal slices as two circular structures. Namely the nuclear ER having a close proximity to the nucleus and the peripheral ER that is tethered to the plasma membrane. The aberrant phenotype can be characterized by the loss of circularity of the ER taking on a straight angular shape. Within the lumen of the aberrant ER the sfGFP accumulates in a denser volume, which is reflected in the greater intensity values per pixel. To address the question whether the changed ER morphology is accompanied by a reduction in ER protein mobility, the FRAP (Fluorescent Recovery After Photobleaching) technique was applied (Figure 22). For this purpose, the ER membrane protein Sec63p was C-terminally tagged with mNeogreen in WT and *mga2*Δ strains. Then in brief, five prebleach frames were recorded to determine the initial fluorescence of the desired region of interest (ROI). Subsequently, a single bleach event was performed with sufficient laser power to reduce the fluorescence signal in the ROI to <20% of the initial value. The recovery of the fluorescent signal, reporting on the diffusion of non-bleached, mNeogreen-tagged Sec63p diffusing into the ROI was followed by confocal microscopy every 150 ms for 40 seconds in total. This information was later used to determine the rate of diffusion of the tagged protein, which is an indirect measure for the fluidity of the ER membrane. In Figure 22 B the recovery times, here defined as the time it takes for the fluorescent signal intensity to reach 50 % of the originally determined value, are shown. For the WT nuclear ER an average recovery time of 1.17 s and for the aberrant ER found in *mga2*Δ strains an average recovery time of 1.5 s was determined (Figure 22 B).

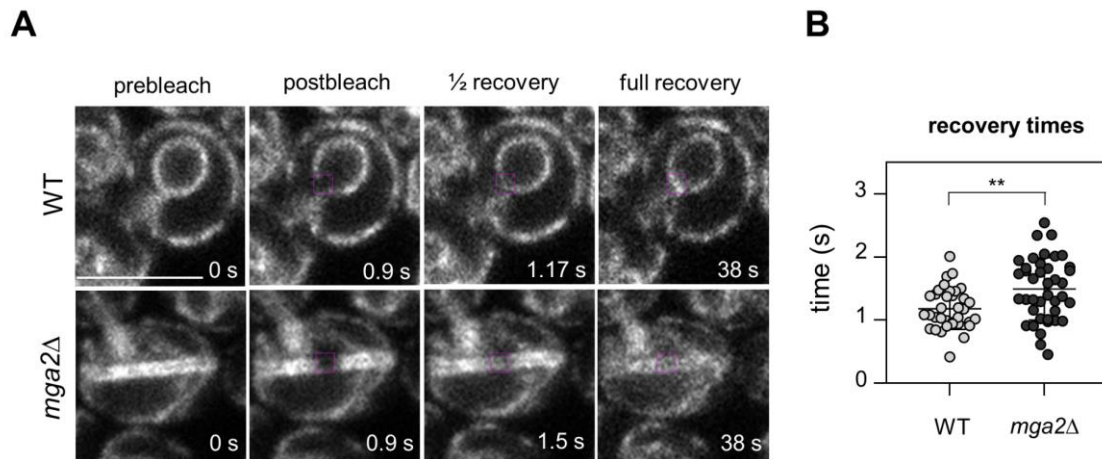


Figure 22: FRAP experiments indicate impaired ER protein mobility in the aberrant ER structure opposed to the WT nuclear ER

In **(A)** a representative image series is shown of the FRAP experiments. For each strain, WT and *mga2Δ*, a prebleach image representing the state of signal intensity before the treatment, the postbleach image as the first image acquired after the bleach pulse (ROI is indicated with the magenta square) and two recovery images reporting on the indicated recovery states are shown. Timestamps are representative for the experimental time course with the exception of ½ recovery, which represents the determined average for each strain shown in **(B)**. In **(B)** the recovery times i.e. how much time has passed to reach ½ of the initially measured intensity in the bleached ROI was achieved is plotted for the WT and *mga2Δ* strain. WT = n of 35; *mga2Δ* = n of 40.

4.3.2 A systematic genome wide high throughput screen with *mga2Δ* to identify phenotype alleviating and aggravating genetic interactions

To identify cellular factors that affect the formation of the aberrant ER structures in the *mga2Δ* background, a microscopy-based, genome wide screen was performed. Dr. Harald Hofbauer constructed a *mga2Δ* strain that harbors two fluorescent markers in the form of an ER directed sfGFP protein with a C-terminal HDEL motive and a secondary fluorescent marker introduced by tagging the ER resident membrane protein Elo3p with mCherry (Figure 23 A). This *mga2Δ* strain served as the query strain to be crossed with the yeast knockout library²⁴⁹ and the DAmP library²⁵⁰ in the lab of Prof. Dr. Maya Schuldiner. Dr. Michael Gecht carried out the screen supervised in the lab of Prof. Dr. Maya Schuldiner. The newly formed library of double mutants allows one to study hypomorphic alleles and evaluate the fitness contribution of the secondary mutant to the observable phenotype of the query strain. The newly formed library was screened with an automated imaging system and the images were manually evaluated by three scientists, Dr. Michael Gecht, John Reinhard and myself. Based on the morphology of the ER, the mutants were sorted into three categories: “unchanged”, “rescue” and “worse”. The “rescue” strains exhibited in fewer cells an aberrant ER morphology compared to the

query strain. The “worse” strains exhibited a greater percentage of cells harboring an aberrant ER when compared to the sole query strain.

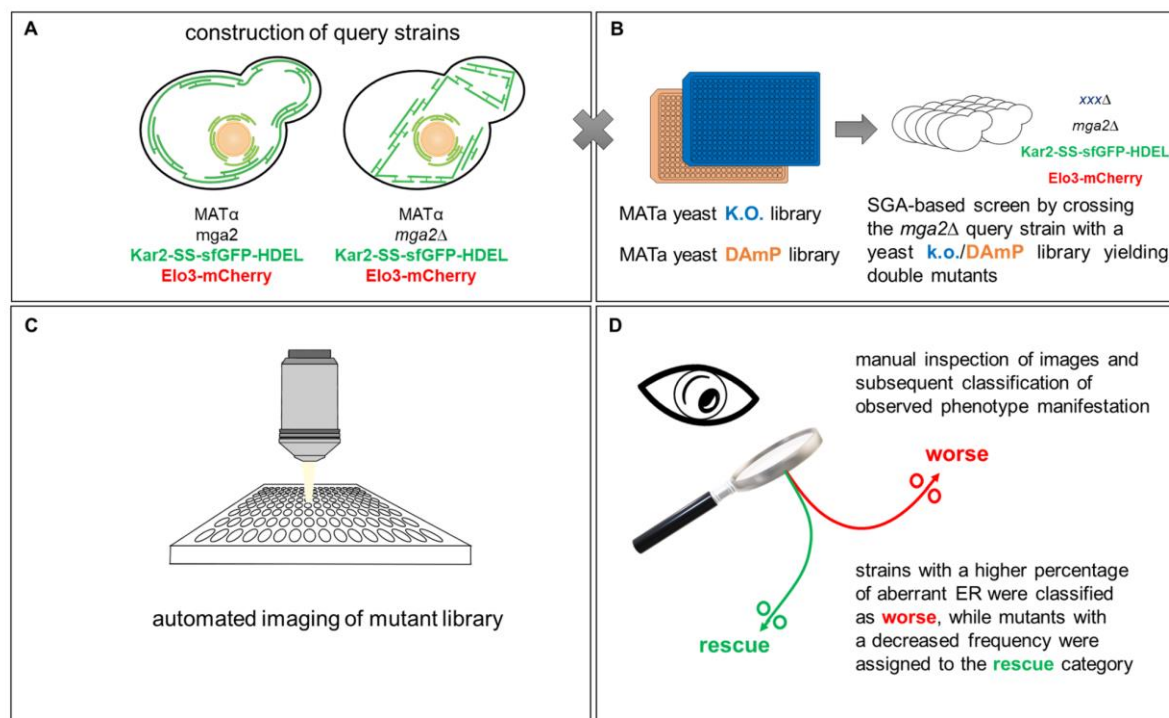


Figure 23 Schematic representation of a genome-wide high throughput screening approach and its evaluation

(A) The construction of the query strains foresaw the genetic integration of an ER luminal marker in the form of a fusion construct consisting of the *KAR2* signal sequence, followed by sfGFP and an ER retention motive of the HDEL sequence. Secondly an ER membrane resident protein, Elo3p, was tagged c-terminally with mCherry. **(B)** In the second step of the screen the *mga2* Δ query strain was crossed against a yeast k.o. and DAmP library so that a library was created in which each strain harbors the *mga2* Δ with the fluorescent reporters next to their specific secondary mutation. The library generated in **(B)** was then imaged with an automated image acquisition system **(C)**. **(D)** All the images taken in **(C)** were then manually inspected for their occurrence of the aberrant ER morphology of the *mga2* Δ strain. If the % of aberrant ER structures was greater than observed to their level in the query *mga2* Δ strain that mutant was assigned to the worse category. In case of a reduced occurrence of aberrant structures the mutant was assigned to the rescue category.

A manual inspection is highly subjective as seen in the Venn diagram in Figure 24. The reviewer’s selections are represented by the differently shaded colors of red for the worse category and green for the rescue category. Due to the subjective nature of the aberrant ER phenotype assessment only common candidates seen by two or all three of us were used for further analysis. All candidates of both categories are listed in Table 14

The common candidates were subjected to a gene set enrichment analysis, which is part of the ModeEnrichr toolkit^{251,252}. This procedure determines to what extent the input gene set (our candidates) overlap with annotated gene sets that are predominantly based on empirical evidence and are linked to publications. This way it is possible to identify pathways and

processes that are most likely contributing to the observed phenotype. The list depicted in Figure 24 contains the results of the gene set enrichment analysis and was normalized after the GO terms were assessed by the p-value based Fisher's exact test, which was adjusted by using the Benjamini-Hochberg method to account for multiple hypotheses testing²⁵³. The strongest hit for the "worse" category was assigned to the "mitochondrial genome maintenance" GO term, followed by "mitochondrial transport", "petite", "mitochondrial distribution" and ending with "respiratory growth" thereby pointing heavily towards a role of mitochondria in the aggravation of the aberrant ER phenotype. The "rescue" category on the other hand has three of the five hits leaning towards the process of mitosis with GO terms "size of nucleus", "cell cycle progression in anaphase" and "cell cycle progression through the G2/M phase transition". The "rescue" list further contains two GO terms associated with prions, namely "prion loss" and "prion formation". While the "worse" category predominantly consists of candidates that are related to mitochondrial functions, the "rescue" category denotes an alleviating property of mutants involved in mitosis. Since not all of the 86 "worse" and 25 "rescue" candidates can be followed up, I decided to reevaluate a subset of candidates regarding their ER phenotype distribution under my controlled growth conditions. The growth conditions for ER morphology assessment in YPD were as described in 3.1.3 and the cells were harvested at an OD₆₀₀ of 0.8 prior to imaging.

The mutant pair *pet309Δmga2Δ* and *coa3Δmga2Δ* are of the "worse" category and both of these genes are involved in the assembly pathway of the cytochrome oxidase, the terminal complex of the respiratory chain²⁵⁴. For the third candidate *atg41Δmga2Δ* it was shown that Atg41p has an influence on the rate of autophagosome formation and that Atg41p shows a peri-mitochondrial distribution within the cell²⁵⁵. These three candidates conclude the choices for the "worse" category, and all three are linked to the mitochondrial theme found via the gene set enrichment analysis. For the "rescue" candidates the choice of candidates is more diverse and covers multiple biological pathways. With *mal33Δmga2Δ* I decided for a member of the MAL gene family, necessary for maltose utilization²⁵⁶. With *ncs2Δmga2Δ* I have decided for a candidate that plays a role in urmylation, an ubiquitin-like modifier that is involved in budding²⁵⁷. Further *ncs2* is required for tRNA modifications in form of a thiolation of 5-methoxycarbonylmethyl-2-thiouridines (mcm₅S₂U) of the wobble position of tRNA^{Lys} UUU, tRNA^{Glu}UUC and tRNA^{Gln}UUG²⁵⁸. With *ubc4Δmga2Δ* I have decided for a candidate lacking the most abundant E2 enzyme²⁵⁹ and as a member of the ubiquitin proteasome system (UPS) has an active role in selective proteolysis thereby contributing to protein homeostasis²⁶⁰. The last candidate gene for the "rescue" category is *YCL001W-AΔ*, which is a gene of unknown function but recently it was discovered via a genetic interaction mapping screen that it has a putative function in RNA metabolism²⁶¹. In that screen it was shown that a *YCL001W-A*

knockout is associated with synthetic sickness in combination with *RRP46* and *NOP56*, two essential genes in RNA processing attenuated through DAmP modification²⁶¹.

Hence a total of seven candidates and the respective controls in the form of the isogenic WT and *mga2Δ* strains were evaluated for their ability to generate aberrant ER structures (Figure 25 B). The *mga2Δ* query strain shows in 74 % of all cells an aberrant ER morphology, while the isogenic WT strain had no aberrant ER structures. All chosen candidates show an ER-phenotype distribution according to their assigned category, where the deletion of *PET309*, *COA3* or *ATG41* in the *mga2Δ* background all lead to elevated levels of aberrant ER structures (88 % for *pet309Δmga2Δ*, 83 % for both *coa3Δmga2Δ* and *atg41Δmga2Δ*). As expected, the opposite is true for the “rescue” category in that all four candidates have reduced tendencies to form aberrant ER structures (19 % for *ncs2Δmga2Δ*, 26 % for *ubc4Δmga2Δ*, 33 % *YCL001W-AΔmga2Δ* and 49% for *mal33Δmga2Δ*). Figure 25 C shows a representative image for each candidate and control strain.

In summary, by using a limited set of strains from both categories, I could verify the findings of the initial screen. Having quantified the occurrence of the aberrant ER via microscopy, I next wanted to use lipidomics to see if the double mutations of both categories affect the degree of lipid saturation and thereby possible correlate the degree of saturation with the occurrence of the aberrant ER.

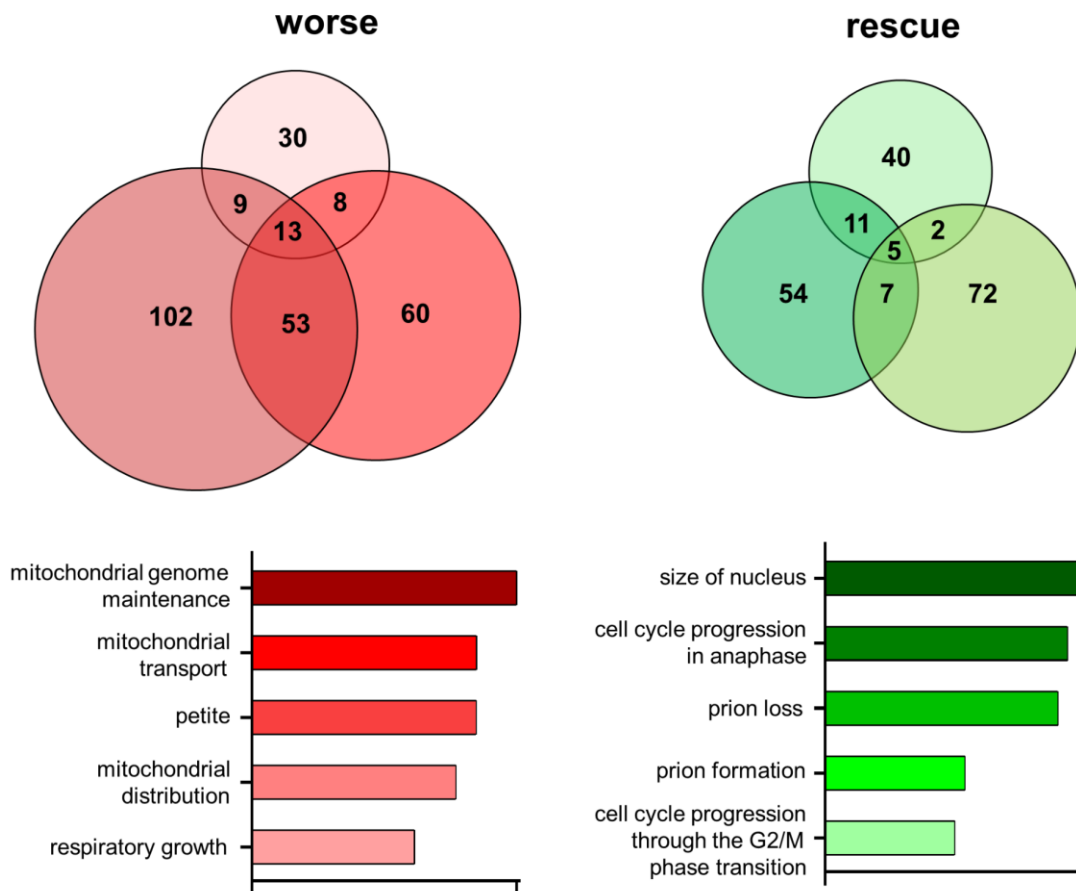


Figure 24 Genome-wide high throughput screening results

The Venn diagrams depict the amount of identified candidates based on three independent inspections (represented by the shaded tones of red and green) for each category. The bar charts contain the results of a gene set enrichment analysis carried out with YeastEnrichr. This evaluation assigned GO terms to the identified screening hits (genes) and thereby allowed for the identification of their function in context of the biological processes involved.

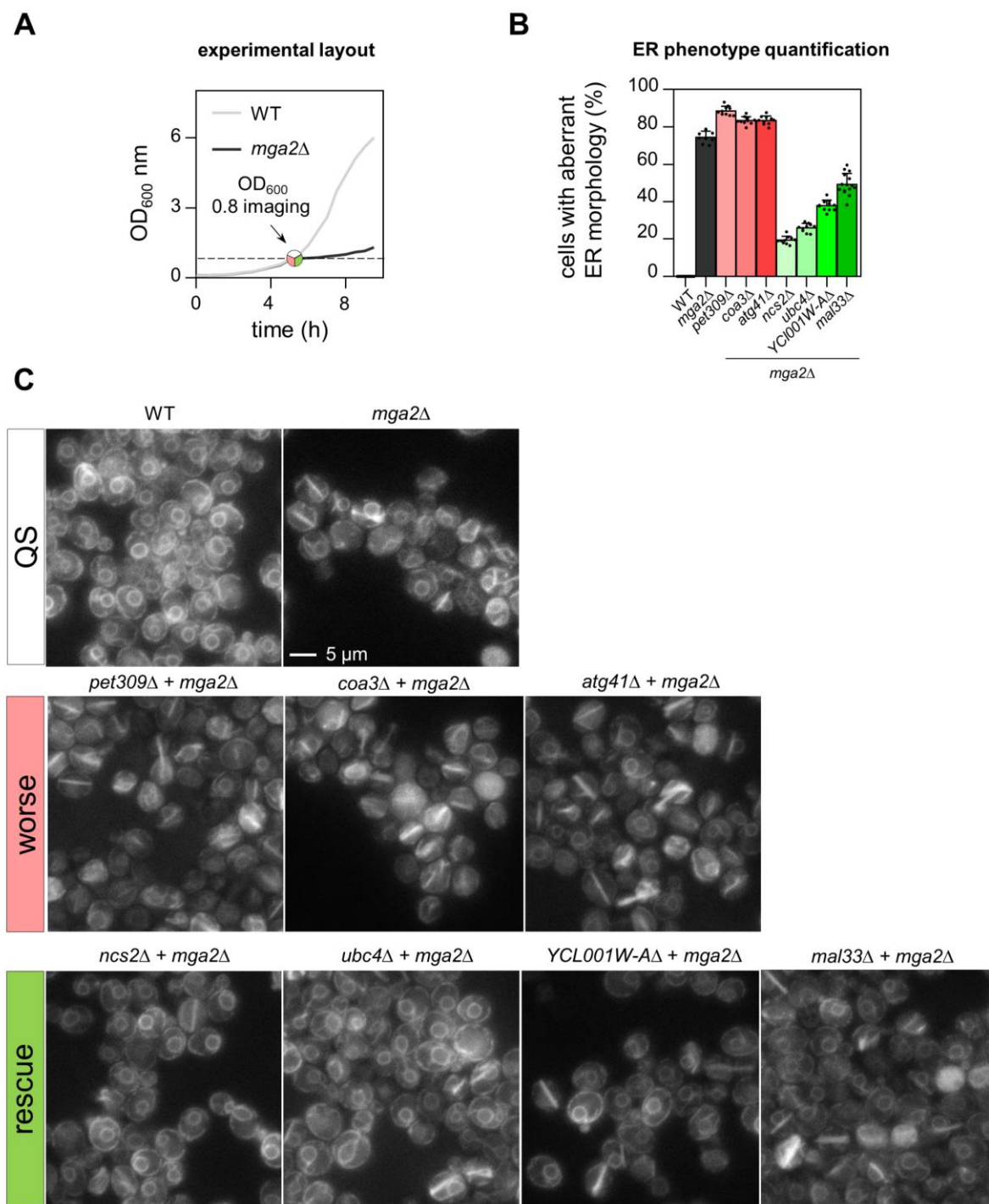


Figure 25 A screening workflow illustration with quantitative and qualitative data for the worse and rescue categories

(A) Experimental layout for the assessment of the aberrant ER structure distribution. Shown is schematic course of a batch cultivation growth curve. Cells were harvested at an OD₆₀₀ of 0.8 (dashed line) and subsequently imaged. (B) The % aberrant ER morphology occurrence is plotted for control and candidates of the “worse” (red colour gradient) and “rescue” (green colour gradient) category. Plotted is the mean and ± SD. The abbreviation fov stands for “field of view” and represents how many images were evaluated next to the number of total cells that were counted within the given fields of view. WT (n=13 fov/500 cells); *mga2*Δ (n=12 fov/633 cells); *pet309*Δ*mga2*Δ (n=10 fov/1105 cells); *coa3*Δ*mga2*Δ (n=10 fov/750 cells); *atg41*Δ*mga2*Δ (n=10 fov/1160 cells); *ncs2*Δ*mga2*Δ (n=10 fov/1949 cells); *ubc4*Δ*mga2*Δ (n= 10 fov/ 3585 cells); *YCL001W-A*Δ*mga2*Δ (n= 12 fov/1816 cells); *mal33*Δ*mga2*Δ (n= 15 fov/1603 cells). In (C) representative images series are shown for each category. Scalebar represents 5 μm

All candidates of both categories are listed in Table 14.

Table 14 Complete list of all overlapping candidates from the *mga2*Δ phenotype screen

Worse category	
Gene	Function
<i>MSS116</i>	Involved in splicing of mitochondrial transcripts, e.g. COX1 mRNA ²⁶²
<i>CBS2</i>	Mitochondrial translational activator, interacts with mitochondrial ribosomes ^{263,264}
<i>ATP22</i>	Encodes the mitochondrial ATPase subunit 6-specific translation factor ²⁶⁵
<i>SOM1</i>	Part of the mitochondrial inner membrane protease (IMP), required for Cox2p processing ²⁶⁶
<i>RSM18</i>	Protein of the yeast mitoribosome ²⁶⁷
<i>ARO2</i>	Bifunctional chorismate synthase ²⁶⁸
<i>VMA21</i>	Integral membrane protein required for assembly of the V-ATPase ²⁶⁹
<i>COA3</i>	Regulator of mitochondrial COX1 translation ²⁷⁰
<i>PET309</i>	Translational activator of the COX1 mRNA ²⁷¹
<i>MRPL3</i>	Protein of the yeast mitochondrial ribosomal protein of the large subunit ²⁷²
<i>PEX12</i>	Required for peroxisomal matrix protein import ²⁷³
<i>YMR052C-A</i>	Dubious open reading frame, genetic linkage with FAR3
<i>FAR3</i>	Core protein of the Far complex, involved in mitophagy with Atg32 ²⁷⁴
<i>ATP25</i>	Protein that gets cleaved between N- and C-terminus during mitochondrial import ²⁷⁵ . N-terminal part interacts with mitoribosome ²⁷⁶ , C-terminal part stabilizes the mRNA of the ATP synthase subunit Atp9p ²⁷⁷ .
<i>YIM2</i>	Dubious open reading frame. Overlaps with IMP1, which is like SOM1 part of the mitochondrial inner membrane protease (IMP) complex.
<i>PPA2</i>	Mitochondrial inorganic pyrophosphatase ²⁷⁸ , loss results in extended lifetime and reduced ATP level ²⁷⁹ .
<i>MSE1</i>	Mitochondrial glutamyl-tRNA Synthetase ²⁸⁰

Table continues next page

<i>SEC62</i>	Essential gene, required for protein translocation into the ER ²⁸¹
<i>MRP51</i>	Mitochondrial ribosomal protein of the small subunit ²⁶⁷ . Interacts with mutated 5'-untranslated leader sequences of <i>COX2</i> and <i>COX3</i> mRNA ²⁸²
<i>COA2</i>	Cytochrome oxidase assembly factor for Cox1p maturation ²⁸³ .
<i>YAR1</i>	Chaperone that protects ribosomal Rps3p from aggregation during nuclear import ^{284,285} .
<i>ATG41</i>	Affects the rate of autophagosome formation ²⁵⁵
<i>YBL100C</i>	Dubious open reading frame, overlaps with ATP1
<i>COQ1</i>	Hexaprenyl pyrophosphate synthetase involved in ubiquinone biosynthesis ²⁸⁶
<i>SCO1</i>	Involved in mitochondrial copper metabolism, important for cytochrome c oxidase assembly ²⁸⁷
<i>TRM7</i>	Encodes for a 2'-O-ribose RNA methyltransferase ²⁸⁸
<i>EXO5</i>	EXOnuclease V involved in mitochondrial genome maintenance ²⁸⁹
<i>FZO1</i>	GTPase involved in mitochondrial outer membrane fusion ²⁹⁰
<i>RIP1</i>	Encodes the Rieske Iron-sulfur Protein 1 a component of the mitochondrial cytochrome bc1 complex ²⁹¹
<i>OXA1</i>	Encodes a mitochondrial inner membrane insertase required for cytochrome oxidase activity ²⁹²
<i>GPP1</i>	Encodes a glycerol-3-phosphate phosphatase required for glycerol biosynthesis ²⁹³
<i>MRPL38</i>	Encodes for a mitochondrial ribosomal protein of the large subunit ²⁹⁴
<i>CBT1</i>	Cbt1p is involved in cytochrome b mRNA processing ^{295,296}
<i>FRS2</i>	Encodes a subunit of yeast phenylalanyl-tRNA synthetase ²⁹⁶
<i>MTF2</i>	Encodes a mitochondrial transcription factor ²⁹⁷
<i>QRI7</i>	Mitochondrial homolog of Kae1p a component of the KEOPS/EKC complex that is involved in tRNA modifications ²⁹⁸
<i>MRPL11</i>	Encodes for a mitochondrial ribosomal protein of the large subunit ²⁹⁴
<i>PAA1</i>	Encodes a polyamine acetyltransferase ²⁹⁹
<i>PET100</i>	Encodes a chaperone involved in the assembly of cytochrome c oxidase ³⁰⁰
<i>MTC5</i>	Encodes a protein that contributes to the capping of telomeres ³⁰¹
<i>COQ4</i>	Coq4p has a role in coenzyme Q biosynthesis ³⁰²
<i>COX20</i>	Cox20p plays a role in the assembly of cytochrome oxidase subunit 2 ³⁰³
<i>MRPL7</i>	Encodes for a mitochondrial ribosomal protein of the large subunit ²⁹⁴

Table continues next page

<i>OPI7</i>	Dubious open reading frame, overlaps with EAF1
<i>QCR7</i>	Encodes the seventh subunit of ubiquinol cytochrome c reductase ³⁰⁴
<i>OLE1</i>	Encodes the sole fatty acid desaturase in yeast ³⁰⁵
<i>MRH4</i>	Encodes mitochondrial DEAD box protein required for mtDNA maintenance ³⁰⁶
<i>YGL069C</i>	Dubious open reading frame, overlaps to 92 % with the open reading frame of MNP1, which encodes a mitochondrial ribosomal protein of the large subunit
<i>MDM34</i>	Mitochondrial component of the ERMES complex ³⁰⁷
<i>COQ6</i>	Encodes a flavin-dependent monooxygenase required for biosynthesis of coenzyme Q ³⁰⁸
<i>PET130</i>	Involved in the processing of mitochondrial tRNAs ³⁰⁹
<i>QCR8</i>	Encodes the eight subunit of ubiquinol cytochrome c reductase ³¹⁰
<i>COX12</i>	Subunit of cytochrome c oxidase ³¹¹
<i>YLR112W</i>	Encodes a protein of unknown function
<i>FAR10</i>	Member of the Far complex involved in mitophagy ³¹²
<i>YLR255C</i>	Encodes a protein of unknown function
<i>MRPL15</i>	Encodes for a mitochondrial ribosomal protein of the large subunit ²⁹⁴
<i>ELO3</i>	Elo3p plays a role in fatty acid elongation and sphingolipid formation ³¹³
<i>NAM2</i>	Encodes a mitochondrial leucyl-tRNA synthetase ³¹⁴
<i>COQ5</i>	Encodes a 2-hexaprenyl-6-methoxy-1,4-benzoquinone methyltransferase and is involved in coenzyme Q biosynthesis ³¹⁵
<i>RSF1</i>	Encodes a protein required for respiratory growth ³¹⁶
<i>SOV1</i>	Encodes a mitochondrial protein of unknown function ³¹⁷
<i>IMP1</i>	Encodes the catalytic subunit of the mitochondrial inner membrane peptidase complex ³¹⁸
<i>FMP42</i>	Part of the mitochondrial proteome ³¹⁹
<i>MTF1</i>	Encodes a mitochondrial transcription factor ²⁹⁷
<i>MRP7</i>	Encodes for a mitochondrial ribosomal protein of the large subunit ²⁹⁴
<i>MSK1</i>	Encodes a mitochondrial lysine-tRNA synthetase ³²⁰
<i>SWS2</i>	Component of the mitochondrial ribosomal small subunit ³²¹
<i>EAF7</i>	Encodes a member of a NuA4 subcomplex the only essential lysine acetyltransferase complex of <i>S. cerevisiae</i> ³²²
<i>YNL198C</i>	Dubious open reading frame unlikely to encode a functional protein.
<i>GCR2</i>	Encodes a transcriptional activator for glycolytic genes ³²³

Table continues next page

<i>MRPS12</i>	Component of the mitochondrial ribosomal small subunit ³²¹
<i>RSM19</i>	Ribosomal Small subunit of Mitochondria ³²¹
<i>BRE5</i>	Encodes Bre5p, a cofactor for Ubp3p role in the de-ubiquitination of Sec23p ³²⁴
<i>MDM12</i>	Mitochondrial component of the ERMES complex ³⁰⁷
<i>MRX11</i>	Encodes a protein that associates with mitochondrial ribosomes ³²⁵
<i>YPL062W</i>	Putative protein of unknown function, null mutants shows reduced levels of terpenoids ³²⁶
<i>RTT10</i>	Encodes a protein involved in post-transcriptional tRNA anticodon modification ³²⁷
<i>ALG5</i>	Encodes a transmembrane protein that enzymatically confers the transfer of glucose from UDP-glucose to dolichyl phosphate. ³²⁸
<i>RRG8</i>	Rrg8p has a role in mitochondrial tRNA processing ³⁰⁹
<i>RIM11</i>	Encodes a protein involved in the expression of meiotic genes ³²⁹
<i>COX19</i>	Encodes a protein required for cytochrome c oxidase expression ³³⁰
<i>YHR050W-A</i>	Protein of unknown function, in direct vicinity to COX6

Rescue category	
-----------------	--

Gene	Function
<i>UBC4</i>	Encodes for the most abundant ubiquitin-conjugating enzyme (E2) ²⁵⁹
<i>SWD3</i>	Subunit protein of the COMPASS complex, involved in telomeric transcriptional silencing ³³¹ .
<i>MAL33</i>	Member of the MAL gene family. All MAL loci are in the telomeric region. ²⁵⁶
<i>YCL001W-A</i>	Gene of unknown function, putative role in RNA metabolism ²⁶¹ .
<i>MSN5</i>	Karyopherin involved in Swi5p mediated cell cycle progression ³³² .
<i>CIN8</i>	Kinesin involved in bipolar mitotic spindle assembly ³³³ .
<i>STE20</i>	Cdc42p-activated signal transducing kinase; involved in pheromone response, pseudohyphal/invasive growth ³³⁴ .
<i>MET18</i>	Part of the cytosolic Fe-S protein assembly (CIA) machinery. Maturation of cytosolic and nuclear iron-sulfur (Fe-S) proteins ³³⁵ .
<i>IES3</i>	Subunit of the INO80 chromatin remodeling complex ³³⁶ .
<i>BER1</i>	Confers microtubule stability (BEnomyl Resistant 1) ³³⁷ .
<i>RPS17A</i>	Ribosomal protein 51 of the small subunit. Associated with slow growth ³³⁸ .

Table continues next page

<i>NST1</i>	Negatively affects Salt Tolerance 1. Interacts physically and genetically with MSL1 ³³⁹ .
<i>NCS2</i>	Role in tRNA modification and urmylation ^{257,258}
<i>MSB4</i>	Cdc42p bud site and bud tip localization. MSB3 and MSB4 deletion cause defects in secretion and actin organization ³⁴⁰ .
<i>CKA2</i>	Catalytic unit of the Casein kinase II involved in flocculation, cell polarity, cell cycle progression and ion homeostasis ³⁴¹ .
<i>SNF8</i>	Sucrose Non Fermenting 8. Growth defect on glycerol ³⁴² .
<i>PIN4</i>	Encodes a protein involved in G2/M transition of mitotic cell cycle ³⁴³
<i>RPS0A</i>	Encodes the ribosomal 40S subunit protein S0A ³⁴⁴
<i>RPL16B</i>	Encodes the ribosomal 60S subunit protein L16B ³⁴⁴
<i>RPL33A</i>	Encodes the ribosomal 60S subunit protein L33A ³⁴⁴
<i>SDH2</i>	Encodes an iron-sulfur protein of the succinate dehydrogenase ³⁴⁵
<i>NHP10</i>	INO80 chromatin remodeling complex subunit ³⁴⁶
<i>SAP30</i>	Component of a histone deacetylase complex ³⁴⁷
<i>ATG10</i>	Atg10p shows E2-like activity and is essential for autophagy ³⁴⁸
<i>SOH1</i>	Component of the Soh1/TRAP18 mediator complex ³⁴⁹

4.3.3 The degree of lipidome saturation correlates with the emergence of aberrant ER morphologies

As the genome-wide screen brought forward two distinct categories that broadened the observable occurrence of aberrant ER morphologies, the question arose whether one can quantitatively assess a link between the degree of saturation in these candidates and the frequency of aberrant ER morphology manifestation. For that I acquired for both control strains, the WT and the *mga2Δ* strain, as well as for all of the seven chosen candidates whole cell lipidomics data.

To see whether the frequencies of aberrant ER morphology formation are rooted in *mga2Δ* lack of unsaturated lipids, all seven candidates were analyzed for their degree of lipid saturation in glycerophospholipid (Figure 26 A for “rescue” candidates, Figure 26 B for “worse” candidates). “Rescue” candidates have a reduced share of fully saturated glycerophospholipids compared to the *mga2Δ* query strain, opposed to the “worse” candidates that show elevated levels of fully saturated glycerophospholipids, with the exception of *atg41Δmga2Δ*, which had fewer fully saturated glycerophospholipids than the *mga2Δ* strain

(48.9 % for *mga2* Δ compared to 43.8 % for *atg41* Δ *mga2* Δ). When the occurrence of aberrant ER morphologies is plotted against the mol% of fully saturated glycerophospholipids a correlation can be seen (Figure 26 C). The only candidate, as previously mentioned that does not follow this trend is *atg41* Δ *mga2* Δ , as its acyl chain composition does deviate from those of the other examples from the worse category, leaning more towards those seen in the rescue category.

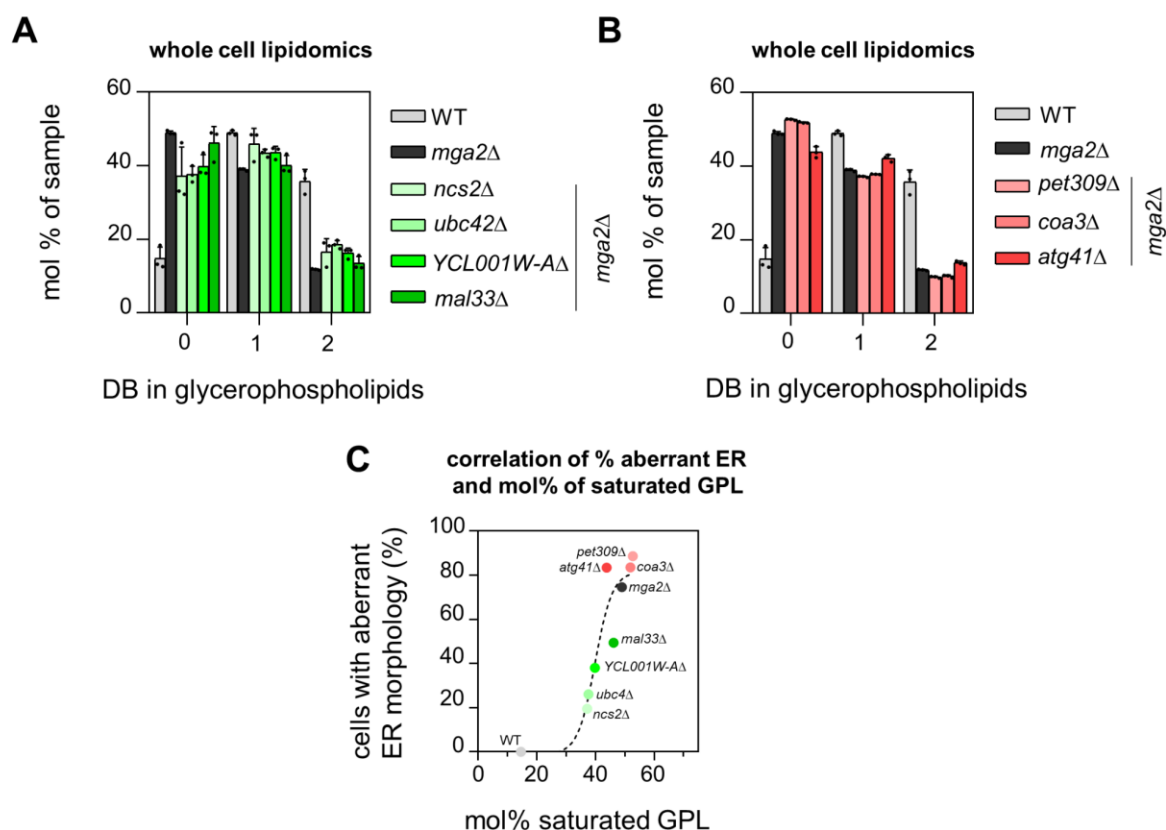


Figure 26 Aberrant ER structure emergence correlates with saturation of lipidome

(A and B) show the amount of double bonds (DB) in glycerophospholipids as the sum of DB in both fatty acid chains for the rescue and worse candidates. Abundance is given in mol% of the sample, in which 0 describes completely saturated, 1 monosaturated and 2 polysaturated glycerophospholipids. Plotted is the average \pm SD of three independent biological replicates. In (C) the combination of the datasets of Figure 25 (B) and Figure 26 (A and B) is shown in which the % aberrant ER morphology is plotted against the total mol% of saturated glycerophospholipids (GPL) found for each sample. To improve legibility for all double knockouts the information that *MGA2* is deleted was omitted. Plotted are the average values. Data was fitted with a sigmoidal 4PL fit (dashed line) in GraphPad prism with an R^2 of 0.88.

Next, I wanted to see whether there are significant differences in the lipid class composition between the WT and *mga2* Δ strain. In Figure 27 I plotted for a direct comparison the lipid composition of both control strains given in mol% of the sample. The lipid class composition of both strains varies, in that ceramide levels of *mga2* Δ are elevated, while for more complex sphingolipids (IPC; MIPC; M(IP)₂C) lower levels are measured. Further, one sees increased levels of PA and DAG in *mga2* Δ (11.8 mol% increase in PA and 6.6 mol% increase in DAG

compared to the WT). Similar to the more complex sphingolipids, levels of the most abundant glycerophospholipid PI, are also reduced in *mga2Δ* (7.2 mol% reduction compared to the WT), although not statistically significant.

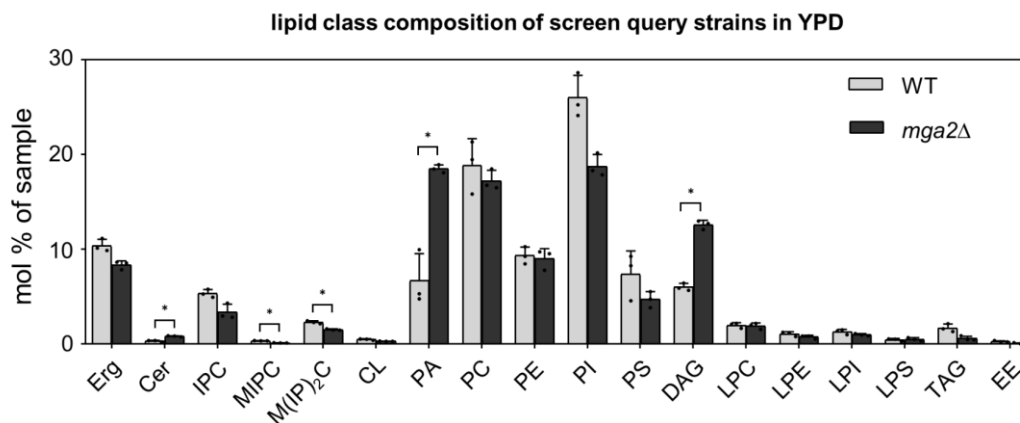


Figure 27 The lipid class composition of wildtype cells and *mga2Δ* cells grown in YPD medium

Shown is the lipid class composition in mol% of the sample. The strains were grown in YPD medium until they reached an OD₆₀₀ of 0.8 prior to harvesting them. Abbreviations translate to Erg = ergosterol; Cer = ceramide; IPC = inositolphosphorylceramide; MPC = mannosyl-IPC; M(IP)₂C = mannosyl-di-IPC; CL = cardiolipin; PA = phosphatidic acid; PC = phosphatidylcholine; PE = phosphatidylethanolamine; PI = phosphatidylinositol; PS = phosphatidylserine; DAG = diacylglycerol; LPC = lyso-PC; LPE = lyso-PE; LPI = lyso-PI; LPS = lyso-PS; TAG = triacylglycerol; EE = ergosteryl ester. Plotted are biological triplicates, their average and ± SD.

In Figure 28 the lipid composition for the seven chosen candidates is depicted. To allow for a side-by-side comparison, the data from both control strains are replotted. For both the “rescue” and “worse” category the differences in the lipid composition between the WT and the *mga2Δ* strain become more pronounced. The “rescue” candidates depicted in Figure 28 B tend to show lower levels of PA and DAG while the level of PI increases making their lipid class composition more comparable to that found in the WT. The “worse” candidates on the other hand (Figure 28 A) surpass the lipidome changes of the sole *mga2Δ* strain in terms of PA and DAG accumulation, while showing a greater reduction in the PI levels. The latter holds true with the exception of *mga2Δatg41Δ*. In case of *pet309Δmga2Δ* and *coa3Δmga2Δ*, the increased PA level and simultaneously decreased PI level are remarkable in that for the first time the PI to PA ratio is reversed and PI is no longer the major constituent of glycerophospholipids (20.5 mol% PA to 17.5 mol% PI for *pet309Δmga2Δ*; 19.1 mol% PA to 18.1 mol% PI for *coa3Δmga2Δ*).

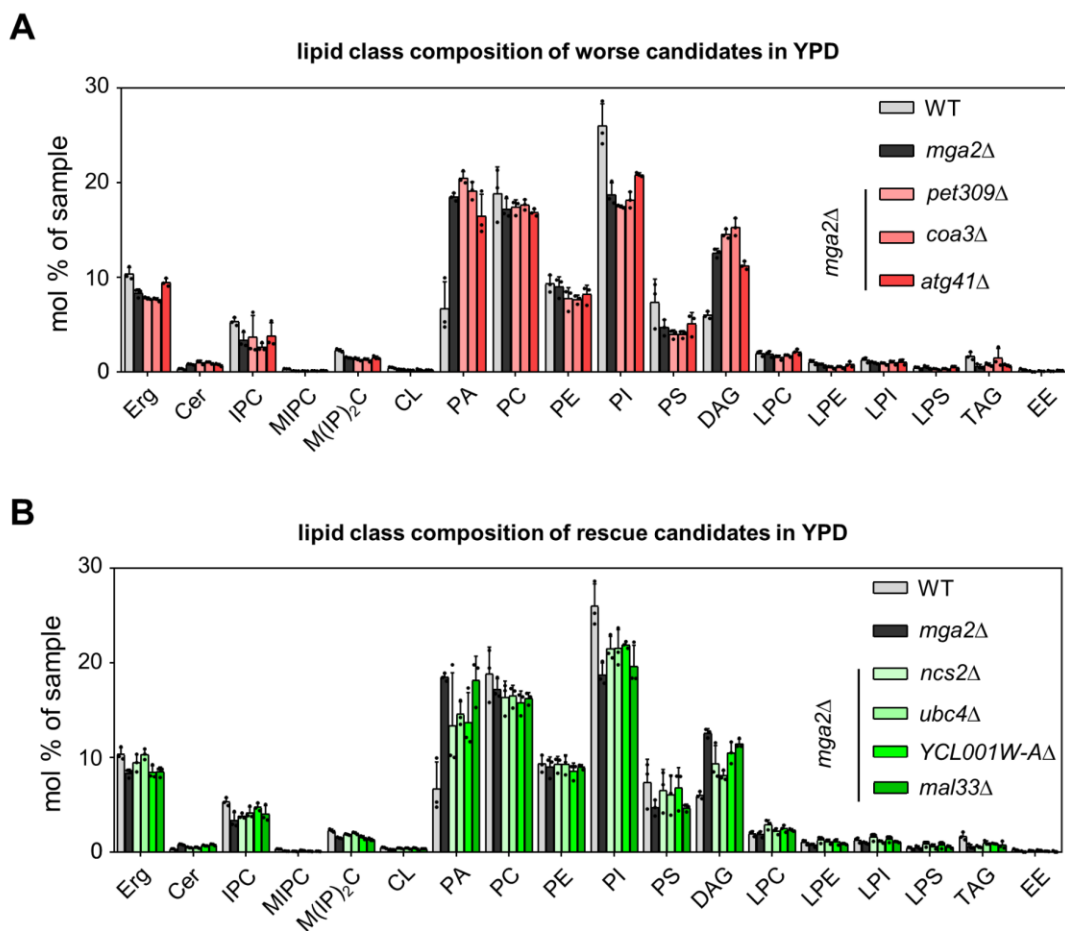


Figure 28 lipid class composition of all candidates from the genome-wide high throughput screen in comparison to that of the query strains

Shown are in **(A)** the lipid class compositions of the rescue candidates in comparison to those of the query strains. Strains were grown in YPD medium, starting at an OD_{600} of 0.1 and were harvested at an OD_{600} of 0.8. In **(B)** the lipid class composition is shown for the worse candidates. The cells have been cultivated identically. The WT and *mga2* Δ graphs are replotted from Figure 27 to allow for a better comparison. Abbreviations translate to Erg = ergosterol; Cer = ceramide; IPC = inositolphosphorylceramide; MIPC = mannosyl-IPC; M(IP)₂C = mannosyl-di-IPC; CL = cardiolipin; PA = phosphatidic acid; PC = phosphatidylcholine; PE = phosphatidylethanolamine; PI = phosphatidylinositol; PS = phosphatidylserine; DAG = diacylglycerol; LPC = lyso-PC; LPE = lyso-PE; LPI = lyso-PI; LPS = lyso-PS; TAG = triacylglycerol; EE = ergosterol ester. Plotted are biological triplicates, their average and \pm SD. Statistical analysis was done with an unpaired two-tailed t-test, assuming Gaussian distribution. Benjamini, Krieger and Yekutieli method was used to correct for false discovery rate ($Q=5\%$).

To validate whether the observed changes in the lipid class composition are based on positive or negative genetic interactions within the double knockout candidates, mutants carrying each single candidate mutation were generated within the WT strain background and their lipidome was determined (Figure 29). The lipidomes of all single mutants show no significantly elevated levels of fully saturated glycerophospholipids (data not shown). Further the levels of PA and DAG that were shown to be highly elevated in *mga2* Δ , are not significantly altered for all single knockout strains (Figure 29). Furthermore, all of them show increased levels of PI compared to the *mga2* Δ query strain. Only the *pet309* Δ mutant shows significantly increased levels of

the storage lipids TAG and EE (Figure 29 A). Noteworthy is the uniform increase in cardiolipin (CL) compared to the WT control strain seen in the single rescue knockout group (Figure 29 B).

In summary, the degree of lipid saturation correlates positively with the occurrence of the aberrant ER. For the lipid class composition, the increased levels of PA and DAG can be seen as a signature deviation introduced by the knockout of *MGA2*. This deviation in the *mga2Δ* strain compared to the WT control strain is less pronounced in strains of the “rescue” category and more pronounced in strains of the “worse” category, with the exception of *atg41Δmga2Δ*. The single mutants of each category, do not show elevated levels for PA or DAG, neither do they show aberrant ER structures or have significantly increased levels of fully saturated glycerophospholipids (data not shown). Therefore, the observed changes in aberrant ER morphology, degree of lipid saturation and disturbed PA and DAG levels are not the result of positive and negative genetic interactions. The single knockouts do not cause any of these phenotypes on their own. Their alleviating or aggravating tendencies are rather masked in presence of *MGA2* and only come through in the *mga2Δ* background.

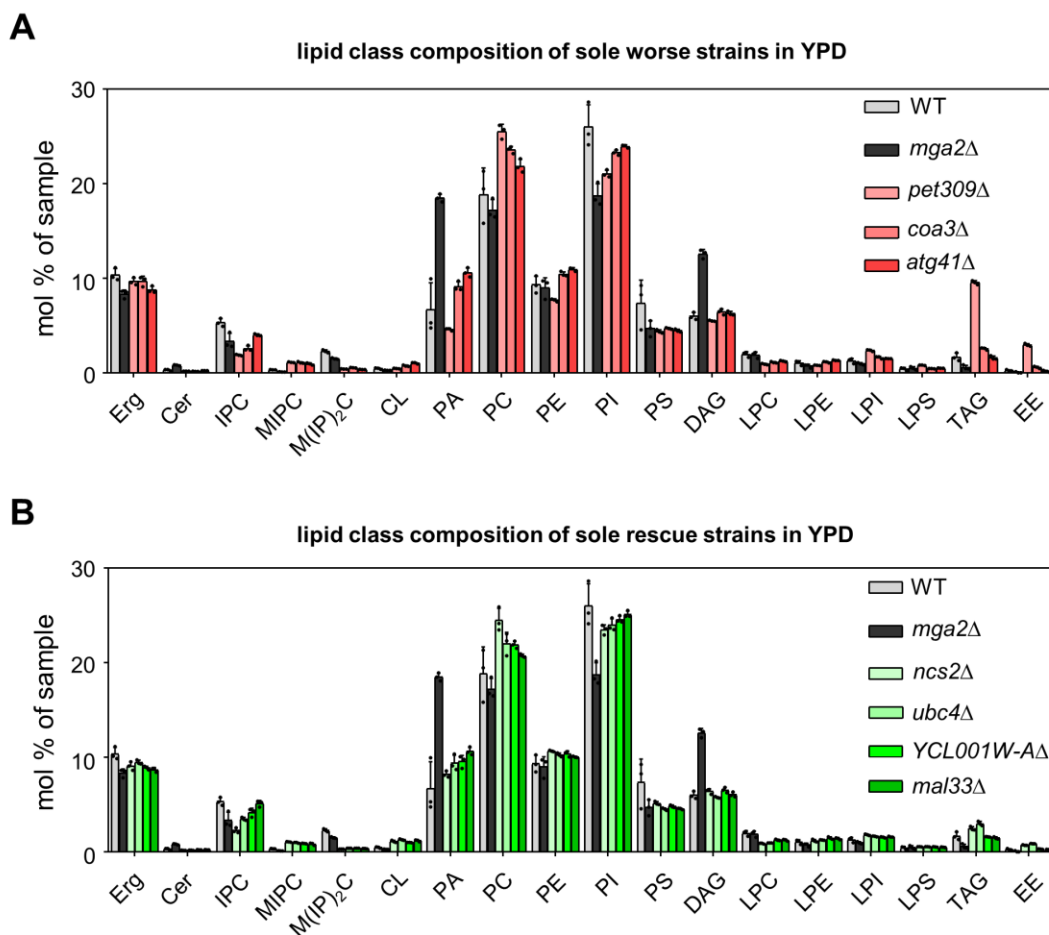


Figure 29 lipid class composition of all candidates from the genome-wide high throughput screen in comparison to that of the query strains

Shown are in **(A)** the lipid class compositions of the rescue candidates in comparison to those of the query strains. Strains were grown in YPD medium, starting at an OD_{600} of 0.1 and were harvested at an OD_{600} of 0.8. In **(B)** the lipid class composition is shown for the worse candidates. The cells have been cultivated identically. The WT and *mga2* Δ graphs are replotted from Figure 27 to allow for a better comparison. Abbreviations translate to Erg = ergosterol; Cer = ceramide; IPC = inositolphosphorylceramide; MIPC = mannosyl-IPC; M(IP)₂C = mannosyl-di-IPC; CL = cardiolipin; PA = phosphatidic acid; PC = phosphatidylcholine; PE = phosphatidylethanolamine; PI = phosphatidylinositol; PS = phosphatidylserine; DAG = diacylglycerol; LPC = lyso-PC; LPE = lyso-PE; LPI = lyso-PI; LPS = lyso-PS; TAG = triacylglycerol; EE = ergosteryl ester. Plotted are biological triplicates, their average and \pm SD. Statistical analysis was done with an unpaired two-tailed t-test, assuming Gaussian distribution. Benjamini, Krieger and Yekutieli method was used to correct for false discovery rate ($Q=5\%$).

4.3.4 Finding the missing link between the UPR and aberrant ER morphology in *mga2* Δ

Because unsaturated fatty acids can be limiting to maintain organelle architectures³⁵⁰, I wanted to explore if the production of unsaturated fatty acids becomes even more limiting upon increased membrane biogenesis. The goal was to determine if ER membrane expansion, which is induced by the UPR, can become harmful in the *mga2* Δ strain. Since membrane expansion is regulated during the cell cycle^{351,352}, this would also provide a link to better understand the alleviating effects of the “rescue” category, which is associated with the process of mitosis.

To manipulate the *de novo* synthesis and mimic membrane expansion, as seen during cell growth or as a consequence of UPR signaling, I generated strains that harbor an inducible ER membrane expansion system. This system is based on the heterodimeric master regulator of membrane biogenesis Ino2p and Ino4p^{353,354}. The Ino2p/Ino4p complex is inhibited by the transcriptional regulator Opi1p, which binds to Ino2p and thereby negatively regulates the expression of Ino2p/Ino4p target genes^{355,356}. Notably, UPR signaling leads to an induction of lipid synthesis genes that are under the control of the Ino2p/Ino4p complex³⁵⁷. Schuck *et al.* and Heyken *et al.* could further show that transcriptional control of phospholipid synthesizing genes can be bypassed by either deleting *OPI1*, or by providing a mutant *ino2(L119A)* that can no longer be bound by Opi1p thereby leading to a constitutive expression of genes involved in lipid biosynthesis^{357,358}. To study the effects of *de novo* lipid biosynthesis on aberrant ER formation in *mga2* Δ a published inducible promoter system was employed that allows for a controlled membrane expansion by introducing the *ino2(L119A)* gene under the control of the metabolically inert β -estradiol expression system (Figure 30)^{207,359}. Hence the here employed system for constitutive membrane synthesis relies on the displacement of wildtype Ino2p with the Opi1p non-repressive Ino2p(L119A) mutant.

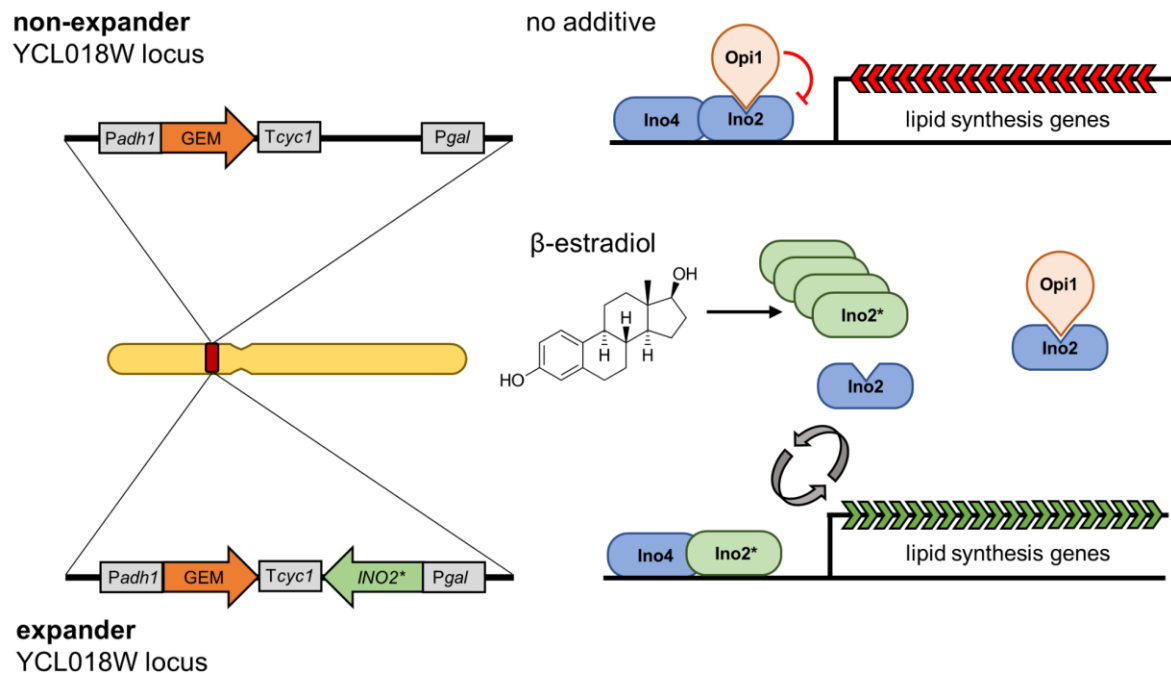


Figure 30 Schematic overview of an inducible ER membrane biogenesis system

The illustration depicts genetic manipulations carried out for an ER membrane expanding system. In brief, a chimeric transcription factor Gal4-ER-Msn2 (GEM) is under the control of the *adh1* promoter (*Padh1*) and *cyc1* terminator (*Tcyc1*) and gets constitutively expressed. The transcription factor is composed of the Gal4 DNA binding domain, the ER ligand binding domain of the human estrogen receptor (EstR, in short ER) and a transcription activation domain derived from Msn2. The addition of β -estradiol will stimulate the expression of any gene under the control of the GAL promoter (*Pgal*). The non-expander strain and the expander strain created differ only in the gene that is under control of the inducible GAL promoter. The expander strain will under β -estradiol supplementation express *INO2(L119A)*, here named *INO2**, which encodes for a mutant that can no longer bind Opi1p and will therefore no longer be repressed, leading to a constant expression of genes under the control of the Ino4p-Ino2p heteromeric transcription factor. The expression of genes under the control of the Ino4p-Ino2p complex will cause an ER-membrane expansion, and thereby mimic a part of the UPR response.

Papagiannidis *et al.* could show that this system induces membrane expansion independent of UPR activation thereby allowing me to study the effect of membrane biogenesis uncoupled from UPR signaling in *mga2 Δ* ²⁰⁷. I generated two strains, termed “non-expander” and “expander” to investigate the impact of membrane expansion on aberrant ER formation in the *mga2 Δ* background. Only the expander strain will express under β -estradiol supplementation the Ino2p(L119A) mutant, while the non-expander strain served as a control as it contains the identical expression system but lacks the *ino2(L119A)* gene for ER membrane biogenesis. The changes in occurrence of % aberrant ER structures for the non-expander and expander strains with and without β -estradiol supplementation are shown in Figure 31 A. The non-expander strain shows under the given growth conditions the lowest percentage of cells with aberrant ER structures with 48 %. The addition of β -estradiol causes an increase of observable aberrant ER morphology to 65 %. For the expander strain this increase is more pronounced.

The expander strain shows in SCD medium already a 69 % proportion of aberrant to healthy ER morphology, which increases upon β -estradiol supplementation to 91 %. The increased number of cells with an aberrant ER morphology in absence of β -estradiol seen for the expander strain opposed to the non-expander strain can be explained by a leakiness of the promotor system and a consequent unwanted expression of Ino2p(L119A). However, the reason for the observed increase in case of the non-expander strain under β -estradiol supplementation remained elusive. To learn why there is a striking increase in aberrant ER morphology occurrence in case of the non-expander strain when β -estradiol is added the PCR cyclor growth assay was used to identify possible off target effects (Figure 31 B). The graph reveals that β -estradiol does not have a noticeable impact on the growth of the WT strain. For the *mga2* Δ strain however, a growth inhibiting effect can be seen, comparable to that when palmitate is fed to the cells (Figure 20 D). Taken together these results show that the β -estradiol inducible system is not optimal to test the hypothesis if increased membrane biogenesis aggravates the formation aberrant ER structures.

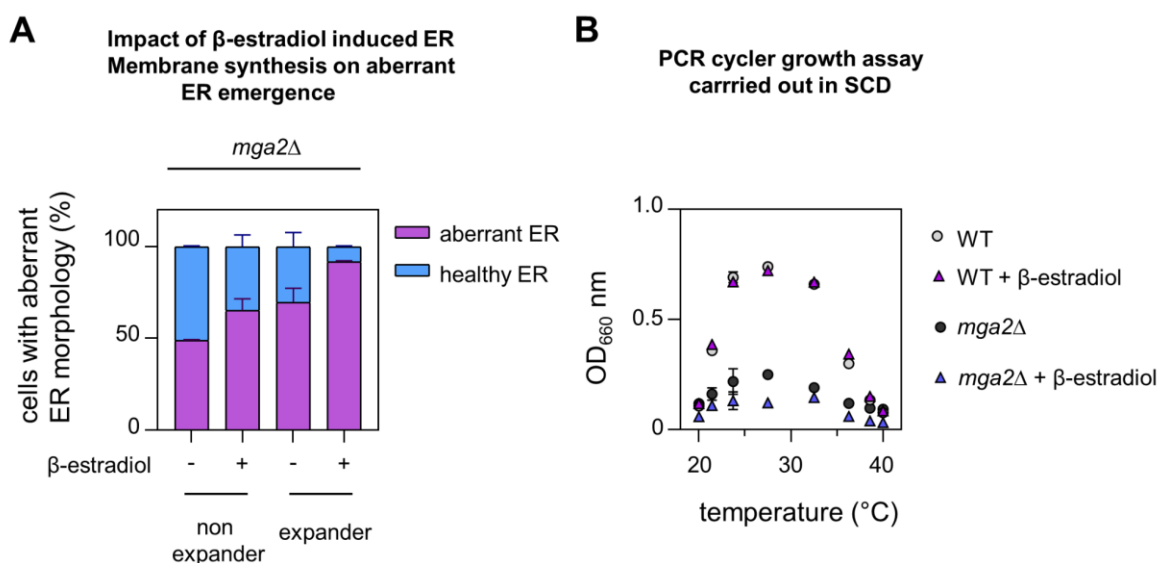


Figure 31 Membrane synthesis as a cause for aberrant ER morphology in *mga2* Δ

Panel (A) shows the results for the ER phenotype distribution for *mga2* Δ + non-expander and *mga2* Δ + expander strains. On the Y-axis the ER phenotype is given as % of totally evaluated ER phenotypes. The legend below the graph reports on the respective treatment, that the cells were given in which a - resembles that the treatment was omitted. Cells were grown in SCD medium for this experiment. Lastly β -estradiol is the compound that induces the expression of a gene under the control of the GAL promoter and it was supplemented at a final concentration of 800 nM. Plotted is the mean \pm SD of the following data: non-expander SCD (n=3 fov/238 cells); non-expander SCD + β -estradiol (n=3 fov/299 cells); expander SCD (n= 3 fov/ 158 cells); expander SCD + β -estradiol (n=3 fov/ 105 cells). The abbreviation fov stands for “field of view” and represents how many images were evaluated next to the number of total cells that were counted within the given fields of view. In (B) wildtype strain (WT) and *mga2* Δ strain were grown at indicated temperatures without agitation with and without β -estradiol supplementation at 800 nM. After 19 h a final OD₆₀₀ measurement was carried out to validate the biomass formed. Plotted is the mean \pm SD of three biological replicates.

Based on the promising trends of the β -estradiol system, multiple alternative inducible expression systems were analyzed and tested for their suitability to verify membrane biogenesis-driven aberrant ER formation in the *mga2* Δ background. Considering the interplay of membrane biogenesis by growth and growth independent membrane synthesis, the widely used galactose-inducible system³⁶⁰ was disqualified as it would require the exchange of carbon source. Another reason for rejecting the galactose-inducible promotor was that it cannot be titrated. As this requirement is important when optimizing a system, I decided for two alternative systems, namely the copper inducible *CUP1* promotor, and the cyanamide inducible *DDI2* promotor, both derived from *S. cerevisiae*^{361,362}. As the strategy for constitutive membrane synthesis relies on the displacement of the wildtype Ino2p by the Opi1p non-repressive Ino2p(L119A) mutant, a system of minimal promotor leakage is mandatory. This requirement dismissed the P_{CUP1} based inducible system as it showed unwanted expression of the Ino2p(L119A) mutant prior to copper sulfate administration (data not shown). The P_{DDI2} based system (Figure 32 A) remained and was optimized for the applicable concentration as cyanamide shows mild toxicity. At an empirically determined concentration of 1 mM cyanamide did not impede the growth of WT or *mga2* Δ strains and therefore was subsequently used to induce the expression of *ino2*(L119A). Further I verified that cyanamide did not lead to an unwanted activation of the UPR within the time course of drug administration via RT qPCR of *HAC1* mRNA (Figure 32 B). When the cyanamide inducible system is induced in *mga2* Δ cells, the fraction of cells harboring an aberrant ER increased more than threefold (Figure 32 C).

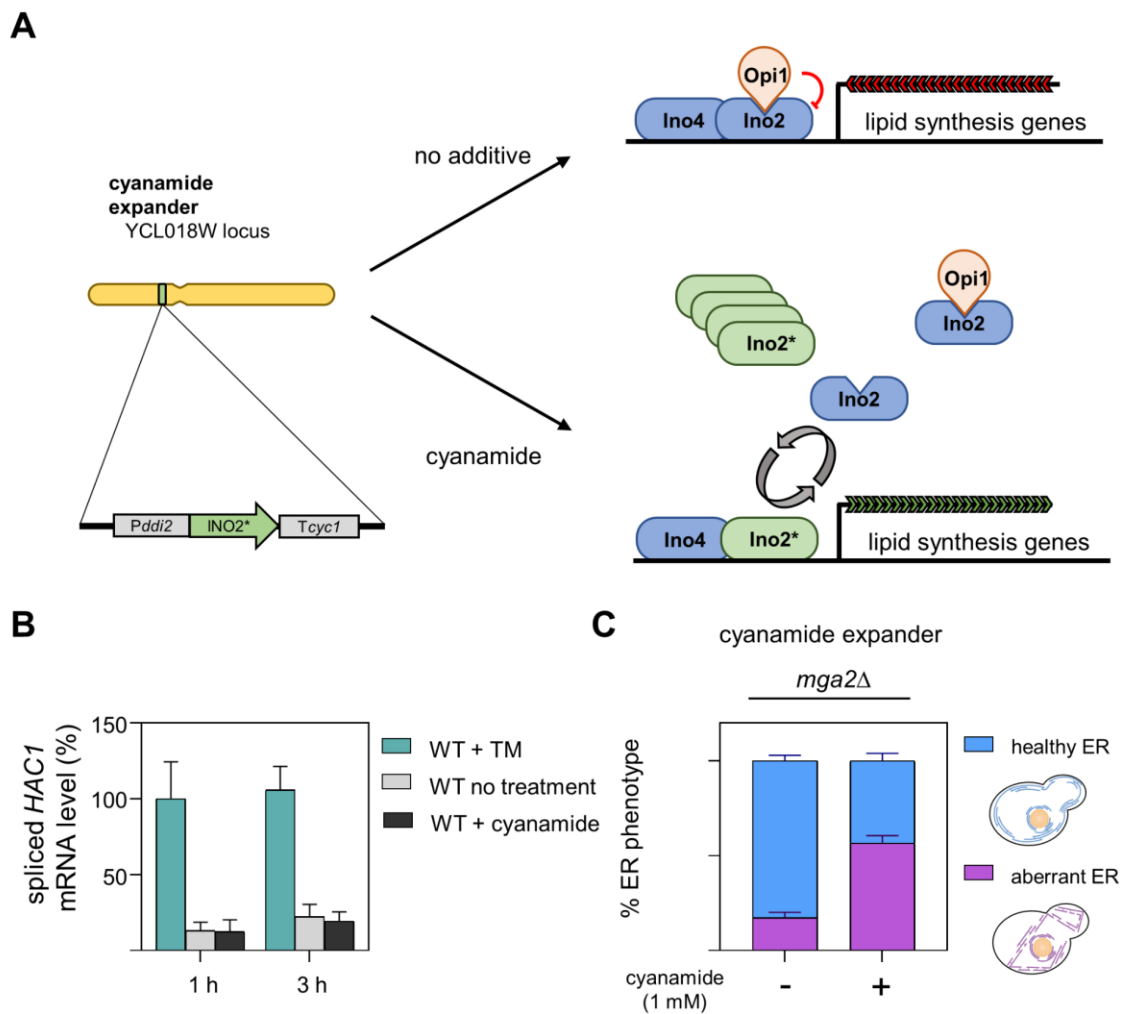


Figure 32 UPR independent ER membrane synthesis is sufficient to promote aberrant ER formation in *mga2Δ*

In (A) the genetic background of the cyanamide inducible strain for ER membrane synthesis is depicted. The gene *INO2**, encoding for the *INO2(L119A)* mutant, was put under control of *DDI2*'s cyanamide inducible promoter and the terminator of *CYC1*. In case of cyanamide administration, this will lead to the expression of *INO2**, causing a displacement of wildtype Ino2p in the heteromeric Ino4p-Ino2p transcription factor dimer, which will ultimately circumvent Opi1p repression, giving rise to ER membrane synthesis. In (B) this system was employed in a wildtype strain background and its effects on UPR activation during a time course was determined via measurement of spliced *HAC1* mRNA levels. Cells exposed to tunicamycin served as a reference treatment and normalization sample. Data is given as the average \pm SD of three independent biological replicates, with technical duplicates. (C) depicts ER phenotype distributions, given in percent, for the cyanamide expander system employed in the *mga2Δ* background. Depicted are the results in absence and presence of 1 mM cyanamide 3h after its administration. Cyanamide - (n= 3 fov/248 cells), cyanamide + (n= 3 / 201 cells). The abbreviation fov stands for "field of view" and represents how many images were evaluated next to the number of total cells that were counted within the given fields of view

4.3.5 The aberrant ER phenotype in *mga2* Δ shows a cell cycle dependent dynamic

Previous data indicated that membrane expansion contributes to the formation of the aberrant ER phenotype in *mga2* Δ cells, hence I wondered whether mutants that differ in their speed of completing the cell cycle and thereby indirectly differ in their rate of lipid synthesis due to growth (Figure 33 A), would also display elevated or reduced levels of aberrant ER structures^{363,364}. To answer this question, I wanted to overexpress genes that interfere with cell cycle progression identified by Niu *et al*³⁶⁴ and genes that cause constitutively elevated levels of intracellular membranes. Since the occurrence of the aberrant ER varies between single cells within an isogenic culture, I wanted to establish an expression system that introduces the lowest possible variance in cell-to-cell expression to not further introduce expression artefacts that contribute in an unspecific manner to the phenotypic heterogeneity. One major source of variance in the degree of protein expression is plasmid copy number differences³⁶⁵. Therefore, I created a system based on findings by Baganz *et al.*³⁶⁶, which allows the stable integration of any gene of interest into the genome at the HO locus as the chosen neutral gene insertion site. The genes in my expression system are under the control of the strong *TDH3* promoter and *CYC1* terminator together with a kanMX cassette for selection. In Figure 33 B the percentage of cells with an aberrant ER morphology is plotted for the small overexpression screen. For a comparison the data of the control strains from Figure 25 B are replotted. The small overexpression screening approach results in two new “rescue” candidates with *SWI5* and *MSN5*, and five additional “worse” candidates in *DOC1*, *ROF1*, *IES3*, *NIP100* and the cell cycle progression unrelated but membrane synthesis related gene *ICE2*²⁰⁷. Interestingly, *SWI5* expression was a plasmid borne rescue in a temperature sensitive screen of a *mga2* Δ and *spt23-ts* strain that basically mimics the knockout of the essential *OLE1* gene, made by Zhang *et al*¹⁹⁹. Among the seven newly identified candidates is the strongest rescue, *MSN5* (11.8 % aberrant ER morphology), and the strongest worse candidate in *ICE2* (91.9 % aberrant ER morphology). *ICE2* overexpression inhibits the lipid phosphatase complex and thereby causes massive ER membrane biogenesis. Hence, *ICE2* increases membrane biogenesis without a need for an inducer such as β -estradiol or cyanamide.

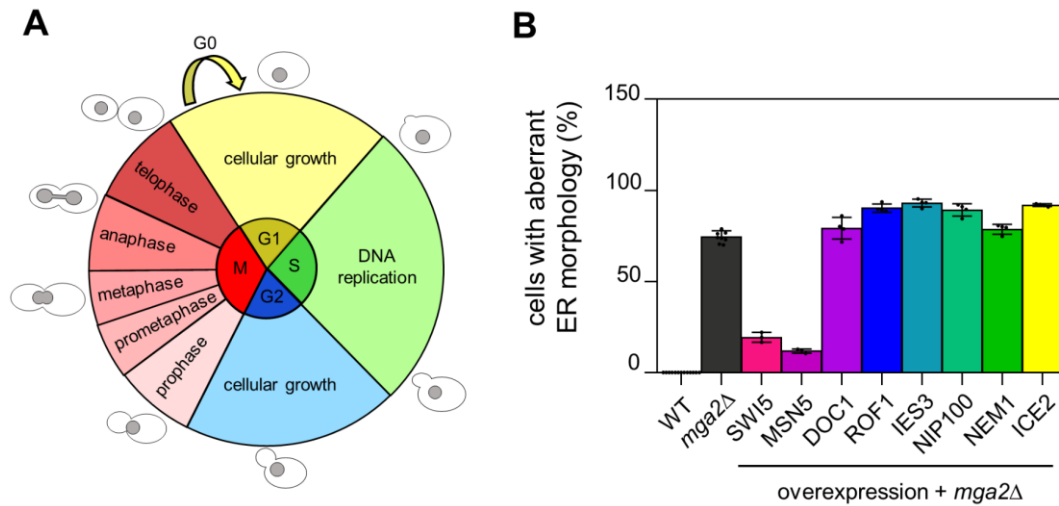


Figure 33 Manipulation of cell cycle progression affects aberrant ER formation

In **(A)** a schematic representation of the cell cycle with the five cell cycle phases, G0, G1, S, G2 and M phase is shown. The M phase is further divided into five mitotic substages, prophase, prometaphase, metaphase, anaphase and telophase. The cell cycle progression is illustrated with schematic representation of the observable morphological changes associated in yeast during the respective sections. In **(B)** the results for a gene overexpression study within the *mga2Δ* strain are shown. All genes annotated with the exception of *ICE2* are reported to manipulate upon overexpression the cell cycle progression. The data for WT and *mga2Δ* are replotted from Figure 25 (B). For all new mutants the mean and \pm SD are plotted. *SWI5* (n=3 fov/200 cells); *MSN5* (n=3 fov/238 cells); *DOC1* (n=4 fov/294 cells); *ROF1* (n=4 fov/266 cells); *IES3* (n=4 fov/563 cells); *NIP100* (n=4 fov/487 cells); *NEM1* (n=4 fov/279 cells); *ICE2* (n=4 fov/506 cells). The abbreviation fov stands for “field of view” and represents how many images were evaluated next to the number of total cells that were counted within the given fields of view

Motivated by these results and newly gained insights during the observation of various *mga2Δ* strains during their growth dependent aberrant ER formation via live-time microscopy studies, I adapted information of a descriptive study by Delobel *et al.*³⁶⁷. Delobel *et al.* shows that in different growth phases of a batch cultivation, the corresponding cells are grouped in different phases of the cell cycle. I have taken advantage of this observation in order to identify a critical cell cycle stage for *mga2Δ* dependent aberrant ER formation. For that I combined their determined growth phase specific cell cycle stage population distribution with my growth curves for the WT and *mga2Δ* control strains (Figure 34 A). To track the impact of changes in cell cycle stages, I expanded my protocol for assessing the percentage of cells that show an aberrant ER beyond my established timepoint that corresponds to an OD₆₀₀ of 0.8 that marks a timepoint at which the proportion of cells harboring an aberrant ER peak. Out of simplicity I compared the dynamics of aberrant ER formation by taking samples as the OD₆₀₀ doubled during a batch cultivation and analyzed the occurrence of the aberrant ER formation via confocal microscopy (Figure 34 B). It becomes evident that the cells that harbor the aberrant ER tend to cluster i.e., are in direct vicinity to one another (e.g. Figure 34 B – OD₆₀₀ 0.8 in the *mga2Δ* panel). This could imply that a recent mitotic division happened in which these structures emerge and are passed on to the daughter cell. The link between the process of mitosis is in line with the GO terms of the “rescue” category and corresponds well with the data obtained from the overexpression screen, which brought forward strong candidates in relation to cell cycle progression. Another observation is that over time the fraction of cells with an aberrant ER can get lost. In fact, there are practically no cells with an aberrant ER at an OD₆₀₀ of 6.4 visible (Figure 34 B). Intriguingly, this coincided with the time at which the growth rate of *mga2Δ* strain increases substantially (Figure 34 A and B).

Intrigued by the possible impact of the cell cycle and the possible inheritance of aberrant ER structures to daughter cells, I turned my interest to genes that are cell cycle dependent upregulated. I found two independent studies that show a cell cycle dependent upregulation of *OLE1* in the early G1 phase^{368,369}. To verify these findings indirectly, I carried out a qPCR with *OLE1* primers for WT and *mga2Δ* cells before (OD₆₀₀ of 0.4) during (OD₆₀₀ of 0.8) and after (OD₆₀₀ of 3.2) the time, where the highest fraction of cells exhibit an aberrant ER (Figure 34 C). Expectedly, the *OLE1* mRNA level is lower in *mga2Δ* compared to WT cells in all tested growth stages (Figure 34 C). For the WT the level of the *OLE1* mRNA declines over time, which would coincide with the fractional decline in growth phase specific G1-state occupying cells, as described by Delobel *et al.*³⁶⁷. In the *mga2Δ* cells on the other hand the initially already lowered levels of *OLE1* mRNA do not significantly change over the entire course of cultivation. Noteworthy is that the reduction of growth rate for *mga2Δ* cells does not take effect at an OD₆₀₀ of 0.4 (see Figure 19 B for a better resolution), which could mean that the cell phase specific

upregulation of *OLE1* mRNA present in WT cells is Mga2p dependent. In support of this notion, I see at the earliest timepoint i.e. OD₆₀₀ of 0.4, a more than 6 fold relative difference in *OLE1* mRNA level between the WT and *mga2Δ* strain, shortly before the amount of aberrant ER structures peak (OD₆₀₀ of 0.8). Next to the *OLE1* mRNA levels I looked at the spliced *HAC1* mRNA levels to check for a potential additional burden from a UPR-dependent membrane expansion that the *mga2Δ* strain would have to face next to the diminished *OLE1* levels (Figure 34 D). Consistent with previous reports^{56,241,370}, the UPR is highly active in *mga2Δ* cells. In fact, the UPR is active at all chosen timepoints and strikingly the greatest amount of spliced *HAC1* mRNA is found at an OD₆₀₀ of 0.4, shortly before the aberrant ER phenotype manifests the strongest at OD₆₀₀ of 0.8. This finding supports the notion that membrane expansion – either through growth or UPR dependent – could be detrimental to the *mga2Δ* strain, as Surma *et al.* could show that the *mga2Δhac1Δ* strain with a non-functional UPR shows fewer aberrant ER structures compared to the sole *mga2Δ* strain²⁴¹.

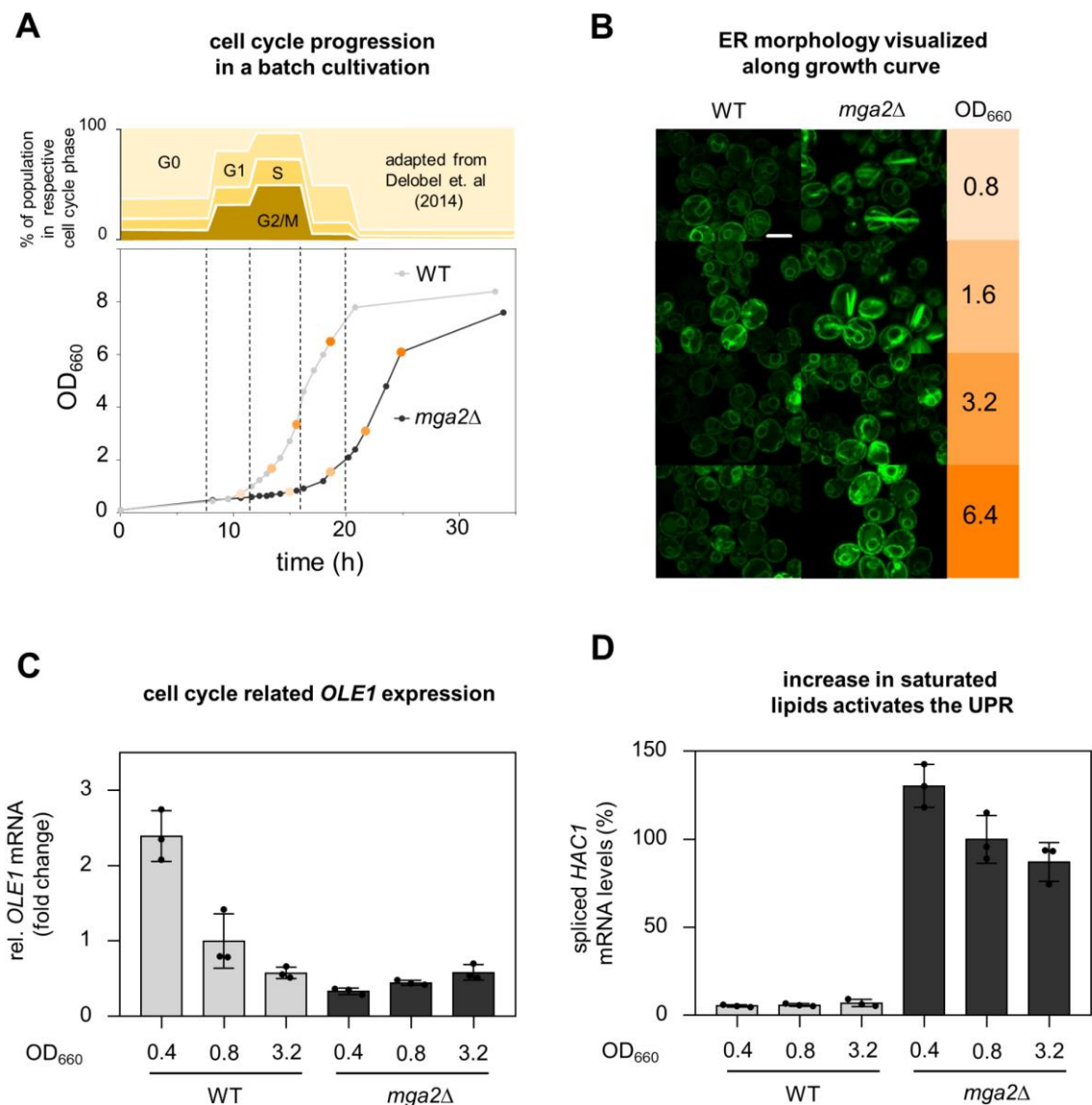


Figure 34 The emergence of the aberrant ER phenotype is dynamic and potentially linked to cell cycle progression during batch cultivation

In **(A)** the cell cycle progression distribution during a WT batch cultivation is schematically indicated by data adapted from Delobel *et al*⁶⁷. Below the schematic a long-time growth curve of a YPD batch cultivation for WT and *mga2Δ* is shown. The dashed lines within the graph are aligned with the growth stages depicted in Delobel *et al* (2014) and the orange shaded data points mark the OD₆₀₀ values depicted in **(B)**. Plotted is the mean \pm SD of $n=3$ for each strain. In **(B)** representative confocal microscopy images of the respective strains are shown at the indicated OD₆₀₀ values. The scalebars represents 5 μ m. In **(C)** the results for a RT-qPCR measurement of *OLE1* cDNA levels are plotted at the indicated OD₆₀₀ values. Plotted is the mean \pm SD of biological triplicates. Data was normalized to WT at OD₆₀₀ of 0.8. In **(D)** the RT-qPCR measurement results for spliced *HAC1* cDNA are plotted for the indicated OD₆₀₀ values. Plotted is the mean \pm SD of biological triplicates. Data was normalized to *mga2Δ* at OD₆₀₀ of 0.8.

4.3.6 Probing the origin of the aberrant ER with a set of distinct localizing subdomain ER-marker proteins

Next, I wanted to further characterize these aberrant ER structures by exploiting the fact that not all ER membrane proteins show an equal distribution between the nuclear and peripheral ER domain. For my characterization I chose Sec63p, a protein that shows no preference for the nuclear or peripheral ER and two additional candidates, Rtn1p as a peripheral ER dominant membrane protein³⁷¹ and Elo3p for a mainly in the nuclear ER situated protein³⁷². All three of these proteins were endogenously tagged with mNeogreen in WT and *mga2Δ* strains and served as marker proteins to study the origin and formation of the aberrant ER. To learn more about the three-dimensional orientation of the aberrant ER representative Z-stack images were recorded (Figure 35). In order to preserve the z-information a color-based depth code was applied in each column, starting at the top and ending with the maximum intensity projection of each stack at the bottom. Comparing the intensity for all three marker proteins in the WT background, it becomes evident that Sec63-mNeogreen is distributed equally between the nuclear and the peripheral ER, while Rtn1-mNeogreen is predominantly localizing to the peripheral ER and Elo3-mNeogreen shows a preference for the nuclear ER. Notably, for Rtn1-mNeogreen a patterned distribution was observed, which differs from the “continuous” signal observed for Sec63-mNeogreen and Elo3-mNeogreen. The distribution for the different marker proteins for the nuclear and peripheral ER described for the WT carries over to the aberrant ER seen in *mga2Δ* cells. While the Rtn1-mNeogreen protein clearly has a preference for the peripheral ER, it does still to a degree reside in the nuclear ER and this faint but yet detectable presence is best documented in the green Rtn1-mNeogreen z-plane for the *mga2Δ* strain (Figure 35). It is further true that Sec63-mNeogreen and Elo3-mNeogreen show a stronger partitioning to the aberrant ER than Rtn1-mNeogreen. The applied approach of using ER-membrane proteins with a distinct preference for the nuclear and peripheral ER thereby adds evidence to the idea that the aberrant ER is related to the nuclear ER subdomain. This potentially hints at a mechanism that is related to the mitotic cell division, as this process is associated with massive nuclear envelope expansion³⁷³, which might be problematic in cells with a disturbed membrane fluidity.

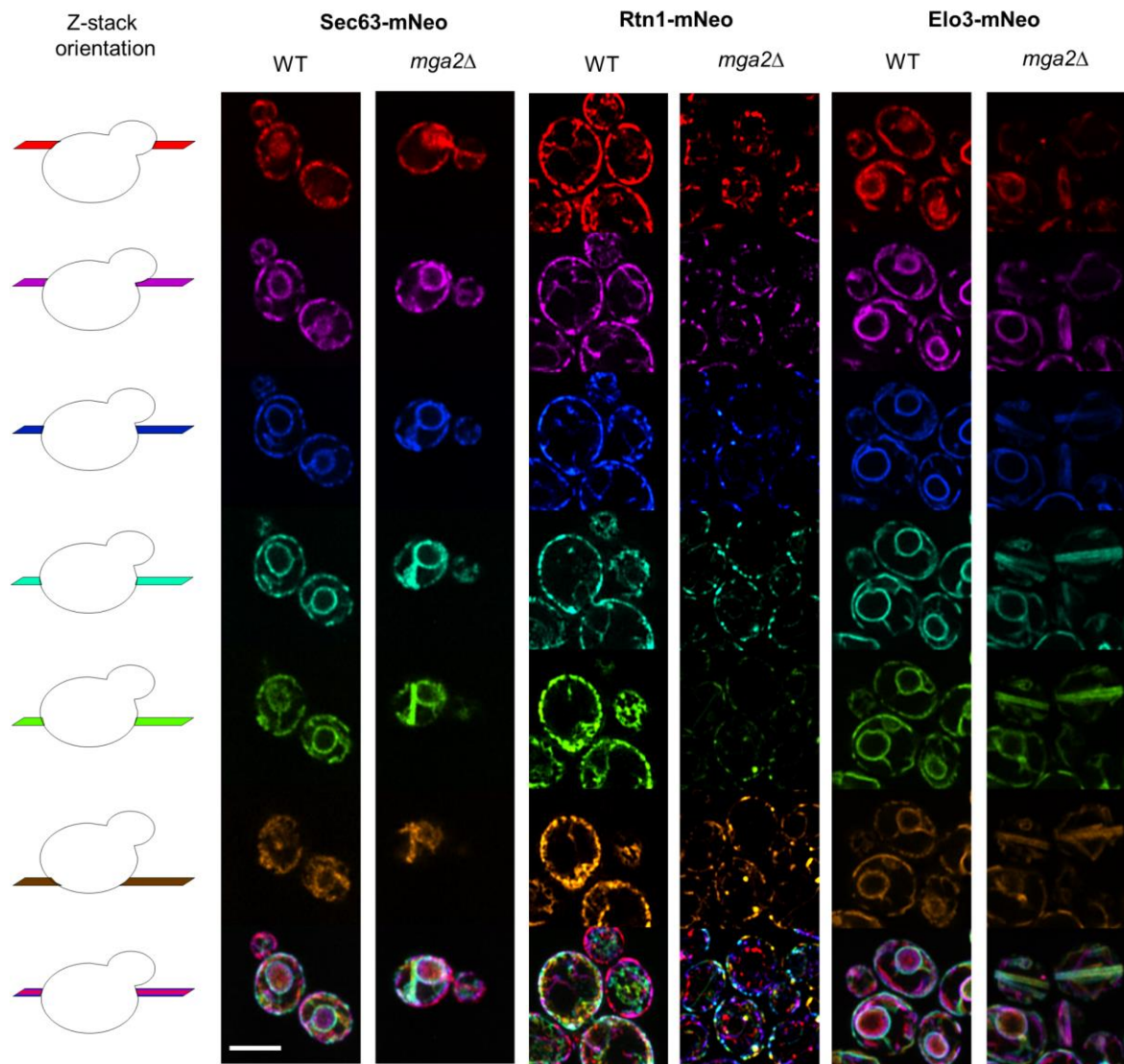


Figure 35 Z-stacks reveal complex 3D orientation of aberrant ER and hint at its nuclear envelope origin

In each column six different z-planes images of a representative z-stack for the indicated strains are shown. The first column is a schematic representation of the origin for each z-plane. The last image in each column represents the maximum intensity projection of each z-plane in its original color to preserve the z-information. The image series in each column was generated with the Z code Stack plugin for FIJI. Scalebar represents 5 μm .

I wanted to find supporting evidence for the assumption that the ER membrane subdomain origin hypothesis is valid. To this end, I introduced a secondary fluorescent ER-luminal marker in the form of a soluble dsRED protein into the existing mNeogreen *mga2Δ* strains by targeting it to the ER lumen via a Kar2p signal sequence and retaining it there by equipping it with an HDEL retrieval sequence. I studied the colocalization of the ER-luminal marker with the Rtn1-mNeogreen, Sec63-mNeogreen and Elo3-mNeogreen. I reasoned that the fluorescent signal of the ER luminal marker should be independent of any ER membrane subdomain and therefore a colocalization between the ER luminal signal and the respective ER-membrane protein should unambiguously reveal if the aberrant ER is derived from a specific subdomain of the ER. In Figure 36 the colocalization data are presented visually in form of an image series for each fluorophore and the respective superimposed image. Further the colocalization was quantitatively determined for three independent cells using the Pearson correlation coefficient. Both approaches imply that the Rtn1-mNeogreen tagged ER resident protein occupies less frequently the aberrant ER structure than Sec63-mNeogreen or Elo3-mNeogreen. Consistent with my findings are the reports made by Zhang *et al.*¹⁹⁹, albeit they published ultrastructures of a temperature sensitive *mga2Δ* and *spt23-ts* mutant, which showed even greater aberrant ER deformations of nuclear origin.

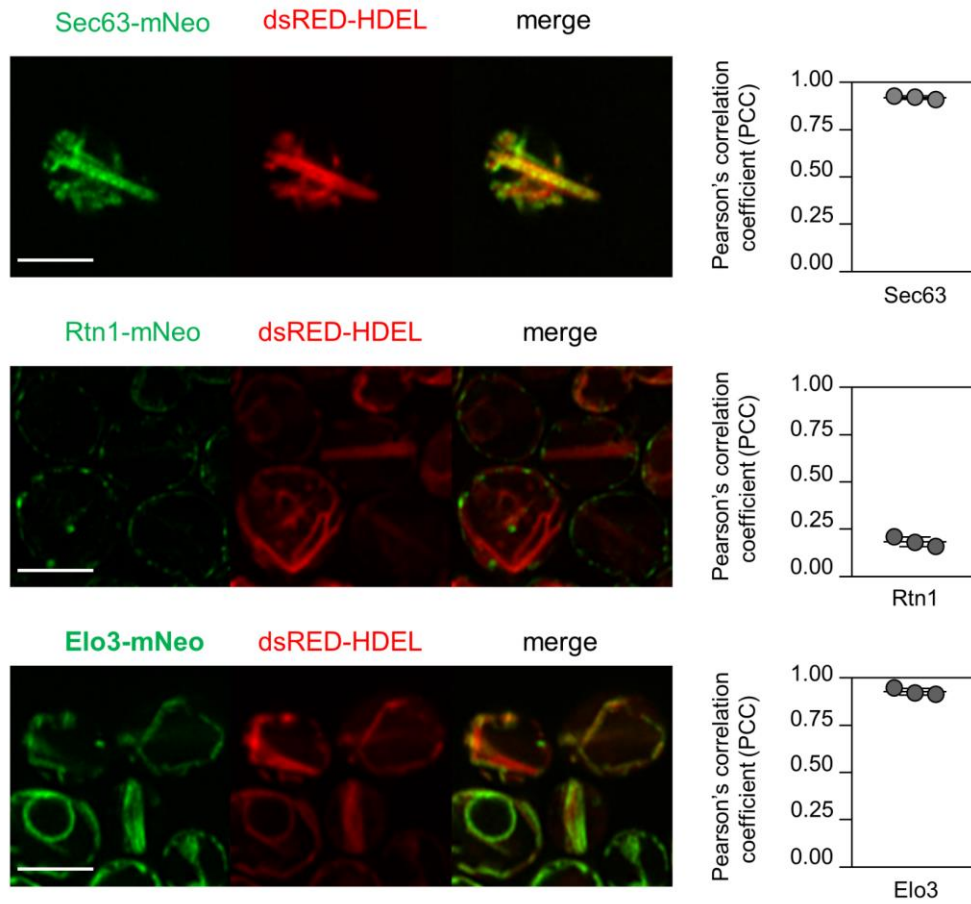


Figure 36 A visual and quantitative colocalization study with a set of distinct localizing ER membrane proteins in *mga2* Δ cells

Each row depicts a representative selection of a focal plane for both fluorophores, the mNeogreen (mNeo) tagged membrane protein and the dsRED-HDEL based ER-luminal marker. Next to the image series are the results of a Pearson correlation coefficient determination plotted for three independent focal planes. Images were prepared with FIJI and co-localization was determined with the JACoP (Just Another Colocalization Plugin). Scalebar represents 5 μ m.

With the conducted image collection at hand further information can be drawn in terms of how the aberrant structures emerge and whether the formation of the aberrant ER will impose a shift in the shared ER subdomains of the affected cell (Figure 37). In the upper panels it is shown that the aberrant ER originates from the nucleus (Figure 37 A) extending from a mother to a daughter cell (Figure 37 B). In the lower panels it can be seen that the Rtn1-mNeongreen clusters decorate the end of the aberrant ER structures (Figure 37 C and D). It will be interesting to learn more about the ultrastructure of the ER in *mga2Δ* cells, the relative abundance of ER tubes and ER sheets and how they are positioned relative to each other. Based on the presented data it is tempting to speculate that the reason for the increased size of Rtn1-mNeongreen clusters (Figure 35 and Figure 37) is a shift in the subdomain prevalence in aberrant ER harboring cells. It will be interesting to see how such a shift in subdomains might affect the oligomerization tendency globally for different ER membrane proteins.

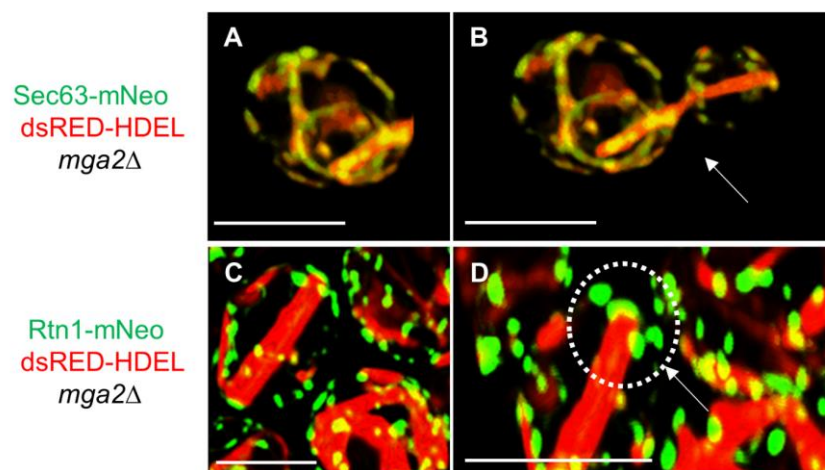


Figure 37 3D rendering of z-stack images of aberrant ER structures reveals the step of inheritance of these structures and gives clues to changes in ER subdomain distribution

The upper panel shows how the aberrant ER originates from the top of the nuclear ER (A) and is passed on to the daughter cell during a mitotic division (B). In the lower panel (C) and the zoomed in image (D) show how Rtn1 was tagged with the fluorophore mNeongreen to label the tubular subdomains of the ER in cells with aberrant structures. Both images show that Rtn1-mNeon is mostly found at the ends of the aberrant ER structures and strongly clusters there, which could in turn allow for the sharp angular changes in direction of the aberrant ER and hint at a change in ER subdomain distribution. All images were subjected to theoretical point spread function processing calculated via the PSF Generator plugin of FIJI. The Born & Wolf 3D optical model was used and supplied with the necessary metadata from the microscopic images. The generated PSF was then used for a deconvolution of the images using the Richardson-Lucy algorithm with 10 iterations (Deconvolution Lab2 plugin in FIJI). All deconvoluted images were subsequently rendered with 3D script in FIJI. Scalebars represent 5 μm .

4.3.7 A putative role for ROS in promoting the formation of aberrant ER structures

While the microscopy approach was useful to gain insights on when the aberrant structures appear I wanted to further characterize why they appear in the first place. Increased lipid saturation has been implicated with mitochondrial aberrances and ROS production^{374,375}. To validate if ROS might contribute to the impaired growth observed in *mga2*Δ cells I carried out a growth based third mini screen to identify possibly interesting additives or genetic interactions that promote or prevent the emergence of aberrant structures. The initial screen was carried out in 96-well plates and used the OD₆₀₀ formed over time as a readout for interesting candidates. An excerpt of the screening data is shown in Figure 38. I plotted the growth curve for the WT, *mga2*Δ and two interesting biologically opposed data sets namely *mga2*Δ with vitamin C supplementation as a radical scavenger and the *mga2*Δ strain combined with the overexpression of the *HAP4* gene, a transcription factor that stimulates mitochondrial biogenesis and whose overexpression triggers ROS production³⁷⁶.

growth screen reveals putative role of ROS in *mga2*Δ vitality

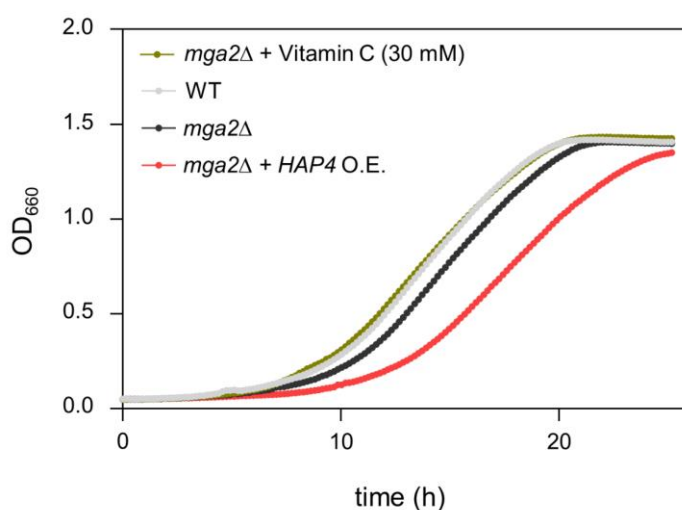


Figure 38 A 96-well plate screening identifies compounds and conditions that promote and inhibit the growth of *mga2*Δ hinting at ROS production as one of the driving forces

Plotted are growth curves measured in a 96-well plate of cells grown for 25 h at 30°C in SCD without shaking. Shown is a selection of conditions that promote (30 mM supplementation of vitamin C) or impede (overexpression of *HAP4*) the growth of *mga2*Δ opposed to the sole *mga2*Δ strain. The WT query strain served as a positive control to score for fully redeeming conditions. Data shown n=1.

To verify if the improved cell growth observed for *mga2Δ* cells supplemented with vitamin C I adapted the screening findings and added an alternative additive in the form of reduced GSH to test the idea whether one can prevent the emergence of aberrant ER structures by providing chemicals that serve as antioxidants. In Figure 39 one can see that by adding vitamin C or reduced GSH to the medium one can prevent the emergence of aberrant ER structures.

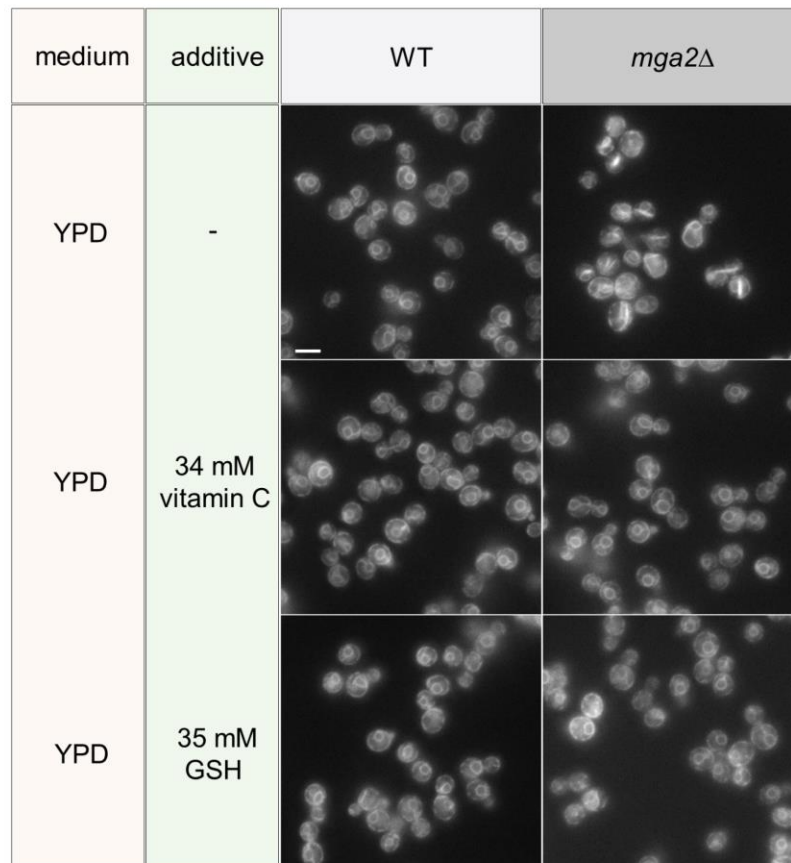


Figure 39 Supplementation of antioxidants to the growth medium prevent the emergence of aberrant ER structures

Depicted are representative microscopic images of the WT and *mga2Δ* query strains grown in YPD with the addition or omission of antioxidant additives in the form of vitamin C or reduced GSH. Scalebar represents 5 μm .

To follow up on the *HAP4* overexpression results I revisited the lipidomic dataset for genome-wide double knockout screening candidates. To gain new insights from my whole cell lipidomic datasets, I focused on cardiolipin species found within these datasets as this could help to identify patterns related to an organelle specific lipid that might help explain the mitochondria related phenotypes (Figure 40 and Figure 41). When plotting all CL species based on their length and degree of saturation one finds that within the *mga2Δ* background no fully saturated CL species are to be found. This is interesting as the whole cell lipidome for the GPL showed an increase of full saturated lipids on the cost of the completely unsaturated GPL (Figure 19 D). Despite the lack of fully saturated CL species, the overall degree of saturation for CL species is elevated for *mga2Δ* and the double knockouts. This data is in agreement with data published by Surma *et al.*, which also did not report on the existence of fully saturated CL species in *mga2Δ* cells²⁴¹. Since ROS scavengers prevent the buildup of the aberrant ER phenotype in *mga2Δ* cells and given CL important role in stabilizing respiratory chain complexes³⁷⁷ and mitochondrial cristae formation³⁷⁸ it is surprising that the genes *TAZ1* and *CLD1* that encode for the two most important CL remodeling enzymes did not show up as hits in the genome-wide screen³⁷⁹.

whole cell lipidomics – cardiolipin (CL) species overview

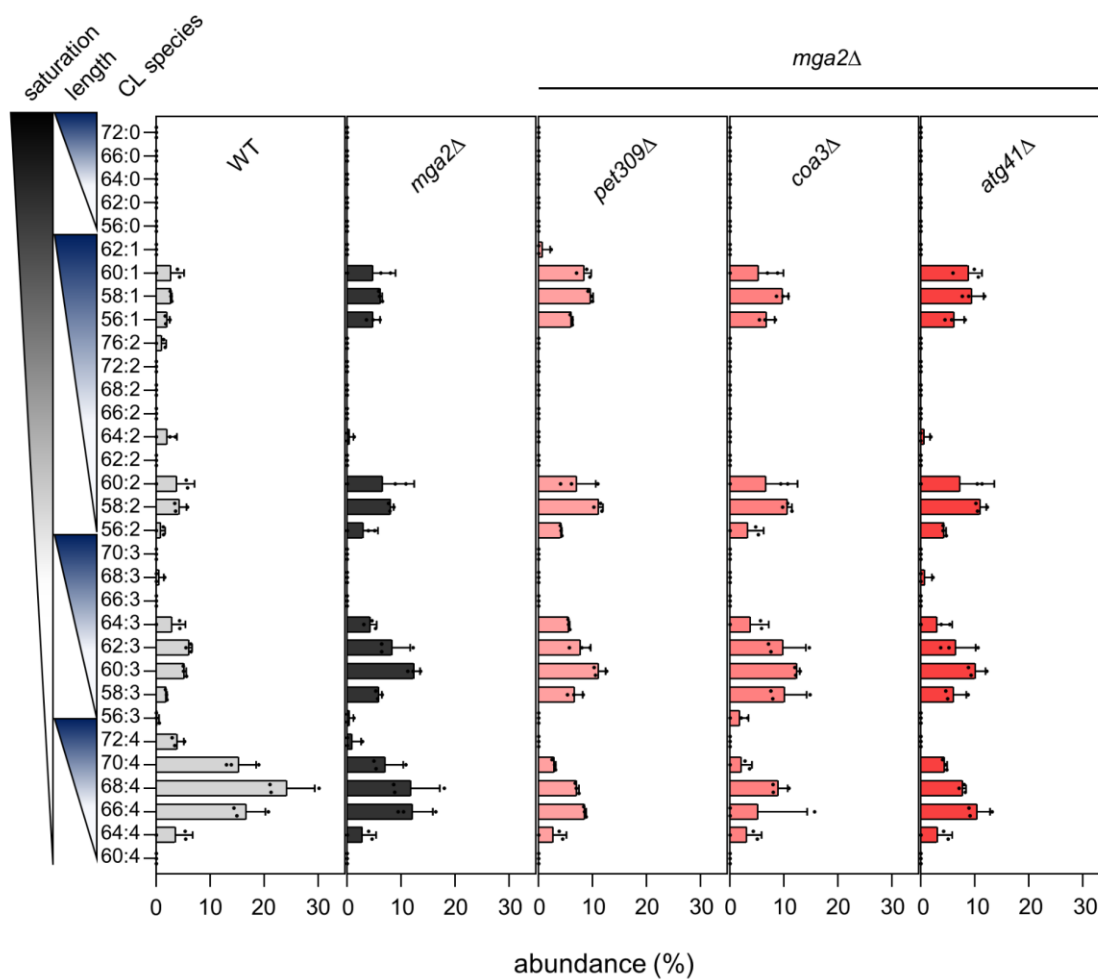


Figure 40 CL species distribution of all worse candidates from the genome wide screen in comparison to those of the WT and *mga2Δ* query strains

Plotted is the abundance (%) of all CL species having 0-4 double bonds (saturation) according to their total amount of carbon atoms (length). Plotted data is taken out of the whole cell lipidomics dataset for each depicted strain and represents that of biological triplicates. Data is shown as the average \pm SD.

whole cell lipidomics – cardiolipin (CL) species overview

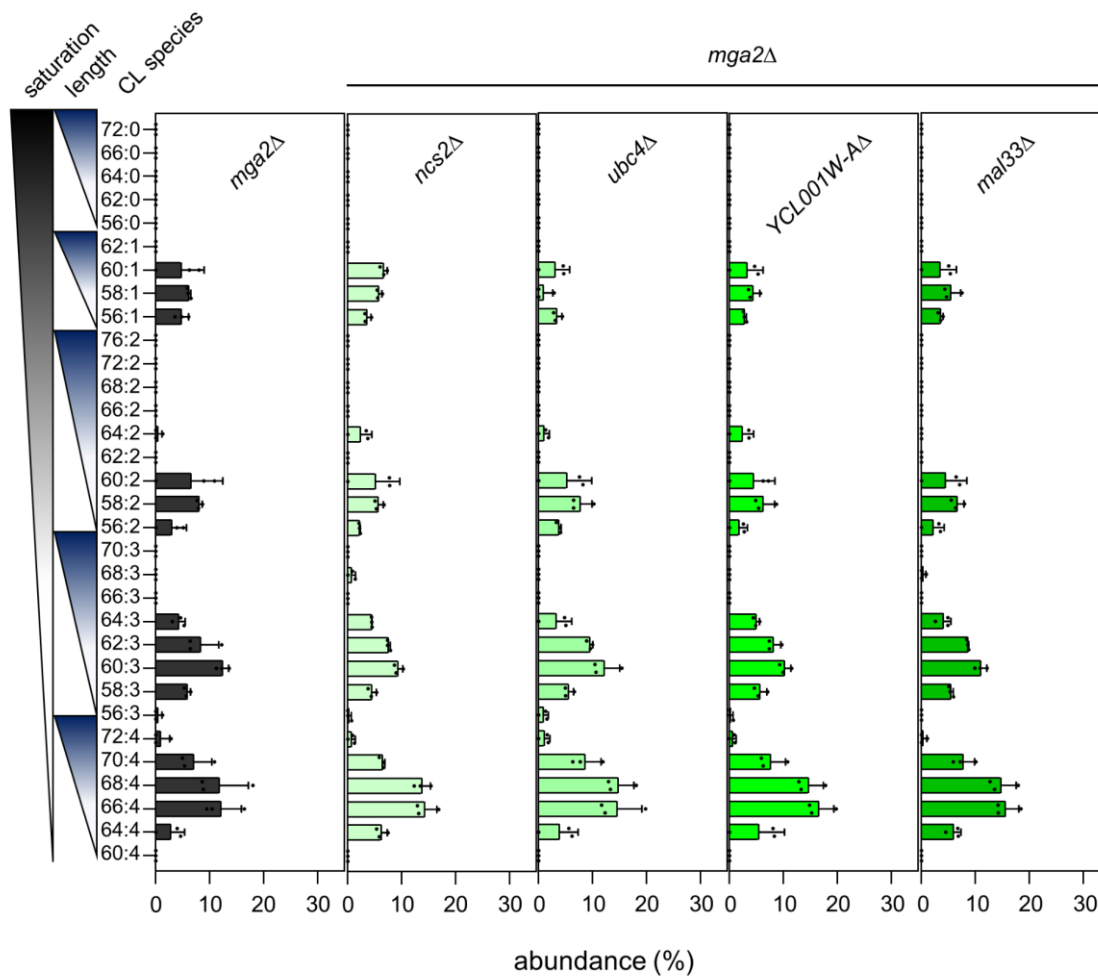


Figure 41 CL species distribution of all rescue candidates from the genome wide screen in comparison the *mga2* Δ query strain

Plotted is the abundance (%) of all CL species having 0-4 double bonds (saturation) according to their total amount of carbon atoms (length). Plotted data is taken out of the whole cell lipidomics dataset for each depicted strain and represents that of biological triplicates. Data is shown as the average \pm SD.

5 Discussion

5.1 The UPR has little to no effect on remodeling of the lipidome within one hour of acute ER-stress

The ER is most known for its role as the protein-folding organelle of the cell. It further houses most enzymes involved in lipid synthesis and acts as the central regulator for the *de novo* synthesis of lipids¹³⁵. To ensure the functionality of this vital organelle, a series of sensors have evolved that monitor different perturbations that could infringe the homeostasis of lipid and protein synthesis⁴⁷. So called ER-stress will invoke a highly conserved pathway, termed the UPR, which in yeast is solely induced by Ire1p, the most conserved UPR sensor among eukaryotes³⁸⁰. In the first section, I established experimental conditions to study this stress response under defined conditions that allow to differentiate between a protein- or lipid-based cause for the activation of the UPR. This pathway has often been studied by exposing cells to drugs that interfere with the folding of proteins. DTT and TM are prominent drugs that differ in their molecular mechanism of action and their impact on the lipidome has never been systematically studied before.

5.1.1 The impact of DTT and TM on the cellular growth of *S. cerevisiae*

To best compare the effect of these drugs, I searched for concentrations that would cause a similar degree of growth inhibition (Figure 7). Interestingly, the dose-response-curves of DTT and TM varied dependent on the medium. Why the cellular resistance to DTT is higher in YPD than in SCD is not clear. DTT is prone to oxidization and it is possible that the complex YPD medium is more effective in oxidizing DTT. Hence, it would be interesting to study the “effective” dose of DTT delivery to the ER by applying a recently published ER-DTT probe that reports on the presence of DTT within the ER³⁸¹. Intriguingly, cells are more resistant to TM in SCD medium than in YPD medium. Other than DTT, TM is not readily inhibited by the medium and it efficiently blocks the N-linked glycosylation machinery for a period of at least eight hours after application as shown by Chawla *et al.*⁸⁶. The impairment of cellular growth by both drugs becomes apparent 1 hour after drug application. This growth arrest is however more pronounced for DTT than for TM under all tested concentrations and media (Figure 8 and Figure 9). The fact that DTT caused an increase in unfolded proteins by interfering with disulfide bond formation within the ER lumen of newly and already existing proteins, might render it more potent. It was further shown that DTT interferes with cellular processes outside

of the ER, e.g. mitochondrial protein import³⁸² and protein palmitoylation³⁸³. TM, on the other hand, interferes only with the N-linked glycosylation of newly synthesized proteins. which would explain why the growth arrest takes longer to take effect. One also has to consider the different doubling times in each medium (86 min in YPD; and 107 min in SCD) to explain the differences in drug potencies in relation to the cultivation medium used. This would help to understand why lower doses of TM are sufficient when cells are grown in YPD as their demand for protein synthesis is greater than during growth in SCD medium.

5.1.2 Impact of the medium on the lipid composition under ER-stress

Unexpectedly, unstressed WT and *ire1Δ* cells do not show any significant changes in their lipidomes for both types of media tested (Figure 10 and Figure 11). This implies that basal UPR signaling does not alter the cellular lipid composition in unstressed conditions^{384–386}. It is, however, noteworthy that PI is far more abundant in cells grown in YPD compared to cells grown in SCD. This difference is relevant for studying the UPR as *IRE1* was identified to encode the inositol-requiring enzyme²²². It was further shown that the UPR can be evoked by inositol-depletion⁵⁶ hence special precautions should be taken when working with SCD as inositol availability in the standard SCD media formulation is a limiting factor for the BY4741 series as reported by Hanscho *et al.*²²¹. Next to the PI difference, the PC-to-PE ratio was found to be unbalanced for cells grown in YPD (Figure 12), which is actively discussed as a cause and hallmark of UPR activation in multiple organisms including yeast^{223–225}. A deficiency of PC is known to cause the UPR and is commonly studied by cultivating *cho2Δ* or *opi3Δ* cells in choline free medium that can no longer sequentially methylate PE to form PC or synthesize PC via the Kennedy pathway³⁸⁷. The increased PC-to-PE ratio is controversially discussed in the field and Ishiwata-Kimata brought forward convincing data, which suggests that the increased PC-to-PE ratio in it of itself is not the driving force but the accumulation of a lipotoxic intermediate namely phosphatidylmonomethylethanolamine (PMME) as a precursor for PC synthesis³⁸⁸. In their study they could show that in presence of extracellularly supplemented choline only the *opi3Δ* mutant but not the *cho2Δ* or *cho2Δopi3Δ* double mutant showed an activation of the UPR. Given that the UPR was compromised by the introduction of the *cho2Δ* into *opi3Δ* cells, and based on the finding that *CHO2* overexpression induced the UPR, Ishiwata-Kimata *et al.* argue that PMME is *per se* a UPR inducing metabolite. Hence, they propose that the UPR stress associated with the PC biosynthesis pathway is either rooted in a PC deficiency, the accumulation of PMME or both but not via an increased PC-to-PE ratio³⁸⁸. This data is further supported by findings from Reinhard *et al.* that could show that an

increased PC-to-PE ratio achieved by supplementing choline to the medium did not trigger the UPR by itself¹⁰⁸. Most importantly, I could show that DTT and TM at growth-inhibitory concentrations have only neglectable effects on the cellular lipidome within 1 hour of cultivation in SCD medium (Figure 11). Together with the fact that the determined 8 mM concentration of DTT in YPD had the most profound impact on remodeling the lipidome of the yeast cell (Figure 10), I propose to use TM at the here tested concentrations for 1 hour in SCD to achieve a purely proteotoxic based UPR induction. The here presented experimental outlines highlight the importance of carefully controlling the medium composition and drug concentration to dissect the contribution of unfolded protein and membrane aberrancies in UPR activation. Since the UPR can be activated by folding aberrancies and lipid bilayer stress, it is important to not ignore the contribution of each of these contributing factors to unambiguously differentiate between cause and effect of the underlying ER-stress.

5.2 Consequences of a maintained TMD architecture of Ire1p dimer under proteotoxic and lipid bilayer stress

The UPR has central functions in adjusting the protein folding capacity but it also has an important role in upregulating *de novo* lipid biosynthesis⁴⁷. More recently, it became also apparent that the UPR is not only activated by unfolded proteins or signals from the protein folding machinery, but also from the membrane through LBS^{87,88,241,389}. While the beginnings of UPR research were embossed by a binary view on activation via protein folding aberrancies and signaling outputs to resolve said aberrancies, the field has adjusted and accepts the interplay between the constant physiological demands towards the ER to maintain proteostasis and lipid homeostasis³⁹⁰. The second section of this thesis aimed to shed light on the structural organization of the transmembrane region of Ire1p in a signaling-active state.

5.2.1 Single-cysteine crosslinking and its potential on completing insights into the structural organization of single-spanning transmembrane proteins

Previous structural work dedicated to understand the architectural arrangement in signaling - active states of Ire1p were based on X-ray crystallography studies of the ER-luminal domains⁷³, i.e. the sensory domain governing homeostasis in the ER lumen, and the cytosolic effector domain that bears the enzymatic activity necessary to relay the signal from the ER to the nucleus⁷⁴. While these X-ray crystallography-based studies revealed information about the three-dimensional structure of Ire1p, these data came with limitations. For one, both structures do not pass the near-atomic resolution criteria, with their respective resolution of 3.0 Å for the ER-luminal domain⁷³ and 3.2 Å for the cytosolic oligomeric domains⁷⁴. Secondly the structures are afflicted with uncertainties as they mirror the structure of a crystalline protein sample and therefore do not reflect the dynamic nature of Ire1p conformational states³⁹¹. This limitation becomes apparent in light of the discrepancy between the predicted direct peptide binding capacity of yeast and human Ire1p ER-luminal domain. The crystal structure of the yeast ER-luminal domain revealed a peptide-binding groove that extends across the dimer, which resembled the peptide-binding groove of the major histocompatibility complex⁷³. This finding was supported by *in vivo* data and *in vitro* binding studies conducted with carboxypeptidase Y*, a mutant model for a misfolded protein^{81,392}. The direct binding model could not be extended to the human Ire1p ER-luminal domain, as its corresponding peptide-binding groove revealed through its crystal structure was considered to be too narrow to accommodate the

binding of peptides⁷⁹. Karagöz *et al.* argued that the crystal structure of the human Ire1p ER-luminal domain represents the “closed” form of the protein and that *in vivo* the human Ire1p ER-luminal domain oscillates between an inactive “closed” and an active “open” form which would allow for a direct peptide binding³⁹³. To validate this assumption, an NMR based method, called methyl transverse relaxation optimized spectroscopy was employed to show that the structure of the human Ire1p ER-luminal domain is indeed dynamic. They followed up with peptide tiling array experiments that demonstrated that the human ER-luminal domain of Ire1p could indeed bind peptides enriched in cysteine, tryptophan, tyrosine and arginine³⁹³. Consequently, the peptide binding would induce a conformational change that can promote oligomerization and subsequently promote trans-autophosphorylation of the cytosolic domains to initiate the activation of the RNase domain. To add to the structural image of Ire1p, a single-cysteine crosslinking strategy was employed that has been used successfully in the past to study the transmembrane helix orientation of the human growth receptor JAK2³⁹⁴. The study conducted by Brooks *et al.* derived a parallel helix pair orientation for the dimer in its inactive form based on a helical periodicity of the crosslinks³⁹⁴. In a series of follow-up experiments that included molecular dynamic simulations the authors were able to show that the transmembrane helices will take on a left-handed crossover arrangement after ligand-induced activation of the JAK2 receptor³⁹⁴. The inferred model of the JAK2 receptor thereby demonstrates the potential of single-cysteine crosslinking studies within the TMD of single-pass transmembrane proteins to gain insights into subdomain rearrangements for distinct signaling states. The crosslinking data for Ire1p under ER-stress disfavors a parallel association of its TMHs as the highest degree of crosslinking occurred predominantly at position F544. Instead, the dominant single residue crosslinking pattern suggests, aided by molecular dynamics simulations that neighboring TMHs in clusters of Ire1p take on an X-shaped active signaling conformation (Figure 17). The derived model of this transmembrane organization supports the previously postulated molecular mechanism of Ire1’s unusual TMD in sensing bulk membrane properties via a hydrophobic mismatch-based mechanism⁸⁷. The positively charged residues situated at the cytosolic end of the TMH and the previously identified AH of Ire1p will jointly contribute to the local membrane deformation. This compression comes with an energetic cost due to lipid acyl chain disordering and the present membrane thickness^{231,232}. The increased energetic costs would therefore act as a driving force for monomeric Ire1p to coalesce its compressed region and thereby promote Ire1p dimerization. Noteworthy for the following discussion is that while the F544 residue is at the intersection of two neighboring TMHs where the membrane deformation is most severe, it does not contribute to maximizing the interaction interface to confer protein-protein stability, as shown by a disruptive mutation by Vãth *et al.*. Instead, stabilization of the signaling-active state is conferred by the overall transmembrane architecture with the membrane-embedded

AH and not by specific residues of the TMH. Hence, the single-cysteine crosslinking approach proved to be vital to substantiate the previously theoretical hydrophobic mismatch model, which was restricted to the monomeric TMD of Ire1p, with structural data in context of dimerization.

5.2.2 Attempting to understand the membrane-based source of ER-stress under prolonged ER-stress inducing conditions

The study of the UPR under proteotoxic or LBS based conditions play out on different time scales. ER-stress from misfolded proteins, either induced by DTT or TM peaks within 30 min to 1 h after application^{56,87,395}. LBS on the other hand takes more time to manifest itself and usually takes 3 h, in case of inositol depletion, or longer (~12 h) as demonstrated for ER-stress related to the PC biosynthesis pathway to fully establish a comparable level of ER-stress^{56,88,206,396}. Interestingly, work by Promlek *et al.*³⁹⁷ and the time course qPCR experiments in Figure 18 demonstrate that proteotoxic stress comes in two forms, an immediate stress in der ER lumen through accumulation of unfolded proteins and a secondary phase of UPR activation from a build-up of a membrane-based stress. It is argued that the secondary phase of UPR activation under DTT exposure happens in absence of misfolded proteins and originates from the membrane as a mutant impaired in the sensing of unfolded proteins, called Δ III-Ire1p, shows an identical activation profile under inositol depletion and for the secondary phase of DTT exposure while it does not react to the acute stress within the first hour of DTT application⁵⁶. The molecular underpinnings of the secondary peak in UPR activation under prolonged proteotoxic stress remain to this day elusive. In a recently published review article Radanović *et al.* lists a number of potential causes that could trigger the UPR via a membrane-based mechanism as a consequence of prolonged ER-stress⁴⁷.

I want to point out three possible scenarios mentioned in this review as they are relevant for the findings made in this thesis. Firstly, an increase in the degree of lipid saturation in membrane lipids is indicated by multiple studies to be a driver of UPR activation^{55,241,370,398}. It was further shown that sterols act synergistically with saturated fatty acids in promoting UPR activation⁵⁵. Elevated sterol levels, an increased degree of lipid saturation or a combination of both directly influence membrane stiffness and as a consequence interfere with transmembrane insertion demonstrated by *in vitro* studies with artificial liposomes or microsomes of the mammalian ER^{399–401}. The increased levels of saturated lipids for instance will promote van-der-Waals interactions between the fully saturated acyl chains and can thereby interfere with the structural integrity of the ER by inducing phase transitions^{402,403}.

Shen *et al.* reported that palmitate feedings can induce solid-like domains within the ER membrane⁴⁰³. Solid like domains are generally thicker and more ordered due to the previously mentioned arrangement of membrane glycerophospholipids and this change in thickness and increased packing density might be especially harmful to the ER, as it is under physiological conditions a “soft” membrane, highly enriched in unsaturated fatty acyl chains¹⁰⁸. The benefit of a “soft” and deformable ER membrane would be that such a lipid environment could accommodate the broad spectrum of transmembrane client proteins of the secretory pathway, as these membrane proteins differ substantially in their mean hydrophobic length of their respective transmembrane domains depending on their final subcellular destination. For ER transmembrane helices Radanovic *et al.* predict an average length of ~21 hydrophobic residues, while transmembrane proteins with an annotated plasma membrane localization have on average a length of ~27 hydrophobic residues⁴⁷. An accumulation of plasma membrane proteins in the ER would therefore contribute to a thickness increase of the ER membrane. Further, a growing number of translocase studies point towards the biological necessity of the ER to regulate its membrane thickness⁴⁰⁴. The Hrd1 complex for instance, responsible for the retro-translocation of misfolded proteins from the ER lumen into the cytosol, requires next to luminal and cytosolic hydrophilic cavities a locally thinned and distorted membrane environment to mediate efficient retro-translocation⁴⁰⁵.

The second scenario for UPR activation that might synergistically contribute to the stiffening and thickening of the membrane is an elevated protein-to-lipid ratio within the ER membrane^{406–408}. Protein trafficking between the ER and the Golgi apparatus is mediated via components of coat protein complex I (COPI) and coat protein complex II (COPII) coated vesicles⁴⁰⁹. The export (anterograde transport) of ER membrane proteins from the ER to the Golgi apparatus is facilitated by recruiting COPII proteins with the respective cargo to specialized regions called ER exit sites (ERES), while proteins that travel back to the ER (retrograde transport) are shuttled in COPI coated vesicles and arrive at ER arrival sites (ERAS)⁴⁰⁹. It has been shown that the collapse of either transport route - either by deletion of genes that encode for crucial components of the COPI or COPII system or by pharmacological interference- will cause an activation of the UPR^{370,410,411}. Amodio *et al.* could show that treating cells with thapsigargin (TG), a non-competitive inhibitor of the sarco/endoplasmic reticulum Ca²⁺ ATPase involved in maintaining calcium homeostasis of the ER, will decrease the number of ERES, hinting at a compromised anterograde trafficking⁴¹¹. In a second study, Amodio *et al.* demonstrated that both TG and DTT lead to a decrease in COPII components (Sar1a/b, Sec31a, and Sec23a) associated with intracellular membranes and, consequently, to decreased COPII vesicle formation⁴¹⁰. In yeast, the anterograde transport of proteins has been shown to be disturbed in the *erv14Δ* strain, a mutant that causes a delay in the transport

of membrane proteins with long TMDs from the ER to the Golgi, which concomitantly evoked the UPR^{370,412,413}. Likewise, interfering with the retrograde transport by blocking COPI vesicle formation through Brefeldin A will result in the disassembly of the Golgi apparatus⁴¹⁴, prevent secretion and trigger the UPR⁴¹⁵. These studies imply that an overcrowding of the ER membrane is sufficient to mount a UPR. Noteworthy would be that an increase in the protein-to-lipid ratio under restraint vesicular trafficking conditions would be exacerbated by the fact that proteins require a functional anterograde transport to leave the ER while lipids can leave the ER via alternative routes e.g. through lipid transport proteins⁴¹⁶. However, it is still a matter of active debate whether the UPR will contribute to a shift in the protein-to-lipid ratio and *per se* cause a retention of proteins in the ER or whether the observed reduced numbers of ERES are a side effect of the stress-inducing agents used to trigger the UPR in the first place. The results in the study by Amodio *et al.* relied on UPR activation via TG, a drug known to cause the depletion of ER luminal calcium, a state which was *per se* shown to inhibit ER-to-Golgi transport without the activation of the UPR⁴¹⁷. In a study by Kitai *et al.* it was shown that ER-to-Golgi trafficking is not disturbed in HeLa cells when the UPR is triggered via palmitic acid treatment or SCD1 knockdown⁴¹⁸. Kitai *et al.* used the temperature-sensitive vesicular stomatitis viral G protein mutant tagged with GFP to monitor ER-to-Golgi trafficking. At 39 °C the protein is misfolded and retained within the ER, but can be readily released into the juxtannuclear Golgi complex in a COPII dependent way by applying a temperature shift to 32 °C^{419,420}. The UPR may even enhance the ER-to-Golgi transport, as suggested in a study by Farhan *et al.* It was shown that under conditions of chronic cargo overload, an Ire1p-mediated UPR is essential for the formation of new ERES⁴²¹. A study by Spear and Ng showed that overexpression of misfolded carboxypeptidase Y induced ER-stress and the UPR but did not interfere with the ER-to-Golgi transport of various cargo proteins⁴²². Interestingly, overexpression of carboxypeptidase Y was in relation to the expression level lethal in *ire1Δ* cells and caused a severe inhibition of the anterograde transport under none lethal conditions, which implies that a functional UPR is essential to support the ER-to-Golgi trafficking in times of greater demand for a secretory capacity. Given the fact that professional secretory cells, such as plasma cells or β -cells, exhibit a constitutively active UPR to maintain their upregulated protein processing machinery in support of the constant synthesis and secretion of larger protein amounts, it is reasonable to assume that under physiological conditions the UPR contributes positively to the ER-to-Golgi trafficking⁴²³. This is in line with upregulated UPR target genes associated with vesicular trafficking in both directions⁵⁷. A study by Reinhard *et al.* reports a general block of secretion for cells exposed to DTT or TM for 4 h, but since it relies on a pharmacologically induction of the UPR it makes it difficult to unambiguously tell if the UPR *per se* is causing the retention of proteins in the ER or if the inhibitory effects

are due to the stress-inducing agents as they might specifically impair the generation of transport-competent-proteins inside of the ER.

The third scenario deals with a decrease in anionic lipids as a driver of UPR activation. The depletion of inositol marks the first treatment of a lipid metabolite related UPR activation²²². It apparently does so without causing a significant increase in the amount of unfolded proteins in the lumen of the ER^{56,233}. This was demonstrated indirectly by FRAP studies that monitored the diffusion of the fluorescently labeled ER-luminal chaperone Kar2p under inositol-depleting conditions and proteotoxic ER-stress²³³. The study showed that only under proteotoxic forms of ER-stress the mobility of the GFP tagged Kar2p is slowed down due to interactions with unfolded proteins, while its mobility remained unaffected under inositol-depletion²³³. Inositol serves as a building block for PI but is also necessary for the *de novo* synthesis of yeast-specific complex sphingolipids⁹¹. All inositol-depletion based protocols that measure the UPR, involve the immediate removal of inositol in the medium of fast-growing cells in the exponential growth phase by thoroughly washing the cells with inositol free medium^{56,88,206,233}. Interestingly, the existence of a lateral diffusion barrier is described for *S. cerevisiae* that involves the arrangement of sphingolipid containing domains, protein ring assemblies and morphological changes during cell division in the anaphase between the nuclear lobes of the mother and daughter cells^{424,425}. One biological function of this diffusion barrier is to confine misfolded proteins of the ER in the mother cell, thereby shielding the daughter cell from potentially harmful misfolded proteins. Interestingly, inositol depletion does not result in a significant decrease in complex sphingolipids of the ER, as reported by Reinhard *et al.*¹⁰⁸ thereby allowing cells to continue with the formation of the diffusion barrier during mitosis, which is in line with the previously reported absence of misfolded proteins under inositol-depleting conditions.

Reinhard *et al.* isolated the ER membrane of unstressed, inositol-depleted and DTT or TM stressed cells and used the highly purified isolates for quantitative proteomics and lipidomics analysis¹⁰⁸. Their data shows for the lipid composition that all forms of ER-stress, either triggered by inositol depletion or via the accumulation of unfolded proteins by DTT or TM exposure, will result in an increased degree of lipid saturation and a decrease in anionic lipids. Further, the proteome of the ER-stressed cells differs greatly from that of unstressed cells in that an ER-stressed proteome shows an accumulation of proteins involved in various biological pathways and function such as ER-luminal chaperones and UPR target proteins (e.g. Kar2p), lipid metabolic enzymes (e.g. Ino1p), components involved in membrane trafficking (e.g. Emp46p) and proteins involved in cell wall synthesis (e.g. Exg1p)¹⁰⁸. The study thereby supports how the previously described scenarios i.e. an increase in lipid saturation, an overcrowding of the ER and a reduced level of anionic lipids and thereby a potentially

lowered negative surface charge density of the ER membrane might jointly contribute to a membrane-based activation of the UPR under conditions of prolonged ER-stress.

5.2.3 Utilizing interface mutants to investigate the contribution of Ire1p's X-shaped signaling-active configuration under acute and prolonged scenarios of ER-stress

Given that the X-shaped configuration of Ire1p's TMHs showed irrespective of the applied form of ER-stress I wanted to study how the X-shaped configuration might contribute to UPR signaling under acute and prolonged scenarios of ER-stress. Answering this question could help to understand how different causes of ER-stress may establish different UPR associated transcriptional programs as recently reported in a study by Ho *et al.*⁸⁸. A possible explanation for the customization of the UPR program may lay in the temporal activation and distribution of dimeric and oligomeric signaling assemblies under the respective forms of ER-stress. The state of oligomerization of Ire1p can be assessed in yeast and mammalian cells by measuring how a fraction of fluorescently tagged Ire1p transitions from its reticulated distribution within the ER in absence of ER-stress into discrete foci or cluster under various forms of ER-stress^{81,204,426}. These clusters are highly dynamic and are subjected to change in form and size over the time course of ER-stress⁴²⁷⁻⁴²⁹. Tran *et al.* could show that under proteotoxic stress clusters of mammalian Ire1p are formed and maintained by two distinct populations of Ire1p: A small fraction of Ire1p that is dispersed in the ER membrane and a larger fraction found in high-oligomeric assemblies⁴²⁹. The latter fraction is found in a specialized ER subdomains whose morphological organization contributes to diffusional constrains of Ire1p found in the core of the clusters⁴²⁸. The subdomains that are enriched in Ire1p appear as a network of narrow (~ 28 nm diameter), anastomosing ER tubes devoid of ribosomes. These subdomains are still in contact with the surrounding ER, which allows for an exchange of Ire1p molecules situated at the peripheries of the subdomains where they merge with the remaining ER, while Ire1p molecules that are positioned further from the subdomain periphery maintain "entrapped" until the clusters are resolved. The authors of this study propose that the confinement of Ire1p in the subdomain will contribute to UPR signaling. For one the subdomain membrane topology will cause an increase in the effective concentration of misfolded proteins in the locally reduced volume of the ER-lumen. Ire1p would thus over time become enriched in these structures by stabilizing the dimer and higher oligomeric state through direct binding of misfolded proteins via the peptide-binding groove. Once locked in the activated state, the helical assembly of higher oligomers and the complex subdomain membrane topology will

reduce the diffusional freedom and therefore contribute to higher oligomeric state stabilization⁴²⁹. A common conception based on the numerous studies on UPR signaling is that the monomer-to-dimer transition serves as the main regulatory activation step for Ire1p and naturally precedes the formation of higher-oligomeric assemblies that exhibit the greatest enzymatic activity^{74,430}. This view is supported by extensive mutagenesis studies of interfaces that facilitate dimer and higher oligomeric states of Ire1p that, when interrupted, were shown to impair UPR signaling, causing cells to become more susceptible to ER-stress^{87,393,430,431}. A recent study by Belyy *et al.* proposes that Ire1p naturally exists to a certain degree as a dimer in the inactive state and that even small oligomers are sufficient for UPR signaling⁴³². How come it is then well-established that clustering of Ire1p i.e. the formation of higher oligomers occurs after ER stressing events?^{87,88,397}. Belyy *et al.* developed and used a single-molecule tracking approach to dissect the state of oligomerization. Given that single molecules, dimers and smaller oligomers can not be resolved with conventional microscopy techniques such as confocal microscopy even when combined with subsequent deconvolution, the assumption that the monomer-to-dimer formation might be the main regulatory step in UPR signaling may be misguided. Most conditions of LBS show reduced levels of oligomerization of Ire1p, for the mammalian as well as for the yeast model system, despite showing similar levels of *XBP1/HAC1* mRNA splicing compared to the acute stress phase caused via an accumulation of unfolded proteins in the ER lumen^{2,88,418,433}. Kitai *et al.* demonstrated that an increase in membrane lipid saturation in HeLa cells leads to an equally strong activation of the UPR, as measured by the amount of spliced *XBP1* mRNA formed, compared to cells treated with TM but without facilitating the clustering of the mammalian Ire1p, which only occurred under the proteotoxic form of ER-stress induced by TM⁴¹⁸. Kitai *et al.* postulate that the mammalian Ire1p can be activated by LBS without the formation of larger Ire1p clusters and that the dimer conformation is sufficient to promote RNase activity. How can this discrepancy be explained? Most studies in the field of the UPR relied on the poorly controllable exogenous overexpression of fluorescently-labeled Ire1p, which given the oligomerization-based mechanism of activation might have introduced a bias since the physiological copy numbers of Ire1p are considered low (~259 molecules/cell based on YeastGFP database). Indeed, a study by Belyy *et al.* showed that the mammalian Ire1p, when expressed at endogenous levels, is activated by reversible assembly of inactive dimers into smaller oligomeric states that no longer show as clusters under proteotoxic stress⁴³². Their model for Ire1p activation proposes that in absence of ER-stress Ire1p is pre-assembled in an inactive unphosphorylated state via the IF1 of the ER-luminal domain. Such a conformation would establish the peptide binding groove in the ER-lumen and align the kinase domains of the dimer in a back-to-back orientation, preventing auto-phosphorylation²³⁴. Under ER-stress short lived reversible assemblies of two dimers via the ER-luminal IF2 would place the adjacent dimers in a face-

to-face orientation and promote partial trans-autophosphorylation of one of the dimers. By repeating this cycle of dimer-dimer interactions a fully phosphorylated Ire1p dimer can emerge with a fully active RNase activity without the need of forming assemblies larger than tetramers i.e. dimers of dimers, which would help to explain why some studies have observed equally high levels of splicing in absence of clusters (most studies used basic confocal microscopy – they thereby can not resolve the monomeric, dimeric or tetrameric assembly states and only visualize larger oligomers). Given that the dimer-dimer interaction can happen also simultaneously i.e. multiple dimers are assembled into higher oligomers, for instance in the specific ER subdomain reported by Tran *et al.*⁴²⁹, this model would help to understand the discrepancies between present studies on Ire1p's tendency to form clusters. This work and previous work by Promlek *et al.*⁵⁶ did show that when Ire1p is carrying ER-luminal domain mutations that prevent it from forming higher oligomers (IF2 mutation) or impair it in its ability to bind unfolded proteins (Δ III mutant), will still allow it to mount a full-blown UPR under forms of prolonged ER-stress. I could verify comparable levels of spliced *HAC1* mRNA for the cysteine-less Ire1p and the cysteine-less Ire1p-F544C mutant that carries the IF2 mutation (Figure 18 C and D), which abrogates the formation of oligomers but conserves Ire1p's ability to form dimers under LBS and prolonged ER-stress after exposure to DTT. As expected, Ire1p carrying the IF2 mutation does no longer form clusters under acute proteotoxic forms of ER-stress and LBS by inositol-depletion² concomitant with its strongly impaired response to the initial acute ER-stress, demonstrated by the absence of spliced *HAC1* mRNA in the first hour of exposure (Figure 18 C and D). Given that the IF2 mutation prevents tetrameric assemblies for trans-autophosphorylation I wondered whether under LBS the AH of Ire1p could overcome the need of a functional ER-luminal domain for a lipid-induced UPR. I wondered whether a disruption of the AH, necessary for the hydrophobic mismatch-based sensing mechanism of Ire1p, would compromise the signaling of Ire1p in context of a scenario that relies solely on dimer-dimer formations. Indeed two mutants (cysteine-less Ire1p E540C & IF2 and cysteine-less Ire1p T541C & IF2) that disrupt the AH character of Ire1p TMD can no longer respond to both prolonged membrane-based forms of ER-stress when paired with the IF2 mutation (Figure 18 C and D). The cysteine-less Ire1p-F544C & IF2 mutant that maintains the functional AH of Ire1p, shows a functional response for both prolonged forms of membrane-based ER stress while lacking the initial acute phase of UPR signaling due to the ER-luminal IF2 mutation. The UPR activity, or the lack thereof, measured by the level of spliced *HAC1* mRNA correlates with the growth data obtained for each strain in a DTT stress resistance assay that measures the growth after 19 h of exposure to various concentration of DTT (Figure 18 B). Here, both AH compromising mutants show a growth comparable to that of the *ire1* Δ strain, while the cysteine-less Ire1p-F544C & IF2 mutant, grows better than the single IF2 mutant but less well than the cysteine-less Ire1p. It is not surprising that a single

point mutation within the TMD of Ire1p has a substantial impact on the ER stress resistance, as it was shown by Ho *et al.* that the Ire1p-R537Q mutant is completely insensitive for LBS⁸⁸. The importance of a functional TMD for sensing lipid-induced ER stress becomes apparent since it was shown for the mammalian and the yeast system that Ire1p remains responsive to LBS when the entire ER-luminal domain is removed^{88,434}. This raises the question whether higher oligomers are needed for UPR signaling in case of LBS. Because as it stands now, the equal amounts of *HAC1* splicing in the background of a IF2 mutant suggests that a functional TMD can in a context of increasing membrane aberrancies overcome the need for a functional IF2 ER-luminal domain. Interestingly, Ishiwata-Kimata *et al.* could elegantly show the C-terminal tagging of Ire1p will prevent dimerization and only allow for higher oligomeric assemblies. Combining the IF2 mutant that prevents higher oligomeric assemblies with the C-terminal tagging strategy leads to a complete inhibition of UPR activity under LBS in form of inositol-depletion⁴³⁵. The assumption that proteotoxic stress and LBS have a different impact on the transcriptome⁸⁸ could be rooted in the fact that Ire1p acts in the dimeric or oligomeric form under the respective applied forms of ER-Stress. One possible scenario that could contribute to modifying the transcriptional response, would be a change in the composition of the "UPRosome", a scaffolding complex composed of multiple-proteins that is actively regulated by Ire1p, potentially with respect to its oligomeric assembly status, and thereby changes the crosstalk between the UPR and other pathways⁴³⁶.

5.3 Establishing an experimental framework to study lipid-induced ER-stress in eukaryotic cells by genetically manipulating the OLE pathway of *S. cerevisiae*

5.3.1 Phenotypes associated with a reduced membrane fluidity in *mga2*Δ

S. cerevisiae serves as a model system to study LBS because of its powerful genetics that facilitated the investigations of its lipid metabolism¹²². Since the lipid class composition for each organism and organelle differ greatly, I focused on the impact of the chemical diversity found in the acyl chains of glycerophospholipids as a driving force of LBS. Numerous papers have shown the UPR evoking potential of saturated fatty acids in liver or pancreatic β -cells^{437,438}. The role of saturated lipids was also investigated in the nematode *C. elegans*, where a disturbance of fatty acid desaturation culminates in a constitutively active UPR⁴³⁹. By feeding palmitic acid to mammalian cells lacking the ER stress sensing ER-luminal domains of IRE1 α or PERK, Volmer *et al.* showed that the TMD of both sensors is sufficient to respond to lipid perturbations⁴³⁴. These findings strengthen the case for a direct effect of membrane saturation on UPR activation.

To evoke a UPR through an increase in lipid saturation *MGA2* was knocked out, which is the transcriptional regulator of the sole desaturase of *S. cerevisiae*, encoded by *OLE1* (Figure 34 C). Consistent with previous findings by Surma *et al.* the increased lipid saturation (Figure 19 D) triggered a robust UPR²⁴¹ (Figure 34 D) and further had direct consequences for the cell vitality and cell viability (Figure 19 A and C). Concomitant with an increase lipid saturation and impaired growth, an aberrant ER morphology manifests in *mga2*Δ cells (Figure 21 B)²⁴¹. Two independent studies on temperature-sensitive mutants of the OLE pathway have already described similar aberrant ER structures, with Zhang *et al.* being the first to observe them^{199,440}. All published ultrastructure studies link these aberrant structures to deformations of the nuclear envelope (NE). The NE is a common structure of all eukaryotes and encases the chromosomes during interphase⁴⁴¹ whereas it undergoes different cell cycle-dependent reorganization during mitosis in lower and higher eukaryotes. Using live cell imaging supported by the Airyscan© technology, I could show that the aberrant ER structures emerge at one specific side of the nucleus during mitosis (Figure 33). Interestingly, Witkin *et al.* demonstrated that a specific region of the NE adjacent to the nucleolus serves as a membrane sink during mitotic delay⁴⁴² (Figure 19 B) and thus could represent the potential site of origin for the aberrant ER. To put their findings into perspective, a brief explanation of mitotic NE dynamics

follows⁴⁴¹. Cells of most metazoans will undergo an “open” mitosis in which the NE breaks down and its components are dispersed during each mitotic event to allow the mitotic spindle to access the chromosomes to initiate segregation. Naturally, this strategy will necessitate the reassembly of the nuclear envelope in both daughter cells once the segregation is completed to re-establish the nuclear compartment. In contrast many fungi, including *S. cerevisiae*, undergo a “closed” form of mitosis i.e. their NE remains intact throughout mitosis⁴⁴¹. The yeast centrosome equivalent, termed spindle pole body, is embedded in the NE and the spindle microtubules can access the chromosomes without NE breakdown. The closed form of mitosis therefore requires a NE expansion to accommodate for chromosome movement during segregation. So how exactly does my observation that the aberrant ER arises on one side of the nucleus tie in with the described “flares” of excess membrane observed by Witkin *et al.* and others^{442,443}? Witkin *et al.* could show that phospholipid synthesis continues⁴⁴² during mitotic delay. I have shown that cell cycle-dependent upregulation of *OLE1* mRNA is disturbed in *mga2Δ* (Figure 34 C), so that more saturated lipids accumulate with each successful cell division because Ole1p levels remain low and, in the absence of Mga2p, no adjustment of Ole1p levels can occur in the interphase of the cell cycle before the next mitosis. Consequently, as growth is impaired by the accumulation of too many saturated lipids a fraction of newly synthesized fully saturated lipids will be sequestered into the NE subdomain associated with the nucleolus. Such a locally confined accumulation could create a highly ordered membrane domain that is possibly prone to cause NE rupture during mitosis, which could explain loss in cell viability (Figure 19 C). One reason for the confined addition of membrane to the region adjacent to the nucleolus could be to preserve the highly organized inter-chromosomal interactions⁴⁴⁴ in the remaining nucleoplasm opposed to the scenario in which the nucleus as a whole would expand isometrically. Further, for reasons unknown as of now, yeast cells show a constant nuclear to cell volume ratio^{445–447}, which might be easier to maintain when excess membrane material is confined at a single location rather than distributed throughout the entire nuclear surface. The yeast polo kinase Cdc5p, is involved in regulating the shape of the mitotic nucleus and its inactivation will enforce an isometric nuclear envelope expansion⁴⁴⁸. Intriguingly, the double mutant of *mga2Δ* and the hypomorph *CDC5* allele did not surface as a potential “rescue” candidate in the screen and grew worse when compared to the single hypomorph *CDC5* mutant. A fluorescent co-localization study could help to establish whether the side of aberrant ER formation coincides with the crescent-shaped nucleolar structure within the nucleus⁴⁴⁹. Next, given that the dynamics of aberrant ER formation are reminiscent in form and duration of the microtubule dynamics during anaphase of mitosis (~ 5 min)⁴⁵⁰, I conducted a co-localization study using fluorescently labeled α -tubulin Tub1p and an ER-luminal marker to investigate the cell-cycle dependent formation of the aberrant ER in context of *mga2Δ* (Figure 45 – Supplementary Information)²⁰⁹. While the Tub1p

signal dynamics did align with the ER-marker signal during anaphase, the loss of Tub1p signal in the telophase due to spindle collapse suggests that the aberrant ER is not stabilized by Tub1p. However, given that Tub1p signal extension coincided with the aberrant ER formation more supportive evidence for the NE expansion model could be found. Based on the Tub1p signal loss it is likely that both mother and daughter cells seem to reach the G1 state after cytokinesis in *mga2Δ* cells. Noteworthy, the genome-wide screen showed a severe growth defect for the *mga2Δ* and hypomorph *TUB1* mutant compared to the single *TUB1* hypomorph mutant. Consequently, no reliable microscopic evaluation of aberrant ER formation could be carried out.

By following markers for different subdomains of the ER, it was possible to identify their relative positions in respect to the aberrant ER domains, visualized by an ER-luminal marker. The Rtn1p-marker concentrated in punctate structures outside the aberrant ER structure (Figure 37). In a WT background Rtn1p was shown to be dominantly associated with the reticular ER present at the cell cortex and involved in the formation of the tubules that connect said cortical ER to the NE while being less abundant in the NE itself³⁷¹. Interestingly, the oligomerization tendency of Rtn1p was increased in the *mga2Δ* background (Figure 35). Further, the UPR inducer Ire1p was also not found in the aberrant ER but instead formed large clusters in the non-aberrant ER subdomains (Figure 46 – Supplementary Information). Although in this study no co-localization of Rtn1p clusters and Ire1p clusters was carried out, it would be interesting to see how the different TMH of both proteins could contribute to such a co-localization. It was shown that the reticulon homology domain (RHD) of Rtn1p is sufficient for its membrane shaping activities^{451,452}. FAM134B, a protein that also contains an RHD, was shown to induce a local thinning of the ER-membrane⁴⁵¹. Given Ire1p hydrophobic mismatch sensing mechanism it is conceivable that Ire1p would “evade” in subdomains that have a thinner ER, which would cause Ire1p to be concentrated with Rtn1p in the non-aberrant ER regions in *mga2Δ* cells^{2,47,87}. Such a change in subdomain distribution could result in a perpetuation of the UPR activity by promoting Ire1p clustering and exacerbate an ER-stress condition by UPR dependent membrane expansion in the context of *mga2Δ*. Another contributing but yet not investigated aspect is that ATP depletion leads to a reduction of Rtn1p mobility due to higher oligomeric states as a consequence of ATP-dependent cluster disassembly⁴⁵³. Further, an increase of the cytoplasmic ADP/ATP ratio, has been linked to UPR activation⁴⁵⁴. Therefore, ATP depletion might synergistically contribute to the remodeling of ER subdomain distribution associated with *mga2Δ* cells.

5.3.2 FRAP experiments show that membrane fluidity is maintained in the aberrant ER

Because lipid saturation is a key regulator of membrane fluidity^{176,180,184,203} and because saturated lipids accumulate in cells lacking *MGA2*, the question arose whether the reduced cellular fitness is a consequence of low membrane fluidity. Membrane fluidity in the ER of live cells was measured indirectly via FRAP of a fluorescently tagged, ER-resident membrane protein (Figure 22). The signal recovery time for the aberrant ER was significantly slower compared to the recovery time determined in the nuclear ER of WT cells. This result would suggest that there is indeed a significant change in the biophysical properties of the aberrant ER as the recovery time is dependent on the mobility of the respective transmembrane protein. By using an equation published by Kang *et al.* that is similar to the Soumpasis equation used to derive diffusion coefficients from confocal FRAP data I obtained for the WT nuclear ER a diffusion coefficient of $0.058 \mu\text{m}^2\text{s}^{-1}$ and for the aberrant ER a value of $0.045 \mu\text{m}^2\text{s}^{-1}$ ⁴⁵⁵. Given that gel-phases have a diffusion coefficient of $\sim 10^{-3} \mu\text{m}^2\text{s}^{-1}$ I would reject the assumption that the increase in saturated lipids causes the entire ER membrane to transition from its liquid-ordered into a solid-ordered state¹⁶³. Furthermore, the difference between the two diffusion coefficients obtained, although significant, is not close to an order of magnitude when compared to differences observed in other *in vivo* model systems. To put my diffusion coefficients into perspective, in the paper of Ghorbandt *et al.*, which used a prokaryotic model system with *E. coli* to study the restricted diffusion in the plasma membrane, an up to 9-fold difference in diffusion coefficients could be achieved with $0.045 \mu\text{m}^2\text{s}^{-1}$ for the control condition and $0.0053 \mu\text{m}^2\text{s}^{-1}$ under UFA depleted conditions¹⁷⁶. The FRAP results must be viewed cautiously as data comes with uncertainties. For one, both structures that got compared to one another differ significantly in their geometry (Figure 35). The aberrant ER seemingly presents itself in multiplane recordings as “compressed” thin planar strips of membranes compared to the spherical appearing nuclear ER (Figure 35 and Figure 37). During the bleaching process, the energy is always applied three-dimensionally to the focal plane as well as – decreasingly, of course – to the planes above and below it. Since the complex three-dimensional shape was not accounted for, and given that the aberrant ER and nuclear ER may differ in their occupied bleached and nonbleached volumes one should exercise caution regarding the obtained recovery times especially if the corona effect of the FRAP technique is considered. The corona effect describes the observation that during the process of irreversible bleaching of fluorophores in the defined ROI, unbleached molecules will enter the ROI from the rim and in this process become bleached as well⁴⁵⁶. This inevitably leads to the formation of a “corona” of unbleached particles that encompass the original defined region of interest

thereby affecting the subsequently measured recovery time. This inherent “error” of the FRAP technique could introduce an error depending on the previously mentioned three-dimensional orientation of the organelle and fluorophore concentration per volume, indicated by higher intensity values per pixel for the aberrant ER. And lastly there is another consideration to be made due to the putative origin of the aberrant ER when compared to the WT nuclear ER control. If my assumption that the aberrant ER arises during a closed mitotic process is correct, and given that several groups have shown that a nuclear diffusion barrier is formed during anaphase, one should also carry out FRAP experiments of WT cell during anaphase to compare the recovery rates^{425,457}. I would further suggest to the extension of FRAP experiments a data set that is devoted to a comparison of recovery times for an ER-luminal marker between the aberrant and healthy ER to more precisely pinpoint that the source for the observed longer recovery times in the aberrant ER is indeed membrane-based. As of now the data does not allow statements whether the FRAP recoveries are solely due to a reduced diffusion rate as a result of a disturbed lipid composition or due to transient protein-protein binding interactions as a result of the unique membrane environment associated with the NE during mitosis.

5.3.3 Homeoviscous adaptation in context of *mga2*Δ

Lipid saturation is one of the key regulated features, which is adapted upon cultivating cells at different temperatures^{100,182}. Because *mga2*Δ cells feature a lipidome, which is dramatically enriched for tightly packing, saturated lipids it was interesting to study how *mga2*Δ cells grow at different temperatures compared to WT cells. The concept of homeoviscous adaptation would suggest that cells with an overly saturated lipidome have severe problems at low temperatures of cultivation, but they may be more resistant when exposed to higher temperatures. Surprisingly, cells lacking Mga2p showed compared to WT cells a reduced growth at the optimal growth temperature (Figure 20). The reduced levels of growth were further present under both extreme ends of the tested temperature conditions giving *mga2*Δ cells no apparent advantage compared to WT cells when cultivated under higher temperatures. The supplementation of unsaturated fatty acids restored growth at all tested temperatures but it did not significantly affect the growth at the lowest and highest tested temperatures. The aforementioned reduction in cellular growth is seemingly nullified when *mga2*Δ strains are provided with fluidity promoting fatty acids in form of oleate and linoleate (Figure 20 B and C). On the contrary, the supplementation with palmitate deteriorates the performance for each tested temperature (Figure 20 D). The experiments further emphasize the importance of acyl chain remodeling, as in this simplified model organism the drawbacks introduced by a paucity of unsaturated acyl chains could not be actively counteracted through

modulation of the lipid class composition (Figure 27). Combined, the data highlights the importance of temperature as a physical parameter in determining cellular growth and that homeoviscous adaptation, facilitated by Ole1p activity in this model system, has a modulating effect only when sufficient amounts of UFA are available to maintain physiologically crucial processes. This experiment underscores the challenges eukaryotic organisms face in meeting the specific membrane fluidity requirements of individual subcellular membrane under widely varying temperatures. The requirements for balancing membrane fluidity are best demonstrated by looking at the different needs of energy-transferring membranes compared to the plasma membrane. Membrane lipids that lower membrane fluidity such as sterols and sphingolipids are generally less abundant in energy-transducing membranes¹⁶³. This evolutionary trait is likely a consequence to allow higher diffusion rates, as the electron transport chain has many diffusion-coupled reactions between the embedded respiratory enzymes and electron carriers that ultimately determine the efficiency of cellular respiration¹⁷⁴. The plasma membrane, on the other hand, is enriched in saturated lipids, sterols and sphingolipids probably because its function as a permeability barrier is paramount over high translational diffusion, which is required to maximize metabolic activity¹⁶³. This may be the reason that the plasma membrane has been liberated of its role in energy production for evolutionary reasons and the entire process has been shifted to intracellular membranes of the mitochondria to allow the various cell membranes to maximize their functional potential.

5.3.4 High throughput genomic screen uncovers cell cycle and mitochondrial processes to be involved in alleviating or aggravating the aberrant ER phenotype

To identify potential modulators of the aberrant ER morphology in *mga2Δ* cells a genome-wide microscopy-based screen was carried out. The screen identified modulators that either reduced the fraction of cells showing the aberrant ER (“rescue” candidates) or increased the fraction of cells showing the aberrant ER morphology (“worse” candidates) (Table 14). For the “rescue” category the overly represented biological functions are associated with cell cycle progression, whereas for the “worse” category mitochondrial functions are the central focus (Figure 24).

5.3.4.1 The "worse" category – a closer inspection

A number of "worse" candidates were associated with the assembly of the cytochrome c oxidase (Table 14). Given that *OLE1* and *MGA2* are upregulated by hypoxia⁴⁵⁸, I wondered whether the impairment of the oxygen depositing enzyme complex or the lack of oxygen as the terminal acceptor might contribute to the development of the aberrant ER through elevated levels of ROS. A study by Kwast *et al.* suggests that oxygen availability in *S. cerevisiae* may be monitored by a redox-sensitive hemoprotein¹⁹¹. Their study presents evidence that cytochrome c oxidase is likely to be this sensor as its functionality and that of the respiratory chain is involved in the transcriptional regulation of a subset of hypoxic genes, including *OLE1*¹⁹¹. Although the authors do not solve the signaling pathway, I want to discuss two scenarios that they propose as I find them interesting in light of my own data. One signaling scenario by which the membrane protein cytochrome c oxidase could mitigate the information from the mitochondria to the nucleus to regulate gene expression would be that an interaction partner of cytochrome c oxidase, potentially cytochrome c, could be released from the mitochondria and initiate a cytosolic signaling cascade. Cytochrome c is an interesting candidate given that it is immediately upstream of cytochrome c oxidase and its release from mitochondria and involvement in signaling is well established e.g. for apoptosis in higher eukaryotes⁴⁵⁹. A recent study attributed CL-bound cytochrome c a peroxidase activity, which might be involved in mitigating the burden of mitochondrial originated ROS^{460,461}. It was further shown that oxidized CL has a reduced affinity for cytochrome c leading to its dissociating from the IMM and subsequent enrichment in the intermembrane space⁴⁶². Given that *mga2Δ* strains have more saturated CL species compared to the WT (Figure 40 and Figure 41) such an increase of the soluble fraction of cytochrome c, which usually takes on the task as an electron carrier, while decreasing the immobile fraction responsible for carrying out peroxidase activity might pose a precondition for the release of cytochrome c under pro apoptotic conditions or for alternative signaling pathways. To validate the involvement of cytochrome c in signal transduction when released from mitochondria, it would be interesting to use a fluorescent fusion protein of cytochrome c that localizes to the mitochondria and functions there as an electron carrier between complex III and complex IV but has been shown to be unable to enter the cytosol when the proapoptotic molecule Bax is co-expressed⁴⁶³. The second proposed model of signal transduction would be rooted in elevated levels of ROS as in mammalian cells it was shown that the V_{max} of cytochrome c oxidase is decreased under hypoxia⁴⁶⁴ and that this decrease alters the redox state of mitochondrial electron carriers upstream of cytochrome c oxidase leading to higher levels of ROS⁴⁶⁵. These ROS could be involved in initiating the crosstalk between the mitochondria and the nucleus. That ROS might play a role in the

formation of the aberrant ER and lower the fitness of *mga2Δ* cells is supported by the observation that vitamin c rescues the growth defect of *mga2Δ* cells while overexpression of *HAP4*, which leads to an increased production of ROS in mitochondria³⁷⁶, impairs growth (Figure 38). Furthermore, supplementation of vitamin c or reduced GSH to the medium prevents the formation of the aberrant ER in *mga2Δ* cells (Figure 39). Interestingly, cyanamide, the compound used in my DDI2 promotor-based membrane expansion experiment, was shown to lead to oxidative stress by inhibiting the catalase activity in grapevine buds⁴⁶⁶. Since I had no system available to measure intracellular ROS levels at the time when I carried out these experiments I would predict, that if cyanamide affects catalase activity in *S. cerevisiae* at the here used none-growth inhibiting concentrations, it might contribute to the aberrant ER formation in absence of an membrane-expanding system, which would further support an active role of ROS in the formation of the aberrant ER. In light of the previously mentioned aspects, it is also tempting to speculate how an increased degree of saturation combined with a disturbed assembly of the respiratory chain contributes to the aggravation of the aberrant ER phenotype. Aside from the ER, the lack of unsaturated lipids in *mga2Δ* cells could pose a problem for mitochondrial membranes. After all, the inner mitochondrial membranes (IMM) protein-to-lipid ratio is one the highest of any subcellular membrane⁴⁶⁷ and lipid-based destabilizing effects for the super-complexes of the respiratory chain have been reported for both reduced levels of cardiolipin and reduced remodeling of the cardiolipin acyl chains^{468,469}. These effects are best studied in the *taz1Δ* strain, which was previously found to have reduced coupling and increased levels of super-complex destabilization^{130,470}, which are both associated with an increase in mitochondrial ROS levels as reported by Barros *et al.*⁴⁷¹. In a study by Chen *et al*, it was found that oleic acid supplementation may contribute to the reduction of oxidative stress in the *taz1Δ* background, which has reduced CL levels and an aberrant fatty acid composition of CL species⁴⁷². Interestingly, only oleic acid (C18:1) supplementation had a beneficial effect, while supplementation with either palmitic acid (16:0), palmitoleic acid (16:1) or stearic acid (C18:0) did not, suggesting that oleic acid may be particularly important for maintaining mitochondrial functionality⁴⁷². The impact of membrane fluidity, determined through modulation of lipid acyl chain composition, on cellular growth and energy production was further elegantly showcased in a study by Budin *et al*¹⁷⁴. Using genetically engineered strains of *E. coli* and *S. cerevisiae* the authors of this study could show that the rate of collisional interaction between electron carriers and the enzymatic components of the oxidative phosphorylation system are crucial for cellular growth and aerobic respiration. Both biological aspects were increased when membrane fluidity was high and decreased when membrane fluidity was low due to a lack of UFA in phospholipids. Interestingly, they observed that the growth rate was subject to a biphasic dependency on the degree of lipid saturation. There was a sharp primary requirement for cellular growth that began at UFA levels

of 15-20% and led to higher growth rates with higher UFA concentrations¹⁷⁴. A secondary constraint on growth rate was imposed by limiting ATP generation during aerobic growth, which was also a function of UFA content, implying that the rate of respiration is also dependent on membrane fluidity^{174,473}. Although the growth dependency was assessed for *E. coli* in the study by Budin *et al.*, my data show a similar effect for *S. cerevisiae mga2Δ* in that there is a sharp decrease in growth rate (Figure 19 A and B) when cells experience a globally lowered UFA content in glycerophospholipids (~ 30 % UFA content for *mga2Δ S. cerevisiae* opposed to 60 % UFA content for WT, Figure 19 D). This decreased growth rate was accompanied by an increase in the proportion of cells harboring the aberrant ER phenotype, and interestingly, the growth rate increased significantly as the overall proportion of cells harboring an aberrant ER decrease as time progresses during a batch cultivation (Figure 34 A and B). Budin *et al.* and the works of other groups favor that coenzyme Q or ubiquinone influences the respiratory flux of electrons in a membrane fluidity-dependent manner^{174,474,475}. However, for ubiquinone to be the rate-limiting molecule, the highly controversial substrate channel theory, i.e. the sequestration of local ubiquinone by super-complexes to gain a kinetic advantage by preventing any exchange with ubiquinone competing pathways, would not have to be valid⁴⁷⁶. Given the proximity of individual components of the respiratory chain within super-complexes, an entrapped quinone pool within these assemblies would basically eliminate any lipid barrier during electron transfer, hence no possibility for ubiquinone to be the dominant molecule to explain the observed differences under various degrees of membrane saturation. Given that the components of the oxidative phosphorylation system are embedded in the plasma membrane of prokaryotes while they were evolutionarily relocated to the IMM in eukaryotes, the study by Budin *et al.* underscores the importance of using biologically different yet evolutionarily related systems to identify fundamentally relevant aspects involved in biological processes such as cellular respiration. It is tempting to speculate whether an increased degree of saturated lipids in the IMM would lead to an increase of reactive oxygen species (ROS) due to super-complex disassembly followed by an increase of the cytoplasmic ADP/ATP ratio, both of which have been linked to UPR activation^{205,454}. Although there are no studies dedicated to morphological or functional changes of mitochondria in *mga2Δ S. cerevisiae* strains, there is data from a study conducted with *Kluyveromyces lactis* that reports on collapsed mitochondrial structures³⁷⁴. In a follow up study with *mga2Δ K. lactis* the Bianchi lab could demonstrate that Mga2p of *K. lactis* is involved in a light stress response and is associated with the expression of ROS protective enzymes³⁷⁵. Their data implies that Mga2p in *K. lactis* could act as a mediator for the oxidative stress response thereby adding another layer of biological regulation next to the already established role in fatty acid biosynthesis. Data that reports on altered mitochondrial functions in *S. cerevisiae* exist for a temperature sensitive variant of Ole1p. In fact, *MDM2* is a gene name

alias of *OLE1*, which stands for mitochondrial distribution and morphology, as under the non-permissive temperature the increased degree of saturation interfered with the movement and inheritance of mitochondria linking potential aspects of mitochondrial activity and organelle distribution to cell cycle progression⁴⁷⁷.

5.3.4.2 The “rescue” category – a closer inspection

Although the hits in the “rescue” category cover somewhat more diverse biological functions than the hits in the “worse” category, which primarily suggested a mitochondrial cause for the increased aberrant ER phenotype, an overarching theme of cell cycle progression emerges for the “rescue” category. One reason for this diversity may be that the screen worked better for mutants that showed a higher percentage of cells with an aberrant ER opposed to mutations with an alleviating effect compared to the percentages of aberrant ER found in the single *mga2Δ* strain. An accumulation of false positive candidates would make the identification of genuine causes for preventing or resolving the aberrant ER more difficult. At the time of implementation, the dynamics of the aberrant ER phenotype were not precisely known, which is reflected in the nonoptimal screening conditions. The query strain for the aberrant ER used in the genome-wide screen showed on average in 7 % of the cells an aberrant ER (data not shown). Hence, the point of reference is far from the optimal value of 50 % to more confidently assign the candidates into the “worse” or “rescue” category. The none optimal average query strain reference value of 7 % is thereby especially punishing towards the “rescue” category making identified candidates here more prone to be false positives. Considering that the image acquisition of the genome wide screen for one 384 well plate takes roughly 3 hours from start to finish, and given that the *mga2Δ* query strain showed under the used screening conditions more aberrant structures when it is imaged later in the process of acquisition, the screen has an additional inherent temporal bias. This bias is difficult to correct for because space for additional wells that could help in monitoring the dynamics of the aberrant ER phenotype are limited and would not help to correct for growth-dependent variations that are bound to occur during a genome-wide screen. Having said that, one could argue that the screen in combination with a subsequent manual analysis of the identified candidates under my optimized culturing conditions was key to identify positive or negative genetic interactions more accurately.

With *UBC4* a “rescue” candidate that encodes for the most abundant E2 enzyme representing a member of the ubiquitin proteasome system (UPS)²⁵⁹ was chosen. Ubc4p is a promiscuous E2 ubiquitin-conjugating enzyme that shows a greater overlap with E3 enzyme targets than all other E2 enzymes, emphasizing the notion that the E3 enzymes confer the target specificity

and ultimately decide which proteins are ubiquitinated²⁵⁹. Ubc4p has a paralog in Ubc5p, with a mere difference of 11 residues⁴⁷⁸. An *in silico* analysis of the physical binding partners of both E2 enzymes revealed a distinct interactome (Figure 42).

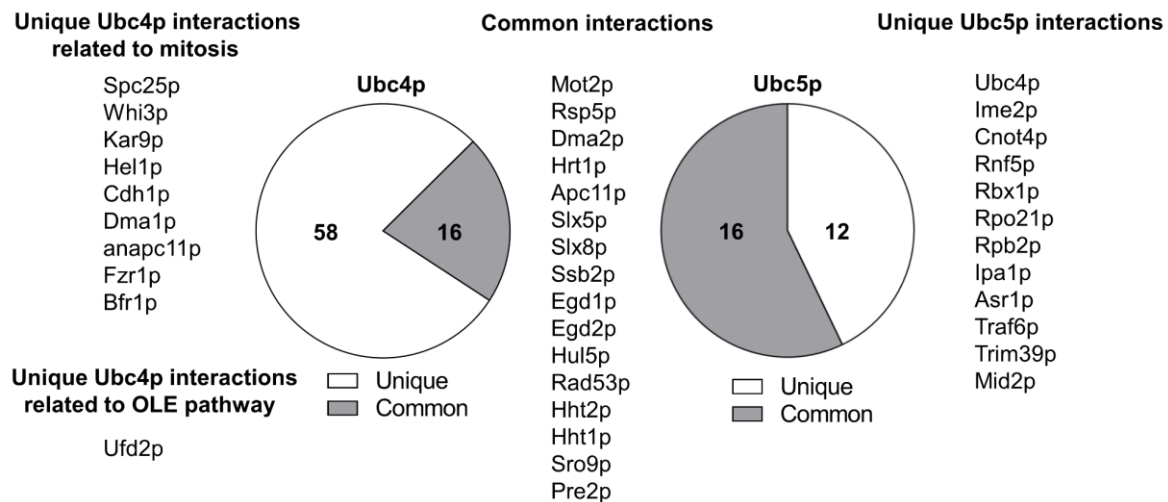


Figure 42 Physical interaction partners of Ubc4p and Ubc5p

The values within each pie chart represent the number of known physical interaction partners of each E2 enzyme. For Ubc4p an excerpt of the unique interaction partners is listed that are related to the process of mitosis as well as a partner related to the OLE pathway. For Ubc5p, all known unique interaction partners are listed together with the common partners shared between both E2 enzymes. The data that went into this illustration was taken from the supplementary materials of Raimalani *et al.* (2020)⁴⁷⁸.

Raimalani *et al.* speculate that each protein caters to cell stage specific needs, as Ubc4p is expressed during the exponential growth phase, while Ubc5p in the stationary phase and under stress conditions^{478,479}. It was indeed shown that Ubc4p is involved in the transition from metaphase to anaphase in conjunction with the E3 ligase referred to as anaphase-promoting complex (APC), as the APC is responsible (together with its E2 enzyme Ubc1p) for the ubiquitination of proteins involved in cell-cycle progression⁴⁸⁰. Out of the 58 unique physical interactions, nine are related to the process of mitosis, e.g. Cdh1p is an activator of the APC and targets the complex to proteins such as Cin8p⁴⁸¹. Another interesting unique interaction partner of Ubc4p is Ufd2p, a E4 ubiquitin ligase that was shown to be involved in the multiubiquitylation of the active p90 fragment of Spt23p, the homolog of Mga2p⁴⁸². This could imply that the rescue effect is due to a stabilized p90 fragment, which would result in increased Ole1p levels that partially rescue the absence of Mga2p. Further, two additional examples from the “rescue” category have been linked to APC-dependent cell cycle progression namely the previously mentioned *CIN8*⁴⁸³, encoding for a kinesin motor protein⁴⁸⁴, and *MSN5* a karyopherin that controls the subcellular localization of Swi5p⁴⁸⁵, a transcription factor involved in cyclin kinase expression⁴⁸⁶. I later could show that the overexpression of *MSN5* and *SWI5*

will both rescue the aberrant ER phenotype with *MSN5* overexpression representing the strongest mutant in terms of alleviating the aberrant ER phenotype as of yet (Figure 33).

With *MALL33* I have decided for a member of the *MAL* multigene family. Each of the five unlinked loci of this multigene family in yeast is sufficient to allow maltose utilization⁴⁸⁷. The typical locus of the *MAL* family contains three functional genes, *MALS*, a structural maltase gene, *MALT* encoding for a transporter i.e. the permease and *MALR* as the regulatory subunit for the expression⁴⁸⁷. The “rescue” candidate *MAL33* encodes for the regulatory subunit of the *MAL3* locus. Interestingly, not all yeast strains carry all *MAL* genes at all five loci⁴⁸⁷. To my surprise *mal33Δmga2Δ* was the only hit of the *MAL* family and deviates from the GO terms of the “rescue” category that predominantly shows GO terms related to mitosis (Figure 24). The absence of all other *MAL* genes on the “rescue” hitlist prompted me to check for possible “off target” effects that fit the proposed role of mitosis related genes in alleviating the aberrant ER phenotype. Interestingly, I only find at the *MAL33* locus a putative operon-based mechanism that could explain the *mal33Δmga2Δ* rescue. In direct vicinity of *MAL33* on the opposite strand *TYC1* can be found, which encodes for Tyc1p, an inhibitor of the anaphase-promoting complex/cyclosome (APC/C)⁴⁸⁸. It could be possible that *TYC1* mRNA level are disturbed as a consequence of kanMX cassette insertion at the *MAL33* locus and thereby the cell-cycle progression is disturbed in a way that benefits the *mga2Δ* strain in preventing the formation of the aberrant ER. With *NCS2* a “rescue” candidate of the ubiquitin-related modifier URM1 pathway was chosen that is involved in the thiolation of uridine at the wobble position of lysine(UUU) and glutamate(UUC) tRNAs⁴⁸⁹. Interestingly, it was shown that disturbed thiolation causes ribosomal pausing and thereby changes the rate of translation resulting in the aggregation of unfolded proteins *in vivo*⁴⁹⁰. It was demonstrated that disturbed tRNA anticodon loop modifications do not result in UPR induction but rather relieve endogenous ER stress⁴⁸⁹. Bruch *et al.* postulate that the increased resistance to UPR inducing drugs in tRNA modification mutants is, as observed with mutants lacking ribosomal proteins⁴⁹¹, a consequence of the reduced translational efficiency, reflected in a slower growth and reduced load of secretory pathway trafficking⁴⁸⁹. The protein species that are prone to aggregation under uridine modification defects imposed by *ncs2Δ* are predominantly of cytosolic nature as shown by similar profiles of the *ncs2Δelp6Δ* mutant compared to that of the *ssb1Δssb2Δ* mutant, which is impaired in co-translational folding⁴⁹⁰. Hence no induction of ER-stress will occur in yeast as a consequence of thiolation deficient cells. Interestingly, *elp6Δ* was a putative “rescue” candidate identified by only one of the three scientist that evaluated the original screening dataset (Figure 24). In line with the theme of cell cycle progression, it was shown in a study by Greenland *et al.* that Ncs2p and with that the urmylation pathway is involved in regulation the size of the spindle pole body during a mitotic cell cycle arrest⁴⁹². An interesting

finding of their study is that Ubc4p, but not Ubc5p, is involved in maintaining the size of the spindle pole body during cell cycle, which is in line with our presented screening data. These findings strengthen the case that cell cycle progression is a crucial aspect for the development of the aberrant ER as two pathways, urmylation and ubiquitination are both involved in the remodeling of the spindle pole body⁴⁹².

5.3.5 *De novo* lipid synthesis – either regulated during the cell cycle or UPR dependent – could be detrimental in context of an impaired OLE pathway

In order for eukaryotic cells to grow and divide cells must tightly coordinate the amount, composition and localization of proteins and lipids in a cell cycle dependent manner⁴⁹³. Apart from the sudden increase of the outer cell surface, each subcellular membrane is experiencing a greater demand for lipid building blocks during growth while maintaining their specific lipid composition to stay functional. In order to transition between the different cell cycle phases or under ER-stress, the demand for synthesizing the appropriate lipids can increase dramatically within short time periods. Proliferation of the ER membrane after DTT exposure was shown to be rapid, doubling in size 40 minutes after cells experiencing ER-stress⁴⁹⁴. *S. cerevisiae* undergoes a closed form of mitosis, keeping the nuclear envelope intact, hence the nuclear envelope is subjected to dramatic rearrangements during cytokinesis as there is a massive expansion within ~20 minutes during anaphase/cytokinesis⁴⁹⁵.

So far multiple lines of evidence point in a direction that increased and rapid membrane expansion contributes to the formation of the aberrant ER.

- 1) The “rescue” category contains hits that are associated with a disturbed cell cycle progression (Table 14 and Figure 24)
- 2) Using the adapted SCD medium formulation proposed by Hanscho *et al.*²²¹, which improves the growth rate of the BY series opposed to the standard SCD medium formulation, leads to the formation of more aberrant ER structures (Figure 43 – supplementary information).
- 3) Enforcing ER membrane expansion with various alterations of an inducible system for ER membrane biogenesis leads to an increase of cells harboring the aberrant ER. This approach was chosen to mimic the UPR driven ER-membrane expansion under ER-stress (Figure 31 and Figure 32).

- 4) A secondary overexpression-based screen, based on mutants that differ in their speed of completing the cell cycle identified in a study by Niu *et al.*³⁶⁴, lead to increased or reduced levels of the aberrant ER in the *mga2Δ* background (Figure 33).
- 5) Overexpression of *ICE2* in *mga2Δ*, which promotes ER membrane biogenesis by inhibiting the lipin phosphatase complex²⁰⁷, has caused the as of yet greatest increase in the fraction of cells showing an aberrant ER phenotype opposed to the single *mga2Δ* strain under my experimental conditions (Figure 33).

Although the ICE2 overexpression-based results were impressive, the data presented so far would benefit from a follow up experiment in which *DGK1* is overexpressed within the *mga2Δ* background. Dgk1p is a diacylglycerol kinase that was shown to be involved in regulating the phospholipid synthesis for NE expansion and interestingly, its overexpression results in a confined proliferation of nuclear membrane without affecting the cortical ER in the process⁴⁹⁶.

While searching for a possible explanation as to why cellular growth might be a contributing factor to the emergence of the aberrant ER structures, I came across two independent studies that report on a cell cycle dependent upregulation of *OLE1*^{368,369}. I could replicate their findings indirectly (Figure 34 C) and along with some of the here described observations a link between lipid metabolism and cell cycle progression emerges. It is for instance imaginable, that the cell cycle specific *OLE1* upregulation is Mga2p dependent, and the absence of this regulatory protein causes the cells to “hit a wall” in terms of cell cycle progression, which is illustrated by the break-in of the growth rate seen in Figure 34 A. With the lower mRNA level of *OLE1*, the *mga2Δ* strain might remain in a G0/1 state until sufficient Ole1p is translated to fix the overly saturated lipidome after an aberrant ER has formed. The reason why the cells do not run into a problem from the beginning might be the result of a “tug of war” like principle, in that the rapid cell division thin out the Ole1p pools of *mga2Δ* cells since the G1 specific upregulation is missing. It is therefore possible to imagine that the enzymatic activity of Ole1p must be sufficiently high to meet the cells commitment to *de novo* membrane synthesis for the cell cycle to progress properly.

The *mga2Δ* dependent lipid perturbations in the form of an increase in the degree of lipid saturation are conserved among *S. cerevisiae*, *K. lactis* and *S. pombe*^{241,497,498}. To my knowledge, the aberrant ER phenotype has only been so far described for *S. cerevisiae*, and always in the form of mutants that are disturbed in their OLE pathway^{199,241,440}. Of course, there are a variety of reasons why an increased degree of lipid saturation does not necessarily have to manifest itself in the form of an aberrant ER, but given the evidence presented in this thesis with respect to cell cycle progression in relation to aberrant ER formation, a key difference

may lie in aspects of yeast cytokinesis. For instance, the fission yeast *S. pombe* is characterized by a symmetrical cell division, whereas *S. cerevisiae* multiplies asymmetrically, with the smaller daughter cell budding from the mother cell. In a study carried out in the Nurse lab the knockout of *MGA2* in *S. pombe* was the strongest hit to introduce cell size variability during division and a subsequent impairment to correct the cell size deviations in the following cell cycle⁴⁹⁹. A particularly interesting finding of that study is that the synchrony of nuclear division was disturbed, leading to the emergence of multinucleated cells. They argue that in the absence of *MGA2* the nuclear membrane composition changes causing a disturbance of the nuclear-cytoplasmic transport of cyclin-dependent kinase regulators as a cause for the observed variations in cell size⁴⁹⁹. I find this proposal very interesting in light of the observed growth defect in *S. cerevisiae mga2Δ* that occurs concomitant with an increase in lipid saturation as overexpression of two cell cycle regulators in the form of *MSN5* and *SWI5* partially rescued the occurrence of the aberrant ER (Figure 33). Another difference between these strains in terms of *de novo* lipid synthesis is found in their respective UPR pathways. While *S. cerevisiae* and *K. lactis* respond to ER stress on the transcriptional level through targeted upregulation via Ire1p-dependent processing of the transcription factor encoding *HAC1* mRNA, this is not possible in *S. pombe*, since it does not encode any *HAC1*. Here, Ire1p reduces the protein load via a selective decay of ER-targeted mRNAs referred to as regulated Ire1p dependent decay (RIDDD)^{500,501}. One reason for the absence of the aberrant ER phenotype in *S. pombe mga2Δ* might be that the UPR of *S. pombe* does not include the membrane expanding program associated with the upregulation of lipid synthesizing genes⁵⁷. This assumption however raises the question why neither *HAC1* nor *IRE1* were identified as “rescue” candidates in the genome wide screen. One reason, why two genes that are essential to a functional UPR could have not shown up in the screen might have been the previously described limitations of dynamic growth-dependent phenotypes in a genome wide high throughput screen in combination with non-optimal screening conditions (see 5.3.4.2). Both candidates, *hac1Δmga2Δ* and *ire1Δmga2Δ*, showed a growth defect opposed to the single *hac1Δ* and *ire1Δ* mutants (data not shown). Given that Surma *et al.* observed in *hac1Δmga2Δ* no whorled ER structures²⁴¹, which represent another form of membrane aberrancies, while being abundant in *mga2Δ* strains, I would highly suggest to investigate the aberrant ER phenotype occurrence in the *mga2Δ* background for both UPR mutants with my established cultivation protocol. Alternatively, a possible explanation for this discrepancy could be that the greatest absolute difference in cell vitality between *mga2Δ* and WT occurs as the cells approach their growth temperature optimum (Figure 20)⁵⁰². Together with the observation that a higher percentage of cells develop aberrant ER structures when grown in growth-promoting medium (Figure 43 – Supplementary information) I believe that the *de novo* membrane synthesis is one major aspect for aberrant ER development. It is plausible that the contribution

of membrane synthesis during cell growth outweighs the burden of an additional UPR-dependent membrane expansion, causing us to overlook the beneficial effects of an absent UPR in *S. cerevisiae* *mga2* Δ . Hence, the absence of a UPR-dependent membrane expansion in *S. pombe* together with the slower growth rate of *S. pombe* may contribute to the lack of an aberrant ER morphology^{503,504}.

5.3.6 The Aberrant ER is related to the lipid composition

In order to find commonalities between the functionally distinct hits from the genome-wide screen on the molecular level, the whole-cell lipidome of each “rescue” and “worse” candidate was determined, next to those of the WT and single *mga2* Δ strain (Figure 28). The lipidomes revealed the following most prominent changes between the WT and the *mga2* Δ strain. Firstly, ceramides are increased in *mga2* Δ compared to the WT cells, accompanied by reduced levels of all remaining sphingolipids. Secondly, the level of PA shows a 3-fold increase for *mga2* Δ cells compared to WT cells. Thirdly, DAG levels are elevated by a factor of two in *mga2* Δ . And lastly, PI levels are reduced in *mga2* Δ . Noteworthy is that these changes were alleviated or aggravated for the “rescue” and “worse” strains, with the “rescue” strains tending to be more similar to the WT and the “worse” strains tending to exacerbate the deviations found in the sole *mga2* Δ lipidome. The most striking observation is the accumulation of PA and DAG in *mga2* Δ cells. The elevated DAG level in *mga2* Δ might originate from the increased PA levels as both of these lipid classes show a similar profile in terms of acyl chain distribution (Figure 44 – supplementary information). PA can serve as a precursor for all major glycerophospholipids but PC, PE and PS levels remain unchanged while PI levels are even lowered, implying that PA is not channeled into glycerophospholipid synthesis. It is surprising that the accumulation of PA does not promote the expression of phospholipid synthesis genes as it was shown that PA can tether the soluble transcriptional repressor of lipid synthesizing genes, Opi1p, to the ER membrane through an amphipathic helix motif^{505,506}. By sequestering Opi1p to the ER membrane Opi1p can no longer prevent expression of phospholipid synthesis genes through the dimeric Ino2p/Ino4p transcription factor³⁵³. Given that all levels of major glycerophospholipids remain stable, and only PI levels are further reduced in *mga2* Δ cells, this could either imply that the activity of Pis1p - the enzyme responsible for phosphatidylinositol synthesis - is reduced, as its activity was shown to be dependent on the lipid environment⁵⁰⁷ or that the drop in PI levels is the result of a shortage of inositol, which would help to explain why the elevated ceramide levels are not converted into more complex sphingolipids. It is striking that both lipids, PA and DAG, are not channeled into TAGs. One reason for that might

be that Dga1p, the enzyme responsible for TAG generation, has an oleoyl-CoA substrate preference, which is presumably scarce in the *mga2Δ* background due to reduced Ole1p enzyme activity⁵⁰⁸. Another explanation for the observed differences in lipid class composition might be a disturbed exchange of metabolites between different organelles given the interwoven lipid synthesis network (Figure 5). A possible reason for the lack of TAGs might be that the terminal enzyme for TAG formation, Dga1p, which predominantly localizes to lipid droplets⁵⁰⁹, can no longer interact with its substrate DAG due to impaired physical contact sites. It was further shown via coarse-grained molecular dynamics simulations that DAGs are prone to undergo phase-separation from lamellar lipids when they accumulate within membranes⁵¹⁰. The consequent formation of DAG-only blisters within the core of the membrane would effectively lower the available pool of DAG molecules to peripheral enzymes such as Dag1p and thereby prevent the synthesis of TAG molecules in combination with acyl-CoA⁵¹⁰. Given that PA and DAG can both serve as precursors for membrane lipid synthesis, it is interesting to speculate whether an inaccessibility of DAG could contribute to the aberrant ER formation given a recent study by Foo *et al.*⁶⁷³. This study demonstrates that in *S. pombe* the conversion of DAG into PA by Dgk1p and the glycerophospholipid synthesis from DAG itself follows a cell-cycle dependent regulation to support NE expansion³⁷³. It would therefore be interesting to understand why both substrates, PA and DAG, accumulate in *S. cerevisiae mga2Δ* and to what extent a failure to convert them into glycerophospholipids to meet the imminent demand for lipids during NE expansion might contribute to the formation of the aberrant ER. Lastly, a putative mitochondrial cause for the development of the aberrant ER calls for a close examination of the cardiolipin composition for all candidates (Figure 40 and Figure 41). Since cardiolipin is a signature lipid of mitochondria, the composition of this class allows inferences about organelle-specific changes despite the nature of the whole-cell lipid data set. Interestingly, no fully saturated CL species appear in the *mga2Δ* strain and the class of fully desaturated CL species is the most abundant class. This is in stark contrast to the trends observed for the whole-cell glycerophospholipid lipidomes, which showed an increase in fully saturated lipids at the expense of fully unsaturated lipids (Figure 19 D). However, the CL species acyl chain composition is in line with reports found in the literature by Surma *et al.* for *mga2Δ* strains²⁴¹. The absence of fully saturated CL species is supported by the fact that PG species, which serve as precursors for CL synthesis, show remarkably the lowest degree of saturated acyl chains in the *mga2Δ* background (Figure 44 – supplementary information), followed by PE. In fact, it has been shown that in yeast PE species with two monounsaturated acyl chain moieties are synthesized from di-unsaturated PS precursors by Psd1p located in the mitochondrial membrane⁵¹¹. Interfering with the ER-to-mitochondria lipid transport e.g. through disruption of the ERMES complex resulted in an accumulation of PE species with saturated fatty acid chains and contribute to global increase of SFA containing lipid species⁵¹¹.

Interestingly, components of the ERMES complex (Table 14) are found in the “worse” category and previously it was shown that growth phenotypes of ERMES mutants can be partially rescued by overexpression of *OLE1*⁵¹².

The outlined and discussed effects of the measured diversity in lipid class composition are complemented by the finding that the degree of lipid saturation found in all glycerophospholipids correlates with the emergence of aberrant ER structures (Figure 26).

5.3.7 A preliminary model for the aberrant ER phenotype

As of now the data presented in the third section of this thesis has led to the following preliminary model for the emergence of the aberrant ER:

- 1) Insufficient amounts of the $\Delta 9$ fatty acid desaturase Ole1p in absence of its regulator Mga2p results in an overly saturated lipidome
- 2) An overly saturated lipidome is the prerequisite for the formation of the aberrant ER
- 3) Ole1p itself is regulated in a cell cycle-dependent manner
- 4) The aberrant ER forms in a cell cycle dependent manner, presumably during the M-phase of the cell cycle
- 5) The abundance of cells harboring an aberrant ER correlates with the degree of saturated glycerophospholipids
- 6) An overly saturated lipidome causes UPR activation and thereby upregulates lipid biosynthesis
- 7) Increased rate of lipid synthesis – either by growth or UPR-dependent ER membrane expansion - leads to the production of even more saturated lipids in the *mga2 Δ* background, presumably causing a perpetuation of the UPR indicated by the formation of large Ire1p cluster concomitant with aberrant ER formation
- 8) Lack of unsaturated lipids affects organelles beyond the ER as indicated by the increased proportion of the saturated mitochondrial signature CL species and demonstrated by the works on mitochondrial distribution by Stewart *et al.*⁴⁷⁷
- 9) ROS play an important role in the formation or the stabilization of the aberrant ER, because addition of vitamin c or reduced GSH to the medium can rescue WT-like ER morphologies in *mga2 Δ* cells.

5.3.8 Outlook

The formation of the aberrant ER is a dynamic process and growth dependent. To better understand the physiological and pathophysiological effects that drive the formation of these aberrant ER structures it is necessary to account for the dynamic nature of the phenotype. For that long-term observations of live cells can be performed with a microfluidic system. To determine the cell cycle-dependent formation of the aberrant ER an approach published by Garmendia-Torres *et al.* would allow to determine individual cell phases during cell cycle progression with high accuracy by fluorescently labeling the HTB2 histone⁴⁹⁵. Combining this approach with the highly photostable StayGold green fluorescent protein would enable to monitor several rounds of successive cell division⁵¹³. Given the heterogeneity of the aberrant ER phenotype, the microfluidic powered live cell imaging would also open up the possibility to monitor the level of important metabolites using various biosensors during aberrant ER formation. For example, it would be possible to follow the H₂O₂ levels via the established Prx- and OxyR-based sensors to study if ROS are indeed involved in the formation of the aberrant ER⁵¹⁴. In support of the H₂O₂ assessment, and given the short half-lives of ROS, a determination of lipid degradation byproducts in form of thiobarbituric acid reactive substances (TBARS) would be interesting as this would help to understand whether ROS are only involved in signaling or have an adverse effect in form of lipid peroxidation. Although saturated fatty acids are less vulnerable to lipid peroxidation than their mono- and polyunsaturated counterparts⁵¹⁵, a study on oxidative stress induced by heavy metals could assess significant differences by applying a TBAR assay in relation to SOD activity⁵¹⁶. Although *S. cerevisiae* was used as a model organism, which is defined by its limited fatty acid pool of mostly C16:1, C18:1 and their respective saturated counterparts the authors could still apply the TBARS assay to determine oxidative stress⁵¹⁶. Carbonyl groups can serve as markers for protein oxidation, hence an alternative approach to verify whether ROS cause increased oxidative stress in *mga2Δ* cells would be to monitor protein carbonylation⁵¹⁷. To better understand the contribution of an aberrant energy metabolism that might contribute to the formation of the aberrant ER it would be interesting to determine the NAD⁺/NADH and NADP⁺/NADPH levels and the cellular ATP/ADP levels^{518–521}. NAD⁺/NADH and NADP⁺/NADPH ratios can be traced with iNap probes, which have a high sensitivity and pH stability⁵¹⁹. If redox-biology indeed plays an important role in the formation of aberrant ER structures, it would be tempting to manipulate and drive this phenotype using a compartment-specific expression of the soluble transhydrogenase EcSTH from *E. coli* to perturb redox metabolism⁵²².

I would further suggest to continue co-localization studies with cytoskeleton components and an appropriate ER marker. The characteristic shape of the aberrant ER might help identifying new connections between the ER and the cytoskeleton.

Observations made in baker's yeast may be transferrable to a large extent also to mammalian cells. A recent unpublished study shows the emergence of aberrant ER-like structures in mouse embryonic fibroblasts in an AdipoR1/2 knock-out cell line⁵²³. These aberrant ER-like structures appear as straight thin lines and, just like in yeast, their long side faces the nucleus. AdipoR1/R2 are lipid hydrolases that catalyze the hydrolysis of ceramides⁵²⁴ and were further shown to regulate the expression of the $\Delta 9$ desaturase stearoyl-CoA desaturase 1 (SCD1) in mammals to maintain membrane fluidity^{523,525}. Volkmar *et al.* demonstrated that, similar to the OLE1 pathway, the mammalian system requires ERAD components to control membrane homeostasis⁵²⁵. In an unbiased proteomic approach, they identify a regulatory pathway consisting of the ER-resident E3 ligase RNF145 and AdipoR2. The current model states that RNF145 is the sensory unit of this sense and response mechanism, as it promotes ubiquitination and subsequent degradation of AdipoR2 in unsaturated lipid membranes, whereas in the presence of an overly saturated ER membrane it exhibits auto ubiquitination that causes its own degradation. The degradation of the E3 ligase AdipoR2, which either directly counteracts membrane stiffening by catalyzing the hydrolysis of ceramides or indirectly by initiating the generation of sphingosine 1-phosphate (S1P) as a signaling molecule to upregulate S1PR3-SREPB and PPAR γ transcription factors, ultimately leading to the upregulation of SCD1⁵²³. Since the work by Ruiz *et al.* does not address the molecular mechanism that causes the mammalian version of the aberrant ER⁵²³, it would be interesting to use the powerful genetics of yeast to pursue the ROS theory and validate whether ROS can contribute to the mammalian version of the aberrant ER. This seems interesting since the mammalian acyl chain composition is far more complex than that of yeast and the presence of PUFAS makes them more susceptible to lipid peroxidation.

Taken together, the third part of my thesis demonstrates that the simple eukaryotic model system *S. cerevisiae* allows one to study how the UPR could contribute to disease development, progression and chronification thereof by perpetuating a stress-inducing conditions as indicated by the clustering of Ire1p concomitant with the manifestation of aberrant ER structures (Figure 46 – supplementary information). The *mga2* Δ strain is an excellent system to study the molecular events that switch the UPR from a beneficial, homeostatic response to a detrimental, cell death inducing program under LBS.

6 References

1. Reinhard J, Mattes C, Väh K, et al. A Quantitative Analysis of Cellular Lipid Compositions During Acute Proteotoxic ER Stress Reveals Specificity in the Production of Asymmetric Lipids. *Front Cell Dev Biol.* 2020;8. doi:10.3389/fcell.2020.00756
2. Väh K, Mattes C, Reinhard J, et al. Cysteine cross-linking in native membranes establishes the transmembrane architecture of Ire1. *Journal of Cell Biology.* 2021;220(8). doi:10.1083/jcb.202011078
3. Dalton J. *A New System of Chemical Philosophy.* Cambridge University Press; 2010. doi:10.1017/CBO9780511736391
4. Anniversary celebrations are due for Mendeleev's periodic table. *Nature.* 2019;565(7741):535-535. doi:10.1038/d41586-019-00281-z
5. Darwin C. *On the Origin of Species by Means of Natural Selection, or the Preservation of Favoured Races in the Struggle for Life.* first edition. John Murray; 1859.
6. Reznick D. The tree and the table: Darwin, Mendeleev and the meaning of 'theory.' *Philosophical Transactions of the Royal Society A: Mathematical, Physical and Engineering Sciences.* 2020;378(2180):20190309. doi:10.1098/rsta.2019.0309
7. Wilde SA, Valley JW, Peck WH, Graham CM. Evidence from detrital zircons for the existence of continental crust and oceans on the Earth 4.4 Gyr ago. *Nature.* 2001;409(6817):175-178. doi:10.1038/35051550
8. Hooke R. *Micrographia: Or, Some Physiological Descriptions of Minute Bodies Made by Magnifying Glasses. With Observations and Inquiries Thereupon.* Printed by J. Martyn and J. Allestry; 1665.
9. Antony van Leeuwenhoek and his "Little Animals": being some Account of the Father of Protozoology and Bacteriology and his Multifarious Discoveries in these Disciplines. *Nature.* 1932;130(3288):679-680. doi:10.1038/130679a0
10. Abbe E. Beiträge zur Theorie des Mikroskops und der mikroskopischen Wahrnehmung. *Archiv für Mikroskopische Anatomie.* 1873;9(1):413-468. doi:10.1007/BF02956173
11. Rayleigh. XXXI. *Investigations in optics, with special reference to the spectroscope.* *The London, Edinburgh, and Dublin Philosophical Magazine and Journal of Science.* 1879;8(49):261-274. doi:10.1080/14786447908639684

12. Ayache J, Beaunier L, Boumendil J, Ehret G, Laub D. Artifacts in Transmission Electron Microscopy. In: *Sample Preparation Handbook for Transmission Electron Microscopy*. Springer New York; 2010:125-170. doi:10.1007/978-0-387-98182-6_6
13. Palade GE. A STUDY OF FIXATION FOR ELECTRON MICROSCOPY. *Journal of Experimental Medicine*. 1952;95(3):285-298. doi:10.1084/jem.95.3.285
14. Porter KR, Claude A, Fullam EF. A STUDY OF TISSUE CULTURE CELLS BY ELECTRON MICROSCOPY. *Journal of Experimental Medicine*. 1945;81(3):233-246. doi:10.1084/jem.81.3.233
15. Appelmans F, Wattiaux R, de Duve C. Tissue fractionation studies. 5. The association of acid phosphatase with a special class of cytoplasmic granules in rat liver. *Biochemical Journal*. 1955;59(3):438-445. doi:10.1042/bj0590438
16. Williams RT, Bridges JW. Fluorescence of solutions: A review. *J Clin Pathol*. 1964;17(4):371-394. doi:10.1136/jcp.17.4.371
17. Baeyer A. Ueber eine neue Klasse von Farbstoffen. *Berichte der deutschen chemischen Gesellschaft*. 1871;4(2):555-558. doi:10.1002/cber.18710040209
18. Coons AH, Creech HJ, Jones RN. Immunological Properties of an Antibody Containing a Fluorescent Group. *Exp Biol Med*. 1941;47(2):200-202. doi:10.3181/00379727-47-13084P
19. Shimomura O, Johnson FH, Saiga Y. Extraction, Purification and Properties of Aequorin, a Bioluminescent Protein from the Luminous Hydromedusan, Aequorea. *J Cell Comp Physiol*. 1962;59(3):223-239. doi:10.1002/jcp.1030590302
20. Chalfie M, Tu Y, Euskirchen G, Ward WW, Prasher DC. Green Fluorescent Protein as a Marker for Gene Expression. *Science (1979)*. 1994;263(5148):802-805. doi:10.1126/science.8303295
21. Gerdes HH, Kaether C. Green fluorescent protein: applications in cell biology. *FEBS Lett*. 1996;389(1):44-47. doi:10.1016/0014-5793(96)00586-8
22. Wang S, Hazelrigg T. Implications for bcd mRNA localization from spatial distribution of exu protein in Drosophila oogenesis. *Nature*. 1994;369(6479):400-403. doi:10.1038/369400a0
23. Stearns T. Green Fluorescent Protein: The green revolution. *Current Biology*. 1995;5(3):262-264. doi:10.1016/S0960-9822(95)00056-X

24. Hell SW, Wichmann J. Breaking the diffraction resolution limit by stimulated emission: stimulated-emission-depletion fluorescence microscopy. *Opt Lett*. 1994;19(11):780. doi:10.1364/OL.19.000780
25. Klar TA, Hell SW. Subdiffraction resolution in far-field fluorescence microscopy. *Opt Lett*. 1999;24(14):954. doi:10.1364/OL.24.000954
26. Singer SJ, Nicolson GL. The Fluid Mosaic Model of the Structure of Cell Membranes. *Science (1979)*. 1972;175(4023):720-731. doi:10.1126/science.175.4023.720
27. Billman GE. Homeostasis: The Underappreciated and Far Too Often Ignored Central Organizing Principle of Physiology. *Front Physiol*. 2020;11. doi:10.3389/fphys.2020.00200
28. Martin WF, Garg S, Zimorski V. Endosymbiotic theories for eukaryote origin. *Philosophical Transactions of the Royal Society B: Biological Sciences*. 2015;370(1678):20140330. doi:10.1098/rstb.2014.0330
29. Martin W, Koonin E v. Introns and the origin of nucleus–cytosol compartmentalization. *Nature*. 2006;440(7080):41-45. doi:10.1038/nature04531
30. Zaremba-Niedzwiedzka K, Caceres EF, Saw JH, et al. Asgard archaea illuminate the origin of eukaryotic cellular complexity. *Nature*. 2017;541(7637):353-358. doi:10.1038/nature21031
31. Ettema TJG, Lindås AC, Bernander R. An actin-based cytoskeleton in archaea. *Mol Microbiol*. 2011;80(4):1052-1061. doi:10.1111/j.1365-2958.2011.07635.x
32. Yutin N, Koonin E v. Archaeal origin of tubulin. *Biol Direct*. 2012;7(1):10. doi:10.1186/1745-6150-7-10
33. Spang A, Saw JH, Jørgensen SL, et al. Complex archaea that bridge the gap between prokaryotes and eukaryotes. *Nature*. 2015;521(7551):173-179. doi:10.1038/nature14447
34. Karnkowska A, Vacek V, Zubáčová Z, et al. A Eukaryote without a Mitochondrial Organelle. *Current Biology*. 2016;26(10):1274-1284. doi:10.1016/j.cub.2016.03.053
35. Vacek V, Novák LVF, Treitli SC, et al. Fe–S Cluster Assembly in Oxymonads and Related Protists. *Mol Biol Evol*. Published online September 1, 2018. doi:10.1093/molbev/msy168

36. Almeida C, Amaral MD. A central role of the endoplasmic reticulum in the cell emerges from its functional contact sites with multiple organelles. *Cellular and Molecular Life Sciences*. 2020;77(23):4729-4745. doi:10.1007/s00018-020-03523-w
37. Barlowe CK, Miller EA. Secretory protein biogenesis and traffic in the early secretory pathway. *Genetics*. 2013;193(2):383-410. doi:10.1534/genetics.112.142810
38. Braakman I, Bulleid NJ. Protein Folding and Modification in the Mammalian Endoplasmic Reticulum. *Annu Rev Biochem*. 2011;80(1):71-99. doi:10.1146/annurev-biochem-062209-093836
39. Wu H, Carvalho P, Voeltz GK. Here, there, and everywhere: The importance of ER membrane contact sites. *Science (1979)*. 2018;361(6401). doi:10.1126/science.aan5835
40. Wu Y, Whiteus C, Xu CS, et al. Contacts between the endoplasmic reticulum and other membranes in neurons. *Proceedings of the National Academy of Sciences*. 2017;114(24). doi:10.1073/pnas.1701078114
41. Gao M, Huang X, Song BL, Yang H. The biogenesis of lipid droplets: Lipids take center stage. *Prog Lipid Res*. 2019;75:100989. doi:10.1016/j.plipres.2019.100989
42. Lin S, Meng T, Huang H, et al. Molecular machineries and physiological relevance of ER-mediated membrane contacts. *Theranostics*. 2021;11(2):974-995. doi:10.7150/thno.51871
43. Castro IG, Shortill SP, Dziurdzik SK, et al. Systematic analysis of membrane contact sites in *Saccharomyces cerevisiae* uncovers modulators of cellular lipid distribution. *Elife*. 2022;11. doi:10.7554/eLife.74602
44. Lynch M, Ackerman MS, Gout JF, et al. Genetic drift, selection and the evolution of the mutation rate. *Nat Rev Genet*. 2016;17(11):704-714. doi:10.1038/nrg.2016.104
45. Gout JF, Li W, Fritsch C, et al. The landscape of transcription errors in eukaryotic cells. *Sci Adv*. 2017;3(10). doi:10.1126/sciadv.1701484
46. Kramer EB, Vallabhaneni H, Mayer LM, Farabaugh PJ. A comprehensive analysis of translational missense errors in the yeast *Saccharomyces cerevisiae*. *RNA*. 2010;16(9):1797-1808. doi:10.1261/rna.2201210
47. Radanović T, Ernst R. The Unfolded Protein Response as a Guardian of the Secretory Pathway. *Cells*. 2021;10(11):2965. doi:10.3390/cells10112965

48. Mori K. The unfolded protein response: the dawn of a new field. *Proc Jpn Acad Ser B Phys Biol Sci.* 2015;91(9):469-480. doi:10.2183/pjab.91.469
49. Preissler S, Rato C, Yan Y, Perera LA, Czako A, Ron D. Calcium depletion challenges endoplasmic reticulum proteostasis by destabilising BiP-substrate complexes. *Elife.* 2020;9. doi:10.7554/eLife.62601
50. Santos CXC, Tanaka LY, Wosniak J, Laurindo FRM. Mechanisms and Implications of Reactive Oxygen Species Generation During the Unfolded Protein Response: Roles of Endoplasmic Reticulum Oxidoreductases, Mitochondrial Electron Transport, and NADPH Oxidase. *Antioxid Redox Signal.* 2009;11(10):2409-2427. doi:10.1089/ars.2009.2625
51. Mujcic H, Rzymiski T, Rouschop KMA, et al. Hypoxic activation of the unfolded protein response (UPR) induces expression of the metastasis-associated gene LAMP3. *Radiotherapy and Oncology.* 2009;92(3):450-459. doi:10.1016/j.radonc.2009.08.017
52. Johnston BP, McCormick C. Herpesviruses and the Unfolded Protein Response. *Viruses.* 2019;12(1):17. doi:10.3390/v12010017
53. Tam AB, Roberts LS, Chandra V, et al. The UPR Activator ATF6 Responds to Proteotoxic and Lipotoxic Stress by Distinct Mechanisms. *Dev Cell.* 2018;46(3):327-343.e7. doi:10.1016/j.devcel.2018.04.023
54. Chattopadhyay A, Kwartler CS, Kaw K, et al. Cholesterol-Induced Phenotypic Modulation of Smooth Muscle Cells to Macrophage/Fibroblast-like Cells Is Driven by an Unfolded Protein Response. *Arterioscler Thromb Vasc Biol.* Published online October 8, 2020. doi:10.1161/ATVBAHA.120.315164
55. Pineau L, Colas J, Dupont S, et al. Lipid-Induced ER Stress: Synergistic Effects of Sterols and Saturated Fatty Acids. *Traffic.* 2009;10(6):673-690. doi:10.1111/j.1600-0854.2009.00903.x
56. Promlek T, Ishiwata-Kimata Y, Shido M, Sakuramoto M, Kohno K, Kimata Y. Membrane aberrancy and unfolded proteins activate the endoplasmic reticulum stress sensor Ire1 in different ways. *Mol Biol Cell.* 2011;22(18). doi:10.1091/mbc.E11-04-0295
57. Travers KJ, Patil CK, Wodicka L, Lockhart DJ, Weissman JS, Walter P. Functional and Genomic Analyses Reveal an Essential Coordination between the Unfolded Protein Response and ER-Associated Degradation. *Cell.* 2000;101(3):249-258. doi:10.1016/S0092-8674(00)80835-1

58. Hetz C, Zhang K, Kaufman RJ. Mechanisms, regulation and functions of the unfolded protein response. *Nat Rev Mol Cell Biol.* 2020;21(8):421-438. doi:10.1038/s41580-020-0250-z
59. Hassler JR, Scheuner DL, Wang S, et al. The IRE1 α /XBP1s Pathway Is Essential for the Glucose Response and Protection of β Cells. *PLoS Biol.* 2015;13(10):e1002277. doi:10.1371/journal.pbio.1002277
60. Lipson KL, Fonseca SG, Ishigaki S, et al. Regulation of insulin biosynthesis in pancreatic beta cells by an endoplasmic reticulum-resident protein kinase IRE1. *Cell Metab.* 2006;4(3):245-254. doi:10.1016/j.cmet.2006.07.007
61. Harding HP, Zeng H, Zhang Y, et al. Diabetes Mellitus and Exocrine Pancreatic Dysfunction in Perk $^{-/-}$ Mice Reveals a Role for Translational Control in Secretory Cell Survival. *Mol Cell.* 2001;7(6):1153-1163. doi:10.1016/S1097-2765(01)00264-7
62. Wang JM, Qiu Y, Yang Z, et al. IRE1 α prevents hepatic steatosis by processing and promoting the degradation of select microRNAs. *Sci Signal.* 2018;11(530). doi:10.1126/scisignal.aao4617
63. Zhang K, Wang S, Malhotra J, et al. The unfolded protein response transducer IRE1 α prevents ER stress-induced hepatic steatosis. *EMBO J.* 2011;30(7):1357-1375. doi:10.1038/emboj.2011.52
64. Yamamoto K, Takahara K, Oyadomari S, et al. Induction of Liver Steatosis and Lipid Droplet Formation in ATF6 α -Knockout Mice Burdened with Pharmacological Endoplasmic Reticulum Stress. *Mol Biol Cell.* 2010;21(17):2975-2986. doi:10.1091/mbc.e09-02-0133
65. Rutkowski DT, Wu J, Back SH, et al. UPR Pathways Combine to Prevent Hepatic Steatosis Caused by ER Stress-Mediated Suppression of Transcriptional Master Regulators. *Dev Cell.* 2008;15(6):829-840. doi:10.1016/j.devcel.2008.10.015
66. Kozutsumi Y, Segal M, Normington K, Gething MJ, Sambrook J. The presence of malfolded proteins in the endoplasmic reticulum signals the induction of glucose-regulated proteins. *Nature.* 1988;332(6163):462-464. doi:10.1038/332462a0
67. Morl K, Ma W, Gething MJ, Sambrook J. A transmembrane protein with a cdc2+CDC28-related kinase activity is required for signaling from the ER to the nucleus. *Cell.* 1993;74(4):743-756. doi:10.1016/0092-8674(93)90521-Q

68. Cox JS, Shamu CE, Walter P. Transcriptional induction of genes encoding endoplasmic reticulum resident proteins requires a transmembrane protein kinase. *Cell*. 1993;73(6):1197-1206. doi:10.1016/0092-8674(93)90648-A
69. Ali MMU, Bagratuni T, Davenport EL, et al. Structure of the Ire1 autophosphorylation complex and implications for the unfolded protein response. *EMBO J*. 2011;30(5):894-905. doi:10.1038/emboj.2011.18
70. Cox JS, Walter P. A Novel Mechanism for Regulating Activity of a Transcription Factor That Controls the Unfolded Protein Response. *Cell*. 1996;87(3):391-404. doi:10.1016/S0092-8674(00)81360-4
71. Sidrauski C, Cox JS, Walter P. tRNA Ligase Is Required for Regulated mRNA Splicing in the Unfolded Protein Response. *Cell*. 1996;87(3):405-413. doi:10.1016/S0092-8674(00)81361-6
72. Kohno K, Normington K, Sambrook J, Gething MJ, Mori K. The promoter region of the yeast KAR2 (BiP) gene contains a regulatory domain that responds to the presence of unfolded proteins in the endoplasmic reticulum. *Mol Cell Biol*. 1993;13(2):877-890. doi:10.1128/mcb.13.2.877-890.1993
73. Credle JJ, Finer-Moore JS, Papa FR, Stroud RM, Walter P. On the mechanism of sensing unfolded protein in the endoplasmic reticulum. *Proceedings of the National Academy of Sciences*. 2005;102(52):18773-18784. doi:10.1073/pnas.0509487102
74. Korennykh A v., Egea PF, Korostelev AA, et al. The unfolded protein response signals through high-order assembly of Ire1. *Nature*. 2009;457(7230):687-693. doi:10.1038/nature07661
75. Shamu CE, Walter P. Oligomerization and phosphorylation of the Ire1p kinase during intracellular signaling from the endoplasmic reticulum to the nucleus. *EMBO J*. 1996;15(12):3028-3039.
76. Sundaram A, Appathurai S, Plumb R, Mariappan M. Dynamic changes in complexes of IRE1 α , PERK, and ATF6 α during endoplasmic reticulum stress. *Mol Biol Cell*. 2018;29(11):1376-1388. doi:10.1091/mbc.E17-10-0594
77. Welihinda AA, Kaufman RJ. The Unfolded Protein Response Pathway in *Saccharomyces cerevisiae*. Oligomerization and trans-phosphorylation of Ire1p (Ern1p) are required for kinase activation. *Journal of Biological Chemistry*. 1996;271(30):18181-18187. doi:10.1074/jbc.271.30.18181

78. Oikawa D, Kimata Y, Takeuchi M, Kohno K. An essential dimer-forming subregion of the endoplasmic reticulum stress sensor Ire1. *Biochemical Journal*. 2005;391(1):135-142. doi:10.1042/BJ20050640
79. Zhou J, Liu CY, Back SH, et al. The crystal structure of human IRE1 luminal domain reveals a conserved dimerization interface required for activation of the unfolded protein response. *Proceedings of the National Academy of Sciences*. 2006;103(39):14343-14348. doi:10.1073/pnas.0606480103
80. Liu CY, Schröder M, Kaufman RJ. Ligand-independent Dimerization Activates the Stress Response Kinases IRE1 and PERK in the Lumen of the Endoplasmic Reticulum. *Journal of Biological Chemistry*. 2000;275(32):24881-24885. doi:10.1074/jbc.M004454200
81. Kimata Y, Ishiwata-Kimata Y, Ito T, et al. Two regulatory steps of ER-stress sensor Ire1 involving its cluster formation and interaction with unfolded proteins. *Journal of Cell Biology*. 2007;179(1):75-86. doi:10.1083/jcb.200704166
82. Gautier R, Douguet D, Antonny B, Drin G. HELIQUEST: a web server to screen sequences with specific α -helical properties. *Bioinformatics*. 2008;24(18):2101-2102. doi:10.1093/bioinformatics/btn392
83. Walter P, Ron D. The Unfolded Protein Response: From Stress Pathway to Homeostatic Regulation. *Science (1979)*. 2011;334(6059):1081-1086. doi:10.1126/science.1209038
84. van Anken E, Pincus D, Coyle S, et al. Specificity in endoplasmic reticulum-stress signaling in yeast entails a step-wise engagement of HAC1 mRNA to clusters of the stress sensor Ire1. *Elife*. 2014;3. doi:10.7554/eLife.05031
85. Rubio C, Pincus D, Korennykh A, Schuck S, El-Samad H, Walter P. Homeostatic adaptation to endoplasmic reticulum stress depends on Ire1 kinase activity. *Journal of Cell Biology*. 2011;193(1):171-184. doi:10.1083/jcb.201007077
86. Chawla A, Chakrabarti S, Ghosh G, Niwa M. Attenuation of yeast UPR is essential for survival and is mediated by IRE1 kinase. *Journal of Cell Biology*. 2011;193(1):41-50. doi:10.1083/jcb.201008071
87. Halbleib K, Pesek K, Covino R, et al. Activation of the Unfolded Protein Response by Lipid Bilayer Stress. *Mol Cell*. 2017;67(4):673-684.e8. doi:10.1016/j.molcel.2017.06.012

88. Ho N, Yap WS, Xu J, et al. Stress sensor Ire1 deploys a divergent transcriptional program in response to lipid bilayer stress. *Journal of Cell Biology*. 2020;219(7). doi:10.1083/jcb.201909165
89. Botstein D, Fink GR. Yeast: An Experimental Organism for 21st Century Biology. *Genetics*. 2011;189(3):695-704. doi:10.1534/genetics.111.130765
90. Goffeau A, Barrell BG, Bussey H, et al. Life with 6000 Genes. *Science (1979)*. 1996;274(5287):546-567. doi:10.1126/science.274.5287.546
91. Daum G, Lees ND, Bard M, Dickson R. Biochemistry, cell biology and molecular biology of lipids of *Saccharomyces cerevisiae*. *Yeast*. 1998;14(16):1471-1510. doi:10.1002/(SICI)1097-0061(199812)14:16<1471::AID-YEA353>3.0.CO;2-Y
92. Levental I, Lyman E. Regulation of membrane protein structure and function by their lipid nano-environment. *Nat Rev Mol Cell Biol*. Published online September 2, 2022. doi:10.1038/s41580-022-00524-4
93. Gonen T, Cheng Y, Sliz P, et al. Lipid-protein interactions in double-layered two-dimensional AQP0 crystals. *Nature*. 2005;438(7068):633-638. doi:10.1038/nature04321
94. Farese R v., Walther TC. Lipid Droplets Finally Get a Little R-E-S-P-E-C-T. *Cell*. 2009;139(5):855-860. doi:10.1016/j.cell.2009.11.005
95. Holthuis JCM, Levine TP. Lipid traffic: floppy drives and a superhighway. *Nat Rev Mol Cell Biol*. 2005;6(3):209-220. doi:10.1038/nrm1591
96. Holthuis JCM, Menon AK. Lipid landscapes and pipelines in membrane homeostasis. *Nature*. 2014;510(7503):48-57. doi:10.1038/nature13474
97. Dufourc EJ. Sterols and membrane dynamics. *J Chem Biol*. 2008;1(1-4):63-77. doi:10.1007/s12154-008-0010-6
98. Thurmond RL, Niemi AR, Lindblom G, Wieslander A, Rilfors L. Membrane Thickness and Molecular Ordering in *Acholeplasma laidlawii* Strain A Studied by 2H NMR Spectroscopy. *Biochemistry*. 1994;33(45):13178-13188. doi:10.1021/bi00249a004
99. Leekumjorn S, Cho HJ, Wu Y, Wright NT, Sum AK, Chan C. The role of fatty acid unsaturation in minimizing biophysical changes on the structure and local effects of bilayer membranes. *Biochimica et Biophysica Acta (BBA) - Biomembranes*. 2009;1788(7):1508-1516. doi:10.1016/j.bbamem.2009.04.002

100. Ernst R, Ejsing CS, Antonny B. Homeoviscous Adaptation and the Regulation of Membrane Lipids. *J Mol Biol.* 2016;428(24):4776-4791. doi:10.1016/j.jmb.2016.08.013
101. Stukey JE, McDonough VM, Martin CE. Isolation and characterization of OLE1, a gene affecting fatty acid desaturation from *Saccharomyces cerevisiae*. *Journal of Biological Chemistry.* 1989;264(28):16537-16544. doi:10.1016/S0021-9258(19)84740-3
102. Nakamura MT, Nara TY. STRUCTURE, FUNCTION, AND DIETARY REGULATION OF $\Delta 6$, $\Delta 5$, AND $\Delta 9$ DESATURASES. *Annu Rev Nutr.* 2004;24(1):345-376. doi:10.1146/annurev.nutr.24.121803.063211
103. Nakamura MT, Nara TY. Essential fatty acid synthesis and its regulation in mammals. *Prostaglandins Leukot Essent Fatty Acids.* 2003;68(2):145-150. doi:10.1016/S0952-3278(02)00264-8
104. Ejsing CS, Sampaio JL, Surendranath V, et al. Global analysis of the yeast lipidome by quantitative shotgun mass spectrometry. *Proceedings of the National Academy of Sciences.* 2009;106(7):2136-2141. doi:10.1073/pnas.0811700106
105. Yetukuri L, Ekroos K, Vidal-Puig A, Orešič M. Informatics and computational strategies for the study of lipids. *Mol BioSyst.* 2008;4(2):121-127. doi:10.1039/B715468B
106. Stordeur C, Puth K, Sáenz JP, Ernst R. Crosstalk of lipid and protein homeostasis to maintain membrane function. *bchm.* 2014;395(3):313-326. doi:10.1515/hsz-2013-0235
107. Keenan TW, Morre DJ. Phospholipid class and fatty acid composition of Golgi apparatus isolated from rat liver and comparison with other cell fractions. *Biochemistry.* 1970;9(1):19-25. doi:10.1021/bi00803a003
108. Reinhard J, Starke L, Klose C, et al. A new technology for isolating organellar membranes provides fingerprints of lipid bilayer stress. *bioRxiv.* Published online January 1, 2022:2022.09.15.508072. doi:10.1101/2022.09.15.508072
109. Zinser E, Sperka-Gottlieb CD, Fasch E v, Kohlwein SD, Paltauf F, Daum G. Phospholipid synthesis and lipid composition of subcellular membranes in the unicellular eukaryote *Saccharomyces cerevisiae*. *J Bacteriol.* 1991;173(6):2026-2034. doi:10.1128/jb.173.6.2026-2034.1991
110. Ermilova I, Lyubartsev AP. Cholesterol in phospholipid bilayers: positions and orientations inside membranes with different unsaturation degrees. *Soft Matter.* 2019;15(1):78-93. doi:10.1039/C8SM01937A

111. Ploier B, Korber M, Schmidt C, Koch B, Leitner E, Daum G. Regulatory link between steryl ester formation and hydrolysis in the yeast *Saccharomyces cerevisiae*. *Biochimica et Biophysica Acta (BBA) - Molecular and Cell Biology of Lipids*. 2015;1851(7):977-986. doi:10.1016/j.bbalip.2015.02.011
112. Kohlwein SD, Veenhuis M, van der Klei IJ. Lipid Droplets and Peroxisomes: Key Players in Cellular Lipid Homeostasis or A Matter of Fat—Store 'em Up or Burn 'em Down. *Genetics*. 2013;193(1):1-50. doi:10.1534/genetics.112.143362
113. Tehlivets O, Scheuringer K, Kohlwein SD. Fatty acid synthesis and elongation in yeast. *Biochimica et Biophysica Acta (BBA) - Molecular and Cell Biology of Lipids*. 2007;1771(3):255-270. doi:10.1016/j.bbalip.2006.07.004
114. Black PN, DiRusso CC. Yeast acyl-CoA synthetases at the crossroads of fatty acid metabolism and regulation. *Biochimica et Biophysica Acta (BBA) - Molecular and Cell Biology of Lipids*. 2007;1771(3):286-298. doi:10.1016/j.bbalip.2006.05.003
115. Zheng Z, Zou J. The Initial Step of the Glycerolipid Pathway. *Journal of Biological Chemistry*. 2001;276(45):41710-41716. doi:10.1074/jbc.M104749200
116. Athenstaedt K, Daum G. Biosynthesis of phosphatidic acid in lipid particles and endoplasmic reticulum of *Saccharomyces cerevisiae*. *J Bacteriol*. 1997;179(24):7611-7616. doi:10.1128/jb.179.24.7611-7616.1997
117. Benghezal M, Roubaty C, Veepuri V, Knudsen J, Conzelmann A. SLC1 and SLC4 Encode Partially Redundant Acyl-Coenzyme A 1-Acylglycerol-3-phosphate O-Acyltransferases of Budding Yeast. *Journal of Biological Chemistry*. 2007;282(42):30845-30855. doi:10.1074/jbc.M702719200
118. Oelkers P, Cromley D, Padamsee M, Billheimer JT, Sturley SL. The DGA1 Gene Determines a Second Triglyceride Synthetic Pathway in Yeast. *Journal of Biological Chemistry*. 2002;277(11):8877-8881. doi:10.1074/jbc.M111646200
119. Ruggles K v., Turkish A, Sturley SL. Making, Baking, and Breaking: the Synthesis, Storage, and Hydrolysis of Neutral Lipids. *Annu Rev Nutr*. 2013;33(1):413-451. doi:10.1146/annurev-nutr-071812-161254
120. Dahlqvist A, Ståhl U, Lenman M, et al. Phospholipid:diacylglycerol acyltransferase: An enzyme that catalyzes the acyl-CoA-independent formation of triacylglycerol in yeast and plants. *Proceedings of the National Academy of Sciences*. 2000;97(12):6487-6492. doi:10.1073/pnas.120067297

121. Oelkers P, Tinkelenberg A, Erdeniz N, Cromley D, Billheimer JT, Sturley SL. A Lecithin Cholesterol Acyltransferase-like Gene Mediates Diacylglycerol Esterification in Yeast. *Journal of Biological Chemistry*. 2000;275(21):15609-15612. doi:10.1074/jbc.C000144200
122. Klug L, Daum G. Yeast lipid metabolism at a glance. *FEMS Yeast Res*. 2014;14(3):369-388. doi:10.1111/1567-1364.12141
123. Dean-Johnson M, Henry SA. Biosynthesis of inositol in yeast. Primary structure of myo-inositol-1-phosphate synthase (EC 5.5.1.4) and functional analysis of its structural gene, the INO1 locus. *J Biol Chem*. 1989;264(2):1274-1283.
124. Nikawa J, Tsukagoshi Y, Yamashita S. Isolation and characterization of two distinct myo-inositol transporter genes of *Saccharomyces cerevisiae*. *J Biol Chem*. 1991;266(17):11184-11191.
125. Nikawa J, Yamashita S. Molecular cloning of the gene encoding CDPdiacylglycerol-inositol 3-phosphatidyl transferase in *Saccharomyces cerevisiae*. *Eur J Biochem*. 1984;143(2):251-256. doi:10.1111/j.1432-1033.1984.tb08366.x
126. Chang SC, Heacock PN, Clancey CJ, Dowhan W. The PEL1 gene (renamed PGS1) encodes the phosphatidylglycero-phosphate synthase of *Saccharomyces cerevisiae*. *J Biol Chem*. 1998;273(16):9829-9836. doi:10.1074/jbc.273.16.9829
127. Osman C, Haag M, Wieland FT, Brügger B, Langer T. A mitochondrial phosphatase required for cardiolipin biosynthesis: the PGP phosphatase Gep4. *EMBO J*. 2010;29(12):1976-1987. doi:10.1038/emboj.2010.98
128. Chang SC, Heacock PN, Mileykovskaya E, Voelker DR, Dowhan W. Isolation and Characterization of the Gene (CLS1) Encoding Cardiolipin Synthase in *Saccharomyces cerevisiae*. *Journal of Biological Chemistry*. 1998;273(24):14933-14941. doi:10.1074/jbc.273.24.14933
129. Beranek A, Rechberger G, Knauer H, Wolinski H, Kohlwein SeppD, Leber R. Identification of a Cardiolipin-specific Phospholipase Encoded by the Gene CLD1 (YGR110W) in Yeast. *Journal of Biological Chemistry*. 2009;284(17):11572-11578. doi:10.1074/jbc.M805511200
130. Brandner K, Mick DU, Frazier AE, Taylor RD, Meisinger C, Rehling P. Taz1, an outer mitochondrial membrane protein, affects stability and assembly of inner membrane protein complexes: implications for Barth Syndrome. *Mol Biol Cell*. 2005;16(11):5202-5214. doi:10.1091/mbc.e05-03-0256

131. Letts VA, Klig LS, Bae-Lee M, Carman GM, Henry SA. Isolation of the yeast structural gene for the membrane-associated enzyme phosphatidylserine synthase. *Proceedings of the National Academy of Sciences*. 1983;80(23):7279-7283. doi:10.1073/pnas.80.23.7279
132. KANFER J, KENNEDY EP. METABOLISM AND FUNCTION OF BACTERIAL LIPIDS. I. METABOLISM OF PHOSPHOLIPIDS IN ESCHERICHIA COLI B. *J Biol Chem*. 1963;238:2919-2922.
133. Voelker DR. Phosphatidylserine decarboxylase. *Biochim Biophys Acta*. 1997;1348(1-2):236-244. doi:10.1016/s0005-2760(97)00101-x
134. Kodaki T, Yamashita S. Yeast phosphatidylethanolamine methylation pathway. Cloning and characterization of two distinct methyltransferase genes. *J Biol Chem*. 1987;262(32):15428-15435.
135. Natter K, Leitner P, Faschinger A, et al. The Spatial Organization of Lipid Synthesis in the Yeast *Saccharomyces cerevisiae* Derived from Large Scale Green Fluorescent Protein Tagging and High Resolution Microscopy. *Molecular & Cellular Proteomics*. 2005;4(5):662-672. doi:10.1074/mcp.M400123-MCP200
136. Nikawa J, Hosaka K, Tsukagoshi Y, Yamashita S. Primary structure of the yeast choline transport gene and regulation of its expression. *J Biol Chem*. 1990;265(26):15996-16003.
137. Kim K, Kim KH, Storey MK, Voelker DR, Carman GM. Isolation and characterization of the *Saccharomyces cerevisiae* EKI1 gene encoding ethanolamine kinase. *J Biol Chem*. 1999;274(21):14857-14866. doi:10.1074/jbc.274.21.14857
138. Kim KH, Voelker DR, Flocco MT, Carman GM. Expression, purification, and characterization of choline kinase, product of the CKI gene from *Saccharomyces cerevisiae*. *J Biol Chem*. 1998;273(12):6844-6852. doi:10.1074/jbc.273.12.6844
139. Min-Seok R, Kawamata Y, Nakamura H, Ohta A, Takagi M. Isolation and characterization of ECT1 gene encoding CTP: phosphoethanolamine cytidyltransferase of *Saccharomyces cerevisiae*. *J Biochem*. 1996;120(5):1040-1047. doi:10.1093/oxfordjournals.jbchem.a021497
140. Tsukagoshi Y, Nikawa J, Yamashita S. Molecular cloning and characterization of the gene encoding cholinephosphate cytidyltransferase in *Saccharomyces cerevisiae*. *Eur J Biochem*. 1987;169(3):477-486. doi:10.1111/j.1432-1033.1987.tb13635.x

141. Hjelmstad RH, Bell RM. The sn-1,2-diacylglycerol ethanolaminephosphotransferase activity of *Saccharomyces cerevisiae*. Isolation of mutants and cloning of the EPT1 gene. *J Biol Chem*. 1988;263(36):19748-19757.
142. Hjelmstad RH, Bell RM. Mutants of *Saccharomyces cerevisiae* defective in sn-1,2-diacylglycerol cholinephosphotransferase. Isolation, characterization, and cloning of the CPT1 gene. *J Biol Chem*. 1987;262(8):3909-3917.
143. Puoti A, Desponds C, Conzelmann A. Biosynthesis of mannosylinositolphosphoceramide in *Saccharomyces cerevisiae* is dependent on genes controlling the flow of secretory vesicles from the endoplasmic reticulum to the Golgi. *Journal of Cell Biology*. 1991;113(3):515-525. doi:10.1083/jcb.113.3.515
144. Hanada K. Serine palmitoyltransferase, a key enzyme of sphingolipid metabolism. *Biochimica et Biophysica Acta (BBA) - Molecular and Cell Biology of Lipids*. 2003;1632(1-3):16-30. doi:10.1016/S1388-1981(03)00059-3
145. Beeler T, Bacikova D, Gable K, et al. The *Saccharomyces cerevisiae* TSC10/YBR265w Gene Encoding 3-Ketosphinganine Reductase Is Identified in a Screen for Temperature-sensitive Suppressors of the Ca²⁺-sensitive *csg2Δ* Mutant. *Journal of Biological Chemistry*. 1998;273(46):30688-30694. doi:10.1074/jbc.273.46.30688
146. Ren J, Hannun YA. Metabolism and Roles of Sphingolipids in Yeast *Saccharomyces cerevisiae*. In: *Biogenesis of Fatty Acids, Lipids and Membranes*. Springer International Publishing; 2016:1-21. doi:10.1007/978-3-319-43676-0_21-1
147. Guillas I. C26-CoA-dependent ceramide synthesis of *Saccharomyces cerevisiae* is operated by Lag1p and Lac1p. *EMBO J*. 2001;20(11):2655-2665. doi:10.1093/emboj/20.11.2655
148. Schorling S, Vallée B, Barz WP, Riezman H, Oesterhelt D. Lag1p and Lac1p Are Essential for the Acyl-CoA-dependent Ceramide Synthase Reaction in *Saccharomyces cerevisiae*. *Mol Biol Cell*. 2001;12(11):3417-3427. doi:10.1091/mbc.12.11.3417
149. Vallée B, Riezman H. Lip1p: a novel subunit of acyl-CoA ceramide synthase. *EMBO J*. 2005;24(4):730-741. doi:10.1038/sj.emboj.7600562
150. Nagiec MM, Nagiec EE, Baltisberger JA, Wells GB, Lester RL, Dickson RC. Sphingolipid Synthesis as a Target for Antifungal Drugs. *Journal of Biological Chemistry*. 1997;272(15):9809-9817. doi:10.1074/jbc.272.15.9809

151. Beeler TJ, Fu D, Rivera J, Monaghan E, Gable K, Dunn TM. SUR1 (CSG1/BCL21), a gene necessary for growth of *Saccharomyces cerevisiae* in the presence of high Ca²⁺ concentrations at 37°C, is required for mannosylation of inositolphosphorylceramide. *Mol Gen Genet.* 1997;255(6):570-579. doi:10.1007/s004380050530
152. Uemura S, Kihara A, Inokuchi J ichi, Igarashi Y. Csg1p and Newly Identified Csh1p Function in Mannosylinositol Phosphorylceramide Synthesis by Interacting with Csg2p. *Journal of Biological Chemistry.* 2003;278(46):45049-45055. doi:10.1074/jbc.M305498200
153. Patton JL, Lester RL. The phosphoinositol sphingolipids of *Saccharomyces cerevisiae* are highly localized in the plasma membrane. *J Bacteriol.* 1991;173(10):3101-3108. doi:10.1128/jb.173.10.3101-3108.1991
154. Zinser E, Paltauf F, Daum G. Sterol composition of yeast organelle membranes and subcellular distribution of enzymes involved in sterol metabolism. *J Bacteriol.* 1993;175(10):2853-2858. doi:10.1128/jb.175.10.2853-2858.1993
155. Hu Z, He B, Ma L, Sun Y, Niu Y, Zeng B. Recent Advances in Ergosterol Biosynthesis and Regulation Mechanisms in *Saccharomyces cerevisiae*. *Indian J Microbiol.* 2017;57(3):270-277. doi:10.1007/s12088-017-0657-1
156. Jordá T, Puig S. Regulation of Ergosterol Biosynthesis in *Saccharomyces cerevisiae*. *Genes (Basel).* 2020;11(7):795. doi:10.3390/genes11070795
157. Miaczynska M, Wagner W, Bauer BE, Schweyen RJ, Ragnini A. Ypt protein prenylation depends on the interplay among levels of Rab escort protein and geranylgeranyl diphosphate in yeast cells. *Yeast.* 2001;18(8):697-709. doi:10.1002/yea.719
158. Jennings SM, Tsay YH, Fisch TM, Robinson GW. Molecular cloning and characterization of the yeast gene for squalene synthetase. *Proceedings of the National Academy of Sciences.* 1991;88(14):6038-6042. doi:10.1073/pnas.88.14.6038
159. Yu C, Kennedy NJ, Chang CCY, Rothblatt JA. Molecular Cloning and Characterization of Two Isoforms of *Saccharomyces cerevisiae* Acyl-CoA: Sterol Acyltransferase. *Journal of Biological Chemistry.* 1996;271(39):24157-24163. doi:10.1074/jbc.271.39.24157
160. Zweytick D, Leitner E, Kohlwein SD, Yu C, Rothblatt J, Daum G. Contribution of Are1p and Are2p to steryl ester synthesis in the yeast *Saccharomyces cerevisiae*. *Eur J Biochem.* 2000;267(4):1075-1082. doi:10.1046/j.1432-1327.2000.01103.x

161. Bateman A, Martin MJ, Orchard S, et al. UniProt: the universal protein knowledgebase in 2021. *Nucleic Acids Res.* 2021;49(D1):D480-D489. doi:10.1093/nar/gkaa1100
162. Eeman Marc, Deleu Magali. From biological membranes to biomimetic model membranes. *Biotechnology, Agronomy and Society and Environment*. Published online December 31, 2010:719-736.
163. van Meer G, Voelker DR, Feigenson GW. Membrane lipids: where they are and how they behave. *Nat Rev Mol Cell Biol.* 2008;9(2):112-124. doi:10.1038/nrm2330
164. Levin IW, Bush SF. Evidence for acyl chain trans/gauche isomerization during the thermal pretransition of dipalmitoyl phosphatidylcholine bilayer dispersions. *Biochimica et Biophysica Acta (BBA) - Biomembranes.* 1981;640(3):760-766. doi:10.1016/0005-2736(81)90106-1
165. Yellin N, Levin IW. Hydrocarbon chain trans-gauche isomerization in phospholipid bilayer gel assemblies. *Biochemistry.* 1977;16(4):642-647. doi:10.1021/bi00623a014
166. Weete JD. *Fungal Lipid Biochemistry*. Springer US; 1974. doi:10.1007/978-1-4684-2829-2
167. Smith P, Owen DM, Lorenz CD, Makarova M. Asymmetric glycerophospholipids impart distinctive biophysical properties to lipid bilayers. *Biophys J.* 2021;120(9):1746-1754. doi:10.1016/j.bpj.2021.02.046
168. Ramstedt B, Slotte JP. Membrane properties of sphingomyelins. *FEBS Lett.* 2002;531(1):33-37. doi:10.1016/S0014-5793(02)03406-3
169. Wang TY, Leventis R, Silvius JR. Fluorescence-Based Evaluation of the Partitioning of Lipids and Lipidated Peptides into Liquid-Ordered Lipid Microdomains: A Model for Molecular Partitioning into "Lipid Rafts." *Biophys J.* 2000;79(2):919-933. doi:10.1016/S0006-3495(00)76347-8
170. Simons K, Ikonen E. Functional rafts in cell membranes. *Nature.* 1997;387(6633):569-572. doi:10.1038/42408
171. Gally HU, Seelig A, Seelig J. Cholesterol-induced rod-like motion of fatty acyl chains in lipid bilayers a deuterium magnetic resonance study. *Hoppe Seylers Z Physiol Chem.* 1976;357(10):1447-1450.
172. Almeida PF, Vaz WL, Thompson TE. Percolation and diffusion in three-component lipid bilayers: effect of cholesterol on an equimolar mixture of two phosphatidylcholines. *Biophys J.* 1993;64(2):399-412. doi:10.1016/S0006-3495(93)81381-X

173. de Almeida RFM, Fedorov A, Prieto M. Sphingomyelin/Phosphatidylcholine/Cholesterol Phase Diagram: Boundaries and Composition of Lipid Rafts. *Biophys J.* 2003;85(4):2406-2416. doi:10.1016/S0006-3495(03)74664-5
174. Budin I, de Rond T, Chen Y, Chan LJG, Petzold CJ, Keasling JD. Viscous control of cellular respiration by membrane lipid composition. *Science (1979).* 2018;362(6419):1186-1189. doi:10.1126/science.aat7925
175. Lee AG. Lipid–protein interactions in biological membranes: a structural perspective. *Biochimica et Biophysica Acta (BBA) - Biomembranes.* 2003;1612(1):1-40. doi:10.1016/S0005-2736(03)00056-7
176. Gohrbandt M, Lipski A, Grimshaw JW, et al. Low membrane fluidity triggers lipid phase separation and protein segregation in living bacteria. *EMBO J.* Published online January 17, 2022. doi:10.15252/emboj.2021109800
177. Strahl H, Bürmann F, Hamoen LW. The actin homologue MreB organizes the bacterial cell membrane. *Nat Commun.* 2014;5(1):3442. doi:10.1038/ncomms4442
178. Adler HI, Fisher WD, Cohen A, Hardigree AA. MINIATURE *escherichia coli* CELLS DEFICIENT IN DNA. *Proceedings of the National Academy of Sciences.* 1967;57(2):321-326. doi:10.1073/pnas.57.2.321
179. Mileykovskaya E, Fishov I, Fu X, Corbin BD, Margolin W, Dowhan W. Effects of Phospholipid Composition on MinD-Membrane Interactions *in vitro* and *in vivo*. *Journal of Biological Chemistry.* 2003;278(25):22193-22198. doi:10.1074/jbc.M302603200
180. Bramkamp M. Fluidity is the way to life: lipid phase separation in bacterial membranes. *EMBO J.* 2022;41(5). doi:10.15252/emboj.2022110737
181. Cornell R, Taneva S. Amphipathic Helices as Mediators of the Membrane Interaction of Amphitropic Proteins, and as Modulators of Bilayer Physical Properties. *Curr Protein Pept Sci.* 2006;7(6):539-552. doi:10.2174/138920306779025675
182. Sinensky M. Homeoviscous Adaptation—A Homeostatic Process that Regulates the Viscosity of Membrane Lipids in *Escherichia coli*. *Proceedings of the National Academy of Sciences.* 1974;71(2):522-525. doi:10.1073/pnas.71.2.522
183. Aguilar PS, Hernandez-Arriaga AM, Cybulski LE, Erazo AC, de Mendoza D. Molecular basis of thermosensing: a two-component signal transduction thermometer in *Bacillus subtilis*. *EMBO J.* 2001;20(7):1681-1691. doi:10.1093/emboj/20.7.1681

184. Ballweg S, Ernst R. Control of membrane fluidity: the OLE pathway in focus. *Biol Chem.* 2017;398(2):215-228. doi:10.1515/hsz-2016-0277
185. Stukey JE, McDonough VM, Martin CE. Isolation and characterization of OLE1, a gene affecting fatty acid desaturation from *Saccharomyces cerevisiae*. *J Biol Chem.* 1989;264(28):16537-16544.
186. Ballweg S, Ernst R. Control of membrane fluidity: the OLE pathway in focus. *Biol Chem.* 2017;398(2):215-228. doi:10.1515/hsz-2016-0277
187. Martin CE, Oh CS, Jiang Y. Regulation of long chain unsaturated fatty acid synthesis in yeast. *Biochim Biophys Acta.* 2007;1771(3):271-285. doi:10.1016/j.bbali.2006.06.010
188. Smith JJ, Marelli M, Christmas RH, et al. Transcriptome profiling to identify genes involved in peroxisome assembly and function. *Journal of Cell Biology.* 2002;158(2):259-271. doi:10.1083/jcb.200204059
189. Dirmeier R, O'Brien KM, Engle M, Dodd A, Spears E, Poyton RO. Exposure of Yeast Cells to Anoxia Induces Transient Oxidative Stress. *Journal of Biological Chemistry.* 2002;277(38):34773-34784. doi:10.1074/jbc.M203902200
190. David PS, Poyton RO. Effects of a transition from normoxia to anoxia on yeast cytochrome c oxidase and the mitochondrial respiratory chain. *Biochimica et Biophysica Acta (BBA) - Bioenergetics.* 2005;1709(2):169-180. doi:10.1016/j.bbabi.2005.07.002
191. Kwast KE, Burke P V., Staahl BT, Poyton RO. Oxygen sensing in yeast: Evidence for the involvement of the respiratory chain in regulating the transcription of a subset of hypoxic genes. *Proceedings of the National Academy of Sciences.* 1999;96(10):5446-5451. doi:10.1073/pnas.96.10.5446
192. Bossie MA, Martin CE. Nutritional regulation of yeast delta-9 fatty acid desaturase activity. *J Bacteriol.* 1989;171(12):6409-6413. doi:10.1128/jb.171.12.6409-6413.1989
193. Gonzalez CI, Martin CE. Fatty Acid-responsive Control of mRNA Stability. *Journal of Biological Chemistry.* 1996;271(42):25801-25809. doi:10.1074/jbc.271.42.25801
194. Beelman CA, Parker R. Degradation of mRNA in eukaryotes. *Cell.* 1995;81(2):179-183. doi:10.1016/0092-8674(95)90326-7
195. Vemula M, Kandasamy P, Oh CS, Chellappa R, Gonzalez CI, Martin CE. Maintenance and Regulation of mRNA Stability of the *Saccharomyces cerevisiae* OLE1 Gene Requires Multiple Elements within the Transcript That Act through Translation-

- independent Mechanisms. *Journal of Biological Chemistry*. 2003;278(46):45269-45279. doi:10.1074/jbc.M308812200
196. WANG L, LEWIS MS, JOHNSON AW. Domain interactions within the Ski2/3/8 complex and between the Ski complex and Ski7p. *RNA*. 2005;11(8):1291-1302. doi:10.1261/rna.2060405
197. van Hoof A, Staples RR, Baker RE, Parker R. Function of the Ski4p (Csl4p) and Ski7p Proteins in 3'-to-5' Degradation of mRNA. *Mol Cell Biol*. 2000;20(21):8230-8243. doi:10.1128/MCB.20.21.8230-8243.2000
198. Kandasamy P, Vemula M, Oh CS, Chellappa R, Martin CE. Regulation of Unsaturated Fatty Acid Biosynthesis in *Saccharomyces*. *Journal of Biological Chemistry*. 2004;279(35):36586-36592. doi:10.1074/jbc.M401557200
199. Zhang S, Skalsky Y, Garfinkel DJ. MGA2 or SPT23 Is Required for Transcription of the $\Delta 9$ Fatty Acid Desaturase Gene, OLE1, and Nuclear Membrane Integrity in *Saccharomyces cerevisiae*. *Genetics*. 1999;151(2):473-483. doi:10.1093/genetics/151.2.473
200. Shcherbik N, Zoladek T, Nickels JT, Haines DS. Rsp5p Is Required for ER Bound Mga2p120 Polyubiquitination and Release of the Processed/Tethered Transactivator Mga2p90. *Current Biology*. 2003;13(14):1227-1233. doi:10.1016/S0960-9822(03)00457-3
201. Hoppe T, Matuschewski K, Rape M, Schlenker S, Ulrich HD, Jentsch S. Activation of a Membrane-Bound Transcription Factor by Regulated Ubiquitin/Proteasome-Dependent Processing. *Cell*. 2000;102(5):577-586. doi:10.1016/S0092-8674(00)00080-5
202. Covino R, Ballweg S, Stordeur C, et al. A Eukaryotic Sensor for Membrane Lipid Saturation. *Mol Cell*. 2016;63(1):49-59. doi:10.1016/j.molcel.2016.05.015
203. Ballweg S, Sezgin E, Doktorova M, et al. Regulation of lipid saturation without sensing membrane fluidity. *Nat Commun*. 2020;11(1):756. doi:10.1038/s41467-020-14528-1
204. V  th K, Mattes C, Reinhard J, et al. Cysteine cross-linking in native membranes establishes the transmembrane architecture of Ire1. *Journal of Cell Biology*. 2021;220(8). doi:10.1083/jcb.202011078
205. Tran DM, Ishiwata-Kimata Y, Mai TC, Kubo M, Kimata Y. The unfolded protein response alongside the diauxic shift of yeast cells and its involvement in mitochondria enlargement. *Sci Rep*. 2019;9(1):12780. doi:10.1038/s41598-019-49146-5

206. Halbleib K, Pesek K, Covino R, et al. Activation of the Unfolded Protein Response by Lipid Bilayer Stress. *Mol Cell*. 2017;67(4). doi:10.1016/j.molcel.2017.06.012
207. Papagiannidis D, Bircham PW, Lüchtenborg C, et al. Ice2 promotes ER membrane biogenesis in yeast by inhibiting the conserved lipin phosphatase complex. *EMBO J*. 2021;40(22). doi:10.15252/embj.2021107958
208. Schäfer JA, Schessner JP, Bircham PW, et al. ESCRT machinery mediates selective microautophagy of endoplasmic reticulum in yeast. *EMBO J*. 2020;39(2). doi:10.15252/embj.2019102586
209. Markus SM, Omer S, Baranowski K, Lee WL. Improved Plasmids for Fluorescent Protein Tagging of Microtubules in *Saccharomyces cerevisiae*. *Traffic*. 2015;16(7):773-786. doi:10.1111/tra.12276
210. Inoue H, Nojima H, Okayama H. High efficiency transformation of *Escherichia coli* with plasmids. *Gene*. 1990;96(1):23-28. doi:10.1016/0378-1119(90)90336-P
211. Ito H, Fukuda Y, Murata K, Kimura A. Transformation of intact yeast cells treated with alkali cations. *J Bacteriol*. 1983;153(1):163-168. doi:10.1128/jb.153.1.163-168.1983
212. Gibson DG, Young L, Chuang RY, Venter JC, Hutchison CA, Smith HO. Enzymatic assembly of DNA molecules up to several hundred kilobases. *Nat Methods*. 2009;6(5):343-345. doi:10.1038/nmeth.1318
213. Livak KJ, Schmittgen TD. Analysis of Relative Gene Expression Data Using Real-Time Quantitative PCR and the $2^{-\Delta\Delta CT}$ Method. *Methods*. 2001;25(4):402-408. doi:10.1006/meth.2001.1262
214. Cohen Y, Schuldiner M. Advanced Methods for High-Throughput Microscopy Screening of Genetically Modified Yeast Libraries. In: ; 2011:127-159. doi:10.1007/978-1-61779-276-2_8
215. Giaever G, Chu AM, Ni L, et al. Functional profiling of the *Saccharomyces cerevisiae* genome. *Nature*. 2002;418(6896):387-391. doi:10.1038/nature00935
216. Breslow DK, Cameron DM, Collins SR, et al. A comprehensive strategy enabling high-resolution functional analysis of the yeast genome. *Nat Methods*. 2008;5(8):711-718. doi:10.1038/nmeth.1234
217. Kozutsumi Y, Segal M, Normington K, Gething MJ, Sambrook J. The presence of malfolded proteins in the endoplasmic reticulum signals the induction of glucose-regulated proteins. *Nature*. 1988;332(6163):462-464. doi:10.1038/332462a0

218. Szegezdi E, Logue SE, Gorman AM, Samali A. Mediators of endoplasmic reticulum stress-induced apoptosis. *EMBO Rep.* 2006;7(9):880-885. doi:10.1038/sj.embor.7400779
219. Klose C, Surma MA, Gerl MJ, Meyenhofer F, Shevchenko A, Simons K. Flexibility of a Eukaryotic Lipidome – Insights from Yeast Lipidomics. *PLoS One.* 2012;7(4):e35063. doi:10.1371/journal.pone.0035063
220. Kawahara T, Yanagi H, Yura T, Mori K. Endoplasmic Reticulum Stress-induced mRNA Splicing Permits Synthesis of Transcription Factor Hac1p/Ern4p That Activates the Unfolded Protein Response. *Mol Biol Cell.* 1997;8(10):1845-1862. doi:10.1091/mbc.8.10.1845
221. Hanscho M, Ruckerbauer DE, Chauhan N, et al. Nutritional requirements of the BY series of *Saccharomyces cerevisiae* strains for optimum growth. *FEMS Yeast Res.* 2012;12(7):796-808. doi:10.1111/j.1567-1364.2012.00830.x
222. Nikawa JI, Yamashita S. IRE1 encodes a putative protein kinase containing a membrane-spanning domain and is required for inositol phototrophy in *Saccharomyces cerevisiae*. *Mol Microbiol.* 1992;6(11):1441-1446. doi:10.1111/j.1365-2958.1992.tb00864.x
223. Thibault G, Shui G, Kim W, et al. The Membrane Stress Response Buffers Lethal Effects of Lipid Disequilibrium by Reprogramming the Protein Homeostasis Network. *Mol Cell.* 2012;48(1):16-27. doi:10.1016/j.molcel.2012.08.016
224. Hou NS, Gutschmidt A, Choi DY, et al. Activation of the endoplasmic reticulum unfolded protein response by lipid disequilibrium without disturbed proteostasis *in vivo*. *Proceedings of the National Academy of Sciences.* 2014;111(22). doi:10.1073/pnas.1318262111
225. Fu S, Yang L, Li P, et al. Aberrant lipid metabolism disrupts calcium homeostasis causing liver endoplasmic reticulum stress in obesity. *Nature.* 2011;473(7348):528-531. doi:10.1038/nature09968
226. Lee KPK, Dey M, Neculai D, Cao C, Dever TE, Sicheri F. Structure of the Dual Enzyme Ire1 Reveals the Basis for Catalysis and Regulation in Nonconventional RNA Splicing. *Cell.* 2008;132(1):89-100. doi:10.1016/j.cell.2007.10.057
227. Wiseman RL, Zhang Y, Lee KPK, et al. Flavonol Activation Defines an Unanticipated Ligand-Binding Site in the Kinase-RNase Domain of IRE1. *Mol Cell.* 2010;38(2):291-304. doi:10.1016/j.molcel.2010.04.001

228. Cormack BP, Bertram G, Egerton M, Gow NAR, Falkow S, Brown AJP. Yeast-enhanced green fluorescent protein (yEGFP): a reporter of gene expression in *Candida albicans*. *Microbiology (N Y)*. 1997;143(2):303-311. doi:10.1099/00221287-143-2-303
229. Sheff MA, Thorn KS. Optimized cassettes for fluorescent protein tagging in *Saccharomyces cerevisiae*. *Yeast*. 2004;21(8):661-670. doi:10.1002/yea.1130
230. Costantini LM, Baloban M, Markwardt ML, et al. A palette of fluorescent proteins optimized for diverse cellular environments. *Nat Commun*. 2015;6(1):7670. doi:10.1038/ncomms8670
231. Mouritsen OG, Bloom M. Mattress model of lipid-protein interactions in membranes. *Biophys J*. 1984;46(2):141-153. doi:10.1016/S0006-3495(84)84007-2
232. Nezil FA, Bloom M. Combined influence of cholesterol and synthetic amphiphilic peptides upon bilayer thickness in model membranes. *Biophys J*. 1992;61(5):1176-1183. doi:10.1016/S0006-3495(92)81926-4
233. Lajoie P, Moir RD, Willis IM, Snapp EL. Kar2p availability defines distinct forms of endoplasmic reticulum stress in living cells. *Mol Biol Cell*. 2012;23(5):955-964. doi:10.1091/mbc.e11-12-0995
234. Korennykh A, Walter P. Structural Basis of the Unfolded Protein Response. *Annu Rev Cell Dev Biol*. 2012;28(1):251-277. doi:10.1146/annurev-cellbio-101011-155826
235. Ralph-Epps T, Onu CJ, Vo L, Schmidtke MW, Le A, Greenberg ML. Studying Lipid-Related Pathophysiology Using the Yeast Model. *Front Physiol*. 2021;12. doi:10.3389/fphys.2021.768411
236. Singh P. Budding Yeast: An Ideal Backdrop for *In vivo* Lipid Biochemistry. *Front Cell Dev Biol*. 2017;4. doi:10.3389/fcell.2016.00156
237. Leamy AK, Egnatchik RA, Young JD. Molecular mechanisms and the role of saturated fatty acids in the progression of non-alcoholic fatty liver disease. *Prog Lipid Res*. 2013;52(1):165-174. doi:10.1016/j.plipres.2012.10.004
238. Pineau L, Ferreira T. Lipid-induced ER stress in yeast and β cells: parallel trails to a common fate. *FEMS Yeast Res*. 2010;10(8):1035-1045. doi:10.1111/j.1567-1364.2010.00674.x
239. Fu S, Yang L, Li P, et al. Aberrant lipid metabolism disrupts calcium homeostasis causing liver endoplasmic reticulum stress in obesity. *Nature*. 2011;473(7348):528-531. doi:10.1038/nature09968

240. Luukkonen PK, Sädevirta S, Zhou Y, et al. Saturated Fat Is More Metabolically Harmful for the Human Liver Than Unsaturated Fat or Simple Sugars. *Diabetes Care*. 2018;41(8):1732-1739. doi:10.2337/dc18-0071
241. Surma MA, Klose C, Peng D, et al. A Lipid E-MAP Identifies Ubx2 as a Critical Regulator of Lipid Saturation and Lipid Bilayer Stress. *Mol Cell*. 2013;51(4):519-530. doi:10.1016/j.molcel.2013.06.014
242. Klose C, Surma MA, Gerl MJ, Meyenhofer F, Shevchenko A, Simons K. Flexibility of a Eukaryotic Lipidome – Insights from Yeast Lipidomics. *PLoS One*. 2012;7(4):e35063. doi:10.1371/journal.pone.0035063
243. de Smet CH, Vittone E, Scherer M, et al. The yeast acyltransferase Sct1p regulates fatty acid desaturation by competing with the desaturase Ole1p. *Mol Biol Cell*. 2012;23(7):1146-1156. doi:10.1091/mbc.e11-07-0624
244. Pineau L, Bonifait L, Berjeaud JM, Alimardani-Theuil P, Bergès T, Ferreira T. A Lipid-mediated Quality Control Process in the Golgi Apparatus in Yeast. *Mol Biol Cell*. 2008;19(3):807-821. doi:10.1091/mbc.e07-06-0600
245. FERREIRA T, RÉGNACQ M, ALIMARDANI P, MOREAU-VAUZELLE C, BERGÈS T. Lipid dynamics in yeast under haem-induced unsaturated fatty acid and/or sterol depletion. *Biochemical Journal*. 2004;378(3):899-908. doi:10.1042/bj20031064
246. Pineau L, Colas J, Dupont S, et al. Lipid-Induced ER Stress: Synergistic Effects of Sterols and Saturated Fatty Acids. *Traffic*. 2009;10(6):673-690. doi:10.1111/j.1600-0854.2009.00903.x
247. Bretscher MS, Munro S. Cholesterol and the Golgi Apparatus. *Science (1979)*. 1993;261(5126):1280-1281. doi:10.1126/science.8362242
248. Jacquemyn J, Cascalho A, Goodchild RE. The ins and outs of endoplasmic reticulum-controlled lipid biosynthesis. *EMBO Rep*. 2017;18(11):1905-1921. doi:10.15252/embr.201643426
249. Giaever G, Chu AM, Ni L, et al. Functional profiling of the *Saccharomyces cerevisiae* genome. *Nature*. 2002;418(6896):387-391. doi:10.1038/nature00935
250. Breslow DK, Cameron DM, Collins SR, et al. A comprehensive strategy enabling high-resolution functional analysis of the yeast genome. *Nat Methods*. 2008;5(8):711-718. doi:10.1038/nmeth.1234

251. Kuleshov M v., Jones MR, Rouillard AD, et al. Enrichr: a comprehensive gene set enrichment analysis web server 2016 update. *Nucleic Acids Res.* 2016;44(W1):W90-W97. doi:10.1093/nar/gkw377
252. Kuleshov M v, Diaz JEL, Flamholz ZN, et al. modEnrichr: a suite of gene set enrichment analysis tools for model organisms. *Nucleic Acids Res.* 2019;47(W1):W183-W190. doi:10.1093/nar/gkz347
253. Benjamini Y, Hochberg Y. Controlling the False Discovery Rate: A Practical and Powerful Approach to Multiple Testing. *Journal of the Royal Statistical Society: Series B (Methodological)*. 1995;57(1):289-300. doi:10.1111/j.2517-6161.1995.tb02031.x
254. Franco LVR, Su CH, Tzagoloff A. Modular assembly of yeast mitochondrial ATP synthase and cytochrome oxidase. *Biol Chem.* 2020;401(6-7):835-853. doi:10.1515/hsz-2020-0112
255. Yao Z, Delorme-Axford E, Backues SK, Klionsky DJ. Atg41/lcy2 regulates autophagosome formation. *Autophagy.* 2015;11(12):2288-2299. doi:10.1080/15548627.2015.1107692
256. Charron MJ, Read E, Haut SR, Michels CA. Molecular evolution of the telomere-associated MAL loci of *Saccharomyces*. *Genetics.* 1989;122(2):307-316. doi:10.1093/genetics/122.2.307
257. Goehring AS, Rivers DM, Sprague GF. Urmylation: a ubiquitin-like pathway that functions during invasive growth and budding in yeast. *Mol Biol Cell.* 2003;14(11):4329-4341. doi:10.1091/mbc.e03-02-0079
258. Leidel S, Pedrioli PGA, Bucher T, et al. Ubiquitin-related modifier Urm1 acts as a sulphur carrier in thiolation of eukaryotic transfer RNA. *Nature.* 2009;458(7235):228-232. doi:10.1038/nature07643
259. Christiano R, Arlt H, Kabatnik S, et al. A Systematic Protein Turnover Map for Decoding Protein Degradation. *Cell Rep.* 2020;33(6):108378. doi:10.1016/j.celrep.2020.108378
260. Marshall RS, Vierstra RD. Dynamic Regulation of the 26S Proteasome: From Synthesis to Degradation. *Front Mol Biosci.* 2019;6. doi:10.3389/fmolb.2019.00040
261. Decourty L, Malabat C, Frachon E, Jacquier A, Saveanu C. Investigation of RNA metabolism through large-scale genetic interaction profiling in yeast. *Nucleic Acids Res.* 2021;49(15):8535-8555. doi:10.1093/nar/gkab680

262. Séraphin B, Simon M, Boulet A, Faye G. Mitochondrial splicing requires a protein from a novel helicase family. *Nature*. 1989;337(6202):84-87. doi:10.1038/337084a0
263. Michaelis U, Körte A, Rödel G. Association of cytochrome b translational activator proteins with the mitochondrial membrane: implications for cytochrome b expression in yeast. *Mol Gen Genet*. 1991;230(1-2):177-185. doi:10.1007/BF00290666
264. Krause-Buchholz U, Barth K, Dombrowski C, Rödel G. *Saccharomyces cerevisiae* translational activator Cbs2p is associated with mitochondrial ribosomes. *Curr Genet*. 2004;46(1):20-28. doi:10.1007/s00294-004-0503-y
265. Zeng X, Hourset A, Tzagoloff A. The *Saccharomyces cerevisiae* ATP22 gene codes for the mitochondrial ATPase subunit 6-specific translation factor. *Genetics*. 2007;175(1):55-63. doi:10.1534/genetics.106.065821
266. Jan PS, Esser K, Pratje E, Michaelis G. Som1, a third component of the yeast mitochondrial inner membrane peptidase complex that contains Imp1 and Imp2. *Mol Gen Genet*. 2000;263(3):483-491. doi:10.1007/s004380051192
267. Desai N, Brown A, Amunts A, Ramakrishnan V. The structure of the yeast mitochondrial ribosome. *Science*. 2017;355(6324):528-531. doi:10.1126/science.aal2415
268. Jones DG, Reusser U, Braus GH. Molecular cloning, characterization and analysis of the regulation of the ARO2 gene, encoding chorismate synthase, of *Saccharomyces cerevisiae*. *Mol Microbiol*. 1991;5(9):2143-2152. doi:10.1111/j.1365-2958.1991.tb02144.x
269. Hirata R, Umemoto N, Ho MN, Ohya Y, Stevens TH, Anraku Y. VMA12 is essential for assembly of the vacuolar H(+)-ATPase subunits onto the vacuolar membrane in *Saccharomyces cerevisiae*. *J Biol Chem*. 1993;268(2):961-967.
270. Mick DU, Vukotic M, Piechura H, et al. Coa3 and Cox14 are essential for negative feedback regulation of COX1 translation in mitochondria. *Journal of Cell Biology*. 2010;191(1):141-154. doi:10.1083/jcb.201007026
271. Manthey GM, McEwen JE. The product of the nuclear gene PET309 is required for translation of mature mRNA and stability or production of intron-containing RNAs derived from the mitochondrial COX1 locus of *Saccharomyces cerevisiae*. *EMBO J*. 1995;14(16):4031-4043.
272. Amunts A, Brown A, Bai XC, et al. Structure of the yeast mitochondrial large ribosomal subunit. *Science*. 2014;343(6178):1485-1489. doi:10.1126/science.1249410

273. Albertini M, Girzalsky W, Veenhuis M, Kunau WH. Pex12p of *Saccharomyces cerevisiae* is a component of a multi-protein complex essential for peroxisomal matrix protein import. *Eur J Cell Biol.* 2001;80(4):257-270. doi:10.1078/0171-9335-00164
274. Innokentev A, Furukawa K, Fukuda T, et al. Association and dissociation between the mitochondrial Far complex and Atg32 regulate mitophagy. *Elife.* 2020;9. doi:10.7554/eLife.63694
275. Woellhaf MW, Sommer F, Schroda M, Herrmann JM. Proteomic profiling of the mitochondrial ribosome identifies Atp25 as a composite mitochondrial precursor protein. *Mol Biol Cell.* 2016;27(20):3031-3039. doi:10.1091/mbc.E16-07-0513
276. Itoh Y, Naschberger A, Mortezaei N, Herrmann JM, Amunts A. Analysis of translating mitoribosome reveals functional characteristics of translation in mitochondria of fungi. *Nat Commun.* 2020;11(1):5187. doi:10.1038/s41467-020-18830-w
277. Zeng X, Barros MH, Shulman T, Tzagoloff A. ATP25, a new nuclear gene of *Saccharomyces cerevisiae* required for expression and assembly of the Atp9p subunit of mitochondrial ATPase. *Mol Biol Cell.* 2008;19(4):1366-1377. doi:10.1091/mbc.e07-08-0746
278. Lundin M, Baltscheffsky H, Ronne H. Yeast PPA2 gene encodes a mitochondrial inorganic pyrophosphatase that is essential for mitochondrial function. *J Biol Chem.* 1991;266(19):12168-12172.
279. Muid KA, Kimyon Ö, Reza SH, Karakaya HC, Koc A. Characterization of long living yeast deletion mutants that lack mitochondrial metabolism genes DSS1, PPA2 and AFG3. *Gene.* 2019;706:172-180. doi:10.1016/j.gene.2019.05.001
280. Tzagoloff A, Shtanko A. Mitochondrial and cytoplasmic isoleucyl-, glutamyl- and arginyl-tRNA synthetases of yeast are encoded by separate genes. *Eur J Biochem.* 1995;230(2):582-586. doi:10.1111/j.1432-1033.1995.tb20599.x
281. Deshaies RJ, Schekman R. SEC62 encodes a putative membrane protein required for protein translocation into the yeast endoplasmic reticulum. *J Cell Biol.* 1989;109(6 Pt 1):2653-2664. doi:10.1083/jcb.109.6.2653
282. Green-Willms NS, Fox TD, Costanzo MC. Functional Interactions between Yeast Mitochondrial Ribosomes and mRNA 5' Untranslated Leaders. *Mol Cell Biol.* 1998;18(4):1826-1834. doi:10.1128/MCB.18.4.1826

283. Pierrel F, Khalimonchuk O, Cobine PA, Bestwick M, Winge DR. Coa2 is an assembly factor for yeast cytochrome c oxidase biogenesis that facilitates the maturation of Cox1. *Mol Cell Biol.* 2008;28(16):4927-4939. doi:10.1128/MCB.00057-08
284. Koch B, Mitterer V, Niederhauser J, et al. Yar1 protects the ribosomal protein Rps3 from aggregation. *J Biol Chem.* 2012;287(26):21806-21815. doi:10.1074/jbc.M112.365791
285. Mitterer V, Gantenbein N, Birner-Gruenberger R, et al. Nuclear import of dimerized ribosomal protein Rps3 in complex with its chaperone Yar1. *Sci Rep.* 2016;6:36714. doi:10.1038/srep36714
286. Ashby MN, Edwards PA. Elucidation of the deficiency in two yeast coenzyme Q mutants. Characterization of the structural gene encoding hexaprenyl pyrophosphate synthetase. *J Biol Chem.* 1990;265(22):13157-13164.
287. Rentzsch A, Krummeck-Weiss G, Hofer A, Bartuschka A, Ostermann K, Rödel G. Mitochondrial copper metabolism in yeast: mutational analysis of Sco1p involved in the biogenesis of cytochrome c oxidase. *Curr Genet.* 1999;35(2):103-108. doi:10.1007/s002940050438
288. Pintard L, Lecointe F, Bujnicki JM, Bonnerot C, Grosjean H, Lapeyre B. Trm7p catalyses the formation of two 2'-O-methylriboses in yeast tRNA anticodon loop. *EMBO J.* 2002;21(7):1811-1820. doi:10.1093/emboj/21.7.1811
289. Burgers PM, Stith CM, Yoder BL, Sparks JL. Yeast exonuclease 5 is essential for mitochondrial genome maintenance. *Mol Cell Biol.* 2010;30(6):1457-1466. doi:10.1128/MCB.01321-09
290. Cohen MM, Amriott EA, Day AR, et al. Sequential requirements for the GTPase domain of the mitofusin Fzo1 and the ubiquitin ligase SCFMdm30 in mitochondrial outer membrane fusion. *J Cell Sci.* 2011;124(Pt 9):1403-1410. doi:10.1242/jcs.079293
291. Graham LA, Brandt U, Sargent JS, Trumpower BL. Mutational analysis of assembly and function of the iron-sulfur protein of the cytochrome bc1 complex in *Saccharomyces cerevisiae*. *J Bioenerg Biomembr.* 1993;25(3):245-257. doi:10.1007/BF00762586
292. Krüger V, Deckers M, Hildenbeutel M, et al. The mitochondrial oxidase assembly protein1 (Oxa1) insertase forms a membrane pore in lipid bilayers. *J Biol Chem.* 2012;287(40):33314-33326. doi:10.1074/jbc.M112.387563
293. Pahlman AK, Granath K, Ansell R, Hohmann S, Adler L. The yeast glycerol 3-phosphatases Gpp1p and Gpp2p are required for glycerol biosynthesis and

- differentially involved in the cellular responses to osmotic, anaerobic, and oxidative stress. *J Biol Chem.* 2001;276(5):3555-3563. doi:10.1074/jbc.M007164200
294. Kitakawa M, Graack HR, Grohmann L, et al. Identification and characterization of the genes for mitochondrial ribosomal proteins of *Saccharomyces cerevisiae*. *Eur J Biochem.* 1997;245(2):449-456. doi:10.1111/j.1432-1033.1997.t01-2-00449.x
295. Ellis TP, Schonauer MS, Dieckmann CL. CBT1 Interacts Genetically With CBP1 and the Mitochondrially Encoded Cytochrome b Gene and Is Required to Stabilize the Mature Cytochrome b mRNA of *Saccharomyces cerevisiae*. *Genetics.* 2005;171(3):949-957. doi:10.1534/genetics.104.036467
296. Sanni A, Mirande M, Ebel JP, Boulanger Y, Waller JP, Fasiolo F. Structure and expression of the genes encoding the alpha and beta subunits of yeast phenylalanyl-tRNA synthetase. *J Biol Chem.* 1988;263(30):15407-15415.
297. Lisowsky T, Michaelis G. Mutations in the genes for mitochondrial RNA polymerase and a second mitochondrial transcription factor of *Saccharomyces cerevisiae*. *Mol Gen Genet.* 1989;219(1-2):125-128. doi:10.1007/BF00261167
298. Srinivasan M, Mehta P, Yu Y, et al. The highly conserved KEOPS/EKC complex is essential for a universal tRNA modification, t6A. *EMBO J.* 2011;30(5):873-881. doi:10.1038/emboj.2010.343
299. Liu B, Sutton A, Sternglanz R. A Yeast Polyamine Acetyltransferase. *Journal of Biological Chemistry.* 2005;280(17):16659-16664. doi:10.1074/jbc.M414008200
300. Forsha D, Church C, Wazny P, Poyton RO. Structure and function of Pet100p, a molecular chaperone required for the assembly of cytochrome c oxidase in *Saccharomyces cerevisiae*. *Biochem Soc Trans.* 2001;29(4):436-441. doi:10.1042/bst0290436
301. Addinall SG, Downey M, Yu M, et al. A Genomewide Suppressor and Enhancer Analysis of *cdc13-1* Reveals Varied Cellular Processes Influencing Telomere Capping in *Saccharomyces cerevisiae*. *Genetics.* 2008;180(4):2251-2266. doi:10.1534/genetics.108.092577
302. Belogradov GI, Lee PT, Jonassen T, Hsu AY, Gin P, Clarke CF. Yeast COQ4 encodes a mitochondrial protein required for coenzyme Q synthesis. *Arch Biochem Biophys.* 2001;392(1):48-58. doi:10.1006/abbi.2001.2448

303. Hell K, Tzagoloff A, Neupert W, Stuart RA. Identification of Cox20p, a novel protein involved in the maturation and assembly of cytochrome oxidase subunit 2. *J Biol Chem.* 2000;275(7):4571-4578. doi:10.1074/jbc.275.7.4571
304. Malaney S, Trumpower BL, Deber CM, Robinson BH. The N Terminus of the Qcr7 Protein of the Cytochromebc 1 Complex Is Not Essential for Import into Mitochondria in *Saccharomyces cerevisiae* but Is Essential for Assembly of the Complex. *Journal of Biological Chemistry.* 1997;272(28):17495-17501. doi:10.1074/jbc.272.28.17495
305. Stukey JE, McDonough VM, Martin CE. Isolation and characterization of OLE1, a gene affecting fatty acid desaturation from *Saccharomyces cerevisiae*. *J Biol Chem.* 1989;264(28):16537-16544.
306. Schmidt U, Lehmann K, Stahl U. A novel mitochondrial DEAD box protein (Mrh4) required for maintenance of mtDNA in *Saccharomyces cerevisiae*. *FEMS Yeast Res.* 2002;2(3):267-276. doi:10.1016/S1567-1356(02)00109-5
307. Kornmann B, Currie E, Collins SR, et al. An ER-mitochondria tethering complex revealed by a synthetic biology screen. *Science.* 2009;325(5939):477-481. doi:10.1126/science.1175088
308. Gin P, Hsu AY, Rothman SC, et al. The *Saccharomyces cerevisiae* COQ6 gene encodes a mitochondrial flavin-dependent monooxygenase required for coenzyme Q biosynthesis. *J Biol Chem.* 2003;278(28):25308-25316. doi:10.1074/jbc.M303234200
309. Guedes-Monteiro RF, Franco LVR, Moda BS, Tzagoloff A, Barros MH. 5' processing of *Saccharomyces cerevisiae* mitochondrial tRNAs requires expression of multiple genes. *Biochim Biophys Acta Mol Cell Res.* 2019;1866(5):806-818. doi:10.1016/j.bbamcr.2019.02.002
310. de Winde JH, Grivell LA. Global regulation of mitochondrial biogenesis in *Saccharomyces cerevisiae*: ABF1 and CPF1 play opposite roles in regulating expression of the QCR8 gene, which encodes subunit VIII of the mitochondrial ubiquinol-cytochrome c oxidoreductase. *Mol Cell Biol.* 1992;12(6):2872-2883. doi:10.1128/mcb.12.6.2872-2883.1992
311. LaMarche AE, Abate MI, Chan SH, Trumpower BL. Isolation and characterization of COX12, the nuclear gene for a previously unrecognized subunit of *Saccharomyces cerevisiae* cytochrome c oxidase. *J Biol Chem.* 1992;267(31):22473-22480.
312. Furukawa K, Innokentev A, Kanki T. Mitophagy regulation mediated by the Far complex in yeast. *Autophagy.* 2021;17(4):1042-1043. doi:10.1080/15548627.2021.1885184

313. Oh CS, Toke DA, Mandala S, Martin CE. ELO2 and ELO3, homologues of the *Saccharomyces cerevisiae* ELO1 gene, function in fatty acid elongation and are required for sphingolipid formation. *J Biol Chem.* 1997;272(28):17376-17384. doi:10.1074/jbc.272.28.17376
314. Herbert CJ, Labouesse M, Dujardin G, Slonimski PP. The NAM2 proteins from *S. cerevisiae* and *S. douglasii* are mitochondrial leucyl-tRNA synthetases, and are involved in mRNA splicing. *EMBO J.* 1988;7(2):473-483. doi:10.1002/j.1460-2075.1988.tb02835.x
315. Barkovich RJ, Shtanko A, Shepherd JA, et al. Characterization of the COQ5 gene from *Saccharomyces cerevisiae*. Evidence for a C-methyltransferase in ubiquinone biosynthesis. *J Biol Chem.* 1997;272(14):9182-9188. doi:10.1074/jbc.272.14.9182
316. Lu L, Roberts G, Simon K, Yu J, Hudson AP. Rsf1p, a protein required for respiratory growth of *Saccharomyces cerevisiae*. *Curr Genet.* 2003;43(4):263-272. doi:10.1007/s00294-003-0398-z
317. Sickmann A, Reinders J, Wagner Y, et al. The proteome of *Saccharomyces cerevisiae* mitochondria. *Proc Natl Acad Sci U S A.* 2003;100(23):13207-13212. doi:10.1073/pnas.2135385100
318. Behrens M, Michaelis G, Pratje E. Mitochondrial inner membrane protease 1 of *Saccharomyces cerevisiae* shows sequence similarity to the *Escherichia coli* leader peptidase. *Mol Gen Genet.* 1991;228(1-2):167-176. doi:10.1007/BF00282462
319. Reinders J, Zahedi RP, Pfanner N, Meisinger C, Sickmann A. Toward the complete yeast mitochondrial proteome: multidimensional separation techniques for mitochondrial proteomics. *J Proteome Res.* 2006;5(7):1543-1554. doi:10.1021/pr050477f
320. Gatti DL, Tzagoloff A. Structure and evolution of a group of related aminoacyl-tRNA synthetases. *J Mol Biol.* 1991;218(3):557-568. doi:10.1016/0022-2836(91)90701-7
321. Desai N, Brown A, Amunts A, Ramakrishnan V. The structure of the yeast mitochondrial ribosome. *Science.* 2017;355(6324):528-531. doi:10.1126/science.aal2415
322. Sathianathan A, Ravichandran P, Lippi JM, et al. The Eaf3/5/7 Subcomplex Stimulates NuA4 Interaction with Methylated Histone H3 Lys-36 and RNA Polymerase II. *J Biol Chem.* 2016;291(40):21195-21207. doi:10.1074/jbc.M116.718742

323. Uemura H, Fraenkel DG. Glucose metabolism in gcr mutants of *Saccharomyces cerevisiae*. *J Bacteriol.* 1999;181(15):4719-4723. doi:10.1128/JB.181.15.4719-4723.1999
324. Cohen M, Stutz F, Belgareh N, Haguenaer-Tsapis R, Dargemont C. Ubp3 requires a cofactor, Bre5, to specifically de-ubiquitinate the COPII protein, Sec23. *Nat Cell Biol.* 2003;5(7):661-667. doi:10.1038/ncb1003
325. Kehrein K, Schilling R, Möller-Hergt BV, et al. Organization of Mitochondrial Gene Expression in Two Distinct Ribosome-Containing Assemblies. *Cell Rep.* 2015;10(6):843-853. doi:10.1016/j.celrep.2015.01.012
326. Chen Y, Wang Y, Liu M, et al. Primary and Secondary Metabolic Effects of a Key Gene Deletion (Δ YPL062W) in Metabolically Engineered Terpenoid-Producing *Saccharomyces cerevisiae*. *Appl Environ Microbiol.* 2019;85(7). doi:10.1128/AEM.01990-18
327. Guy MP, Podyma BM, Preston MA, et al. Yeast Trm7 interacts with distinct proteins for critical modifications of the tRNAPhe anticodon loop. *RNA.* 2012;18(10):1921-1933. doi:10.1261/rna.035287.112
328. Heesen S, Lehle L, Weissmann A, Aebi M. Isolation of the ALG5 locus encoding the UDP-glucose:dolichyl-phosphate glucosyltransferase from *Saccharomyces cerevisiae*. *Eur J Biochem.* 1994;224(1):71-79. doi:10.1111/j.1432-1033.1994.tb19996.x
329. Bowdish KS, Yuan HE, Mitchell AP. Analysis of RIM11, a yeast protein kinase that phosphorylates the meiotic activator IME1. *Mol Cell Biol.* 1994;14(12):7909-7919. doi:10.1128/mcb.14.12.7909-7919.1994
330. Nobrega MP, Bandeira SCB, Beers J, Tzagoloff A. Characterization of COX19, a Widely Distributed Gene Required for Expression of Mitochondrial Cytochrome Oxidase. *Journal of Biological Chemistry.* 2002;277(43):40206-40211. doi:10.1074/jbc.M207348200
331. Krogan NJ, Dover J, Khorrami S, et al. COMPASS, a histone H3 (Lysine 4) methyltransferase required for telomeric silencing of gene expression. *J Biol Chem.* 2002;277(13):10753-10755. doi:10.1074/jbc.C200023200
332. Taberner FJ, Quilis I, Sendra J, Bañó MC, Igual JC. Regulation of cell cycle transcription factor Swi5 by karyopherin Msn5. *Biochim Biophys Acta.* 2012;1823(4):959-970. doi:10.1016/j.bbamcr.2012.02.009

333. Saunders WS, Hoyt MA. Kinesin-related proteins required for structural integrity of the mitotic spindle. *Cell*. 1992;70(3):451-458. doi:10.1016/0092-8674(92)90169-d
334. Peter M, Neiman AM, Park HO, van Lohuizen M, Herskowitz I. Functional analysis of the interaction between the small GTP binding protein Cdc42 and the Ste20 protein kinase in yeast. *EMBO J*. 1996;15(24):7046-7059.
335. Paul VD, Mühlenhoff U, Stümpfig M, et al. The deca-GX3 proteins Yae1-Lto1 function as adaptors recruiting the ABC protein Rli1 for iron-sulfur cluster insertion. *Elife*. 2015;4:e08231. doi:10.7554/eLife.08231
336. Yu EY, Steinberg-Neifach O, Dandjinou AT, et al. Regulation of telomere structure and functions by subunits of the INO80 chromatin remodeling complex. *Mol Cell Biol*. 2007;27(16):5639-5649. doi:10.1128/MCB.00418-07
337. Fiechter V, Cameroni E, Cerutti L, de Virgilio C, Barral Y, Fankhauser C. The evolutionary conserved BER1 gene is involved in microtubule stability in yeast. *Curr Genet*. 2008;53(2):107-115. doi:10.1007/s00294-007-0169-3
338. Abovich N, Gritz L, Tung L, Rosbash M. Effect of RP51 gene dosage alterations on ribosome synthesis in *Saccharomyces cerevisiae*. *Mol Cell Biol*. 1985;5(12):3429-3435. doi:10.1128/mcb.5.12.3429-3435.1985
339. Goossens A, Forment J, Serrano R. Involvement of Nst1p/YNL091w and Msl1p, a U2B'' splicing factor, in *Saccharomyces cerevisiae* salt tolerance. *Yeast*. 2002;19(3):193-202. doi:10.1002/yea.815
340. Bi E, Chiavetta JB, Chen H, Chen GC, Chan CS, Pringle JR. Identification of novel, evolutionarily conserved Cdc42p-interacting proteins and of redundant pathways linking Cdc24p and Cdc42p to actin polarization in yeast. *Mol Biol Cell*. 2000;11(2):773-793. doi:10.1091/mbc.11.2.773
341. Glover CVC. On the Physiological Role of Casein Kinase II in *Saccharomyces cerevisiae*. In: ; 1997:95-133. doi:10.1016/S0079-6603(08)61030-2
342. Yeghiayan P, Tu J, Vallier LG, Carlson M. Molecular analysis of the SNF8 gene of *Saccharomyces cerevisiae*. *Yeast*. 1995;11(3):219-224. doi:10.1002/yea.320110304
343. Pike BL, Yongkiettrakul S, Tsai MD, Heierhorst J. Mdt1, a novel Rad53 FHA1 domain-interacting protein, modulates DNA damage tolerance and G(2)/M cell cycle progression in *Saccharomyces cerevisiae*. *Mol Cell Biol*. 2004;24(7):2779-2788. doi:10.1128/MCB.24.7.2779-2788.2004

344. Mager WH, Planta RJ, Ballesta JG, et al. A new nomenclature for the cytoplasmic ribosomal proteins of *Saccharomyces cerevisiae*. *Nucleic Acids Res.* 1997;25(24):4872-4875. doi:10.1093/nar/25.24.4872
345. Chapman KB, Solomon SD, Boeke JD. SDH1, the gene encoding the succinate dehydrogenase flavoprotein subunit from *Saccharomyces cerevisiae*. *Gene.* 1992;118(1):131-136. doi:10.1016/0378-1119(92)90260-v
346. Conaway RC, Conaway JW. The INO80 chromatin remodeling complex in transcription, replication and repair. *Trends Biochem Sci.* 2009;34(2):71-77. doi:10.1016/j.tibs.2008.10.010
347. Zhang Y, Sun ZW, Iratni R, et al. SAP30, a novel protein conserved between human and yeast, is a component of a histone deacetylase complex. *Mol Cell.* 1998;1(7):1021-1031. doi:10.1016/s1097-2765(00)80102-1
348. Shintani T, Mizushima N, Ogawa Y, Matsuura A, Noda T, Ohsumi Y. Apg10p, a novel protein-conjugating enzyme essential for autophagy in yeast. *EMBO J.* 1999;18(19):5234-5241. doi:10.1093/emboj/18.19.5234
349. Bourbon HM, Aguilera A, Ansari AZ, et al. A Unified Nomenclature for Protein Subunits of Mediator Complexes Linking Transcriptional Regulators to RNA Polymerase II. *Mol Cell.* 2004;14(5):553-557. doi:10.1016/j.molcel.2004.05.011
350. Barelli H, Antonny B. Lipid unsaturation and organelle dynamics. *Curr Opin Cell Biol.* 2016;41:25-32. doi:10.1016/j.ceb.2016.03.012
351. Merta H, Carrasquillo Rodríguez JW, Anjur-Dietrich MI, et al. Cell cycle regulation of ER membrane biogenesis protects against chromosome missegregation. *Dev Cell.* 2021;56(24):3364-3379.e10. doi:10.1016/j.devcel.2021.11.009
352. McCusker D, Kellogg DR. Plasma membrane growth during the cell cycle: unsolved mysteries and recent progress. *Curr Opin Cell Biol.* 2012;24(6):845-851. doi:10.1016/j.ceb.2012.10.008
353. Schwank S, Ebbert R, Rautenstrauss K, Schweizer E, Schüller HJ. Yeast transcriptional activator INO2 interacts as an Ino2p/Ino4p basic helix-loop-helix heteromeric complex with the inositol/choline-responsive element necessary for expression of phospholipid biosynthetic genes in *Saccharomyces cerevisiae*. *Nucleic Acids Res.* 1995;23(2):230-237. doi:10.1093/nar/23.2.230

354. Ambroziak J, Henry SA. INO2 and INO4 gene products, positive regulators of phospholipid biosynthesis in *Saccharomyces cerevisiae*, form a complex that binds to the INO1 promoter. *Journal of Biological Chemistry*. 1994;269(21):15344-15349. doi:10.1016/S0021-9258(17)36612-7
355. Wagner C, Dietz M, Wittmann J, Albrecht A, Schüller HJ. The negative regulator Opi1 of phospholipid biosynthesis in yeast contacts the pleiotropic repressor Sin3 and the transcriptional activator Ino2. *Mol Microbiol*. 2001;41(1):155-166. doi:10.1046/j.1365-2958.2001.02495.x
356. Carman GM, Henry SA. Phosphatidic acid plays a central role in the transcriptional regulation of glycerophospholipid synthesis in *Saccharomyces cerevisiae*. *J Biol Chem*. 2007;282(52):37293-37297. doi:10.1074/jbc.R700038200
357. Schuck S, Prinz WA, Thorn KS, Voss C, Walter P. Membrane expansion alleviates endoplasmic reticulum stress independently of the unfolded protein response. *Journal of Cell Biology*. 2009;187(4):525-536. doi:10.1083/jcb.200907074
358. Heyken WT, Repenning A, Kumme J, Schüller HJ. Constitutive expression of yeast phospholipid biosynthetic genes by variants of Ino2 activator defective for interaction with Opi1 repressor. *Mol Microbiol*. 2005;56(3):696-707. doi:10.1111/j.1365-2958.2004.04499.x
359. Pincus D, Aranda-Díaz A, Zuleta IA, Walter P, El-Samad H. Delayed Ras/PKA signaling augments the unfolded protein response. *Proc Natl Acad Sci U S A*. 2014;111(41):14800-14805. doi:10.1073/pnas.1409588111
360. West RW, Chen SM, Putz H, Butler G, Banerjee M. GAL1-GAL10 divergent promoter region of *Saccharomyces cerevisiae* contains negative control elements in addition to functionally separate and possibly overlapping upstream activating sequences. *Genes Dev*. 1987;1(10):1118-1131. doi:10.1101/gad.1.10.1118
361. Wang Y, Zhang K, Li H, et al. Fine-tuning the expression of target genes using a DDI2 promoter gene switch in budding yeast. *Sci Rep*. 2019;9(1):12538. doi:10.1038/s41598-019-49000-8
362. Lin A, Zeng C, Wang Q, et al. Utilization of a Strongly Inducible DDI2 Promoter to Control Gene Expression in *Saccharomyces cerevisiae*. *Front Microbiol*. 2018;9:2736. doi:10.3389/fmicb.2018.02736
363. Stevenson LF, Kennedy BK, Harlow E. A large-scale overexpression screen in *Saccharomyces cerevisiae* identifies previously uncharacterized cell cycle genes.

- Proceedings of the National Academy of Sciences*. 2001;98(7):3946-3951. doi:10.1073/pnas.051013498
364. Niu W, Li Z, Zhan W, Iyer VR, Marcotte EM. Mechanisms of Cell Cycle Control Revealed by a Systematic and Quantitative Overexpression Screen in *S. cerevisiae*. *PLoS Genet*. 2008;4(7):e1000120. doi:10.1371/journal.pgen.1000120
365. Lee ME, DeLoache WC, Cervantes B, Dueber JE. A Highly Characterized Yeast Toolkit for Modular, Multipart Assembly. *ACS Synth Biol*. 2015;4(9):975-986. doi:10.1021/sb500366v
366. Baganz F, Hayes A, Marren D, Gardner DCJ, Oliver SG. Suitability of replacement markers for functional analysis studies in *Saccharomyces cerevisiae*. *Yeast*. 1997;13(16):1563-1573. doi:10.1002/(SICI)1097-0061(199712)13:16<1563::AID-YEA240>3.0.CO;2-6
367. Delobel P, Tesnière C. A Simple FCM Method to Avoid Misinterpretation in *Saccharomyces cerevisiae* Cell Cycle Assessment between G0 and Sub-G1. *PLoS One*. 2014;9(1):e84645. doi:10.1371/journal.pone.0084645
368. Spellman PT, Sherlock G, Zhang MQ, et al. Comprehensive Identification of Cell Cycle-regulated Genes of the Yeast *Saccharomyces cerevisiae* by Microarray Hybridization. *Mol Biol Cell*. 1998;9(12):3273-3297. doi:10.1091/mbc.9.12.3273
369. Cho RJ, Campbell MJ, Winzeler EA, et al. A Genome-Wide Transcriptional Analysis of the Mitotic Cell Cycle. *Mol Cell*. 1998;2(1):65-73. doi:10.1016/S1097-2765(00)80114-8
370. Jonikas MC, Collins SR, Denic V, et al. Comprehensive Characterization of Genes Required for Protein Folding in the Endoplasmic Reticulum. *Science (1979)*. 2009;323(5922):1693-1697. doi:10.1126/science.1167983
371. De Craene JO, Coleman J, Estrada de Martin P, et al. Rtn1p Is Involved in Structuring the Cortical Endoplasmic Reticulum. *Mol Biol Cell*. 2006;17(7):3009-3020. doi:10.1091/mbc.e06-01-0080
372. Kohlwein SD, Eder S, Oh CS, et al. Tsc13p Is Required for Fatty Acid Elongation and Localizes to a Novel Structure at the Nuclear-Vacuolar Interface in *Saccharomyces cerevisiae*. *Mol Cell Biol*. 2001;21(1):109-125. doi:10.1128/MCB.21.1.109-125.2001
373. Foo S, Cazenave-Gassiot A, Wenk MR, Oliferenko S. Diacylglycerol at the inner nuclear membrane fuels nuclear envelope expansion in closed mitosis. *J Cell Sci*. 2023;136(3). doi:10.1242/jcs.260568

374. Ottaviano D, Montanari A, de Angelis L, et al. Unsaturated fatty acids-dependent linkage between respiration and fermentation revealed by deletion of hypoxic regulatory *KIMGA2* gene in the facultative anaerobe-respiratory yeast *Kluyveromyces lactis*. *FEMS Yeast Res.* 2015;15(5):fov028. doi:10.1093/femsyr/fov028
375. Camponeschi I, Montanari A, Beccaccioli M, Reverberi M, Mazzoni C, Bianchi MM. Light-Stress Response Mediated by the Transcription Factor *KIMga2* in the Yeast *Kluyveromyces lactis*. *Front Microbiol.* 2021;12. doi:10.3389/fmicb.2021.705012
376. Leadsham JE, Gourlay CW. cAMP/PKA signaling balances respiratory activity with mitochondria dependent apoptosis via transcriptional regulation. *BMC Cell Biol.* 2010;11(1):92. doi:10.1186/1471-2121-11-92
377. Zhang M, Mileykovskaya E, Dowhan W. Gluing the Respiratory Chain Together. *Journal of Biological Chemistry.* 2002;277(46):43553-43556. doi:10.1074/jbc.C200551200
378. Harner ME, Unger AK, Izawa T, et al. Aim24 and MICOS modulate respiratory function, tafazzin-related cardiolipin modification and mitochondrial architecture. *Elife.* 2014;3. doi:10.7554/eLife.01684
379. Xu Y, Anjaneyulu M, Donelian A, et al. Assembly of the complexes of oxidative phosphorylation triggers the remodeling of cardiolipin. *Proceedings of the National Academy of Sciences.* 2019;116(23):11235-11240. doi:10.1073/pnas.1900890116
380. Zhang L, Zhang C, Wang A. Divergence and Conservation of the Major UPR Branch IRE1-bZIP Signaling Pathway across Eukaryotes. *Sci Rep.* 2016;6(1):27362. doi:10.1038/srep27362
381. Mehmood AH, Dong B, Lu Y, Song W, Sun Y, Lin W. The development of an endoplasmic reticulum-targeting fluorescent probe for the imaging of 1,4-dithiothreitol (DTT) in living cells. *Analytical Methods.* 2021;13(19):2204-2208. doi:10.1039/D0AY00443J
382. Mesecke N, Terziyska N, Kozany C, et al. A Disulfide Relay System in the Intermembrane Space of Mitochondria that Mediates Protein Import. *Cell.* 2005;121(7):1059-1069. doi:10.1016/j.cell.2005.04.011
383. Levental I, Lingwood D, Grzybek M, Coskun U, Simons K. Palmitoylation regulates raft affinity for the majority of integral raft proteins. *Proceedings of the National Academy of Sciences.* 2010;107(51):22050-22054. doi:10.1073/pnas.1016184107

384. Cui HJ, Liu XG, McCormick M, et al. PMT1 deficiency enhances basal UPR activity and extends replicative lifespan of *Saccharomyces cerevisiae*. *Age (Omaha)*. 2015;37(3):46. doi:10.1007/s11357-015-9788-7
385. Scrimale T, Didone L, de Mesy Bentley KL, Krysan DJ. The Unfolded Protein Response Is Induced by the Cell Wall Integrity Mitogen-activated Protein Kinase Signaling Cascade and Is Required for Cell Wall Integrity in *Saccharomyces cerevisiae*. *Mol Biol Cell*. 2009;20(1):164-175. doi:10.1091/mbc.e08-08-0809
386. Rutkowski DT, Hegde RS. Regulation of basal cellular physiology by the homeostatic unfolded protein response. *Journal of Cell Biology*. 2010;189(5):783-794. doi:10.1083/jcb.201003138
387. Thibault G, Shui G, Kim W, et al. The membrane stress response buffers lethal effects of lipid disequilibrium by reprogramming the protein homeostasis network. *Mol Cell*. 2012;48(1):16-27. doi:10.1016/j.molcel.2012.08.016
388. Ishiwata-Kimata Y, Le QG, Kimata Y. Induction and Aggravation of the Endoplasmic-Reticulum Stress by Membrane-Lipid Metabolic Intermediate Phosphatidyl-N-Monomethylethanolamine. *Front Cell Dev Biol*. 2022;9. doi:10.3389/fcell.2021.743018
389. Cohen N, Breker M, Bakunts A, et al. Iron affects Ire1 clustering propensity and the amplitude of endoplasmic reticulum stress signaling. *J Cell Sci*. Published online January 1, 2017. doi:10.1242/jcs.201715
390. Aragón T, van Anken E. The Ire1 Twist that Links Proteostatic with Lipostatic Control of the Endoplasmic Reticulum. *Trends Cell Biol*. 2017;27(10):699-700. doi:10.1016/j.tcb.2017.08.010
391. Acharya KR, Lloyd MD. The advantages and limitations of protein crystal structures. *Trends Pharmacol Sci*. 2005;26(1):10-14. doi:10.1016/j.tips.2004.10.011
392. Gardner BM, Walter P. Unfolded Proteins Are Ire1-Activating Ligands That Directly Induce the Unfolded Protein Response. *Science (1979)*. 2011;333(6051):1891-1894. doi:10.1126/science.1209126
393. Karagöz GE, Acosta-Alvear D, Nguyen HT, Lee CP, Chu F, Walter P. An unfolded protein-induced conformational switch activates mammalian IRE1. *Elife*. 2017;6. doi:10.7554/eLife.30700

394. Brooks AJ, Dai W, O'Mara ML, et al. Mechanism of Activation of Protein Kinase JAK2 by the Growth Hormone Receptor. *Science* (1979). 2014;344(6185). doi:10.1126/science.1249783
395. Kimata Y, Oikawa D, Shimizu Y, Ishiwata-Kimata Y, Kohno K. A role for BiP as an adjustor for the endoplasmic reticulum stress-sensing protein Ire1. *Journal of Cell Biology*. 2004;167(3):445-456. doi:10.1083/jcb.200405153
396. Thibault G, Shui G, Kim W, et al. The Membrane Stress Response Buffers Lethal Effects of Lipid Disequilibrium by Reprogramming the Protein Homeostasis Network. *Mol Cell*. 2012;48(1):16-27. doi:10.1016/j.molcel.2012.08.016
397. Promlek T, Ishiwata-Kimata Y, Shido M, Sakuramoto M, Kohno K, Kimata Y. Membrane aberrancy and unfolded proteins activate the endoplasmic reticulum stress sensor Ire1 in different ways. *Mol Biol Cell*. 2011;22(18):3520-3532. doi:10.1091/mbc.e11-04-0295
398. Piccolis M, Bond LM, Kampmann M, et al. Probing the Global Cellular Responses to Lipotoxicity Caused by Saturated Fatty Acids. *Mol Cell*. 2019;74(1):32-44.e8. doi:10.1016/j.molcel.2019.01.036
399. Kamel M, Löwe M, Schott-Verdugo S, Gohlke H, Kedrov A. Unsaturated fatty acids augment protein transport via the SecA:SecYEG translocon. *FEBS J*. 2022;289(1):140-162. doi:10.1111/febs.16140
400. Nilsson I, Ohvo-Rekilä H, Slotte JP, Johnson AE, von Heijne G. Inhibition of Protein Translocation across the Endoplasmic Reticulum Membrane by Sterols. *Journal of Biological Chemistry*. 2001;276(45):41748-41754. doi:10.1074/jbc.M105823200
401. Brambillasca S, Yabal M, Soffientini P, et al. Transmembrane topogenesis of a tail-anchored protein is modulated by membrane lipid composition. *EMBO J*. 2005;24(14):2533-2542. doi:10.1038/sj.emboj.7600730
402. Borradaile NM, Han X, Harp JD, Gale SE, Ory DS, Schaffer JE. Disruption of endoplasmic reticulum structure and integrity in lipotoxic cell death. *J Lipid Res*. 2006;47(12):2726-2737. doi:10.1194/jlr.M600299-JLR200
403. Shen Y, Zhao Z, Zhang L, et al. Metabolic activity induces membrane phase separation in endoplasmic reticulum. *Proceedings of the National Academy of Sciences*. 2017;114(51):13394-13399. doi:10.1073/pnas.1712555114
404. Wu X, Rapoport TA. Translocation of Proteins through a Distorted Lipid Bilayer. *Trends Cell Biol*. 2021;31(6):473-484. doi:10.1016/j.tcb.2021.01.002

405. Wu X, Siggel M, Ovchinnikov S, et al. Structural basis of ER-associated protein degradation mediated by the Hrd1 ubiquitin ligase complex. *Science* (1979). 2020;368(6489). doi:10.1126/science.aaz2449
406. Preston AM, Gurisik E, Bartley C, Laybutt DR, Biden TJ. Reduced endoplasmic reticulum (ER)-to-Golgi protein trafficking contributes to ER stress in lipotoxic mouse beta cells by promoting protein overload. *Diabetologia*. 2009;52(11):2369-2373. doi:10.1007/s00125-009-1506-5
407. Hikiji T, Norisada J, Hirata Y, et al. A highly sensitive assay of IRE1 activity using the small luciferase NanoLuc: Evaluation of ALS-related genetic and pathological factors. *Biochem Biophys Res Commun*. 2015;463(4):881-887. doi:10.1016/j.bbrc.2015.05.132
408. Fang J, Liu M, Zhang X, et al. COPII-Dependent ER Export: A Critical Component of Insulin Biogenesis and β -Cell ER Homeostasis. *Molecular Endocrinology*. 2015;29(8):1156-1169. doi:10.1210/me.2015-1012
409. Roy Chowdhury S, Bhattacharjee C, Casler JC, Jain BK, Glick BS, Bhattacharyya D. ER arrival sites associate with ER exit sites to create bidirectional transport portals. *Journal of Cell Biology*. 2020;219(4). doi:10.1083/jcb.201902114
410. Amodio G, Venditti R, de Matteis MA, Moltedo O, Pignataro P, Remondelli P. Endoplasmic Reticulum stress reduces COPII vesicle formation and modifies Sec23a cycling at ERESs. *FEBS Lett*. 2013;587(19):3261-3266. doi:10.1016/j.febslet.2013.08.021
411. Amodio G, Renna M, Paladino S, et al. Endoplasmic reticulum stress reduces the export from the ER and alters the architecture of post-ER compartments. *Int J Biochem Cell Biol*. 2009;41(12):2511-2521. doi:10.1016/j.biocel.2009.08.006
412. Herzig Y, Sharpe HJ, Elbaz Y, Munro S, Schuldiner M. A Systematic Approach to Pair Secretory Cargo Receptors with Their Cargo Suggests a Mechanism for Cargo Selection by Erv14. *PLoS Biol*. 2012;10(5):e1001329. doi:10.1371/journal.pbio.1001329
413. Pagant S, Wu A, Edwards S, Diehl F, Miller EA. Sec24 Is a Coincidence Detector that Simultaneously Binds Two Signals to Drive ER Export. *Current Biology*. 2015;25(4):403-412. doi:10.1016/j.cub.2014.11.070
414. Fujiwara T, Oda K, Yokota S, Takatsuki A, Ikehara Y. Brefeldin A causes disassembly of the Golgi complex and accumulation of secretory proteins in the endoplasmic

- reticulum. *Journal of Biological Chemistry*. 1988;263(34):18545-18552. doi:10.1016/S0021-9258(19)81393-5
415. Liu ES, Ou JH, Lee AS. Brefeldin A as a regulator of grp78 gene expression in mammalian cells. *Journal of Biological Chemistry*. 1992;267(10):7128-7133. doi:10.1016/S0021-9258(19)50547-6
416. Lev S. Non-vesicular lipid transport by lipid-transfer proteins and beyond. *Nat Rev Mol Cell Biol*. 2010;11(10):739-750. doi:10.1038/nrm2971
417. Helm JR, Bentley M, Thorsen KD, et al. Apoptosis-linked Gene-2 (ALG-2)/Sec31 Interactions Regulate Endoplasmic Reticulum (ER)-to-Golgi Transport. *Journal of Biological Chemistry*. 2014;289(34):23609-23628. doi:10.1074/jbc.M114.561829
418. Kitai Y, Ariyama H, Kono N, Oikawa D, Iwawaki T, Arai H. Membrane lipid saturation activates IRE1 α without inducing clustering. *Genes to Cells*. 2013;18(9):798-809. doi:10.1111/gtc.12074
419. Presley JF, Cole NB, Schroer TA, Hirschberg K, Zaal KJM, Lippincott-Schwartz J. ER-to-Golgi transport visualized in living cells. *Nature*. 1997;389(6646):81-85. doi:10.1038/38001
420. Kuge O, Dascher C, Orci L, et al. Sar1 promotes vesicle budding from the endoplasmic reticulum but not Golgi compartments. *Journal of Cell Biology*. 1994;125(1):51-65. doi:10.1083/jcb.125.1.51
421. Farhan H, Weiss M, Tani K, Kaufman RJ, Hauri HP. Adaptation of endoplasmic reticulum exit sites to acute and chronic increases in cargo load. *EMBO J*. 2008;27(15):2043-2054. doi:10.1038/emboj.2008.136
422. Spear ED, Ng DTW. Stress Tolerance of Misfolded Carboxypeptidase Y Requires Maintenance of Protein Trafficking and Degradative Pathways. *Mol Biol Cell*. 2003;14(7):2756-2767. doi:10.1091/mbc.e02-11-0717
423. Acosta-Alvear D, Zhou Y, Blais A, et al. XBP1 Controls Diverse Cell Type- and Condition-Specific Transcriptional Regulatory Networks. *Mol Cell*. 2007;27(1):53-66. doi:10.1016/j.molcel.2007.06.011
424. Zavala E, Marquez-Lago TT. The Long and Viscous Road: Uncovering Nuclear Diffusion Barriers in Closed Mitosis. *PLoS Comput Biol*. 2014;10(7):e1003725. doi:10.1371/journal.pcbi.1003725

425. Clay L, Caudron F, Denoth-Lippuner A, et al. A sphingolipid-dependent diffusion barrier confines ER stress to the yeast mother cell. *Elife*. 2014;3:e01883. doi:10.7554/eLife.01883
426. Oikawa D, Kitamura A, Kinjo M, Iwawaki T. Direct Association of Unfolded Proteins with Mammalian ER Stress Sensor, IRE1 β . *PLoS One*. 2012;7(12):e51290. doi:10.1371/journal.pone.0051290
427. Ricci D, Marrocco I, Blumenthal D, et al. Clustering of IRE1 α depends on sensing ER stress but not on its RNase activity. *The FASEB Journal*. 2019;33(9):9811-9827. doi:10.1096/fj.201801240RR
428. Belyy V, Tran NH, Walter P. Quantitative microscopy reveals dynamics and fate of clustered IRE1 α . *Proceedings of the National Academy of Sciences*. 2020;117(3):1533-1542. doi:10.1073/pnas.1915311117
429. Tran NH, Carter SD, de Mazière A, et al. The stress-sensing domain of activated IRE1 α forms helical filaments in narrow ER membrane tubes. *Science (1979)*. 2021;374(6563):52-57. doi:10.1126/science.abh2474
430. Aragón T, van Anken E, Pincus D, et al. Messenger RNA targeting to endoplasmic reticulum stress signalling sites. *Nature*. 2009;457(7230):736-740. doi:10.1038/nature07641
431. Li H, Korennykh A v., Behrman SL, Walter P. Mammalian endoplasmic reticulum stress sensor IRE1 signals by dynamic clustering. *Proceedings of the National Academy of Sciences*. 2010;107(37):16113-16118. doi:10.1073/pnas.1010580107
432. Belyy V, Zuazo-Gaztelu I, Alamban A, Ashkenazi A, Walter P. Endoplasmic reticulum stress activates human IRE1 α through reversible assembly of inactive dimers into small oligomers. *Elife*. 2022;11. doi:10.7554/eLife.74342
433. Ishiwata-Kimata Y, Promlek T, Kohno K, Kimata Y. BiP-bound and nonclustered mode of Ire1 evokes a weak but sustained unfolded protein response. *Genes to Cells*. 2013;18(4):288-301. doi:10.1111/gtc.12035
434. Volmer R, van der Ploeg K, Ron D. Membrane lipid saturation activates endoplasmic reticulum unfolded protein response transducers through their transmembrane domains. *Proceedings of the National Academy of Sciences*. 2013;110(12):4628-4633. doi:10.1073/pnas.1217611110

435. Ishiwata-Kimata Y, Hata T, Kimata Y. Self-association status-dependent inactivation of the endoplasmic reticulum stress sensor Ire1 by C-terminal tagging with artificial peptides. *Biosci Biotechnol Biochem.* 2022;86(6):739-746. doi:10.1093/bbb/zbac038
436. Urra H, Pihán P, Hetz C. The UPRosome – decoding novel biological outputs of IRE1 α function. *J Cell Sci.* 2020;133(15). doi:10.1242/jcs.218107
437. Fu S, Yang L, Li P, et al. Aberrant lipid metabolism disrupts calcium homeostasis causing liver endoplasmic reticulum stress in obesity. *Nature.* 2011;473(7348):528-531. doi:10.1038/nature09968
438. Cunha DA, Hekerman P, Ladrière L, et al. Initiation and execution of lipotoxic ER stress in pancreatic β -cells. *J Cell Sci.* 2008;121(14):2308-2318. doi:10.1242/jcs.026062
439. Hou NS, Gutschmidt A, Choi DY, et al. Activation of the endoplasmic reticulum unfolded protein response by lipid disequilibrium without disturbed proteostasis *in vivo*. *Proceedings of the National Academy of Sciences.* 2014;111(22):E2271-E2280. doi:10.1073/pnas.1318262111
440. Huang LJ, Chen RH. Lipid saturation induces degradation of squalene epoxidase for sterol homeostasis and cell survival. *Life Sci Alliance.* 2023;6(1):e202201612. doi:10.26508/lsa.202201612
441. Hetzer MW. The Nuclear Envelope. *Cold Spring Harb Perspect Biol.* 2010;2(3):a000539-a000539. doi:10.1101/cshperspect.a000539
442. Witkin KL, Chong Y, Shao S, et al. The Budding Yeast Nuclear Envelope Adjacent to the Nucleolus Serves as a Membrane Sink during Mitotic Delay. *Current Biology.* 2012;22(12):1128-1133. doi:10.1016/j.cub.2012.04.022
443. Wang R, Huang A, Wang Y, et al. High-Resolution Microscopy to Learn the Nuclear Organization of the Living Yeast Cells. *Stem Cells Int.* 2021;2021:1-7. doi:10.1155/2021/9951114
444. van de Vosse DW, Wan Y, Wozniak RW, Aitchison JD. Role of the nuclear envelope in genome organization and gene expression. *WIREs Systems Biology and Medicine.* 2011;3(2):147-166. doi:10.1002/wsbm.101
445. Cantwell H, Nurse P. Unravelling nuclear size control. *Curr Genet.* 2019;65(6):1281-1285. doi:10.1007/s00294-019-00999-3

446. Jorgensen P, Edgington NP, Schneider BL, Rupeš I, Tyers M, Fitcher B. The Size of the Nucleus Increases as Yeast Cells Grow. *Mol Biol Cell*. 2007;18(9):3523-3532. doi:10.1091/mbc.e06-10-0973
447. Neumann FR, Nurse P. Nuclear size control in fission yeast. *Journal of Cell Biology*. 2007;179(4):593-600. doi:10.1083/jcb.200708054
448. Walters AD, May CK, Dauster ES, et al. The Yeast Polo Kinase Cdc5 Regulates the Shape of the Mitotic Nucleus. *Current Biology*. 2014;24(23):2861-2867. doi:10.1016/j.cub.2014.10.029
449. Oakes M, Nogi Y, Clark MW, Nomura M. Structural alterations of the nucleolus in mutants of *Saccharomyces cerevisiae* defective in RNA polymerase I. *Mol Cell Biol*. 1993;13(4):2441-2455. doi:10.1128/MCB.13.4.2441
450. Straight AF, Marshall WF, Sedat JW, Murray AW. Mitosis in Living Budding Yeast: Anaphase A But No Metaphase Plate. *Science (1979)*. 1997;277(5325):574-578. doi:10.1126/science.277.5325.574
451. Bhaskara RM, Grumati P, Garcia-Pardo J, et al. Curvature induction and membrane remodeling by FAM134B reticulon homology domain assist selective ER-phagy. *Nat Commun*. 2019;10(1):2370. doi:10.1038/s41467-019-10345-3
452. Zurek N, Sparks L, Voeltz G. Reticulon Short Hairpin Transmembrane Domains Are Used to Shape ER Tubules. *Traffic*. 2011;12(1):28-41. doi:10.1111/j.1600-0854.2010.01134.x
453. Shibata Y, Voss C, Rist JM, et al. The Reticulon and Dp1/Yop1p Proteins Form Immobile Oligomers in the Tubular Endoplasmic Reticulum. *Journal of Biological Chemistry*. 2008;283(27):18892-18904. doi:10.1074/jbc.M800986200
454. Le QG, Ishiwata-Kimata Y, Phuong TH, Fukunaka S, Kohno K, Kimata Y. The ADP-binding kinase region of Ire1 directly contributes to its responsiveness to endoplasmic reticulum stress. *Sci Rep*. 2021;11(1):4506. doi:10.1038/s41598-021-83890-x
455. Kang M, Day CA, Kenworthy AK, DiBenedetto E. Simplified Equation to Extract Diffusion Coefficients from Confocal FRAP Data. *Traffic*. 2012;13(12):1589-1600. doi:10.1111/tra.12008
456. Lippincott-Schwartz J, Snapp EL, Phair RD. The Development and Enhancement of FRAP as a Key Tool for Investigating Protein Dynamics. *Biophys J*. 2018;115(7):1146-1155. doi:10.1016/j.bpj.2018.08.007

457. Zavala E, Marquez-Lago TT. The long and viscous road: uncovering nuclear diffusion barriers in closed mitosis. *PLoS Comput Biol.* 2014;10(7):e1003725. doi:10.1371/journal.pcbi.1003725
458. Jiang Y, Vasconcelles MJ, Wretzel S, et al. Mga2p Processing by Hypoxia and Unsaturated Fatty Acids in *Saccharomyces cerevisiae*: Impact on LORE-Dependent Gene Expression. *Eukaryot Cell.* 2002;1(3):481-490. doi:10.1128/EC.1.3.481-490.2002
459. Kluck RM, Bossy-Wetzel E, Green DR, Newmeyer DD. The Release of Cytochrome c from Mitochondria: A Primary Site for Bcl-2 Regulation of Apoptosis. *Science (1979).* 1997;275(5303):1132-1136. doi:10.1126/science.275.5303.1132
460. Kagan VE, Borisenko GG, Tyurina YY, et al. Oxidative lipidomics of apoptosis: redox catalytic interactions of cytochrome c with cardiolipin and phosphatidylserine. *Free Radic Biol Med.* 2004;37(12):1963-1985. doi:10.1016/j.freeradbiomed.2004.08.016
461. Yin V, Shaw GS, Konermann L. Cytochrome c as a Peroxidase: Activation of the Precatalytic Native State by H₂O₂-Induced Covalent Modifications. *J Am Chem Soc.* 2017;139(44):15701-15709. doi:10.1021/jacs.7b07106
462. Orrenius S, Zhivotovsky B. Cardiolipin oxidation sets cytochrome c free. *Nat Chem Biol.* 2005;1(4):188-189. doi:10.1038/nchembio0905-188
463. Roucou X, Prescott M, Devenish RJ, Nagley P. A cytochrome c -GFP fusion is not released from mitochondria into the cytoplasm upon expression of Bax in yeast cells. *FEBS Lett.* 2000;471(2-3):235-239. doi:10.1016/S0014-5793(00)01404-6
464. Duranteau J, Chandel NS, Kulisz A, Shao Z, Schumacker PT. Intracellular Signaling by Reactive Oxygen Species during Hypoxia in Cardiomyocytes. *Journal of Biological Chemistry.* 1998;273(19):11619-11624. doi:10.1074/jbc.273.19.11619
465. Chandel NS, Budinger GRS, Schumacker PT. Molecular Oxygen Modulates Cytochrome c Oxidase Function. *Journal of Biological Chemistry.* 1996;271(31):18672-18677. doi:10.1074/jbc.271.31.18672
466. Pérez FJ, Vergara R, Rubio S. H₂O₂ is involved in the dormancy-breaking effect of hydrogen cyanamide in grapevine buds. *Plant Growth Regul.* 2008;55(2):149-155. doi:10.1007/s10725-008-9269-4
467. Schenkel LC, Bakovic M. Formation and Regulation of Mitochondrial Membranes. *Int J Cell Biol.* 2014;2014:1-13. doi:10.1155/2014/709828

468. Pfeiffer K, Gohil V, Stuart RA, et al. Cardiolipin Stabilizes Respiratory Chain Supercomplexes. *Journal of Biological Chemistry*. 2003;278(52):52873-52880. doi:10.1074/jbc.M308366200
469. Gu Z, Valianpour F, Chen S, et al. Aberrant cardiolipin metabolism in the yeast taz1 mutant: a model for Barth syndrome. *Mol Microbiol*. 2003;51(1):149-158. doi:10.1046/j.1365-2958.2003.03802.x
470. Ma L, Vaz FM, Gu Z, Wanders RJA, Greenberg ML. The Human TAZ Gene Complements Mitochondrial Dysfunction in the Yeast taz1 Δ Mutant. *Journal of Biological Chemistry*. 2004;279(43):44394-44399. doi:10.1074/jbc.M405479200
471. Barros M. H₂O₂ generation in *Saccharomyces cerevisiae* respiratory pet mutants: effect of cytochrome c. *Free Radic Biol Med*. 2003;35(2):179-188. doi:10.1016/S0891-5849(03)00307-1
472. Chen S, He Q, Greenberg ML. Loss of tafazzin in yeast leads to increased oxidative stress during respiratory growth. *Mol Microbiol*. 2008;68(4):1061-1072. doi:10.1111/j.1365-2958.2008.06216.x
473. Andersen KB, von Meyenburg K. Are growth rates of *Escherichia coli* in batch cultures limited by respiration? *J Bacteriol*. 1980;144(1):114-123. doi:10.1128/jb.144.1.114-123.1980
474. Ragan CI, Reed JS. Regulation of electron transfer by the quinone pool. *J Bioenerg Biomembr*. 1986;18(5):403-418. doi:10.1007/BF00743012
475. Chazotte B, Hackenbrock CR. Lateral diffusion as a rate-limiting step in ubiquinone-mediated mitochondrial electron transport. *J Biol Chem*. 1989;264(9):4978-4985.
476. Nesci S, Trombetti F, Pagliarani A, et al. Molecular and Supramolecular Structure of the Mitochondrial Oxidative Phosphorylation System: Implications for Pathology. *Life*. 2021;11(3):242. doi:10.3390/life11030242
477. Stewart LC, Yaffe MP. A role for unsaturated fatty acids in mitochondrial movement and inheritance. *J Cell Biol*. 1991;115(5):1249-1257. doi:10.1083/jcb.115.5.1249
478. Raimalani V, Panchamia B, Prabha CR. Construction and Characterization of UBC4 Mutants with Single Residues Swapped from UBC5. *Cell Biochem Biophys*. 2020;78(1):43-53. doi:10.1007/s12013-019-00894-1

479. Cook WJ, Jeffrey LC, Xu Y, Chau V. Tertiary structures of class I ubiquitin-conjugating enzymes are highly conserved: Crystal structure of yeast Ubc4. *Biochemistry*. 1993;32(50):13809-13817. doi:10.1021/bi00213a009
480. Rodrigo-Brenni MC, Morgan DO. Sequential E2s Drive Polyubiquitin Chain Assembly on APC Targets. *Cell*. 2007;130(1):127-139. doi:10.1016/j.cell.2007.05.027
481. Hildebrandt ER, Hoyt MA. Cell cycle-dependent degradation of the *Saccharomyces cerevisiae* spindle motor Cin8p requires APC(Cdh1) and a bipartite destruction sequence. *Mol Biol Cell*. 2001;12(11):3402-3416. doi:10.1091/mbc.12.11.3402
482. Bohm S, Lamberti G, Fernandez-Saiz V, Stapf C, Buchberger A. Cellular Functions of Ufd2 and Ufd3 in Proteasomal Protein Degradation Depend on Cdc48 Binding. *Mol Cell Biol*. 2011;31(7):1528-1539. doi:10.1128/MCB.00962-10
483. Hildebrandt ER, Hoyt MA. Cell Cycle-dependent Degradation of the *Saccharomyces cerevisiae* Spindle Motor Cin8p Requires APC^{Cdh1} and a Bipartite Destruction Sequence. *Mol Biol Cell*. 2001;12(11):3402-3416. doi:10.1091/mbc.12.11.3402
484. Shapira O, Goldstein A, Al-Bassam J, Gheber L. Possible physiological role for bi-directional motility and motor clustering of the mitotic kinesin-5 Cin8. *J Cell Sci*. Published online January 1, 2017. doi:10.1242/jcs.195040
485. Taberner FJ, Quilis I, Sendra J, Bañó MC, Igual JC. Regulation of cell cycle transcription factor Swi5 by karyopherin Msn5. *Biochimica et Biophysica Acta (BBA) - Molecular Cell Research*. 2012;1823(4):959-970. doi:10.1016/j.bbamcr.2012.02.009
486. Knapp D, Bhoite L, Stillman DJ, Nasmyth K. The transcription factor Swi5 regulates expression of the cyclin kinase inhibitor p40SIC1. *Mol Cell Biol*. 1996;16(10):5701-5707. doi:10.1128/MCB.16.10.5701
487. Chow THC, Sollitti P, Marmur J. Structure of the multigene family of MAL loci in *Saccharomyces*. *Mol Gen Genet*. 1989;217(1):60-69. doi:10.1007/BF00330943
488. Schuyler SC, Wu YFO, Chen HY, et al. Peptide inhibitors of the anaphase promoting-complex that cause sensitivity to microtubule poison. *PLoS One*. 2018;13(6):e0198930. doi:10.1371/journal.pone.0198930
489. Bruch A, Klassen R, Schaffrath R. Unfolded Protein Response Suppression in Yeast by Loss of tRNA Modifications. *Genes (Basel)*. 2018;9(11):516. doi:10.3390/genes9110516

490. Nedialkova DD, Leidel SA. Optimization of Codon Translation Rates via tRNA Modifications Maintains Proteome Integrity. *Cell*. 2015;161(7):1606-1618. doi:10.1016/j.cell.2015.05.022
491. Steffen KK, McCormick MA, Pham KM, et al. Ribosome Deficiency Protects Against ER Stress in *Saccharomyces cerevisiae*. *Genetics*. 2012;191(1):107-118. doi:10.1534/genetics.111.136549
492. Greenland KB, Ding H, Costanzo M, Boone C, Davis TN. Identification of *Saccharomyces cerevisiae* Spindle Pole Body Remodeling Factors. *PLoS One*. 2010;5(11):e15426. doi:10.1371/journal.pone.0015426
493. Campbell K, Westholm J, Kasvandik S, di Bartolomeo F, Mormino M, Nielsen J. Building blocks are synthesized on demand during the yeast cell cycle. *Proceedings of the National Academy of Sciences*. 2020;117(14):7575-7583. doi:10.1073/pnas.1919535117
494. Bernales S, McDonald KL, Walter P. Autophagy counterbalances endoplasmic reticulum expansion during the unfolded protein response. *PLoS Biol*. 2006;4(12):e423. doi:10.1371/journal.pbio.0040423
495. Garmendia-Torres C, Tassy O, Matifas A, Molina N, Charvin G. Multiple inputs ensure yeast cell size homeostasis during cell cycle progression. *Elife*. 2018;7. doi:10.7554/eLife.34025
496. Han GS, O'Hara L, Carman GM, Siniossoglou S. An Unconventional Diacylglycerol Kinase That Regulates Phospholipid Synthesis and Nuclear Membrane Growth. *Journal of Biological Chemistry*. 2008;283(29):20433-20442. doi:10.1074/jbc.M802903200
497. Micolonghi C, Ottaviano D, di Silvio E, Damato G, Heipieper HJ, Bianchi MM. A dual signalling pathway for the hypoxic expression of lipid genes, dependent on the glucose sensor Rag4, is revealed by the analysis of the KIMGA2 gene in *Kluyveromyces lactis*. *Microbiology (N Y)*. 2012;158(7):1734-1744. doi:10.1099/mic.0.059402-0
498. Burr R, Stewart E v., Shao W, et al. Mga2 Transcription Factor Regulates an Oxygen-responsive Lipid Homeostasis Pathway in Fission Yeast. *Journal of Biological Chemistry*. 2016;291(23):12171-12183. doi:10.1074/jbc.M116.723650
499. Scotchman E, Kume K, Navarro FJ, Nurse P. Identification of mutants with increased variation in cell size at onset of mitosis in fission yeast. *J Cell Sci*. 2021;134(3). doi:10.1242/jcs.251769

500. Hernández-Elvira M, Torres-Quiroz F, Escamilla-Ayala A, et al. The Unfolded Protein Response Pathway in the Yeast *Kluyveromyces lactis*. A Comparative View among Yeast Species. *Cells*. 2018;7(8). doi:10.3390/cells7080106
501. Li W, Okreglak V, Peschek J, et al. Engineering ER-stress dependent non-conventional mRNA splicing. *Elife*. 2018;7. doi:10.7554/eLife.35388
502. Walsh RM, Martin PA. GROWTH OF SACCHAROMYCES CEREVISIAE AND SACCHAROMYCES UVARUM IN A TEMPERATURE GRADIENT INCUBATOR. *Journal of the Institute of Brewing*. 1977;83(3):169-172. doi:10.1002/j.2050-0416.1977.tb06813.x
503. Moreno S, Klar A, Nurse P. Molecular genetic analysis of fission yeast *Schizosaccharomyces pombe*. *Methods Enzymol*. 1991;194:795-823. doi:10.1016/0076-6879(91)94059-I
504. Petersen J, Russell P. Growth and the Environment of *Schizosaccharomyces pombe*. *Cold Spring Harb Protoc*. 2016;2016(3):pdb.top079764. doi:10.1101/pdb.top079764
505. Loewen CJR, Gaspar ML, Jesch SA, et al. Phospholipid metabolism regulated by a transcription factor sensing phosphatidic acid. *Science*. 2004;304(5677):1644-1647. doi:10.1126/science.1096083
506. Hofbauer HF, Gecht M, Fischer SC, et al. The molecular recognition of phosphatidic acid by an amphipathic helix in Opi1. *J Cell Biol*. 2018;217(9):3109-3126. doi:10.1083/jcb.201802027
507. Bochud A, Conzelmann A. The active site of yeast phosphatidylinositol synthase Pis1 is facing the cytosol. *Biochimica et Biophysica Acta (BBA) - Molecular and Cell Biology of Lipids*. 2015;1851(5):629-640. doi:10.1016/j.bbailip.2015.02.006
508. Oelkers P, Cromley D, Padamsee M, Billheimer JT, Sturley SL. The DGA1 Gene Determines a Second Triglyceride Synthetic Pathway in Yeast. *Journal of Biological Chemistry*. 2002;277(11):8877-8881. doi:10.1074/jbc.M111646200
509. Sorger D, Daum G. Synthesis of triacylglycerols by the acyl-coenzyme A:diacyl-glycerol acyltransferase Dga1p in lipid particles of the yeast *Saccharomyces cerevisiae*. *J Bacteriol*. 2002;184(2):519-524. doi:10.1128/JB.184.2.519-524.2002
510. Campomanes P, Zoni V, Vanni S. Local accumulation of diacylglycerol alters membrane properties nonlinearly due to its transbilayer activity. *Commun Chem*. 2019;2(1):72. doi:10.1038/s42004-019-0175-7

511. Renne MF, Bao X, Hokken MW, et al. Molecular species selectivity of lipid transport creates a mitochondrial sink for di-unsaturated phospholipids. *EMBO J.* 2022;41(2). doi:10.15252/embj.2020106837
512. Kojima R, Kajiura S, Sesaki H, Endo T, Tamura Y. Identification of multi-copy suppressors for endoplasmic reticulum-mitochondria tethering proteins in *Saccharomyces cerevisiae*. *FEBS Lett.* 2016;590(18):3061-3070. doi:10.1002/1873-3468.12358
513. Hirano M, Ando R, Shimozone S, et al. A highly photostable and bright green fluorescent protein. *Nat Biotechnol.* 2022;40(7):1132-1142. doi:10.1038/s41587-022-01278-2
514. Kritsiligkou P, Shen TK, Dick TP. A comparison of Prx- and OxyR-based H₂O₂ probes expressed in *S. cerevisiae*. *Journal of Biological Chemistry.* 2021;297(1):100866. doi:10.1016/j.jbc.2021.100866
515. Rael LT, Thomas GW, Craun ML, Curtis CG, Bar-Or R, Bar-Or D. Lipid Peroxidation and the Thiobarbituric Acid Assay: Standardization of the Assay When Using Saturated and Unsaturated Fatty Acids. *BMB Rep.* 2004;37(6):749-752. doi:10.5483/BMBRep.2004.37.6.749
516. Wang J, Fang Z, Gao J, et al. Comparative Study of Cytotoxicity, DNA Damage and Oxidative Stress Induced by Heavy Metals Cd(II), Hg(II) and Cr(III) in Yeast. *Curr Microbiol.* 2021;78(5):1856-1863. doi:10.1007/s00284-021-02454-4
517. Dirmeier R, O'Brien K, Engle M, Dodd A, Spears E, Poyton RO. Measurement of Oxidative Stress in Cells Exposed to Hypoxia and Other Changes in Oxygen Concentration. In: ; 2004:589-603. doi:10.1016/S0076-6879(04)81038-3
518. Kyere-Yeboah K, Denteh J, Liu K, Ye P, Gao EB. Monitoring Nicotinamide Adenine Dinucleotide and its phosphorylated redox metabolism using genetically encoded fluorescent biosensors. *Sens Biosensing Res.* 2019;26:100307. doi:10.1016/j.sbsr.2019.100307
519. Tao R, Zhao Y, Chu H, et al. Genetically encoded fluorescent sensors reveal dynamic regulation of NADPH metabolism. *Nat Methods.* 2017;14(7):720-728. doi:10.1038/nmeth.4306
520. Nguyen PTM, Ishiwata-Kimata Y, Kimata Y. Monitoring ADP/ATP ratio in yeast cells using the fluorescent-protein reporter PercevalHR. *Biosci Biotechnol Biochem.* 2019;83(5):824-828. doi:10.1080/09168451.2019.1574204

521. Yaginuma H, Okada Y. Live cell imaging of metabolic heterogeneity by quantitative fluorescent ATP indicator protein, QUEEN-37C. *bioRxiv*. Published online January 1, 2021:2021.10.08.463131. doi:10.1101/2021.10.08.463131
522. Heacock ML, Abdulaziz EN, Pan X, et al. A genetically encoded tool to increase cellular NADH/NAD⁺ ratio in living cells. *bioRxiv*. Published online January 1, 2022:2022.09.20.508785. doi:10.1101/2022.09.20.508785
523. Ruiz M, Devkota R, Panagaki D, et al. Sphingosine 1-Phosphate Mediates Adiponectin Receptor Signaling Essential For Lipid Homeostasis And Embryogenesis. *bioRxiv*. Published online January 1, 2022:2021.08.12.456080. doi:10.1101/2021.08.12.456080
524. Vasiliauskaitė-Brooks I, Sounier R, Rochaix P, et al. Structural insights into adiponectin receptors suggest ceramidase activity. *Nature*. 2017;544(7648):120-123. doi:10.1038/nature21714
525. Volkmar N, Gawden-Bone CM, Williamson JC, et al. Regulation of membrane fluidity by RNF145-triggered degradation of the lipid hydrolase ADIPOR2. *EMBO J*. 2022;41(19). doi:10.15252/embj.2022110777

7 Supplementary Information

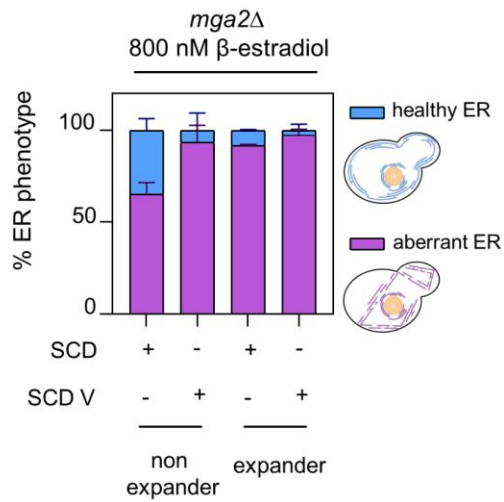


Figure 43 Membrane synthesis – by growth or ER membrane expansion - promotes aberrant ER formation in *mga2Δ*

Shown is the ER phenotype distributions, given in percent, for the β -estradiol expander system employed in the *mga2Δ* background. Depicted are the results for cells cultivated in SCD or SCD V, a medium formulation adapted from Hanscho *et al*²²¹. Plotted is the mean \pm SD of the following data: non-expander SCD (n=3 fov/299 cells); non-expander SCD V (n= 6 fov/ 106 cells); expander SCD (n=3 fov/ 105 cells); expander SCD V (n=6 fov/ 119 cells)

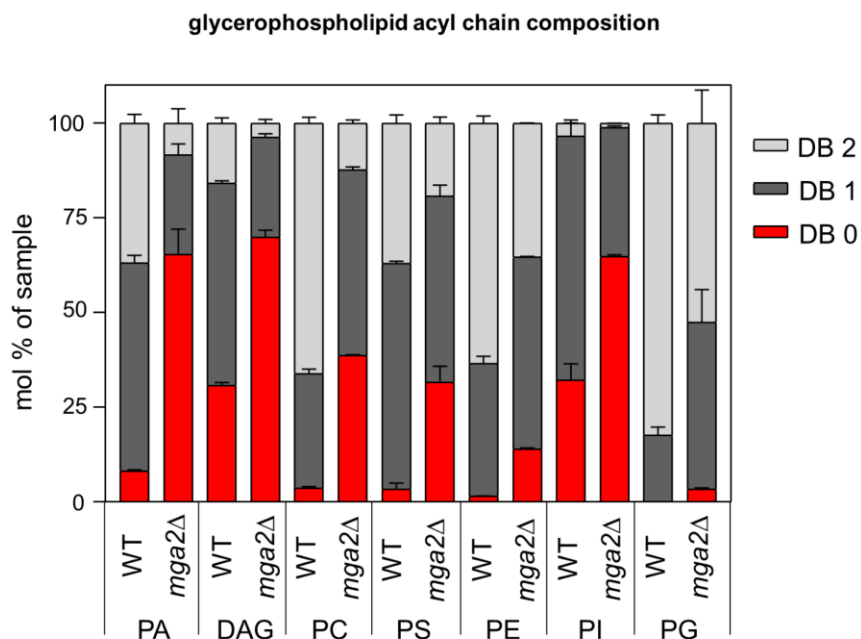


Figure 44 The *mga2Δ* strain accumulates in all glycerophospholipids saturated acyl chains – albeit to various degrees compared to the WT.

Plotted is the mol % for each glycerophospholipid class as the mean \pm SD from three biological replicates for the WT and *mga2Δ* strain. PA = phosphatidic acid; DAG = diacylglycerol; PC = phosphatidylcholine; PS = phosphatidylserine; PI = phosphatidylinositol; PG = phosphatidylglycerol. DB = double bond

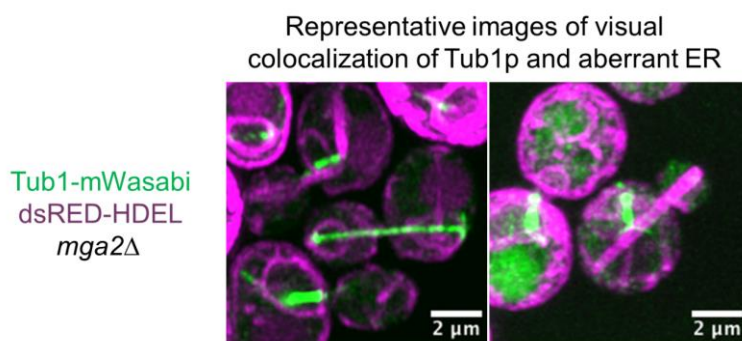


Figure 45 Visual co-localization of aberrant ER and microtubules (Tub1-mWasabi)

Shown are representative images for a visual co-localization of the aberrant ER and the microtubule Tub1p. While the extension of tubulin might be reminiscent of the form and shape of the aberrant ER these two elements do not co-localize once the aberrant ER has formed and the microtubules disassembly in telophase. Scalebars represent the indicated 2 μ m.

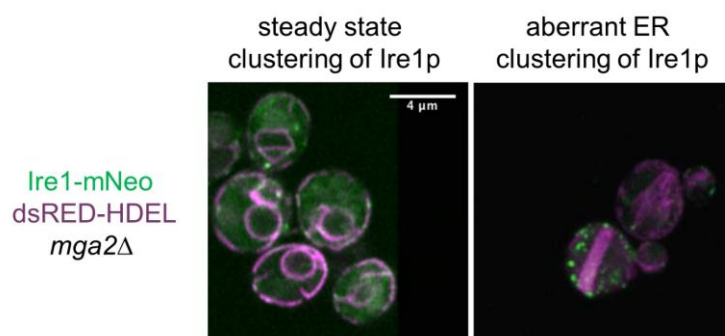


Figure 46 The aberrant ER might be involved in perpetuating the UPR by entrapping Ire1p in subdomains thereby promoting the clustering of Ire1p

Shown is the clustering behavior of Ire1p in a steady state i.e. cells that do not have formed an aberrant ER compared to the clustering behavior for cells harboring the aberrant ER. The number and size of clusters is increased in the aberrant ER cell state and further the aberrant ER seemingly excludes Ire1p. Scalebar represents 4 μ m for both images.

8 Acknowledgements

For everyone who has read this thesis in its entirety, and not just skipped to the acknowledgements, I want to say thank you for taking the time and having the endurance. Hopefully some of the ideas and findings speak to you and will motivate you in progressing with your research.

I want to devote this section to a number of people that supported me since I started out doing research.

I want to start off by saying thank you to my first mentor, Gideon. As my supervisor during my bachelor thesis, you left me with a profound idea what it takes to become an excellent mentor. You had an unmatched enthusiasm to share hard-won knowledge because you wanted me and everyone else to flourish and progress in their scientific endeavors. You enabled that by being an excellent communicator which required you to be an empathic listener at times and speak up in a respectful and candid way at others. In hindsight, I think what really empowered me in doing research was that you allowed me to have an element of autonomy early on in my research after establishing together a solid experimental groundwork. So, thank you again Gideon, for your enthusiasm, trust and personal investment, it is appreciated.

I want to also express my gratitude to Prof. Dr. Rita Bernhardt and Dr. Frank Hannemann. Working with them resulted in my first publication and allowed me to gain insight into the process of going from the bench side to a peer reviewed publication. This process can be painful at times, and therefore it is crucial to have the right people surrounding you when going through such a phase. Thankfully I had an amazing team consisting of old friends and new wonderful colleagues.

I want to specially thank Daniela, my former partner in crime during the bachelor studies. You were not always just smarter and funnier than me, you were also better at looking out for people. I learned a lot from you and don't want to miss the bachelor time. I further don't want to miss the time I spend with Lukas during the master. You have a heart of gold and, as a recurring theme, I am still fascinated with how much rigor, creativity and clarity you addressed research questions.

I also want to acknowledge Robert for giving me the opportunity to do research in his lab. You are a scientist through and through and your passion for science was a great source of motivation. I appreciated the freedom you gave me to explore many areas of my research project.

When I joined Roberts lab I found a team with an outstanding camaraderie and collaborative spirit. Good science does not happen in a void, and just as they say that appetite comes with eating, the best ideas come as you surround yourself with people that are equally excited in doing research.

This thesis reflects the collaborative working atmosphere we have in the lab and, on that note, I want to thank Kristina for allowing me to be a part of her crosslinking story. I will not forget that you offered me the co-authorship on your paper and I am very happy that I could contribute in making your results public. Thank you.

During my first lab tour I was introduced to John who was wearing a lab coat and was amidst of one of his -many to be made- immuno-isolations. I naturally assumed he was the chief student. And to me you always were a very much welcomed oasis of calm and comfort. If you enjoyed working with me half as much as I did working with you, then I feel relieved knowing you had an amazing time. I am really happy and grateful that I had you as a colleague and I wish you nothing but the best for your post doc with Alwin Köhler.

I also want to express my thanks and admiration to Toni. You changed a lot, everybody says that. And you did so in a good way. You were the heart of the lab, always invested in maintaining harmony, balance and naturally "order". Thank you for looking out for everybody and elevating every birthday, holiday or lab party by contributing with your endless creativity. I am looking forward to the day when Stockholm is calling and I will be honored to share the stage with you. Until then I am down with hanging from a wall as you reach for the top boulders/stars.

Philipp is what we call in German a Tausendsassa. As a licensed pilot, hobby beekeeper, programmer and recently approbated medical doctor you impressed me the most with your curiosity and humbleness. Thankfully, I don't have to be humble when I speak of you and I want to say that I am very fortunate to have met you. I am excited for how you will expand the aforementioned list in the future but I am sure that any way you decide it will turn out great.

I am also very happy to have had the chance to work alongside Jona. You are in many aspects a better version of me. At times I could not tell who the mentor and who the mentee is. But I know for a fact that we both should not become German travel guides. May there always be filled candy drawers for you.

I am also glad for Charlotte to have joined the lab. You are naturally funny and have one of the most contagious laughter I have ever encountered that will just light up every room. They say that laughter is the best medicine, going by that logic you already have what it takes to become an excellent doctor and knowing how smart and hard-working of a person you are the rest will come easy to you. I hope I can one day become as great of a friend as you.

Ich möchte mich auch noch bei Aamna bedanken. Du hast nicht nur mich, sondern alle im Labor mit deiner Zielstrebigkeit und deinem Eifer beeindruckt. Ich hoffe, jetzt wo du den Vertrag verstehst den du damals unterschrieben hast, bereust du es nicht zu uns gekommen zu sein. Du bist dein eigener Mensch mit unzähligen Talenten und es braucht keinen Vergleich. Mach weiter dein Ding und denke immer daran halt die Ohren steif!

Despite not being directly responsible for you Louis, I enjoyed complementing your bacterial based *in vitro* work by teaching you some of the *in vivo* yeast methods in the lab. I appreciate that you entrusted me in return with the ultimate symbiosis of the two systems by gifting me a part of your starter culture for bakery purposes. I am striving to replicate your pulchritudinous pretzels which only pale in their beauty when compared to your graceful handwriting.

I guess it is always a compliment when you say that you had wished someone would have been around earlier. And I can say that about Alex. You have quite the delicate humor and from the short time our paths have crossed I know there is much to be learned from you beyond science.

Thank you, Julia, for being an up-beat person and rightful major of the party office. You have created many memorable moments for me and other people in the lab by organizing the many after work get togethers. I also want to say thank you that you not only kept the mini bar, but also your ears open for many of us in times of demanding workload and stress.

I especially want to say thank you to Heike for enduring me all this time. Together we made an amazing duo, made each task at hand look easy with you being the better left, and me being the better right hand. Thank you for being someone I could always rely on and for never getting tired of giving honest feedback.

I also want to kindly thank Sandra. With the very first introduction of your "cake days" you had a profound impact on everybody's holiday scheduling. My former boss Rita used to tell me that wet lab skills translate equally well into baking skills. You would therefore not have only been in her eyes one of the world's greatest scientists but also through mine. People like you, that are equally passionate about science as they about mentoring their people, are desperately needed in science. I wish you nothing but the best.

I also want to express my gratitude and appreciation to all former and present members of the AG Schrul. I especially want to thank Martin for being kind-hearted and able to bring a smile to everyone's face at all times. To Fabian who would have been a brilliant scientist but decided to become a vigilant doctor. Last but not least I want to express my gratitude to Steffi. I really admire your ability to recall information ad hoc and hope I will be one day as knowledgeable, funny and at ease with myself as you.

To everyone who I could not praise in isolation you know that you have had a contribution to this work and together with the vast number of papers cited in this thesis I think it is clear that I view science in this modern day and age as a team effort. An effort that did not start with me and will not end with me. I want to end on two quotes that in an unusual way reflect how the scientific process can be viewed for any novice students that might be overwhelmed by the vast amount of pre-existing knowledge and the speed of its growth.

The first quote I want to share is, naturally, from a smarter person than myself and was brought to my attention by yet another much smarter person than myself and speaks on the continuous character of scientific work and when a dissertation is "finished".

“So eine Arbeit ist eigentlich nie fertig, man muss sie für fertig erklären, wenn man nach Zeit und Umständen das Mögliche getan hat“

Johann Wolfgang von Goethe

The second quote is from yet another outstanding poet and represents an excerpt of his induction ceremony acceptance speech to the Hollywood walk of fame for his lifetime achievements.

„I want to thank me for believing in me, I want to thank me for doing all this hard work. I wanna thank me for having no days off. I wanna thank me for never quitting. I wanna thank me for always being a giver and trying to give more than I receive. I wanna thank me for trying to do more right than wrong. I wanna thank me for being me at all times, Snoop Dogg you a bad mother&\$\$^@“

Snoop Dogg

9 Lebenslauf

Aus datenschutzrechtlichen Gründen wird der Lebenslauf in der elektronischen Fassung der Dissertation nicht veröffentlicht